UNIVERSITY OF LIVERPOOL

National Oceanography Centre
NATURAL ENVIRONMENT RESEARCH COUNCIL

University of Liverpool

Doctoral Thesis

Estimating the distribution of the mass component of sea level trends using tide gauges, altimetry and steric reconstructions.

Author:

Clare Bellingham

Supervisors:

Prof. Ric Williams

Prof. Chris Hughes

Dr. Simon Holgate

Examiners:

Prof. Philip Woodworth

Prof. Mikis Tsimplis

A thesis submitted in fulfilment of the requirements
for the degree of Doctor of Philosophy
in the

Department of Earth, Ocean and Ecological Sciences
SCHOOL OF ENVIRONMENTAL SCIENCES

June 2015

Declaration of Authorship

I, Clare Bellingham, declare that this thesis titled, 'Estimating the distribution of the mass component of sea level trends using tide gauges, altimetry and steric reconstructions.' and the work presented in it are my own. I confirm that:

- This work was done wholly or mainly while in candidature for a research degree at this University.
- Where any part of this thesis has previously been submitted for a degree or any other qualification at this University or any other institution, this has been clearly stated.
- Where I have consulted the published work of others, this is always clearly attributed.
- Where I have quoted from the work of others, the source is always given. With the exception of such quotations, this thesis is entirely my own work.
- I have acknowledged all main sources of help.
- Where the thesis is based on work done by myself jointly with others, I have made clear exactly what was done by others and what I have contributed myself.

Signed: Clare Bellingham

Date: 10th June 2015

"People ask: Why should I care about the ocean? Because the ocean is the cornerstone of Earth's life support system, it shapes the climate and weather. It holds most of the life on Earth. 97% of Earth's water is there. It's the blue heart of the planet - we should take care of our heart. It's what makes life possible for us. We still have a really good chance to make things better than they are. They won't get better unless we take the action and inspire others to do the same thing. No one is without power. Everybody has the capacity to do something."

Sylvia Earle

UNIVERSITY OF LIVERPOOL

Abstract

Department of Earth, Ocean and Ecological Sciences
SCHOOL OF ENVIRONMENTAL SCIENCES

Doctor of Philosophy

Estimating the distribution of the mass component of sea level trends using tide gauges, altimetry and steric reconstructions.

by Clare Bellingham

The recent global mean sea level rise is dominated by the addition of water to the oceans, accounting for around two thirds of the increase. In contrast, altimetry trends from 1993 to 2010 reveal that the local trends are dominated by the steric contribution, involving density expansion from warming and freshening. We explore an intermediate view between the global and local reconstructions based upon zonal averaging. By combining altimetry or tide gauges along with steric reconstructions, we provide two independent estimates of the zonal average of the mass component of sea level trends. We find that the trend in the increase of mass is spatially dependent and can be partly explained using mass redistribution predictions from gravitational fingerprints. Our two estimates, though, have different zonally averaged patterns. We find that the mass contribution implied by altimetry results in a higher rate of sea level rise in the southern hemisphere and the tropics, while the tide gauges imply a higher rate of rise within the tropics. These different views can be reconciled by the sparse tide gauge data in the southern hemisphere and the tropics. We show that while various land movement corrections at each gauge can alter the magnitude of the trend, this does not impact on the general shape of their latitudinal distributions.

Acknowledgements

This thesis is written with full acknowledgement of the contributions, discussions and insight from my supervisors Ric Williams, Chris Hughes and Simon Holgate. Additional discussions from Mark Tamisiea concerning the fingerprints, Svetlana Jevrejeva concerning tide gauges and land corrections and Simon Williams concerning the annealing code were invaluable.

Thanks to the University of Liverpool and the National Oceanography Centre Liverpool for offering me this valuable and rewarding experience.

With thanks for initial discussions and the use of the Smith et al. (2007) data set from Doug Smith and to everyone at PSMSL for help with using tide gauge data.

Thanks to the University of Hawai'i at Mãnoa, especially to Mark Merrifield and Phil Thompson for inspiring talks and useful comments towards this thesis.

Grateful acknowledgements to NERC for funding this PhD and to the University of Liverpool John Lennon Memorial Scholarship for the award to help with my childcare.

Special thanks to my children Leon, Jessie, Kara and Elliot for the inspiration to keep learning, and to friends and family who make it all worth while.

Contents

List of Figures

List of Tables

Abbreviations

AAO	**A**nt**a**rctic **O**scillation
AO	**A**rctic **O**scillation
ASBO	**A**rctic **S**ynoptic **B**asin-wide **O**bservations
ASL	**A**bsolute **S**ea **L**evel
AVISO	**A**rchiving **V**alidation and **I**nterpretation of **S**atellite **O**ceanographic data
BSL	**B**arystatic **S**ea **L**evel
CCI	**C**limate **C**hange **I**nitiative
CMA	**C**entre **M**ultimissions **A**ltimétrique
CTD	**C**onductivity **T**emperature **D**epth
CNES	**C**entre **N**ational d'**É**tudes **S**patiales
CSIRO	**C**ommonwealth **S**cientific and **I**ndustrial **R**esearch **O**rganisation
ENACT	**E**nhanced ocea**N** data **A**ssimilation and **C**limate predic**T**ion
ESA	**E**uropean **S**pace **A**gency
FOAM	**F**orecasting **O**cean **A**ssimilation **M**odel
GIA	**G**lobal **I**sostatic **A**djustment
GIS	**G**reenland **I**ce **S**heet
GPS	**G**lobal **P**ositioning **S**ystem
GRACE	**G**ravity **R**ecovery **A**nd **C**limate **E**xperiment
GTSPP	**G**lobal **T**emperature-**S**alinity **P**rofile **P**rogram
IERS	**I**nternational **E**arth **R**otation and Reference **S**ystems Service
IOC	**I**ntergovernmental **O**ceanographic **C**ommission
IOD	**I**ndian **O**cean **D**ipole
IPCC	**I**ntergovernmental **P**anel for **C**limate **C**hange
IAPSO	**I**nternational **A**ssociation for the **P**hysical **S**ciences of the **O**ceans

IB	**I**nverse **B**arometer
ITRF	**I**nternational **T**errestrial **R**eference **F**rame
JMSDF	**J**apan **M**aritime **S**elf-**D**efence **F**orce
MBT	**M**echanical **B**athy**T**hermograph
MOC	**M**eridional **O**verturning **C**irculation
NAO	**N**orth **A**tlantic **O**scillation
NASA	**N**ational **A**eronautics and **S**pace **A**dministration
NCEP	**N**ational **C**enters for **E**nvironmental **P**rediction
NOAA	**N**ational **O**ceanic and **A**tmospheric **A**dministration
NODC	**N**ational **O**ceanography **D**ata **C**enter
NOC	**N**ational **O**ceanography **C**entre
PDO	**P**acific **D**ecadal **O**scillation
PSMSL	**P**ermanent **S**ervice for **M**ean **S**ea **L**evel
PSU	**P**ractical **S**alinity **U**nits
RLR	**R**evised **L**ocal **R**eference
RSL	**R**elative **S**ea **L**evel
SAM	**S**outhern **A**nnular **M**ode
SCOR	**S**cientific **C**ommittee on **O**ceanographic **R**esearch
SIRAL	**S**ynthetic **A**perture **I**nterferometric **R**adar **A**ltimeter
SLE	**S**ea **L**evel **E**quivalent
SOI	**S**outhern **O**scillation **I**ndex
SONEL	**S**ystème d'**O**bservation du **N**iveau des **E**aux **L**ittorales
SSH	**S**ea **S**urface **H**eight
SSL	**S**teric **S**ea **L**evel
UHSLC	**U**niversity of **H**awai'i **S**ea **L**evel **C**enter
VLD	**V**ertical **L**and **D**isplacement
WOA	**W**orld **O**cean **A**tlas
WOCE	**W**orld **O**cean **C**irculation **E**xperiment
WOD	**W**orld **O**cean **D**atabase
XBT	e**X**pendable **B**athy**T**hermograph

Symbols

ρ	density	$\mathrm{kgm^{-3}}$
τ	Augmented Dynamic Topography	m
T	Dynamic Topography	m
σ	one standard error	
CT	Conservative temperature	^{o}C
G	Gravitational potential surface	$\mathrm{m^2\ s^{-2}}$
G_o	Geoid	$\mathrm{m^2\ s^{-2}}$
S_A	Absolute Salinity	$\mathrm{g\ kg^{-1}}$
S_P	Practical Salinity	PSU
$\hat{\delta}$	specific volume anomaly	$\mathrm{m^3\ kg^{-1}}$
p	pressure	Pa

Dedicated to

Peter Thomas Bellingham
Clockmaker, father and inspiration
and
Judy Bellingham
Fairtrade Campaigner, mother and inspiration

Chapter 1

Background of Sea Level Trends

Sea levels are currently rising at a rate of 3.2 ±0.4 mm yr^{-1} (Stocker et al., 2013). This is due mostly to the oceans warming and the ice sheets and glaciers melting. This rate is twice the rate of global sea level rise over the last century, meaning that recent sea levels are rising much more rapidly than in the observed past. This is important because a large amount of the Earth's population live in coastal cities and towns and a rise in the global mean sea level increases the risk of flooding and storm surge damage. We can observe from satellites that the Greenland Ice Sheet and many of Earth's glaciers are melting due to the increase in atmospheric and ocean temperatures. Theory tells us that an increase in water into the ocean from melting glaciers and ice sheets will not uniformly spread over the globe. This is because of changes in the gravitational attraction between the former large ice masses and the ocean. The melting ice causes a reduction in this attraction and a decrease in sea level closer to the melt region is what is seen. Equally (or more) important, the solid Earth responds to the changing mass distribution, rising where mass reduced (causing a fall in relative sea level) and falling (causing a rise in relative sea level) where the mass increases. The increase in sea level should be seen much further away. This means that if both of the Earth's ice sheets at polar latitudes lose significant mass, the increase in sea level would be much worse at tropical latitudes, where low lying coasts and islands, deltas and atolls are much more at risk and extreme events are more likely due to increased tropical ocean temperatures. This thesis gives two independent estimates of recent mass trends and the redistribution of this mass to broaden our understanding of these recent changes using observations available to date.

Ocean total volume increases from either an increase in ocean mass, or from ca reduction in the density arising from an increase in ocean temperature or decrease in salinity (termed steric changes). Sea level can be used to estimate changes to ocean total volume, however sea level is also affected by changes in the ocean basins through solid Earth processes including crustal movements, changes to the Earth's spatial distribution of its gravitational field (due to processes such as mantle movement and from changes in ice coverage), that add to changes in sea level due to ocean dynamics forced by many processes such as the overturning circulation and ocean and atmospheric coupling.

The mass component of sea level trends has only been measured directly since March 2002 when the Gravity Recovery and Climate Experiment (GRACE) was launched into orbit. To quantify the trends of the mass component of sea level prior to that we must assume that the mass change can be derived from total sea level minus the contribution to the steric volume change from thermal expansion. This requires knowledge and expertise from many disciplines within the oceanography community. One motivation behind revisiting issues within this thesis is the broad range of expertise at Liverpool within both the University of Liverpool and the National Oceanography Centre Liverpool. Expert knowledge was sourced within the fields of sea level (Dr Simon Holgate, Dr Svetlana Jevrejeva, Prof Chris Hughes, Dr Andrew Matthews, Prof Philip Woodworth) and the Permanent Service for Mean Sea Level (PSMSL), ocean heat content (Prof Ric Williams, Dr Vassil Roussenov), GIA and fingerprint analysis (Dr Mark Tamisiea), satellite altimetry, ocean dynamics (Prof Chris Hughes) and the Global Positioning System (GPS) (Dr Simon Williams). Discussions were also sought from the Sea Level Center at the University of Hawai'i at Mãnoa (UHSLC) with Prof. Mark Merrifield and Dr Philip Thompson. Useful discussion was provided by Prof John Church of Commonwealth Scientific and Industrial Research Organisation (CSIRO) and Dr Catia Domingues (University of Tasmania).

Societally, coastal sea level is of prime importance due to the large number of coastal town and city dwellers and the associated infrastructure. As a climate scientist, it is the change in the global total volume of ocean (from both mass and steric changes) which is important, as this is a real indicator of changes in the climate system. Our study in this thesis assesses the link between the local and the global state of sea level as we provide an estimate of how recent changes to global ocean mass are redistributed over a broad scale. Time scales of global variability

are of a duration that separating natural trends from amplified signals caused by anthropogenic forcing is complex (Cazenave and Llovel, 2010). Leuliette and Willis (2011) estimate that a minimum of 10 years is needed to meaningfully interpret and separate trends in global sea level rise and the mass and steric components.

Ocean heat content and sea level changes are valuable indicators of climate change which are reported by the Intergovernmental Panel on Climate Change Fifth Assessment Report(IPCC AR5) in chapters 3 (Oceans (Rhein et al., 2013)), 4 (Cryosphere (Vaughan et al., 2013)) and 13 (Sea Level (Church et al., 2013)), outlining the results of the most recent research. Many studies have focused on balancing the sea level budget (Gregory et al., 2012, Leuliette and Willis, 2011, Wake et al., 2006). The fluid dynamics of the ocean and it's connectivity to the atmosphere means that in order to make interpretations of sea level change over a period of time, the sea level budget (comprising of mass and steric changes while incorporating crustal, gravitational and dynamical factors) must be closed. By quantifying the causes of sea level change we will be able to better predict and adapt to future changes.

The following sections discuss various aspects to sea level and outline the current published work regarding sea level science within these areas.

1.1 Paleo sea level

Paleo studies point to sea level being much higher than we measure today, at certain points in Earth's history. For instance, during the middle Pliocene (approximately 3.3-2.9 Ma), global climate models estimate that sea level was 20 ±10 m above current levels due to there being less polar and glacial ice (Miller et al., 2012). This reduced ice mass was associated with the Greenland and West Antarctic ice sheets and less associated with the East Antarctic ice sheet (Church et al., 2013).

During the last interglacial around 125,000 years ago, global mean sea level was probably around 6 m above present day values (Dutton and Lambeck, 2012, Kopp et al., 2009). The primary source of the higher sea level compared to sea levels today is again due to mass editions from ice melt from glaciers, West Antarctica and Greenland. The contribution from thermal expansion was thought to be smaller, at around 0.3 ±0.4 m. The largest mass input is thought to have originated

from the Antarctic ice sheet with an input of between 4.1 and 5.8 m (McKay et al., 2011), compared with Greenland's contribution around 2 m. The evidence is lacking to estimate how much mass glaciers added during this period, however current ice mass held within glaciers globally is around 0.6 m of equivalent sea level (Church et al., 2013). I comparison, at the peak of the last glacial period around 20,000 years ago, sea levels were around 120 m lower than those of today (Gornitz, 2009).

1.2 Salt marsh and long tide gauges

For the period covering the past 2000 years, salt marsh records have provided reconstructions of sea level which can be validated using regional tide gauge records for the latest period. These salt marsh proxy records suggest that recent sea level rates increase from the late Holocene to present times by an order of magnitude, from around 0.2 mm yr^{-1} to the rates seen today of around 3 mm yr^{-1} (Gehrels and Woodworth, 2013). Six long tide gauge records date back to the 1700s, although they are all based in north-western Europe. More tide gauges were gradually installed, although that were also located mostly in the northern hemisphere and as they were fixed to land, were sensitive to crustal movement. Due to the inhomogeneous nature of the tide gauge data set, some studies have chosen to sub-sample the data set, excluding gauges affected by large local land movements (Jevrejeva et al., 2006, 2008), or only using those with long continuous time series (Hay et al., 2015, Holgate, 2007, Holgate and Woodworth, 2004).

1.3 The global mean sea level time series

The global sea level curve is reconstructed by, amongst others, both Church et al. (2011) and Jevrejeva et al. (2009) from 1860 onwards. Both curves show a stable or slight increase in trend for the first 30 years of the 20th century. Church et al. (2011) estimate a global mean sea level rise of around 210 mm from 1880-2009 (130 years) making the trend over this period 1.61 mm yr^{-1}. Inter-annual variability of the global mean anomaly in sea level from Church and White (2011) reconstructions is maximum of around 25 mm in 1880 and minimum of around

6 mm in 1988. Most inter-annual variability is within one standard deviation uncertainty estimates.

After 1930 both reconstructions show an increase in rate of sea level rise to around 1.7 ±0.3 mm yr^{-1}. Both global mean sea level curves show decadal variability which is linked to natural variability of varying frequencies linked to regional forcing (Holgate, 2007, Woodworth et al., 2009). The most recent part of the global time series shows the global trend over 1993-2011 (computed using an ensemble mean of five different analyses of altimeter data) reported as 3.2 ±0.6 mm yr^{-1} (Ablain et al., 2015, Church et al., 2011, Leuliette and Scharroo, 2010, Stocker et al., 2013), which is twice the size of the overall trend for the time series.

1.4 The steric contribution

The global mean steric sea level has also increased over the observational period and this increase is estimated at 0.7 mm yr^{-1} for 1972-2008 (Church and White, 2011). The increase over the more recent 1993-2003 period is estimated at 1.3 mm yr^{-1} (Ishii and Kimoto, 2009, Levitus et al., 2009). On average the ocean warming accounts for approximately 1 ±0.3 mm yr^{-1} for 1993-2010 (Cazenave and Llovel, 2010, Stocker et al., 2013). The abyssal ocean is estimated to have contributed 0.1 ±0.15 mm yr^{-1} to this rise (Purkey and Johnson, 2010).

Some of the variability in the global steric curve appears to be linked to major volcanic eruptions which cause cooling over the ocean temporarily, and account for negative anomalies in the time series (Church and White, 2006, Grinsted et al., 2007). The cooling process is forced by the volcanic stratospheric aerosol. Interestingly, Grinsted et al. (2007) find a considerable increase in sea level in the first year after the eruption (9 ±3 mm) which they account for by the initial disturbance to the global hydrological cycle, where the decrease in radiative forcing from the aerosol reduces the ocean evaporation, leading to an anomalous increase in ocean mass from an imbalance in the mass fluxes.

Steric changes account for the component of volume expansion caused by increase in temperature or a decrease in salinity. Over the length of the time series the instruments used to measure these quantities have been developed. Shipboard measurements accounted for most measurements prior to 2000 with the addition of ARGO profiling floats since 2000 (Roemmich et al., 2012). Instrumental biases

have been detected amongst all measuring devices and several corrections are made available for this bias (Gouretski and Koltermann, 2007, Lyman et al., 2010, Wijffels et al., 2008).

In the same way that calculating historical global sea level is problematic due to gaps in spatial and temporal observations, calculating the steric changes from observed measurements faces the same issues. Until fairly recently measurements were confined to the top 700 m of the water column. Considering the overturning circulation of the global ocean this coverage is clearly inadequate, and the contribution of the steric changes within the deep and abyssal ocean are still relatively uncertain today. Ship based measurements from the World Ocean Circulation Experiment (WOCE), an internationally coordinated observations program, has provided unprecedented measurements from 1988-1998, with repeat cruises allowing differences in time to be monitored. Significant warming in the abyssal waters have been reported (Johnson, 2008, Kouketsu et al., 2011, Purkey and Johnson, 2010, 2012) with Church et al. (2011) estimating the thermal expansion rate, including deep and abyssal contributions (below 700 m), was 0.7 ±0.2 mm yr^{-1} for the time period 1972-2008.

Steric estimates for 1993-2003 are estimated at 1.3 mm yr^{-1} (Ishii and Kimoto, 2009, Levitus et al., 2009). The IPCC AR5 (Stocker et al., 2013) states that observations indicate that the steric contribution to sea level rise accounts for 30%-40% of the total observed rate. Cazenave and Llovel (2010) report that for the period 1993-2010, steric sea level is around 1.0 ±0.3 mm yr^{-1}, which is approximately 30% of the trend reported from altimetry measurements. Analysis reveal that the oceans have warmed over all basins (Levitus et al., 2009), and also that there is a spatial dependence of warming trends over certain time periods which often can be linked to events such as El Niño, or are correlated with circulation patterns such as the Meridional Overturning circulation (MOC) (Lozier et al., 2008).

1.5 Global sea level budget

While the global sea level change is reasonably well understood, the individual contribution estimates are still uncertain and exact values have changed even between IPCC AR4 (2007) and IPCC AR5 (2013). New technology provides new data and, as our understanding of the underlying variability of the climate system

increases, our ability to quantify the errors involved improves. Given the sparsity of the historical records understanding the different components of sea level trends is still a challenge, and the true errors involved, rather than statistical errors, are hard to adequately quantify. Estimates of sea level trends are higher over recent periods when compared to a longer time series suggesting that there is also an acceleration in changes of sea level. Domingues et al. (2008) find that rates of sea level trends for 1961-2003 were 1.6 ±0.2 mm yr^{-1}. The budget in their estimates was split such that the steric contribution was 0.7 ±0.5 mm yr^{-1} and the mass contribution based on melting from glaciers and ice caps was 0.8 ±0.5 mm yr^{-1}. They noted that their estimates contained differences in the decadal variability between their estimated total sea level (which compared well with altimetry) and the sum of the contributions of the steric and mass components, highlighting the uncertainties still faced to give exact estimates on short or even decadal time scales of the components of sea level. The sum of their contributions for the later period of 1993-2003 is 2.4 mm yr^{-1}.

Leuliette and Willis (2011) compare components of the sea level budget using ARGO floats for the steric component and GRACE measurements for the mass estimates. They compare the sum of these two components with sea level measured by altimetry. The time series spans 2005-2010, which was the length of the GRACE time series at the time. Both the steric and the mass components increase during this time period, however it can be seen that the rate of increase in mass is greater than the rate of increase in steric results towards the end of the time series.

Jevrejeva et al. (2008) use tide gauges in their study of the mass and steric contributions to sea level and find a correlation of 0.78 between global sea level and global ocean heat content. The difference in the two time series they explain by the introduction of mass caused by fresh water input. They also note that land storage plays a part. Their global sea level trend for the period 1993 to 2010 is 2.4 ±1.0 mm yr^{-1}. They compare this with 2.6 ±0.7 mm yr^{-1} from their calculations of altimetry measurements from TOPEX/Poseidon. Jevrejeva et al. (2008) conclude that 47% of the contribution to global sea level is from glaciers and ice caps, with only 25% from thermal expansion. Prior to this, stated in the IPCC AR4 (Solomon et al., 2007) it was thought that the thermosteric contribution was nearer to 50% of the contribution to sea level rise. Jevrejeva et al. (2008) explain the missing 28% to be partly underestimating the contribution from melting ice

masses and partly from the decadal variability associated with the hydrological cycle and terrestrial storage.

Church et al. (2011) evaluate the sea level budget in a more detailed analysis quantifying contributions from shallow (0-700 m, 0.71 ±0.31 mm yr^{-1}), deep (700-3000 m, 0.07 ±0.10 mm yr^{-1}) and abyssal (300 m-bottom, 0.10 ±0.06 mm yr^{-1}) ocean heat content, estimating a total thermal contribution between 1993-2008 of 0.88 ±0.33 mm yr^{-1}. The mass contribution is detailed in terms of ice contribution and terrestrial storage. They estimate that glaciers and ice caps contribute 0.99 ±0.04 mm yr^{-1} between 1993-2008. Of the ice sheets, they estimate that Greenland contributes 0.31 ±0.17 mm yr^{-1} while Antarctica contributes 0.43 ±0.20 mm yr^{-1} over the same time period leading to a combined contribution from the cryosphere of 1.73 ±0.27 mm yr^{-1}. Terrestrial storage influences the global budget by -0.08 ±0.19 mm yr^{-1} which is the combined effects of groundwater depletion (0.35 ±0.07 mm yr^{-1}), dam retention (-0.30 ±0.15 mm yr^{-1}) and natural storage (-0.14 ±0.10 mm yr^{-1}) for the same time span. Their combined thermal and mass components produce a sea level trend of 2.54 ±0.46 mm yr^{-1}. This is compared with their two total sea level estimates calculated using tide gauges, 2.61 ±0.55 mm yr^{-1} and tide gauge and altimetry combined, 3.22 ±0.41 mm yr^{-1}.

1.6 Altimetric measurements

Since 1992 a near global set of precise sea level measurements (10 day intervals for latitudes ±66°) has been provided by TOPEX/Poseidon and Jason 1 and 2. Cazenave and Llovel (2010) note that global measurements of sea level using altimeters was not initially part of their design. Early precision from the Topex/-Poseidon altimeters was over 5 cm for a single sea surface height measurement (Chelton et al., 2001). Measurements of sea surface height need to be within 1-2 cm in order to enable measuring trends to within around 0.1 mm yr^{-1} which was possible due to the development of corrections and data processing techniques (Leuliette et al., 2004, Nerem et al., 2010, 2006). These corrections allowed for orbit, dry and wet troposphere, the ionosphere, sea state bias, ocean tide and loading tide, combined atmospheric correction (which included the inverse barometer correction), the solid earth tide, the pole tide and some corrections specific to individual instruments (Ablain et al., 2009, Beckley et al., 2007).

The rate of global sea level rise measured by altimetry during 1993-2008 is estimated at 3.4 ±0.4 mm yr^{-1} (Cazenave and Llovel, 2010) when allowing for the ocean basin isostatic response to the last ice age (Peltier, 2004). This estimate compares well within error to other estimates over a similar time period (Ablain et al., 2009, Beckley et al., 2007, Nerem et al., 2006). This rate is reduced slightly to 3.2 ±0.5 mm yr^{-1} for the period 1993-2010 (Church et al., 2013). Satellite altimetry, by sampling on a more regular temporal and spatial scale, has enabled a new perspective on the distribution of global sea level trends. It has been shown that some areas of ocean (western Pacific, North Atlantic, south-eastern Indian ocean and around Australia) have up to 3 times higher rates than the global mean over the same time period (1993-2010) (Cazenave and Llovel, 2010). In other areas (eastern Pacific and the west Indian oceans), trends were lower than the global mean. While the uneven regional distribution of sea level trends was already known from tide gauge measurements, altimetry allows for coverage of the open ocean. Wunsch et al. (2007) describe the regional variability seen as attributed to ocean warming and cooling, atmospheric-ocean freshwater exchanges and redistribution of water masses, emphasizing that the ocean has a long term memory through which observations reflect both recent forcing patterns and historical forcing and past internal changes. This sea level variability then, will probably lead to different geographical patterns of sea level trends in the future to those observed today.

1.7 Mass changes

Measuring the mass component of sea level change has only become a reality with the launch of the Gravity Recovery and Climate Experiment (GRACE) satellites. GRACE is now used to measure mass change in the ocean itself and in the individual components of the cryosphere (ice sheets and glaciers) and terrestrial hydrosphere. Before data from the GRACE satellites was available, ice measurements were either direct and then extrapolated, or models were employed. Globally there are over 100,000 glaciers (Cogley, 2012), with a wide geographical distribution and often in remote and inaccessible locations. Only a very limited number of glaciers have point measurements which have to be then upscaled. Only 31 glaciers have a long time series of measurements (Meier et al., 2007). Prior to 2009 the World

Glacier Inventory only contained around 10% of estimated total global glacier area (Church et al., 2013, Stocker et al., 2013).

The IPCC AR4 estimated that the contribution to sea level rise due to mass addition from glaciers was 0.77 ±0.22 mm yr^{-1} for 1993-2003 (Solomon et al., 2007) although reports from glaciers were highly variable due to the sparse data. Cogley (2012), Stocker et al. (2013) assessment of recent mass loss from glaciers, including those from Greenland and West Antarctica, report an equivalent of sea level rise of 0.94 ± 0.04 mm yr^{-1} for 1993-2009 with the largest loss rates from Arctic Canada and Alaska.

The mass contributions from the Greenland and Antarctic ice sheets are estimated from satellite and airborne measurements. Mass budgets are calculates from accumulation due to snowfall and outflow of icebergs or calving, and run off from snow melt. Greenland's contribution to sea level rise is likely to have increased over the past 2 decades with an estimated contribution of 0.34 ±0.04 mm yr^{-1} for the period 1993-2009 and 0.61 ±0.18 mm yr^{-1} for the period 2005-2009. Antarctica is estimated at contributing 0.24 ±0.09 mm yr^{-1} for the period 1993-2009, and 0.4 ±0.19 mm yr^{-1} for the period 2005-2009. This gives a total mass contribution to sea level rise from both ice sheets of 0.58 ±0.19 mm yr^{-1} for the period 1993-2009, and 1.01 ±0.37 mm yr^{-1} for the period 2005-2009 (Church et al., 2013, Stocker et al., 2013).

In addition to ice melt from glaciers and ice sheets, changes in mass balance of the oceans occur due to changes in land based water storage. Again, observations are inadequate and global hydrological models are used to help assess fresh water storage in rivers, lakes and human built reservoirs, aquifers and wetlands (Church et al., 2013). Location of precipitation is also a factor in the variability of ocean mass. Global mean sea level is seen to be correlated with El Niño and Southern Oscillation (ENSO) indices because during El Niño events, ocean precipitation increases, whereas during La Niña events precipitation increases over land (Llovel et al., 2011). This influence on ocean mass by precipitation was shown by Boening et al. (2012), when a strong La Niña event in 2010 reduced global mean sea level (through a reduction in ocean mass) by 5 cm. From GRACE and ocean models the annual cycle of water mass exchange between the ocean, cryosphere and hydrosphere is equivalent to around 1 cm of sea level (Pugh and Woodworth, 2014, Williams et al., 2014).

Lorbacher et al. (2012) show with a global, coupled ocean sea-ice model that the response of ice-melt to the increase in ocean mass plays a dominant role in the barotropic response of sea level. They have shown that all regions of the global ocean experience sea level rise within 7-8 days after the initialization of polar ice melt through barotropic waves travelling at 200 m s^{-1}. This rapid response is in comparison to the steric changes linked to density changes, where the response is around 100 times slower, through baroclinic wave and advective processes. Interestingly, the heat required to raise the global sea level by 1 cm through thermal expansion is 40-70 times greater than the heat required to melt the equivalent amount of land ice (Leuliette and Willis, 2011).

Obtaining mass estimates from GRACE measurements is not entirely straightforward due to the data resolution, separating the land and ocean measurements, and considering mantle movement. Errors on estimates of ocean mass change can reach 0.5 mm yr^{-1} (Quinn and Ponte, 2010, Stocker et al., 2013). GRACE measurements are also sensitive to mass redistribution due to Global Isostatic Adjustment (GIA). The corrections applied to GRACE measurements associated with GIA can range from 1.2 mm yr^{-1} to 1.7 mm yr^{-1} due to different GIA models giving different results (Chambers and Schröter, 2011, Peltier, 2004, Tamisiea, 2011).

Estimates of the mass contribution to sea level rise from GRACE since 2002 range from 1 mm yr^{-1} to 1.5 mm yr^{-1}, and for the time period 2005-2010 are estimated at 1.1 $\pm$0.6 mm yr^{-1} (Leuliette and Willis, 2011, Stocker et al., 2013). This is a smaller estimate of the mass component that from other sources and possible reasons for this difference could be GIA uncertainty along with other residual errors not yet evaluated within this new technique. The difference could also be due to an error in evaluating melt water from glaciers, with the additional water mass possibly remaining on the continents rather than running into the oceans (Stocker et al., 2013), as this value is significantly lower than the combined estimate from glaciers and ice sheets.

1.8 Large scale variability

All global data sets are influenced significantly by major modes of variability in the climate system. In the Pacific, the Walker circulation produces easterly Trade

winds which result in warm water being moved to the west of the ocean basin. Water is piled up resulting in the sea surface topography within this area being tens of centimetres higher than on the eastern side of the basin. Pressure differences between Tahiti and Darwin define the Southern Oscillation Index (SOI). When the SOI is negative, the Trade winds relax and is associated with an El Niño event. The warm pool of water is transferred from the western to the eastern side of the Pacific basin, raising the sea level and deepening the thermocline. This event happens approximately every 3-7 years. The Pacific is restored to its normal state the following year (La Niña). The Pacific Decadal Oscillation (PDO) also affects Pacific ocean temperatures north of 20° N over longer time scales of 20-30 years. The Indian Ocean Dipole (IOD) is a quasi-periodic oscillation that impacts regional monsoon weather in the Indian ocean. In the Atlantic ocean, the North Atlantic Oscillation (NAO) is defined by the air pressure contrast between the Azores high and the Icelandic low, and provides a measure of the strength and direction of westerly winds, and the jet stream. It is correlated with the Arctic Oscillation (AO). Both the NAO and the AO do not generally follow a particular periodicity. Other modes of large scale variability include the Southern Annular Mode (SAM), or Antarctic Oscillation (AAO), a measure of the meridional pressure gradient in the Southern Ocean and so related to the westerly winds and the Antarctic Circumpolar Current (ACC). Each mode is described in terms of an index based on sea surface temperatures (ENSO, PDO) or air pressures (ENSO, NAO, AO, SAM) (Pugh and Woodworth, 2014). Any time series of mean sea level will contain variability of short and long time scales, and is related to a combination of climate modes.

1.9 Acceleration in sea level

An acceleration in sea level is not assessed in this thesis, but for completion of the current discussion it is worth noting that there are studies revealing an acceleration in sea level trends. Jevrejeva et al. (2008) find an acceleration of 0.01 mm yr^{-2} for 1700-2003. Church and White (2011) estimate the acceleration to be 0.009 ±0.004 mm yr^{-2} for 1900-2009. Woodworth et al. (2011, 2009) note that they observe significant positive and negative accelerations over different times, but that they are consistent with natural climate variability on a regional scale.

Paleo sea level data finds evidence over the past 2,000 years for an increase in sea level trends in the late 19th century (1840–1920) from low rates of change to an order of magnitude increase to recent sea level trends. Long tide-gauge records and reconstructions of global averaged sea level extending back to the 19th century confirm this acceleration (Stocker et al., 2013). The acceleration signal from the salt marsh proxy is seen in both the northern and southern hemispheres (Gehrels and Woodworth, 2013, Stocker et al., 2013).

1.10 The use of zonal averages

The trend in sea level rise has almost doubled from the long term trend of the last century to the recent trend seen over the altimetry period. Some higher rates have though been recorded in the 1940s and late 1970s (Church and White, 2011, Holgate and Woodworth, 2004, Jevrejeva et al., 2008, Mitchum et al., 2010). Merrifield et al. (2009) argue, though, that the recent trend is distinct to earlier decadal variability as the observed trends occur simultaneously in the tropics and southern hemisphere, which is not seen in earlier periods. While this thesis looks at some regional spatial distribution of trends, the main results are shown as latitudinal averages for the following reasons. The poor spatial sampling of the tide gauge data lead to a bias within some areas in the Northern Hemisphere. By interpreting the results as latitudinal averages, the stronger regional trends are down weighted and the focus becomes the broader scale average, providing an intermediate view between global and regional averages. This analysis allows us to compare tide gauges with altimetry to provide two independent views of zonally-averaged sea level trends. This broad scale view is relevant when estimating mass trends due to the expected broad scale redistribution pattern of mass trends. The broad scale view is also a technique to look more closely at the global mass trend signal while not getting too caught up with the regional details, given the relatively large errors still at play within all current measuring techniques of the observational data.

The aspects discussed in this Chapter will be explored further in the following Chapters.

Chapter 2

Theoretical Background

2.1 Introduction

The aim of Chapter 2 is to establish the theoretical background that links the various sea level definitions to one another in a physical manner. We introduce the term Augmented Dynamic Topography (τ) to make our variables consistent, allowing us to compare sea level derived from tide gauges and altimetry, to steric sea level derived using temperature and salinity from ocean profiles. When observing sea level on a global scale over time, we have to incorporate land displacement and changes in the Earth's gravity field. These complex relationships are all defined in Chapter 2 and examined in more detail in Chapters 3, 4 and 5. The results are then used in Chapter 6 to estimate and analyse the recent distribution of ocean mass trends.

Sea level change occurs for many different reasons, such as change in waves, tides, winds, atmospheric pressure, ocean circulation, density and mass contributions. These changes happen over varying time scales. We can measure the tidal effects hourly and daily, seasonally and annually. We look at relationships between sea level and ocean heat content. Regional variability is dominated by the thermal contribution (Cazenave and Llovel, 2010), however its global trend is dominated by the addition of mass, which is currently estimated to account for two thirds of the recent increase in sea level. There is, however, currently a problem with measuring this mass contribution. Our approach is to use trends over latitude bands. This choice is intermediate between the local and the global viewpoint. The motivation for the work follows Merrifield et al. (2009), where an anomalous acceleration

in sea level is diagnosed within the southern and tropical latitudes; Purkey and Johnson (2010), who show that warming in the abyssal ocean is significant to sea level trends; and Tamisiea et al. (2001), who show that the redistribution of mass in the ocean from ice sheet and glacial melt has a non uniform pattern (or fingerprint).

Ocean heat content is examined through changes in the steric height caused by density changes from thermal expansion and changing salinity. Changes in heat content are well correlated with sea level within some ocean basins (Jevrejeva et al., 2008). This trend is not yet fully understood, although links with atmospheric modes and long term oscillations have become apparent through global coverage of sea surface height using satellite altimetry. Understanding this variability is vital to identifying vulnerable coastlines and making sea level predictions as sea levels rise during decades to come.

The problem with all components relating to sea level is the lack of data that we have, from the thin and clustered spatial distribution of tide gauges and short altimetry records, to sparse temperature and salinity data and even more limited bottom pressure records. This lack of data also extends to measurements of ice caps and glaciers, where large uncertainties remain as to the amount of melt water entering the oceans and the effects of this mass redistribution. At a time when sea level is changing rapidly, new technology has also increased. Satellite altimetry has revealed regional variability of sea level trends, and ARGO floats now provide temperature and salinity data to 2000 m, but because the length of these new time series is short, natural variability can mask long term trends. All uncertainty within the measurements add to the value of the error.

This thesis examines total sea level as well as its individual components of **steric** and **mass** related sea level. Volume expansion and contraction occur due to changes in temperature and/or salinity. The mean mass component changes sea level through the addition and subtraction of water to the ocean. This can occur through evaporation and precipitation, river run off, water storage on land and melting/accumulation of ice caps and glaciers. Changes to the regional mass component of sea level can also occur through changes in water mass circulation. Natural variability of both the steric and mass components occurs on short, seasonal and longer, decadal time-scales.

Comparing measurements from different systems is a complex issue. The measuring reference frame of each system must be carefully considered and ultimately corrections need to be applied to bring all measuring systems into the same reference frame. The theoretical background sets the scene for how each measured component is linked and how these corrections need to be applied.

2.1.1 Mean sea level

We define mean sea level MSL as sea level averaged over time (typically one year). Longer trends in sea level are changes to the mean sea level and are an important indicator of climate change. The distribution of mean sea level trends is observed to have regional complexity. Long term changes to mean sea level have a significant impact on the likelihood of higher frequency of extreme events. For example, on the east coast of England, an increase in the local mean sea level by 15 cm can double the frequency of flooding events because the high tides during storm surges are raised (Woodworth and Blackman, 2004).

2.1.2 Geoid and definitions

The geoid is a surface which is perpendicular to the local direction of gravity (Hughes and Bingham, 2008). If the oceans were not influenced by currents or atmospheric forcing then sea level (the ocean surface) would coincide exactly with the geoid (Pugh and Woodworth, 2014). Ocean dynamics cause the sea surface to depart from the geoid and this distance (from the geoid to the dynamical ocean surface) is called the dynamic topography T. The geoid undulates by up to ±100 m globally (Hughes and Bingham, 2008). This gravity field is a combination of both the mass composition of the Earth and the centrifugal forces. Global measurements of the geoid G_o and it's temporal variability have only been possible since GRACE was launched in 2002.

The definition of the geoid has varied within literature and the Earth science communities since it was initially defined in 1873 (Listing, 1873). Geodesists denote the geoid as a defined equipotential surface (W_0). The value of this potential value is 62,636,856.0 m^2 s^{-2} in the International Earth Rotation and Reference Systems Service (IERS) conventions (IERS, 2010, Pugh and Woodworth, 2014).

There are an infinite number of surfaces with a constant potential. The definition of the gravitational surface G is defined within this thesis as an equipotential surface over the Earth, with a geopotential that nearest matches the observed mean sea level MSL. This surface will change over time as physical processes affect the Earth's spatial distribution of the gravitational field. These processes include movement of the Earth's mantle, land displacement and ice growth or ice melt.

2.1.3 Basic definitions

ASL	=	Absolute Sea Level (the height above the ellipsoid)
RSL	=	Relative Sea Level (height above Earth's crust, or ocean thickness)
MSL	=	Mean Sea Level (annual average of sea level)
VLD	=	Vertical Land Displacement (height of Earth's crust relative to ellipsoid)
SSL	=	Steric Sea Level (Density related component)
BSL	=	Barystatic Sea Level (Mass component)
G_o	=	Geoid (height of the gravity field above the ellipsoid)
G	=	Gravitational potential surface
T	=	Dynamic Topography (height of sea level above G)
τ	=	Augmented Dynamic Topography ($T + \overline{RSL}$)
V	=	Ocean Volume
A	=	Ocean Area
$\overline{RSL}$	=	V/A

where overline represents an average over the area of the ocean.

2.1.4 Absolute and Relative Sea Level

$$\underbrace{\Delta ASL}_{\substack{\text{Change in}\\ \text{absolute sea level}}} = \underbrace{\Delta RSL}_{\substack{\text{Change in}\\ \text{relative sea level}}} + \underbrace{\Delta VLD}_{\substack{\text{Change in}\\ \text{Vertical Land}\\ \text{Displacement}}} \tag{2.1}$$

Our sea level data is obtained from both tide gauges and satellite altimeters. Tide gauges record what we define as *relative* sea level (RSL), where the sea level is measured from land and is relative to a fixed benchmark on the land. Each gauge is referenced to its own benchmark located within close proximity to the gauge. Tide gauges have our longest time series of sea level, some of which date back over 200 years. RSL represents sea surface height measured relative to the crust

over the whole basin. Tide gauges are a measure of this at the coast. Sea level at coastlines are subject to processes that would not be seen in the open ocean, such as western boundary currents.

Altimetry records what we define as *absolute* sea level (ASL) and is the distance of the sea surface above a reference ellipsoid. Measurements are made within a framework based on the centre of mass of the Earth system; the solid Earth plus the ocean and atmosphere. Absolute and relative sea level (and therefore altimetry and tide gauge data) are related through Vertical land displacement (VLD) as shown in equation 2.1. Δ implies the change over time. The exact relationships defined in equation 2.1 become more approximate when measuring them directly with instruments as we are limited to the precision the instruments themselves as well as by data quality from gaps in the time series.

2.1.5 Steric and mass components

$$\Delta RSL = \underbrace{\Delta SSL}_{steric} + \Delta mass \tag{2.2}$$

$$\Delta ASL = \Delta SSL + \Delta mass + \Delta VLD \tag{2.3}$$

Relative sea level changes can be defined by physical processes. The physics can be split into two categories; **steric** and **mass**. The term barystatic has been introduced by Gregory et al. (2012) to describe the mass component of sea level. We use estimates of barystatic sea level BSL in Chapter 6 to compare our reconstructions to the expected theoretical redistribution from weighted fingerprints (Tamisiea et al., 2001). Regionally there will be a tendency for the ocean mass and VLD in equation (2.3) to partially cancel out in order to reduce gravitational anomalies. Locally, when the crust rises the water column shrinks and so the local mass reduces.

Steric change causes sea level rise and fall from volume change due to variation in density. These steric changes can further be split into thermal and haline components. Thermosteric change occurs from heat exchange with the atmosphere and regionally between water masses. Halosteric change refers to the change in density from changes in salinity content.

The mass change involves addition or subtraction of water to the ocean. Processes include evaporation and precipitation, melting of ice sheets and glaciers and water storage on land. Both steric and mass changes can occur locally due to the redistribution of either density or mass as a result of ocean circulation.

2.1.6 Gravitational corrections

$$\Delta T = \Delta \overline{T} + \Delta T' \tag{2.4}$$

$$\Delta ASL = \Delta T + \Delta G \tag{2.5}$$

$$\Delta RSL = \Delta T + \Delta G - \Delta VLD \tag{2.6}$$

In order to compare the measurements from altimetry and tide gauges with ocean processes involving density and mass changes, we must be aware that sea level data contains information resulting from gravitational changes. Gravitational changes occur from change in the distribution of the Earth's mass and are linked to crustal displacement, as well as to ice mass loss, change within the mantle and changes in ocean circulation (Tamisiea and Mitrovica, 2011). Changes in the spatial distribution of the Earth's gravity affect the gravitational surface (G), an equipotential reference surface describing the Earth's gravity field. In the convention we will follow here, G is defined here as the surface where the global area average of the mean dynamic topography ($\overline{T}$) is zero. T is comprised of a global mean $\overline{T}$ plus temporal deviation from that mean, T' as set out in equation (2.4). Change to the global mean sea level then changes $\overline{G}$ rather than $\overline{T}$, which is defined to be zero. The value of G is adjusted with changes in $\overline{RSL}$ and $\overline{ASL}$ so that $\overline{T}$ remains zero. Equations (2.5) and (2.6) describe the dynamic topography in terms of absolute and relative sea level.

While the theory is relatively simple, in practice measurements of changes to the geoid G_o and any equipotential gravitational surface G are only recently becoming available through satellite gravitational measurements. The Gravity Recovery and Climate Experiment (GRACE) satellites were launched in 2002 (Adam, 2002). GRACE enables measurements of the difference from the mean of G, or G'. Change in G as a result of GIA (ΔG_{GIA}) is modelled using mass redistribution models (Peltier, 2004, Tamisiea, 2011).

2.1.7 Crustal Motion

$$\Delta VLD = \Delta VLD_{GIA} + \Delta VLD_{nonGIA} \tag{2.7}$$

$$\Delta G = \Delta G_{GIA} + \Delta G_{nonGIA} \tag{2.8}$$

We can now go on to further define crustal motion as the vertical component of land displacement of Earth's crust. VLD occurs, for example from local effects such as subsidence caused by mining or groundwater extraction, tectonic motion causing abrupt displacement through tremors and earthquakes and also as a rebound effect from ice melt over land. VLD can be decomposed as in equation (2.7). The displacement involves both a current response from ice melting over Greenland, Antarctica and glaciers, as well as an ongoing response from the last glacial maximum around 20,000 years ago. During this time, large areas of land at high latitudes in the northern hemisphere, namely North America and Europe, were under ice several kilometres thick. The solid Earth is viscous and the weight of the ice caused a depression of the land and displacement in the mantle below it. As the process reversed during melting, the loading on the crust decreased. Subsequently the land rebounded and from this uplift the mantle was redistributed. This rebound effect is still ongoing today, generally typically -1 to 2 mmyr^{-1} and reaching up to 10 mmyr^{-1} in parts of Canada. This response is called Glacial Isostatic Adjustment (GIA). The GIA influence is not uniform over the globe, but has different patterns varying according to the mass loss (Tamisiea, 2011), which is shown in Chapter 3, figure (3.9). All other contributions to vertical displacement is grouped together and termed nonGIA effects.

Changes in G can be defined in GIA and nonGIA terms (equation (2.8)). ΔG_{nonGIA} defines all changes to G other than from GIA. This includes any recent melting and uplift effects. We do not explicitly correct for ΔG_{nonGIA} in this thesis, however, we use *fingerprints* (Tamisiea et al., 2001) of the predicted mass redistribution controlling changes in local gravity, to look at recent ice melt in Chapter 6.

2.2 Augmented Dynamic Topography

$$\Delta\tau = \Delta T + \Delta\overline{RSL} \tag{2.9}$$

$$\Delta\overline{\tau} = \Delta\overline{RSL} \tag{2.10}$$

$$\Delta\overline{T} = 0 \tag{2.11}$$

$$\Delta\overline{ASL} = \Delta\overline{G} \tag{2.12}$$

In the ocean model environment, gravitational and crustal changes are ignored and sea level is typically defined as mean sea level (a constant value spatially) plus the dynamic topography. This is termed the Augmented Dynamic Topography (τ) and it is through this term that we can understand the link between absolute and relative sea level and our density related components in subsection 2.1.5.

We have defined the dynamic topography in subsection 2.1.6 as sea level above the surface G. We can state by this definition that $\overline{T}$, the global average dynamic topography $= 0$. This though, precludes T from representing any global mean sea level change. Using Augmented Dynamic Topography, τ we can now write equation 2.9, where $\overline{RSL}$ is the mean of relative sea level over the ocean and is what used to be referred to as eustatic sea level.

The volume of the ocean V is the area A multiplied by its average thickness $\overline{RSL}$, equation (2.13).

$$\frac{V}{A} = \overline{RSL} = \overline{\tau} \tag{2.13}$$

This shows that τ represents a form of sea level for which all latitude and longitude values are dynamically maintained.

We can use these relationships to relate τ to our observable quantities ASL, RSL, VLD and G. Starting with equation (2.9), using equation (2.5) to substitute for ΔT and (2.1) to substitute for ΔRSL we obtain

$$\Delta\tau = \Delta ASL - \Delta G + \Delta\overline{ASL} - \Delta\overline{VLD} \tag{2.14}$$

Then using (2.12) to substitute for $\overline{ASL}$ we derive

$$\Delta\tau = \Delta ASL - (\Delta G' + \Delta\overline{VLD}) \tag{2.15}$$

where

$$\Delta G' = \Delta G - \Delta\overline{G} \tag{2.16}$$

This is our relationship between τ and ASL as seen by altimetry. The term $(\Delta G' + \overline{VLD})$ represents the change to ASL with *only* changes to the surface G

and crust, with no change to net ocean volume or dynamical processes (although some of these processes may be due to the addition of mass).

We can also relate τ to RSL. Starting with equation (2.1) to substitute for ASL into equation 2.1 we get

$$\Delta\tau = \Delta RSL + \Delta VLD - (\Delta G' + \Delta\overline{VLD}) \tag{2.17}$$

which becomes

$$\Delta\tau = \Delta RSL - (\Delta G' - \Delta VLD') \tag{2.18}$$

where

$$\Delta VLD' = \Delta VLD - \Delta\overline{VLD} \tag{2.19}$$

This is the relationship between τ and tide gauge measurements. $(\Delta G' - \Delta VLD')$ is the relative sea level which is due to change in the gravitational surface and vertical crustal displacement rather than changes in ocean volume or dynamical processes.

We can think of these corrections to ASL and RSL such that in the absence of changes in ocean volume or dynamical processes, the sea surface, ASL will move with the gravity surface G (except for a constant offset to conserve volume) and the tide gauge will move with the crust VLD.

2.3 Applying observing systems

$$\begin{aligned} \Delta ASL &\approx \Delta ASL_{altimetry} \\ \Delta RSL &\approx \Delta RSL_{tidegauge} \\ \Delta VLD &\approx \Delta VLD_{GPS} \end{aligned}$$

There is not a globally complete set of observational corrections for vertical land displacement, and yet the size of the signal is of the same order of magnitude as that of the trend in sea level. While there are some measurements, these are taken above sea level on land and the crustal displacement below sea level is virtually unknown. We use and examine 3 techniques to estimate land motion. It should be noted, however, that these 3 techniques are not equivalent. Vertical land displacement is caused by both long term (e.g. GIA) and short term (e.g. earth tremors and subsidence) processes. Both the long and short term processes

are local to each tide gauge or altimetry data point. Techniques in section 2.3.1 and 2.3.2 correct for both GIA and nonGIA effects for all land displacement while the technique in subsection 2.3.3 corrects only for the long term GIA trend. We compare the three techniques as there are significant errors attached to each technique, either in the assumptions that they make or due to the lack of data currently available. The approximate sign in the above equations refers to the error associated with the measuring equipment.

2.3.1 VLD correction to tide gauges using altimetry

Tide gauge trends can be corrected for land displacement by using altimetry trends from the nearest location to the tide gauge and over the same time period. Under the assumption that the land displacement trend has been constant over the whole time period of the tide gauge and that the point of the altimetry data is spatially close enough to the tide gauge, then the tide gauge can be corrected for crustal motion over the whole data time series. We arrive at this technique by rearranging equation 2.1. to form equation 2.20.

$$\Delta VLD = \Delta ASL - \Delta RSL \tag{2.20}$$

Using this technique to correct the tide gauge over the altimetry period is the same as sub-sampling the altimetry record at tide gauge sites. We then remove ΔG using the Tamisiea et al. (2001) modelled data to obtain the augmented dynamic topography.

2.3.2 VLD correction to tide gauges using the Global Positioning System (GPS).

We use vertical land displacement data from GPS receivers positioned near to tide gauges to correct for vertical land displacement. The trend from GPS is added to the tide gauge trend to give the land corrected sea level trend from the tide gauge. We equate altimetry and tide gauges using GPS data for the VLD correction using equation (2.1)

There are issues associated with this method. We do not have a GPS station at the exact location of each tide gauge (see section 3.4.5). Some gauges are hundreds

of kilometres from the nearest reliable GPS station. GPS data needs to be selected from the exact tide gauge location to record the correct land displacement. Differences in land displacement effects can be highly variable even within metres of the tide gauge. GPS data is only available for a recent time period. Assumptions have to be made that the trend in crustal motion has been constant over a longer time span. Although there is a very good accuracy with this technique for individual tide gauges, there is a large error when using the whole tide gauge network. This technique connects RSL to ASL by removing the VLD. We use the Tamisiea et al. (2001) modelled data to remove ΔG at each tide gauge location and altimetry point to obtain the augmented dynamic topography τ.

2.3.3 GIA only correction to tide gauges and altimetry

We use a mass redistribution model gridded estimate of GIA from Peltier (2004) and Tamisiea et al. (2001) to correct tide gauges and altimetry for the viscoelastic long term rebound. These models correct for both the land uplift and local gravity changes (affecting the local G from the redistribution of mantle beneath the Earth's crust). We can correct altimetry and tide gauge data by using the nearest value in terms of latitude and longitude location from the GIA model output.
This technique is limited to removing only the model predicted crustal and gravitational movement expected to be due to GIA. Recent and long-term changes not associated with GIA are not removed from the data. There are also differences between versions of model results highlighting that we still cannot predict the GIA response completely accurately.
We use the terms ΔVLD_{GIA} (equation (2.7)) and ΔG_{GIA} (equation (2.8)) only in this correction to obtain the augmented dynamic topography (GIA corrected only).

2.4 Barystatic Sea Level

Within this thesis the term barystatic sea level BSL is used to term the mass component of sea level trends independently to the influence of changes in the gravitational field. The definition of barystatic sea level is derived from earlier equations where τ, RSL, ASL and SSL are defined. Using equation (2.13) to

write equation (2.21),

$$\Delta\tau = \Delta SSL + \Delta BSL \tag{2.21}$$

we then make BSL the subject and combine equation (2.21) with (2.17). Equation (2.23) is then able to describe BSL in terms or RSL. To describe BSL in terms of ASL, equation (2.21) is combined with (2.15) to get equation (2.24)

$$\begin{aligned}
\Delta BSL &= \Delta\tau - \Delta SSL && (2.22)\\
&= \Delta RSL - \Delta SSL + \Delta VLD - (\Delta G' + \overline{\Delta VLD}) && (2.23)\\
&= \Delta ASL - \Delta SSL - (\Delta G' + \overline{\Delta VLD}) && (2.24)\\
& && (2.25)
\end{aligned}$$

In Chapter 6 the $\Delta VLD - (\Delta G' + \overline{\Delta VLD})$ part of equation (2.23) is split into two components, one which is caused by the effects of GIA and one which is caused by *other* causes, which includes recent melting (as well as other causes and errors). The same method is applied to equation (2.24) for the $(\Delta G' + \overline{\Delta VLD})$ part of the equation. This allows us to compare the gravitational fingerprints with the assumption that *other* causes are predominantly from recent melting. It should be noted that as BSL is determined by the dynamic topography, any dynamics also remain in the BSL results.

2.5 Summary

- Within Chapter 2 we have defined our variables; relative, absolute and steric sea level, and shown how they relate to one another physically through the derived term augmented dynamic topography (τ). Chapters 3, 5 and 4 go on to evaluate their respective trends in sea level. These trends are then combined to estimate ocean mass trends in Chapter 6.

- Vertical land displacement corrections and have been defined. Set out are 3 different approaches to correct for VLD; using altimetry, a mass redistribution model (ICE-5G), and the Global Positioning System. These corrections are applied in sections 3.4.4 to 3.4.5 of Chapter 3.

- The effects of changes in the Earth's geopotential arising from the redistribution of mass are accounted for by including changes to the gravitational surface G. We apply these changes in Chapters 3, 4 and 5.

- Barystatic sea level is defined in terms of both RSL and ASL and SSL using equations (2.21, 2.23 and 2.24). Equations (2.23 and 2.24) are used in Chapter 6 to compare our mass trend anaylsis with the gravitational fingerprints (Tamisiea et al., 2001).

Chapter 3

Tide Gauge Trends in Sea Level and the Effects of Different Subsets

In Chapter 3 tide gauges are used to calculate relative sea level trends. Relative sea level trends are then converted into augmented dynamic topography in order to compare with both steric and altimetry observations in Chapters 4 and 5. Our analysis focuses on trends from 1993 to 2010 in order to compare our results with those from altimetry, although some longer trends within this Chapter are shown for comparison due to tide gauges having longer time series available.

Tide gauge data is of high quality, but there are gaps in both the temporal and spatial coverage. Due to this limited sampling, there are different criteria for selecting subsets of gauges, such as selecting long records or having short records with more uniform global coverage. The analysis in this Chapter shows results from 4 different sets of tide gauges: all tide gauges, long time series gauges, a set offering uniform spatial coverage and 500 gauges chosen using an algorithm to balance good spatial coverage with length of time series.

We compare 3 different corrections for Vertical Land Displacement, VLD, as there is not one global solution available. We use model based estimates for Glacial Isostatic Adjustment GIA, the difference of tide gauge and altimetry trends and Global Positioning System measurements.

Our analysis provides reasoning behind the tide gauge choices which are subsequently taken forward into Chapter 6 when estimating the mass component of sea level.

3.1 Introduction

Merrifield et al. (2009) show that the trend in sea level is regionally variable, rather than the same as the global trend. They plot contributions from the north (25°N - 65°N), tropics (25°S - 25°N) and south (25°S - 65°S) and show that variability within the tropics and south are key to understanding the increase in global-average trend over the past 20 years, where sea level rates rose from around 1.7 mm yr^{-1} in the 20th century to around 3.2 mm yr^{-1} between 1993-2010. Merrifield et al. (2009) show that the variability of the trend in the tropics and south has been out of phase for the earlier part of the time series (1955 - 1990), but became in phase after 1990, creating an increase in trend which is seen in the global mean. We explore this interpretation in more depth by further breaking down sea level trends into the steric and mass components and use altimetry (in Chapter 5) to independently verify our results.

Global mean sea level was estimated to have risen at an average rate of 1.7 mm yr^{-1} between 1901 and 1990 (Stocker et al., 2013). The contributions to this global mean was estimated to be 0.37 mm yr^{-1} from thermal expansion due to changes in density, 0.7 mm yr^{-1} from glaciers and -0.11 mm yr^{-1} from changes in land water, leaving a 0.5 mm yr^{-1} residual (potentially accounted for through changes in the ice sheets). One problem with estimating the historical change in global mean sea level using tide gauges is that due to their scattered locations, the redistribution of water may be undetected or misdiagnosed (Pugh and Woodworth, 2014). The global mean sea level variations over 1993-2011 computed using an ensemble mean of five different analyses of altimeter data is reported as 3.2 ±0.6 mm yr^{-1} (Ablain et al., 2015, Church et al., 2011, Leuliette and Scharroo, 2010, Stocker et al., 2013) meaning that the trends for the later years in the times series are twice the size of the earlier years. Our measurements of the contributions to this trend are therefore important for out understanding of the cause of this increase.

Tide gauges were historically set up for local needs and long time series gauges are clustered over the Northern Hemisphere. Global trends are the weighted average

of regional trends although regional variability tends to be much larger than the global trend. Tai (2011) has shown how the global mean sea level can be inferred from 237 tide gauges, but that on short time scales the trends are dominated by natural variability which gives the trend calculation a large error. A global time series of mean sea level in the IPCC AR4 (Solomon et al., 2007) compares a time series from 1950 of coastal tide gauges (Holgate and Woodworth, 2004) with the time series of mean sea level measured by both altimetry (Leuliette et al., 2004) and a reconstructed time series of sea level since 1870, (Church and White, 2006) and shows that they are in good agreement at 90% confidence intervals.

We show variability in 4 variations of the global trend using our 4 different sets of tide gauges and obtain a statistical error (σ) in section 3.6. In Chapter 6 we redefine these errors to better quantify their size. We also explore the effect that the spatial bias of tide gauge distribution has on the time series of global trends by comparing global trends calculated with all gauges (figure (3.18a)) to the time series of all northern hemisphere sea level trends (figure (3.19)).

3.1.1 Regional trends

Causes of regional trends are wide ranging. The high trends in sea level around the western tropical Pacific are now well documented using altimetry data (Cazenave and Llovel, 2010). Merrifield et al. (2012) have shown them to be strongly linked to trade wind variability and well correlated with the Pacific Decadal Oscillation (PDO). Regional trends from local variability can influence the global mean on annual to multi decadal time-scales to the magnitude of ~10 mm yr^{-1}. Merrifield et al. (2012) do not expect this pattern to continue, but to reverse in sign over the east and west Pacific as the Pacific Decadal Oscillation reverses. A similar region of high positive trends in sea level change is found in tide gauges on the Atlantic coast of North America. Sallenger et al. (2012), using tide gauges, show that there is evidence for a large recent decadal acceleration here. This acceleration might be accounted for by changes in the North Atlantic Oscillation, weakening of the gyre system and hence sea level gradients. These events also coincide with melting of the Greenland Ice Sheet (GIS), causing warming and/or freshening of the surface waters of the sub-polar North Atlantic and weakening the pressure gradients of the Atlantic Meridional Overturning Circulation. Calafat et al. (2012) have found that tide gauges exhibit decadal variability of up to 15cm in the North

East Atlantic and Mediterranean and are highly correlated with long-shore winds as well as with the North Atlantic Oscillation and with each other. Significant changes are reported in the Southern Ocean, such as the potential contributor to sea level through the warming of abyssal waters (Purkey and Johnson, 2010) and the upper 1000 m (Gille, 2002, Stocker et al., 2013).

3.2 Tide gauge data

Chapter 3 is a concise study of the effects that different choices make on the results of tide gauge derived trends and provides justification of the choices made within this study over following chapters, especially Chapter 6, where we use selected tide gauge trends combined with steric trends to imply zonally averaged mass trends.

Tide gauge data is provided by the Permanent Service for Mean Sea Level (PSMSL) (Holgate et al., 2012) using the research quality data from the Revised Local Reference (RLR) set. Because tide gauges are all levelled to different bench marks, when comparing gauges on a global level we use annual trends as opposed to sea levels themselves. Only data which has eleven out of twelve months per year is considered sufficient to form their annual average. The RLR data set currently involves 1357 gauges. Each gauge within the tide gauge network is individually managed. They can be influenced locally by natural events such as earthquakes, but also can be affected by human intervention such as gauge upgrading and repositioning while retaining the same name. PSMSL record any local event on their website and the effects of these individual factors has been assessed during this analysis. Data from gauges which do not meet the strict RLR criteria is still available from the metric data set. Figure (3.1) shows the locations of all RLR tide gauges (black circles) and those with data (70% complete, so at least 12 of the 18 years) over the altimetry period within this study of 1993 to 2010 (red dots). The VLD correction was applied to the trend in annual mean (mm yr^{-1}) in each case.

Some studies attempt to overcome the question of spatial selection by choosing gauges which represent well either longer trends (Holgate, 2007), or are globally well spaced (Merrifield et al., 2009). There are valid reasons for gauge selecting and so in this Chapter we look at how 4 different gauge choices affect our zonal average results. These 4 choices are: all tide gauges, long records of 70 years, a set

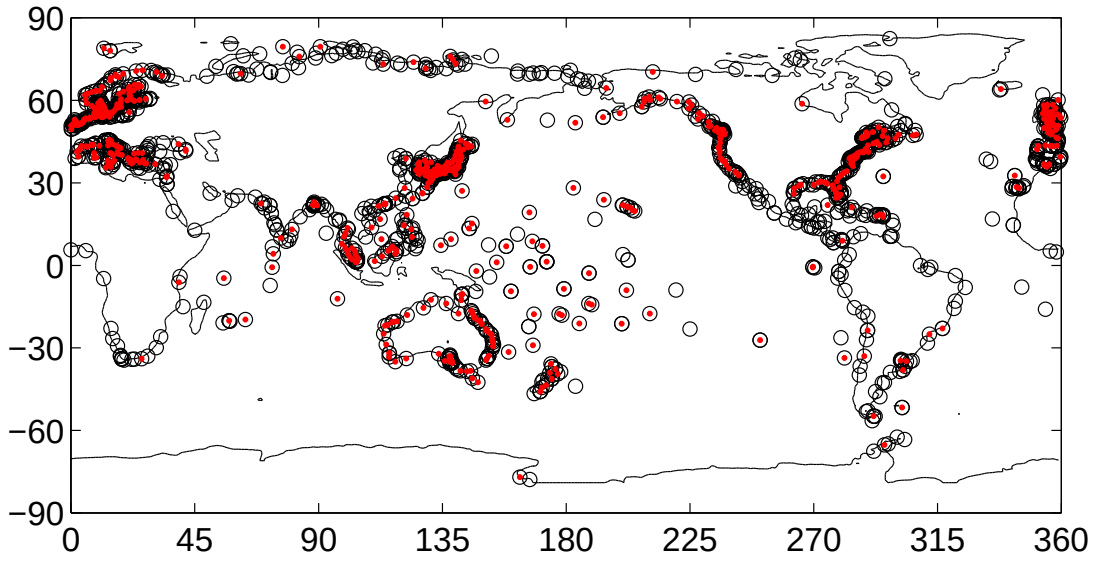

FIGURE 3.1: Map showing locations of all tide gauges in the PSMSL database (black circles) and those with data during 1993 - 2010 (red).

created for uniform spatial coverage and 500 gauges for optimal spatial-temporal coverage. Chapter 3 therefore displays a range of results for 3 VLD solutions for 4 sets of tide gauge.

Sea level responds to changes in air pressure where sea level will rise and fall in response to changes in pressure from the atmosphere. The sea level will rise (fall) in response to a decrease (increase) in local air pressure by approximately 1 cm / mbar (Pugh and Woodworth, 2014) and can reach around ±15 cm. Correcting for this response to atmospheric pressure is termed the Inverse Barometer (IB). Tide gauge corrections are available via atmospheric pressure data from the National Centers for Environmental Prediction (NCEP) reanalysis model as monthly gridded global fields. The correction should be applied using the relation in equation 3.1

$$\Delta z = \frac{\Delta P_a}{\rho g} \tag{3.1}$$

where Δz represents the change in sea level (m), ΔP_a denotes the deviation of atmospheric pressure (mb) from the mean, ρ is the density of seawater and g is the acceleration due to gravity. Average values of 1026 kg m^{-3} and 9.81 m s^{-1} are assumed for ρ and G respectively. Church et al. (2004) estimate that the pressure correction results in an increase of the global sea level rise rate (1950–2000) of about 0.16 mm yr^{-1}. Inverse barometer corrections were not applied to tide gauges

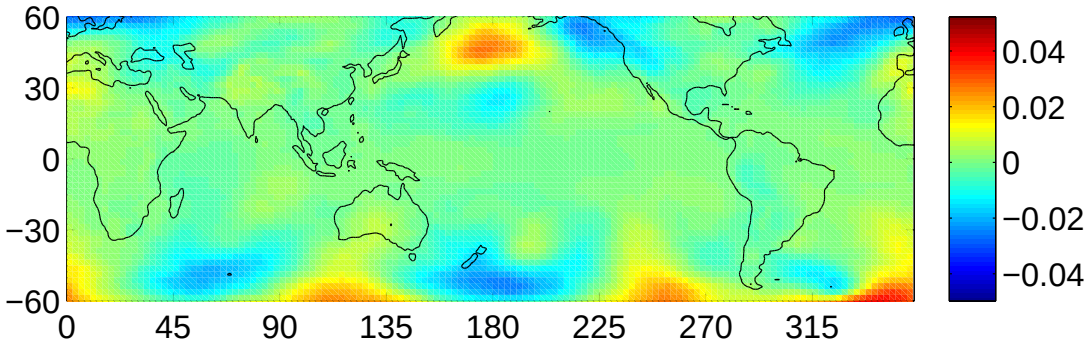

(A) Inverse barometer trend 1993-2010 (mm yr^{-1}).

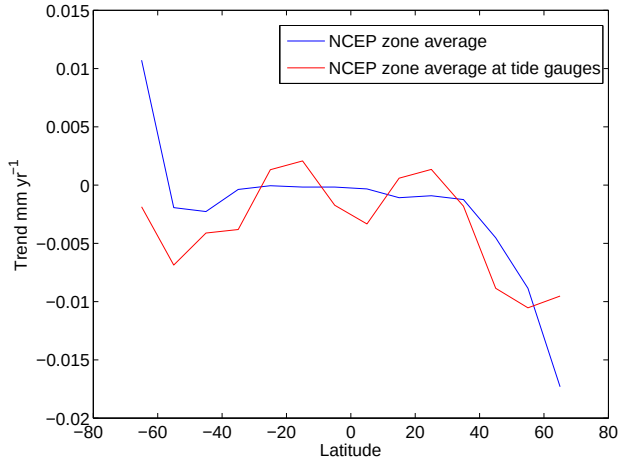

(B) Zonally averaged inverse barometer trend 1993-2010 (mm yr^{-1}).

FIGURE 3.2: Map of the inverse barometer correction for 1993-2010 calculated using equation 3.1 using data downloaded from NCEP (figure (3.2a)). Shown also as zonal averages (figure (3.2b)) both at all grid points (blue) and at tide gauge locations (red).

in the present study under the assumption that the effect would be small over the long time period. This may not be true latitudinally if there were a shift in atmospheric pressure over the southern hemisphere during this time period, for instance. The IB trend between 1993-2010 was therefore examined as a global map (figure (3.2a)) and from this the zonal average in trend was found (figure (3.2b)). Annual mean values were calculated from monthly averages and the trend of the deviation in atmospheric pressure from the mean was calculated and applied to 3.1

The IB trend shows a regional distribution which varies from ±0.04 mm yr^{-1}. Higher latitudes show the highest and lowest trends. When zonally averaged the

IB trend between -50° S and 40° N is practically zero. Northern high latitudes see an overall negative IB trend by up to -0.015 mm yr^{-1} and zonally averaged southern high latitudes see an overall increase by 0.01 mm yr^{-1} (blue line in figure (3.2b)). When the zonal average of the atmospheric trend is calculated only from tide gauge locations with trends that are 70% complete during 1993-2010 (i.e. the tide gauges that would need to be IB corrected for this study), the result is seen from the red line in figure (3.2b) where values vary between approximately ±0.005 mm yr^{-1} except at 50° N - 60° N where the trend value reaches -0.01 mm yr^{-1}. Due to the small magnitude of the IB trend as a function of latitude during the 1993-2010 period it was concluded that the tide gauge results would not be affected by the IB correction.

3.2.1 Calculating tide gauge trends

Trends have been calculated over 18 years. Recent trends for the 18 year period 1993 to 2010 were used to show zonal averages as a function of latitude. This time period was used to minimise the influence of short time scale variability while maximising the available data from altimetry (Chapter 5). This study aims ultimately to determine any changes to the distribution of ocean mass trends and so by using the 18 year trend we filter out much of the daily, seasonal, annual and inter annual variability (Jevrejeva et al., 2008) as well as to dampen any decadal variability (Holgate, 2007).

We note that the nodal tide does have a period of 18.6 years, which is the same length as the trends calculated here. However we expect the nodal tide effect to be small (up to 2 mm in absolute height and therefore associated trends will be much smaller than this) and so do not include the nodal tide correction here (Haigh et al., 2011, Woodworth, 2011). Global trends were calculated as the sum of area weighted zonal means (weighted by the area of ocean within each 10° latitude zone) of 18 year trends and plotted as running means centred on the middle year.

Trends were only included if the records met our criterion of being 70% complete within the 18 year period. The length of this trend meant that exclude shorter tide gauges from the study. Where errors are plotted they represent ± 1 standard error (σ) and are the statistical error based purely on the quality of fit. Where there were gaps in the data, if the gap appeared at the beginning or the end of the 18 year time this did influence the magnitude of the trend value. This will have an

influence on a small number of gauges, especially when all tide gauges were used, however although this is noted, no correction was applied for the influence of end points.

3.3 Choosing a subset

Due to inhomogeneities in the tide gauge data set over time and space, problems can arise associated with spatial clustering (many of the longest gauges are in the Northern Hemisphere around Europe and North America). Using tide gauges for global and regional reconstructions can also introduce bias in that, due to their proximity at the coast they are not representative of the open ocean (Williams and Hughes, 2012). Gauges with shorter time series can add temporal bias by incorporating shorter period natural variability. We explored the influence that the choice of tide gauges makes on the global and zonal average by using four different selections of tide gauges within the database.

Gauge choice, then, becomes a play off between temporal and spatial features and user knowledge of the tide gauge network is advantageous. Our choices of tide gauges are:-

1. All gauges (Holgate et al., 2012). Advantage is that all available data is included, although distorted by short and patchy records.
2. Long records. Better sampling in the Northern Hemisphere but very poor sampling in the Southern Hemisphere.
3. Uniform spatial coverage (Merrifield et al., 2009). Better coverage in the south, but some of the northern signals are now lost.
4. 500 gauges of optimal spatial-temporal coverage. A good compromise between long gauge length and spatial sampling.

The subsets are discussed in the following sections. The number of gauges which goes into each latitude band can be seen in figure (3.3) and the locations of these gauges can be seen in figure (3.4), for each of the 4 subsets. One can see from the maps of the locations of the tide gauges that as the number of gauges used increases, they are not evenly distributed but begin to be weighted most heavily

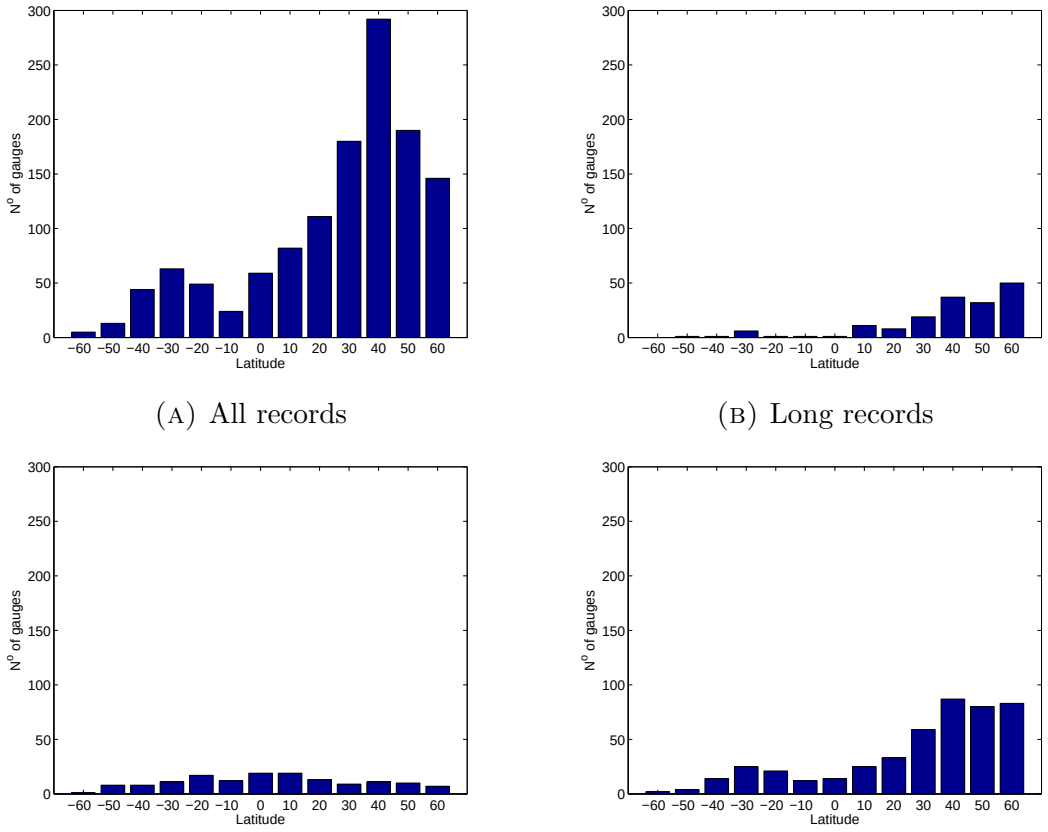

(A) All records

(B) Long records

(C) Uniform spatial coverage records (as used in Merrifield et al. (2009)).

(D) 500 gauge records for optimal coverage (Using the Simon Williams algorithm)

FIGURE 3.3: Number of gauges within each of the 10° latitude bands for the four subsets of tide gauges

along northern coastlines. This means that for the small number of gauges in the long time series subset shown in figure (3.4b) the data is biased to the north. The latitudes for this analysis are limited from 65°S to 65°N due to the lack of available altimetry data above these latitudes for comparison. This means that when using all of the tide gauge records, 96 available records are excluded from the northern hemisphere and 3 are excluded from the southern hemisphere.

3.3.1 All tide gauges

Jevrejeva et al. (2006) show that an increase in the number of tide gauges will substantially reduce the error involved in global and regional sea level trends and therefore we use all tide gauges in the PSMSL RLR data base for our initial evaluation. Figure (3.1) shows all available tide gauges (black circles). There are still long stretches of coastline that are not reached by the tide gauge network,

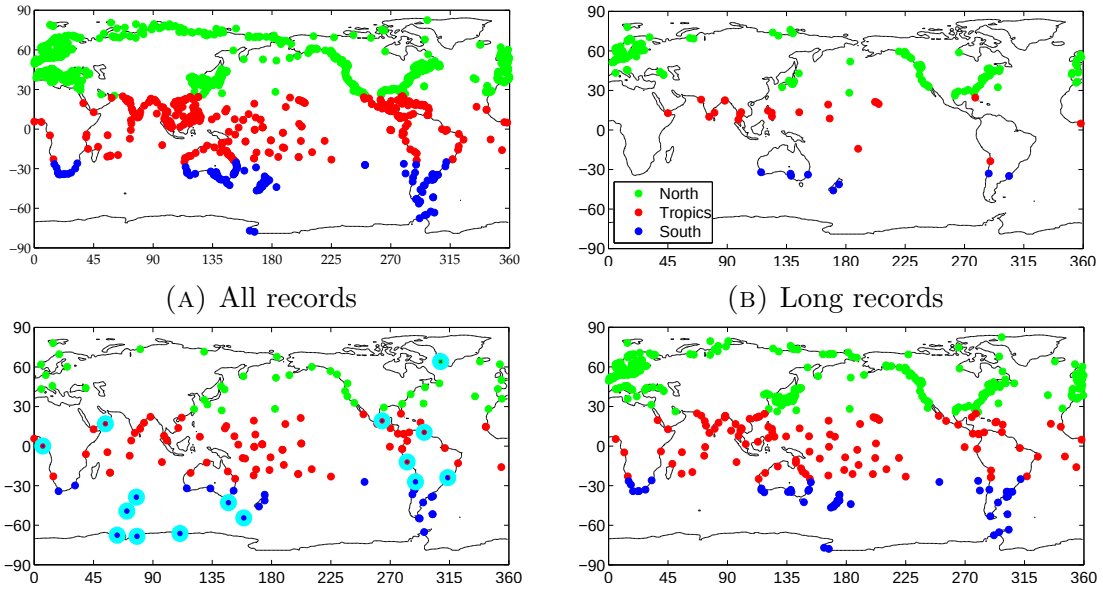

(A) All records

(B) Long records

(C) Uniform spatial coverage records

(D) 500 records

FIGURE 3.4: Location of tide gauge stations for the four subsets of tide gauge records. Coverage is colour coded over the regions north (green), tropics (red) and south (blue). Figure (3.4c) has an extra marker, a cyan ring denoting the station locations within the uniform spatial coverage subset where the data is taken from the metric database of PSMSL. All other data is taken from the RLR database.

such as parts of Africa and Greenland. The red dots in this figure show tide gauges that have data measurements which are 70% complete from 1993 to 2010. With this temporal limit the spatial coverage is further decreased and now a large part of the African coastline and South American coastline are under-sampled. The Pacific Islands provide measurements away from the main continents within the Pacific Ocean but the Atlantic and Indian Ocean are less sampled away from the continents. The Southern Ocean is the most sparsely sampled.

Figure (3.5a) shows the relative sea level from each tide gauge plotted in order of latitude within 10 degree zonal bands. The mean sea surface height from each time series is removed individually. Some coherent signals can be seen between gauges such as some inter annual variability north of around 50° N. There is a slight suggestion of a general increase in sea level towards the later years although it should be noted that the RLR has a different datum at each site and this has not been addressed within this figure other than removing the mean. The main purpose of figure (3.5a) is to show how each subset of gauges is represented as a function of latitude for the time 1955 to 2010. At high Northern latitudes sea level fell, which is consistent with what we would expect from GIA if measured at the

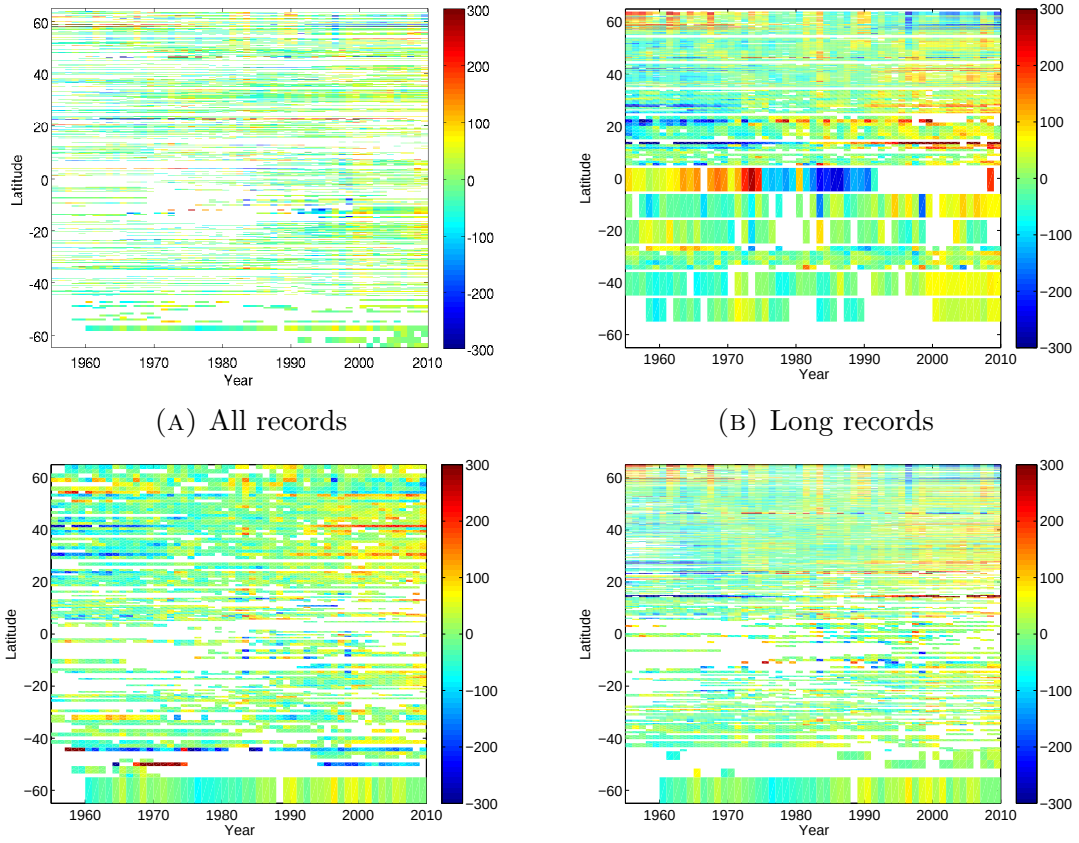

(A) All records

(B) Long records

(C) Uniform spatial coverage records

(D) 500 records

FIGURE 3.5: Relative sea level heights for the time period 1955 to 2010 plotted annually as a function of latitude (mm). The individual mean from each time series has been removed. Tide gauge records are restricted in the plot to their 10° latitude band, therefore at latitude bands where there are many tide gauges, the record data appears as a thinner line and those latitude bands where there are few gauges, the record data line is thicker.

tide gauge sites. Short records and gaps in the data make clearer signals hard to pick out, especially in the tropics and Southern latitudes. While using all gauges has the highest number of records in the South, many of them are short records and in the 60° S latitude band there is only one long record which is the Argentine Islands (also known as Faraday or Vernadsky).

3.3.2 Long time series gauges

It has been shown by Holgate (2007) that 9 long and near continuous records can represent well the decadal trends observed from 168 long tide gauges (Holgate and Woodworth, 2004). Nearby stations show high correlations, showing that they are subject to similar large scale processes. While using fewer tide gauges will increase

the statistical error, there is evidence here that a good quality gauge can represent well the local variability, which can be just as important.

On this basis, we select tide gauges within the PSMSL Revised Local Reference data set which have a minimum 70% complete record of relative sea level from 1955 to 2010. There are 168 tide gauges which fit this criteria within the PSMSL Revised Local Reference database. Many of them, though, are located in the Northern hemisphere and many are clustered on European and North American coastlines, meaning that this relatively small subset of gauges is biased towards the north.

Using this selection of tide gauges increases the temporal coverage but it also increases the spatial variability owing to sparse global coverage. This can be seen in the relative sea level heights of the tide gauge data in figure (3.5b). While the overall temporal coverage is good over the whole of the time period, and the northern hemisphere is well represented, latitudes in the Southern Hemisphere are poorly represented by long time series gauges and the latitudes around 60°S covering the Southern Ocean have no long time series gauges at all. Latitudes around 50°S, 40°S, 20°S, 10°S and the equator only contain one tide gauge to obtain a trend for the whole zone and so is reliant on that gauge not only being accurate, but also being a correct representation of all ocean variability for those latitudes. This is highlighted if we focus on the equatorial tide gauge used for this long time series study. Here the tide gauge is called Takoradi and has the ID 331 in the PSMSL database. Based in Ghana the time series currently runs from 1929-2012. While the first and final parts of the time series have passed the stringent quality control, data from 1966 onwards, before recent data is flagged as unreliable. The tide gauge was decommissioned in 1992 due to age but recent relative sea level has become available again due to the Intergovernmental Oceanographic Commission (IOC) (Woodworth et al., 2009), to the same benchmark. Due to this addition of this new data this gauge remains useful for the long trend but the additional error incurred must be taken into account when only this gauge is included at this latitude.

3.3.3 Uniform spatial coverage gauges

For reference we consider a study from the University of Hawaii Sea Level Centre (Merrifield et al., 2009), which chose a well spaced set of tide gauges avoiding

clustering. Some of the gauges used were not part of the PSMSL RLR database, but were part of the metric database. PSMSL advises caution when using this data as research quality. The metric (non Revised Local Reference) gauges are shown on figure (3.4c) outlined in cyan. The metric gauges chosen were mostly in the Southern Hemisphere but also the African coastline, Greenland and South America. Merrifield et al. (2009) originally included them to fill sparse data areas. As our analysis also studies trends in sea level these metric gauges have been again included with caution.

Another issue which became apparent from cross referencing with published work was that the University of Hawaii Sea Level Centre does not have an identical storage of tide gauge data. There were instances where gauges have different names, or more importantly, a choice may have been made in one data centre to link two data sets and not in the other, leaving small but relevant differences when trends are formed.

3.3.4 500 gauges

To achieve a globally distributed set of sites that balances their location and length of time series we used a simulated annealing algorithm to choose the most optimum set of N tide gauge sites from the total set of tide gauges in the RLR set, M. The spatial cost function is based on the volume created by the convex hull of the locations of the tide gauges. The more evenly distributed across the globe the N sites are, the larger the volume of the convex hull will be. The temporal cost function is simply the length of the time series. The spatial and temporal cost functions are then combined using a weighting scheme that attempts to produce an optimal balance between the two. The annealing algorithm was written by Dr Simon Williams from the National Oceanography Centre, Liverpool.

We compared the results of varying N from 50, 100, 250 and 500 gauges and were confident that in using more gauges (i.e. larger values of N), we were better representing the global mean sea level. This benefit becomes offset as many of the extra gauges included will have short time series. From this analysis we focus on the results of using 500 gauges. The size of the convex hull from these 500 gauges can be seen in figure (3.6). The areas with least representation are in the Southern Ocean and parts of the tropics. Figure (3.3d) shows how the gauges are spread out in terms of latitude bands, figure (3.4d) shows their locations and the

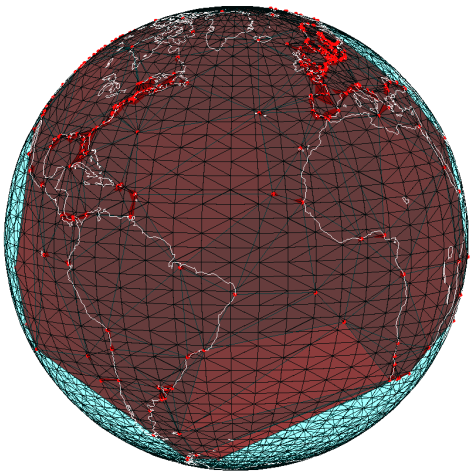

FIGURE 3.6: The convex hull (red space) is the volume of Earth best represented with 500 tide gauges (red dots) chosen by the annealing algorithm written by Dr. Simon Williams of the National Oceanography Centre, Liverpool when given the criteria of best representation of both ocean volume and length of record. (Figure courtesy of Dr. Simon Williams `https://noc.ac.uk/people/sdwil`)

time series data is shown as a function of latitude in figure (3.5d). This subset of tide gauges allows for the patterns between gauges to be seen more clearly and retains a good coverage of gauges in the Southern Hemisphere within the limits of the network. Equatorial regions are still patchy especially for the years 1955 to 1975.

3.3.5 Data analysis

Tide gauge data was only selected from the Revised Local Reference (RLR) data base from PSMSL, except for the uniform spatial coverage subset, where the aim was to use the same tide gauges as in the Merrifield et al. (2009) paper. The RLR tide gauge monthly and annual mean data has all been reduced to a common datum. This reduction is performed by the PSMSL making use of the tide gauge datum history provided by the supplying authority (`http://www.psmsl.org/data/obtaining/rlr.php`). Without knowledge of the datum, time series analysis is unreliable and therefore, tide gauges without provision of full benchmark datum history information are not part of the RLR data set. As previously discussed, tide gauge trends were also not used if there was not 70% complete data between 1993 and 2010. The time series were formed from annual mean values.

The PSMSL criteria for forming the annual mean is that 11 of the 12 months must be available.

Even with full datum history, some tide gauges show large trends which are likely due to local geophysical events affecting the land that the tide gauge is referenced to. The range of trends within a latitude band was assessed by looking at the spread of the data using histograms. This was effective for two reasons. Firstly it allowed the range of trends to make up the zonal average and highlighted any tide gauges with exceptionally high or low trends, that could then be further investigated. PSMSL documentation was again used to ascertain whether an event such as an earthquake had occurred over the length of the time series creating a sharp jump in the time series through the information provided for each tide gauge. Not all large trends are due to extreme events. Decadal and multi-decadal natural variability can also produce large trends depending on the length of the trend and the start and end points of the trend. We made no adjustments for large trends that were not identified as being due to a geophysical event. When events were identified, affected parts of the time series were excluded from the analysis.

Time series of 18 year trends from each tide gauge were plotted together, centred on the middle year, within each 10 degree latitude band to observe how zonal trends developed over time (figures (3.7a - 3.7m). No correction has been made for VLD. For the 18 year trend period from 1993-2010 only the very last data point is relevant and is plotted centred on the mid-point of 2001. Both the individual signature of tide gauge observations and the capture of long time scale trends from the group array are apparent from these figures. Tide gauges experiencing local extreme events are observed and omitted if the event cannot be accounted for within the land movement correction. An example is in figure (3.7j) where a high trend is seen at the tide gauge Miyake Sima (RLR 1060) for 1993-2010. PSMSL documentation records elevated mean levels during 2000-2001 due to island sinking as a result of the volcanic eruption of Oyama during June to August of 2000. Only one tide gauge within the 60^o S latitude band has observational data available in the RLR data base during the years 1993-2010, the Argentine Islands (also known as Faraday and Vernadsky). The trend for this tide gauge is shown in cyan in figure (3.7a). The tide gauge observes long time scale variability which is possibly partly due to land movement caused by changes in glacial thickness. During 1993-2010 the trend is at a lower point of this cycle and therefore provides a negative trend for this zonal average. Another tide gauge within this zonal band is Puerto Soberania

(RLR 1603) which became inactive in 2002. This gauge observed positive trends prior to 2002.

Histograms for all tide gauges can be seen in figure (3.8). These histograms show the tide gauge trends from all tide gauges which have data to meet the criteria between 1993 and 2010 for each of the 13 latitude bands. The trend is shown on the x axis in mm yr^{-1} and the number of gauges within each bin is shown on the y axis. The number within a bin varies from 0 to 9. When there are more tide gauges within a latitude band, the spread of the trends that make up the zonal average tends towards a more Gaussian distribution. The histograms show the distribution of trends in latitude bands where there are only a few gauges does not show this normal distribution. The latitude bands that use more gauges are more likely to have gauges showing the more extreme trends, meaning that some more extreme variability is possibly not being observed at less represented latitude bands. All gauges with trends ±3 standard deviations from the zonal mean were investigated.

The histogram analysis also allowed us to view the spread of the trend values that made up the mean value in each latitude band. When a large number of gauges were used, a normal distribution was observed and can be seen most clearly at latitudes 30 N (figure (3.7j), 40 N (figure (3.7k), 50 N (figure (3.7l) and 60 N (figure (3.7m). This meant that at these latitudes a statistical analysis of the errors was plausible. When only a few tide gauges were within a latitude band, the normal distribution was replaced with a more random distribution of trend values and therefore a statistical error analysis became unreliable (figures (3.7a-3.7i). This provided the motivation to develop some more realistic errors to the mass trends as shown in Chapter 6.

3.4 VLD and G changes

3.4.1 Converting ASL to τ

As described in Chapter 2 we wish to convert the RSL measured by tide gauges to Augmented Dynamic Topography τ. This conversion requires knowledge of vertical land displacement, VLD, and changes in the gravitational potential surface G. We do this in 2 stages.

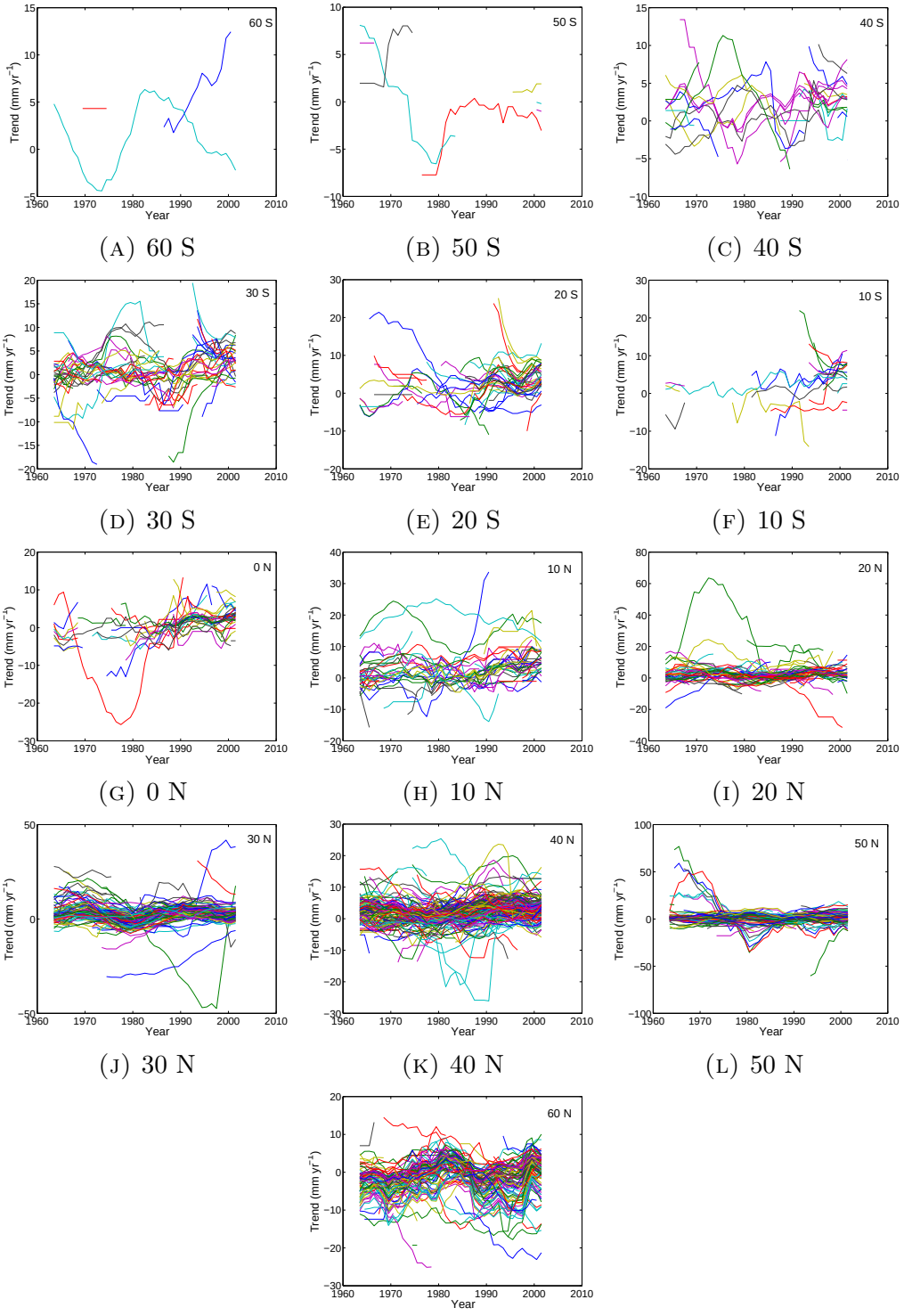

(A) 60 S (B) 50 S (C) 40 S

(D) 30 S (E) 20 S (F) 10 S

(G) 0 N (H) 10 N (I) 20 N

(J) 30 N (K) 40 N (L) 50 N

(M) 60 N

FIGURE 3.7: Time series (1955-2010) of tide gauge 18 year running trends (mm yr^{-1}) within latitude bands (figures (3.7a-3.7m), y axis limits are not equal) from all tide gauges for the available years meeting the discussed criteria. All trends shown are uncorrected for changes in G and VLD. The trend from 1993-2010 is the last shown data point, centred on the mid-point of 2001.

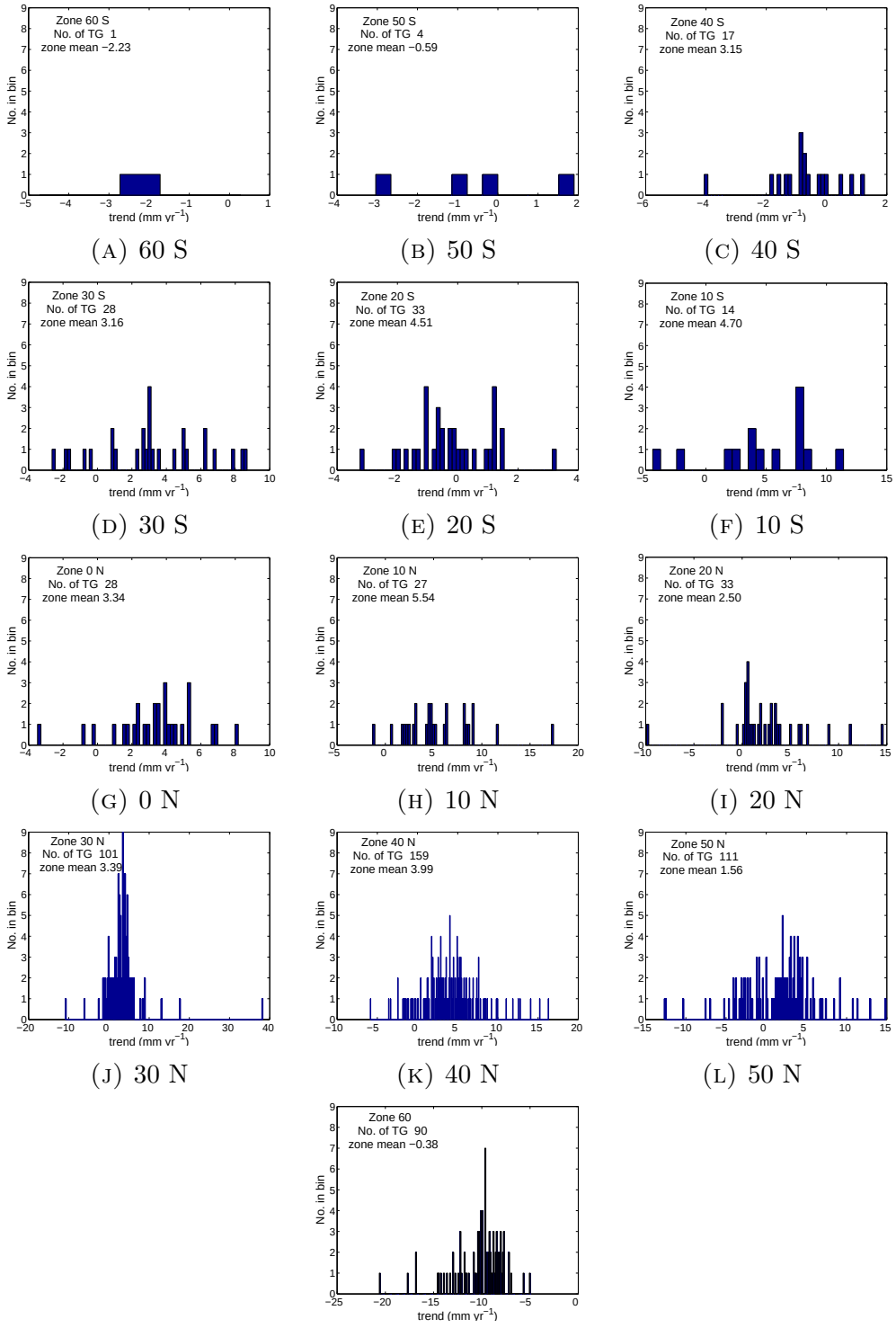

(A) 60 S (B) 50 S (C) 40 S

(D) 30 S (E) 20 S (F) 10 S

(G) 0 N (H) 10 N (I) 20 N

(J) 30 N (K) 40 N (L) 50 N

(M) 60 N

FIGURE 3.8: Histograms showing tide gauge trends from all tide gauges with trends from 1993 - 2010 for each latitude band. Trends in mm yr^{-1} are on the x axis (x axis labels are not equal) and the number of tide gauges within each bin are on the y axis (values 0-9). All trends shown are uncorrected for changes in G and VLD

Firstly, we use the VLD to convert RSL to ASL as in equation (2.1)

$$ASL = RSL + VLD$$

Secondly we remove the change in G (equation 2.15) to convert ASL to τ.

$$\tau = ASL - (G' + \overline{VLD})$$

There is not one consistent database of VLD corrections for tide gauges. King et al. (2012) compared GIA uplift from the model ICE-5G (Peltier, 2004) to VLD seen at tide gauges by ~300 GPS stations and found regionally coherent signals of ± 0.5 - 2 mm yr^{-1}. Bouin and Wöppelmann (2010) compared VLD from 148 GPS sites near tide gauges and found that half of their sites were consistent with the mass redistribution model, ICE-5G (Peltier, 2004) to within 1σ. Mitchum et al. (2010), using an earlier version of the mass redistribution model, ICE-4G compared the model rates of VLD to those of altimetry at tide gauge locations and found different trends mostly at mid to high northern latitudes, with the ICE-4G model predicting lower rates, by 2-3 mm yr^{-1}.
Santamaría-Gómez et al. (2014) introduced a further technique where they use a double difference between two nearby tide gauges and two satellite altimetry points. They difference between the tide gauge trends and the altimetry trends and then compare the results to infer a trend difference. Any specific local land displacement will not be accounted for. We do not analyse this technique here.

We investigate three techniques of calculating VLD:

1. Mass redistribution model corrections for GIA (using ICE-5G (Peltier, 2004)).
2. Altimetry corrected tide gauge values (Cazenave et al., 1999), (Nerem and Mitchum, 2002) and (Mitchum et al., 2010).
3. Global Positioning System (GPS) values of VLD (Santamaría-Gómez et al., 2012).

3.4.2 Correcting ASL for GIA effects

We use a single source for all conversions to τ to account for changes to the surface G. This correction is the whole term

$$\Delta(G' + \overline{VLD})$$

It is used in the format of gridded values and has been provided by Mark Tamisiea from the National Oceanography Centre, Liverpool (Tamisiea, 2011). The global distribution of this field is shown in figure (3.9) and tide gauge locations are marked as white dots. There is an increase in values over areas which have had a negative ice mass loading, including Canada, Northern Europe and Antarctica. A decrease in ice mass has led to an uplifting of the crust and a redistribution of underlying mantle to these areas, leading to increased gravitational attraction and hence an uplift in G. There is an overall negative value over the oceans which represents the ongoing sinking of the crust via VLD_{GIA}. As we do not have corrections for mass redistributions other than due to GIA or measures of the crust motion under the ocean, in all further calculations $(G' + \overline{VLD})$ is assumed to be approximately equal to $(G'_{GIA} + \overline{VLD}_{GIA})$. Recent ice melt will also be affecting the $(G' + \overline{VLD})$ correction and effects from this remain in our calculation of τ. The fact that this signal remains is exploited later to compare our mass estimates with the fingerprints in Chapter 6.

Figure 3.9 reveals that most tide gauges are within an area where the $\Delta(G' + \overline{VLD})$ correction using this data is around ± 1 mm yr^{-1}

3.4.3 Mass redistribution model - Relative solutions for GIA

We use model solutions for VLD taken from the PSMSL web site (20th November 2013). Corrections were provided by Peltier (2004), using the ice model ICE-5G v1.3, for each tide gauge as an estimate for VLD due to GIA. The values are added to each tide gauge individually and shown in figure (3.10). The advantage of using a mass redistribution model is that there are values for VLD available at every grid square. The disadvantages of this method are that the correction is only an estimate for GIA and does not account for other sources of land displacement.

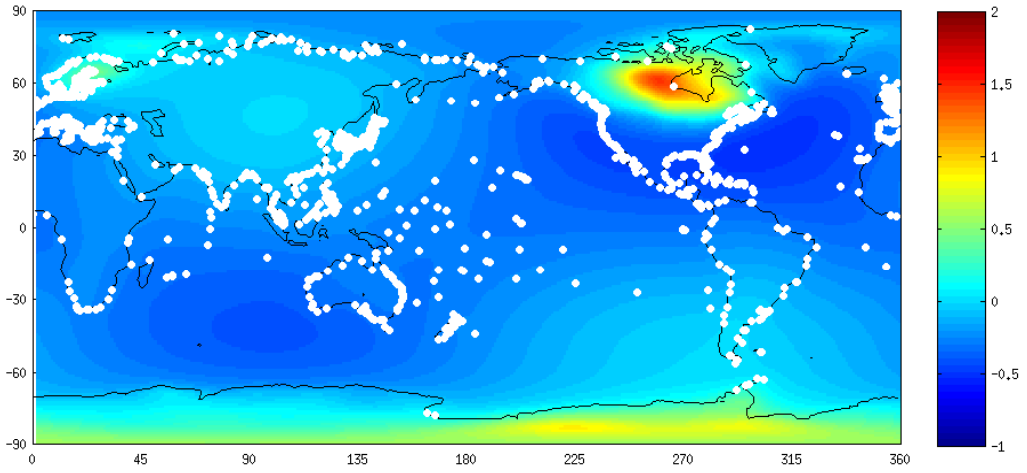

FIGURE 3.9: *GIA* contribution to rate of change of $(G' + \overline{VLD})$, being the correction needed to convert *ASL* (as observed by altimetry) into augmented dynamic topography τ (mm yr^{-1}). The values were provided by Dr. Mark Tamisiea from NOC Liverpool (`https://noc.ac.uk/people/mtam`).

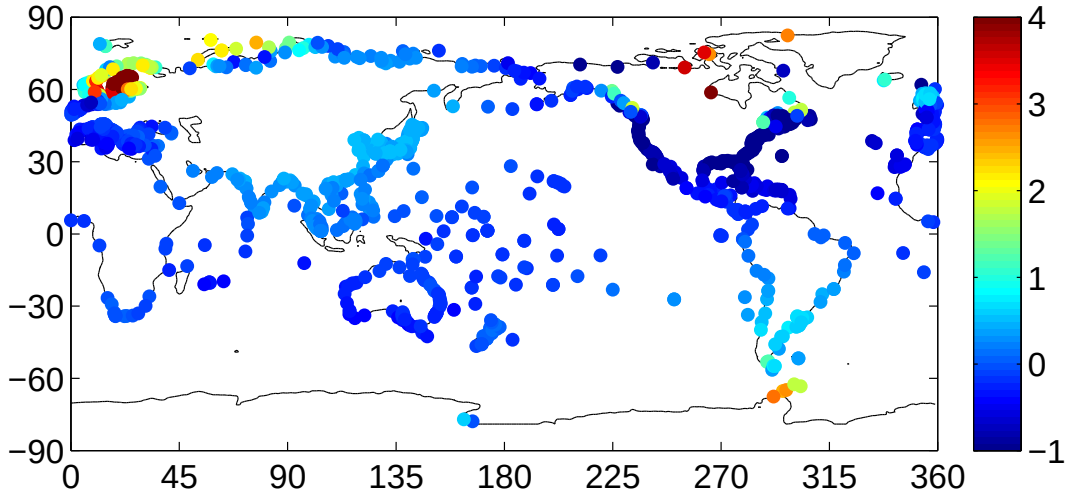

FIGURE 3.10: *VLD* values added to each tide gauge as a correction for *GIA* using the mass redistribution model, ICE-5G (Peltier, 2004) (mm yr^{-1}).

There is also uncertainty in the model, as it has been published with different versions of both ice history and Earth rheology models. The sensitivity of global sea level to the GIA model was The spatial structure of the trends is relatively smooth globally, varying between ± 1 mm yr^{-1}, with the lowest rate being -2.59 mm yr^{-1}. The exceptions are over the areas we know to have had large ice loading such as Scandinavia, Northern Canada and West Antarctica. Here we can see

much higher rates, with the highest trend given as 12.92 mm yr^{-1} at Churchill in Canada.

The sensitivity of the GIA model was investigated by Jevrejeva et al. (2014) by comparing a previous version of the ICE-5G model (Peltier, 2004), ICE-4G (Peltier, 2001), who found that the mean difference in global sea level during the time period since 1807 was 3.2 mm with a maximum difference of 28 mm during the 1990s. The mean difference in rate for the whole time period was 0.03 mm yr^{-1}, and there was a maximum difference of 0.6 mm yr^{-1} during the 6 decades from the 1920s to the 1980s. They note that the difference was almost zero for the past decade. Further comparison of GIA models was not continued in this study as our trends, however for completion of the longer trend study, other GIA models should be considered.

3.4.4 Altimetry at tide gauges

We can estimate the VLD trend using AVISO altimetry (Chapter 5) by differencing altimetry and tide gauge trends. The difference in trend is the implied VLD. We choose the nearest altimetry point to the tide gauge latitude and longitude location. We find the four surrounding altimetry grid points and obtain a weighted mean depending on their distance from the tide gauge to provide an unbiased altimetry value. We add the difference in trend to the tide gauge rate. Over the period 1993 to 2010 this is then in principle equivalent to using altimetry at tide gauge locations. Making this correction converts our trend data from relative sea level to absolute sea level. We need to correct the altimetry corrected tide gauge trends for changes in G, which is shown in subsection 3.4.2, and convert the trends to augmented dynamic topography (τ).

Figure (3.12) shows these differences in trend between 1993 and 2010. Only locations with gauges that have data over the period 1993 to 2010 are shown. The same high trends over Scandinavia and Hudson Bay can be seen as well as the Antarctic Peninsula. Elsewhere, however there is more of a scatter of positive and negative trends as opposed to the smoother model results of figure (3.10). Results here range from -12 to 14 mm yr^{-1}.

The value of this technique is that we can correct the whole time series of the tide gauge if we assume that the land displacement has been constant over the

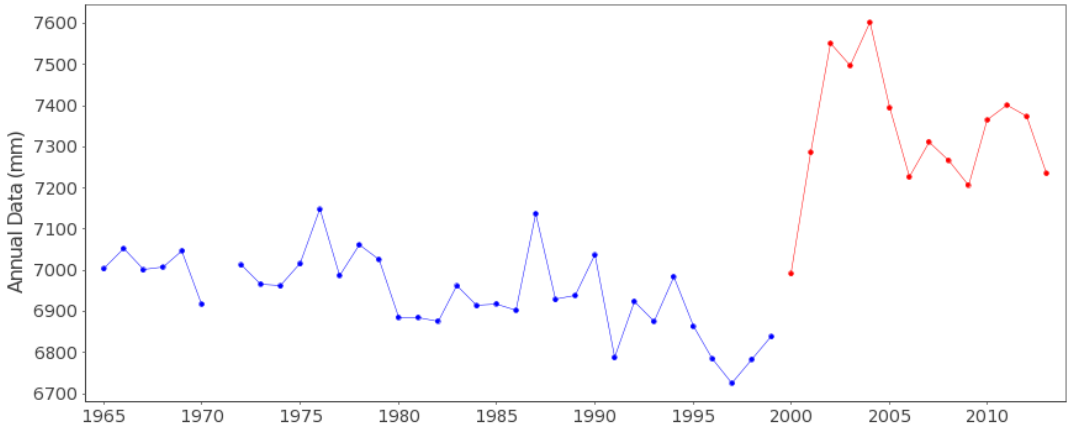

FIGURE 3.11: Miyake Sima time series (mm).

whole time period of the tide gauge time series. This can also be a disadvantage as this method relies on the assumption that all VLD trends have been linear in time. There is a slight mismatch in exact location using this method as altimetry does not have resolution which extends accurately to the coast. This mismatch in location can lead to errors due to difference in dynamical signals associated with the different position. When applied over the altimetry period only, this method is equivalent to simply replacing the tide gauge rate with the altimetry rate and therefore describe this method as altimetry at tide gauges.

The tide gauge Miyake Sima (RLR 1060) in Japan would be a good example here of how GIA alone cannot account for recent land displacement This island began to see a large trend in 2001 and then in March 2011 the area saw a huge earthquake and tsunami. The time series can be seen in figure (3.11). A similar step in the trend was seen in the nearby gauge, Kozu Sima. The land movement in this area is picked up by the trend difference between altimetry and tide gauge as a very large signal, but the GIA is a very small signal in comparison.

3.4.5 Global Positioning System

When we use the Global Positioning System to measure for VLD we are observing both GIA and nonGIA land movement combined, as the system does not distinguish between the two. The GPS data used in this thesis is sourced from Système d'Observation du Niveau des Eaux Littorales (SONEL) (Santamaría-Gómez et al., 2012). The ULR5 Vertical-Velocities Table from SONEL provides the vertical GPS velocities and uncertainties for the 326 stations fulfilling the criteria of 3 years of

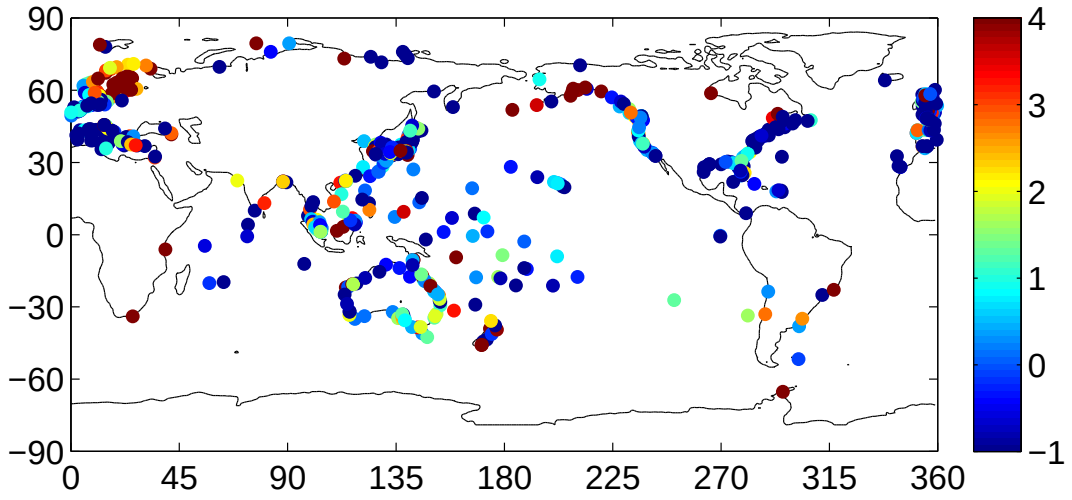

FIGURE 3.12: Tide gauge locations showing the difference in trend for 1993 to 2010 between altimetry and tide gauges. This difference in trend is the implied VLD (mm yr^{-1}.)

minimum length without discontinuities and with data gaps not exceeding 30%. The data includes information about the length of the time series and the completeness of the record. The data records span from 3.04 to 15.98 years, with a mean length of 10.22 years. The records are between 28.1% and 100% complete, with an average completeness of 92.61%. GPS data was provided as annual mean values. GPS receivers are capable of high frequency data response and therefore the use of annual mean values may not be appropriate for adequate capture of the VLD signal

We find the nearest GPS data point to all 1357 tide gauges. We then limit the distance from the GPS to the tide gauge before we allow it to be used to estimate the VLD. Ideally, the GPS should be at the exact location as the tide gauge if an accurate land movement observation is to be recorded. That is not currently possible, and so while GPS is a valuable technique because of its accuracy, for the purpose of this study we have to make the assumption that, due to the distance of the gauge from the GPS receiver in most cases we are only able to estimate large scale land movement. This again assumes that the large scale land movement is broadly consistent over distance. The errors involved in using tide gauges to study regional variability would become significantly reduced if each had a GPS receiver within immediate proximity.

Not all of the GPS receivers are at the coast, some are inland. We look at the

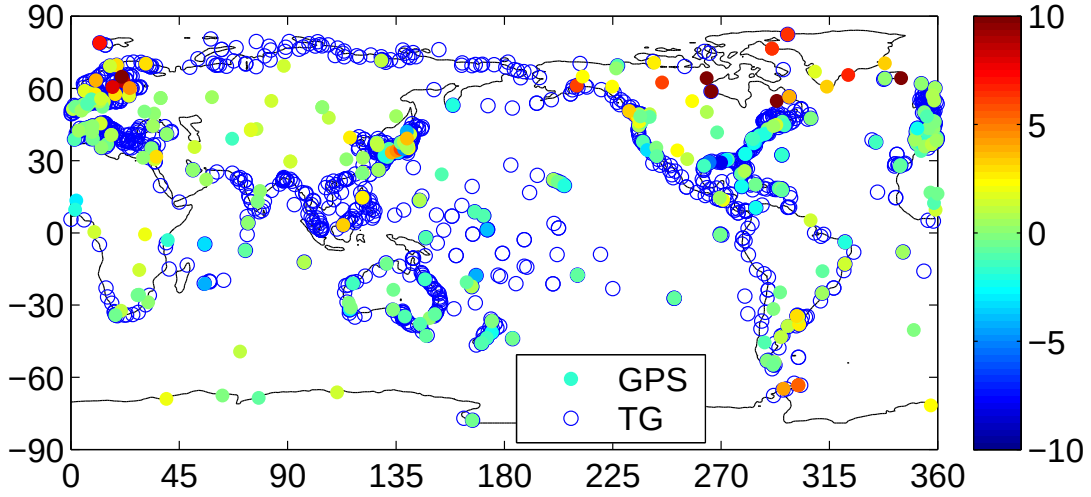

FIGURE 3.13: Location of tide gauges (blue circles) and location of GPS sites (coloured dots). Colours correspond to the values of the GPS derived VLD trends at each site (mm yr^{-1}).

number of gauges left in the sample if we limit the distance between gauge and GPS receiver. Figures (3.14a) and (3.14b) show how many gauges are excluded if we limit by 500 and 1000 km respectively. When using all of the RLR tide gauge set, 1042 of the 1357 gauges are over 50 km away, 861 are over 100 km, 321 are over 500 km and 130 are over 1000 km away. For comparison, when using the 500 tide gauge sub set 333 of the 500 are over 50 km away, 279 are over 100 km away, 103 are over 500 km away and 52 are over 1000 km away. We choose to limit the distance to under 500 km in order to keep a reasonable number of gauges in the reconstruction.

Figure (3.13) shows the tide gauge and GPS locations and figure (3.15a) shows the rates from GPS used to correct the tide gauges. We can see high VLD rates where we would expect to see the GIA signal (Scandinavia and Hudson Bay), but there are exceptions, e.g. Japan, which will be due to local processes such as tectonic movement and subsidence. Figure (3.15a) shows the rate applied at each tide gauge for the VLD. As gauges sometimes use the same GPS value, regions might see intensified regional trends as a result. Only gauges within 500 km are used. The standard errors associated with GPS trend values are shown in figure (3.15b). There is a seemingly random spread to the errors which are up to 0.5 mm yr^{-1}.

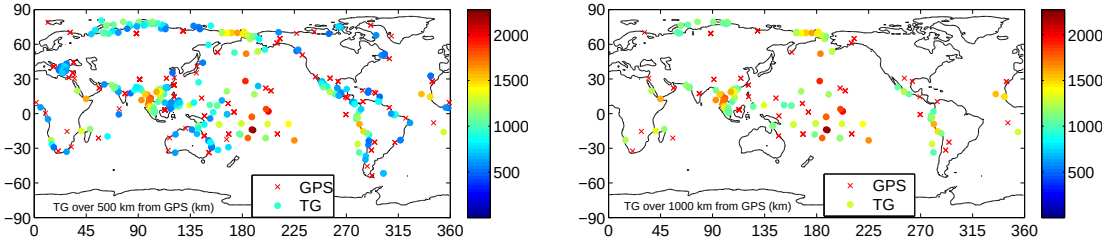

(A) Tide gauge stations (coloured dots) 500+ km from GPS (x) (km)

(B) Tide gauge stations (coloured dots) 1000+ km from GPS (x) (km)

FIGURE 3.14: The coloured dots are the distances of tide gauge stations from GPS sites (x). 3.14a shows all stations over 500 km apart, 3.14b shows all stations over 1000 km apart. Colour bar units are km.

3.5 Comparing corrected tide gauge trends

Figure (3.16) shows all uncorrected tide gauge rates for 1993 to 2010. Even without any corrections there is a certain amount of regional correlation between trends at tide gauges over this period. The negative trends of the North American Pacific coastline contrast with the positive trends of the North Atlantic North American coast. The Australian coastline sees higher trends on the Western coastline. Low rates in Scandinavia show the effects of GIA on RSL where it appears that sea level is falling when in fact the land is uplifting. Regionally uncorrelated trends such as around the coast of Japan point to specific factors relating to individual gauges.

Both the VLD and the $(G' + \overline{VLD})$ corrections have been applied in figure (3.17). The Scandinavian trends have gone from negative to positive as the influence from the moving crust has been removed and it can be seen that sea levels are rising in this region. Regional coasts are generally correlated to a certain degree. The altimetry at tide gauge analysis shows the most coherent signals (figure (3.17b)) highlighting that some land movement remains unexplained in the Peltier (2004) and GPS estimates. The GPS corrected trends appear the least coherent, possibly arising from using VLD corrections which were sourced at long distances from the tide gauge.

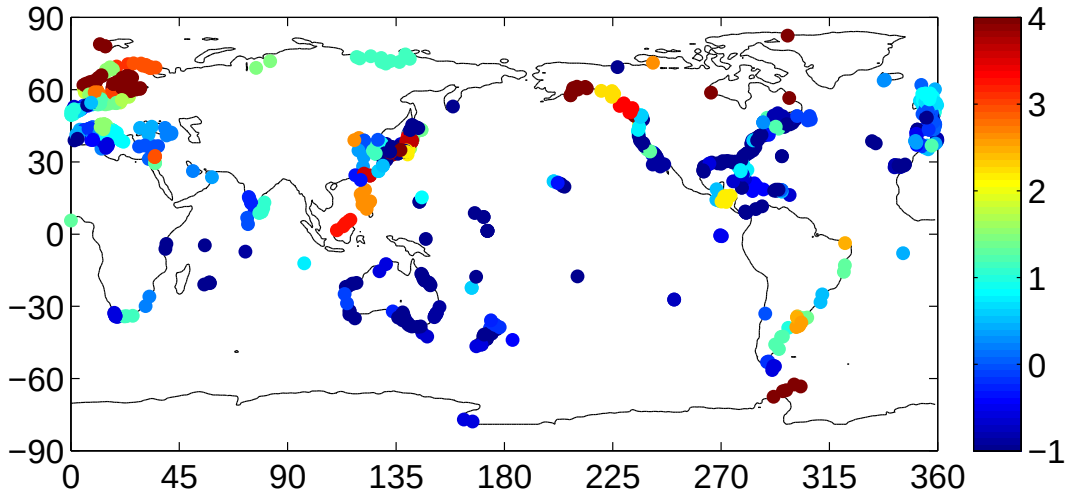

(A) VLD at tide gauges using the nearest GPS station rate (Santamaría-Gómez et al., 2012). Only gauges within 500 km of a GPS station are used (mm yr^{-1})

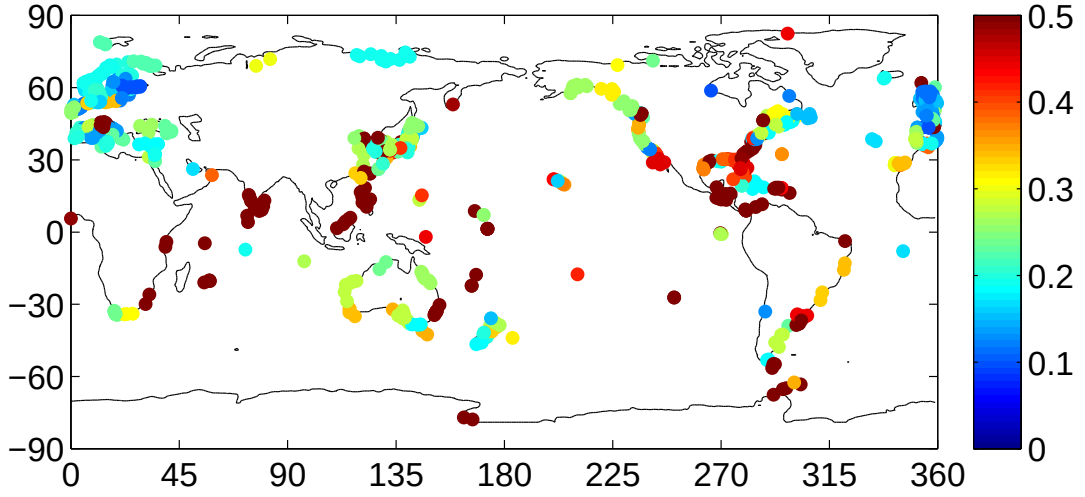

(B) GPS quoted errors for nearest VLD to tide gauge locations (mm yr^{-1})

FIGURE 3.15: Values of VLD at GPS corrected tide gauge stations (mm yr^{-1})

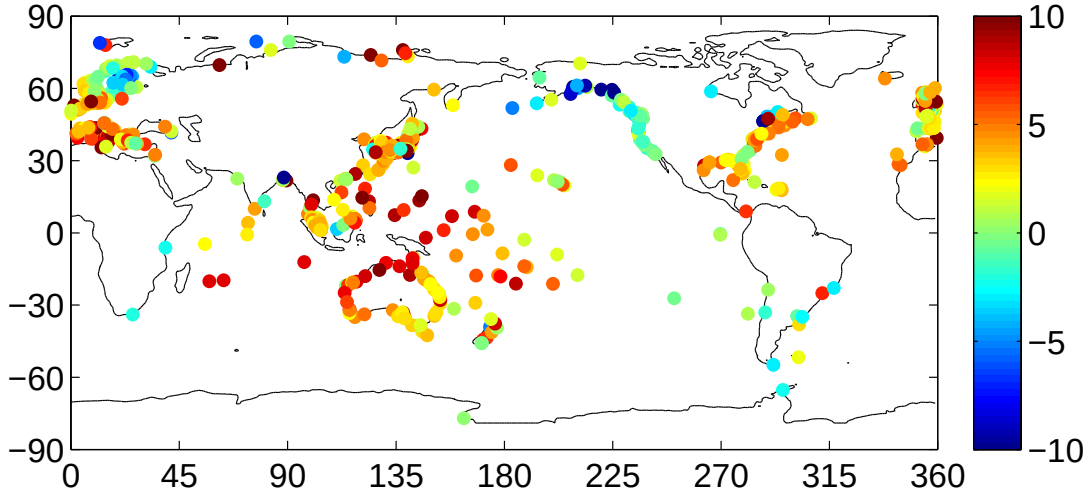

FIGURE 3.16: All uncorrected PSMSL RLR tide gauges rates for the period 1993 to 2010 (mm yr^{-1})

3.6 The global average from tide gauges

As our time series for tide gauges are longer than those from altimetry, we can plot the global trend in τ from tide gauges from 1950 to 2010 assuming the same rates of VLD and G over the whole time series. Tide gauges are sorted into latitude bands. Tide gauge trends corrected for land movement are area weighted (using the cosine of the latitude weighting), and then summed to calculate the global mean trend (mm yr^{-1}). The time series of trends is shown as the running mean of 18 year trends, centred on the middle year. Tide gauge time series must be 70% complete during the 18 year period in order for the trend to be calculated. Plotting long term trends masks the short term seasonal and annual variability and highlights longer variability.

Figure (3.18) shows the global trends from the four choices of the tide gauges. Each of the four plots show clear long trend variability, as well as differences which we assume to be caused by spatial aliasing. When gauge distribution is taken into account, Figures (3.3, 3.4b and 3.18b) indicate that the distribution of long tide gauge (being mostly in the Northern Hemisphere) are not capturing recent trend increases in the global mean. While these gauges represent well the decadal variability, they are not capturing apparent trend increases in the Southern Hemisphere. Global trends formed from using all gauges and the 500 gauge set show most similarities, with higher trends around the late 60's and early 70's.

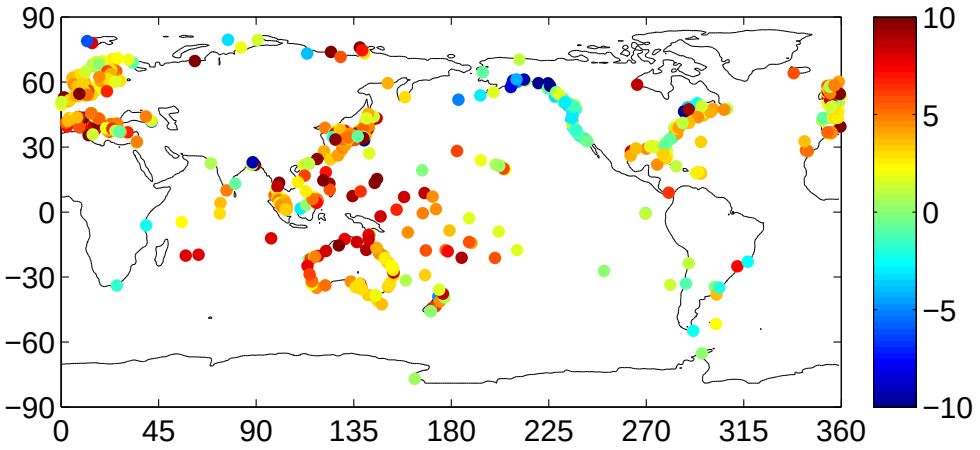

(A) Trends of τ using a mass redistribution model (ICE-5G) (Peltier, 2004) for 1993 to 2010 (mm yr^{-1}).

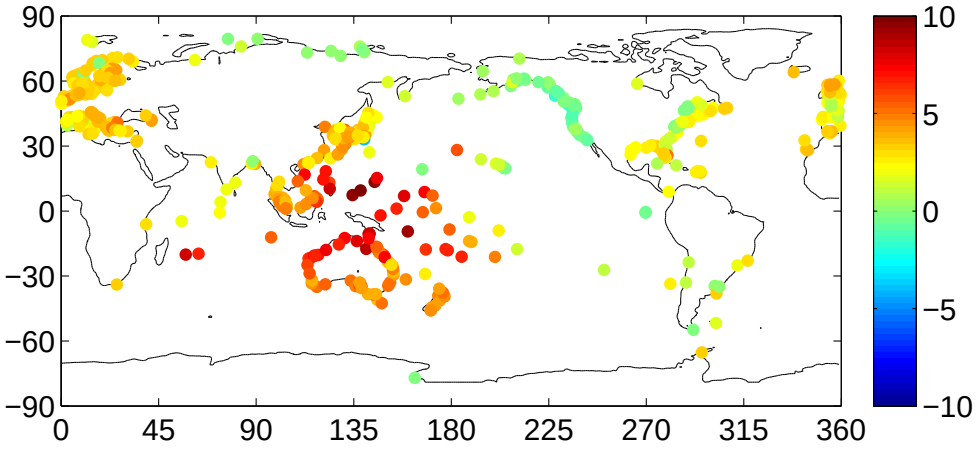

(B) Trends of τ using altimetry at tide gauges for 1993 to 2010 (mm yr^{-1}).

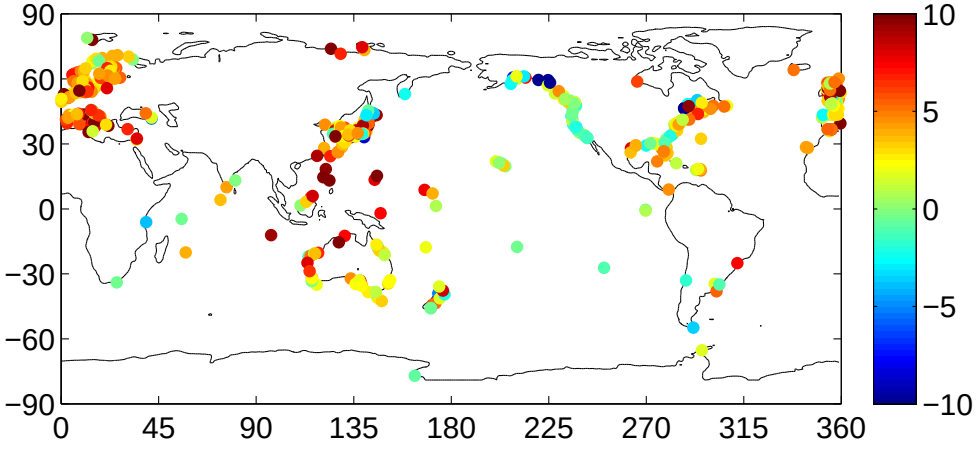

(C) Trends of τ using GPS (Santamaría-Gómez et al., 2012) for 1993 to 2010 (mm yr^{-1}).

FIGURE 3.17: All tide gauges corrected for VLD and $(G' + \overline{VLD})$ showing sea level trends for 1993 to 2010. Figure (3.16) shows tide gauge rates before correction. Figures (3.17b, 3.17a and 3.17c) show rates of τ after corrections have been applied to RSL for VLD and $(G' + \overline{VLD})$ using the mass redistribution model (ICE-5G), altimetry at tide gauges and GPS respectively. All have the same GIA correction for $(G' + \overline{VLD})$ (Tamisiea et al., 2001).

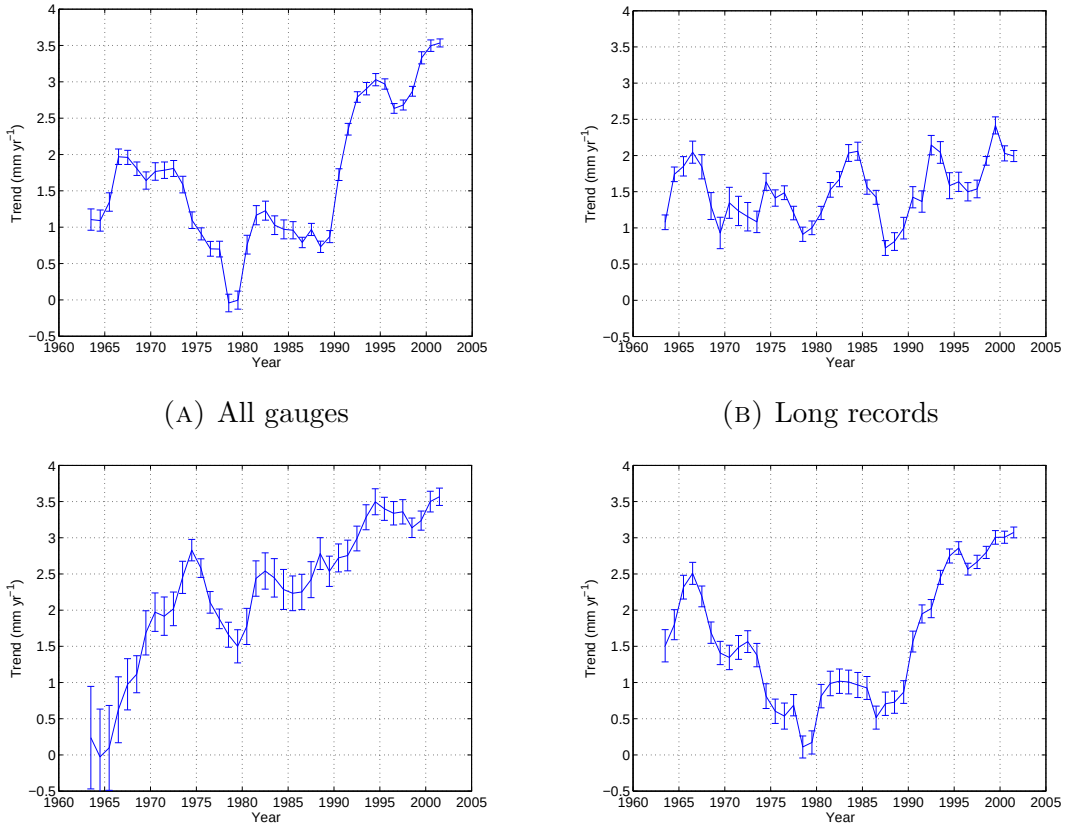

(A) All gauges

(B) Long records

(C) Spatially uniform gauges

(D) 500 gauges

FIGURE 3.18: The global trend for sea level using all tide gauges, corrected for VLD using the altimetry technique described in subsection 3.4.4 and calculated as running trends 18 years long, plotted on the mid point (mm yr^{-1}) with one standard error (σ).

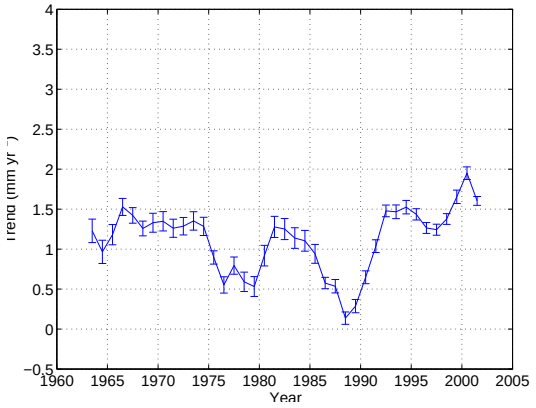

FIGURE 3.19: Trend as in 3.18a but for all gauges only in the Northern Hemisphere between latitudes 20°N to 60°N (mm yr^{-1})

A decrease in trend during the middle part of the time series, especially around 1980, and then an increase towards 2010 with the last decade seeing trend values higher than for any other year. The uniform gauge subset contains the smallest number of gauges and this is reflected with larger statistical errors. This group does not show such a decrease in trend at the 1980 point and values are generally highest within this group after about 1971. This data set is the same group as was used in Merrifield et al. (2009) and the global trend here varies slightly from their published global trend. This is due to data from Merrifield et al. (2009) being retrieved from the University of Hawaii Sea Level Centre (UHSLC) where there are occasional differences in data management holdings compared to the PSMSL dataset.

It was noted by Woodworth (1990) and Holgate (2007) that European trends tended to be lower than the global mean. We test the theory that the recent increase in global trend is dominated by trends in the tropics and Southern Hemisphere Merrifield et al. (2009) by repeating the global trend using all gauges (as for figure (3.18a)), but limit the global summation to the Northern Hemisphere (20°N to 60°N). Figure (3.19) shows the Northern Hemisphere mean from the sum of ocean area weighted latitude means using all gauges at these latitudes, confirming that gauges in the Southern Hemisphere and tropics are contributing the recent higher trends to the global mean from tide gauges.

3.7 Trends 1993 to 2010 as a function of latitude

Tide gauges are sorted into 13 latitude bands between 65° S and 65° N. This excludes 98 gauges beyond 65° N and 3 gauges beyond 65° S. The mean of each latitude band is found and used to represent the zonal average and plotted as a function of latitude with one standard error. Figure (3.20) shows how the area of ocean is distributed at these latitudes. There is most ocean at the tropical latitudes and least at high latitudes in the Northern Hemisphere. There is over 3.5 times more ocean area within the 0° latitude band as in the 60°N band. This technique works well within latitude bands that have many tide gauges but it should be noted that at 60°S there is only one tide gauge which has data to enable a trend for 1993 to 2010 to be computed, the Argentine Islands gauge which is 98% complete from 1958 to 2013. This gauge does show some long term variability which could be a local VLD effect.

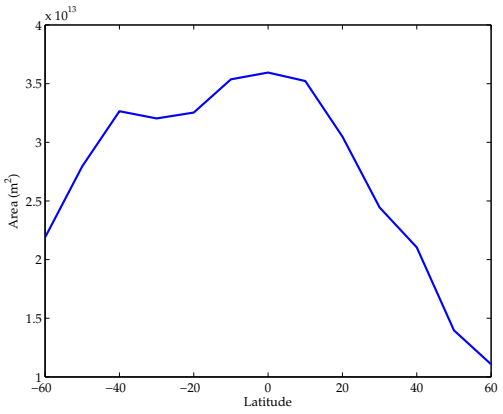

FIGURE 3.20: Area of ocean within each latitude band (m^2)

The structures of the trends are shown in figure (3.21) for the four tide gauge subsets. Each subset has three evaluations: tide gauges corrected using ICE-5G (blue), altimetry at the tide gauge sites in the selection (black) and tide gauges corrected with GPS (green). All of the trends have been corrected with the same $(G' + \overline{VLD})$ correction as described in subsection 3.4.2.

Each of the 4 tide gauge subsets show the importance of the correction for VLD as the difference between the 3 VLD corrections is significant in each case. There is a reasonable agreement between all gauges and the 500 and uniform subsets and the long gauge subset differs most. There is largest agreement between latitudes 20° N and 50° N. Trends at a similar distance from the equator in the Southern Hemisphere are in the region of twice the size, although the spread from the different VLD corrections is also larger in the Southern Hemisphere. The GPS corrected trends all (except the long gauges), show lower trends in the Southern Hemisphere which could indicate a reference frame issue. There is an interesting strong agreement in the long tide gauge subset (figure (3.21b)) with the tide gauges corrected for VLD with GPS and those corrected with ICE-5G but the poor spatial coverage makes it hard to draw conclusions from this subset.

While the method depicted in figures (3.21) is good for examining the pattern of sea level change as a function of latitude, it does not give a good picture of the contribution of each latitude to the global mean, as there is a greater area of ocean in the Southern Hemisphere than the Northern Hemisphere. Figure (3.20) shows the area of ocean at each latitude. Figure (3.22d) area weights the zonal averages to show the contribution from each latitude band, in a way that allows the global mean rate to be read as the sum of the contributions from each zonal band.

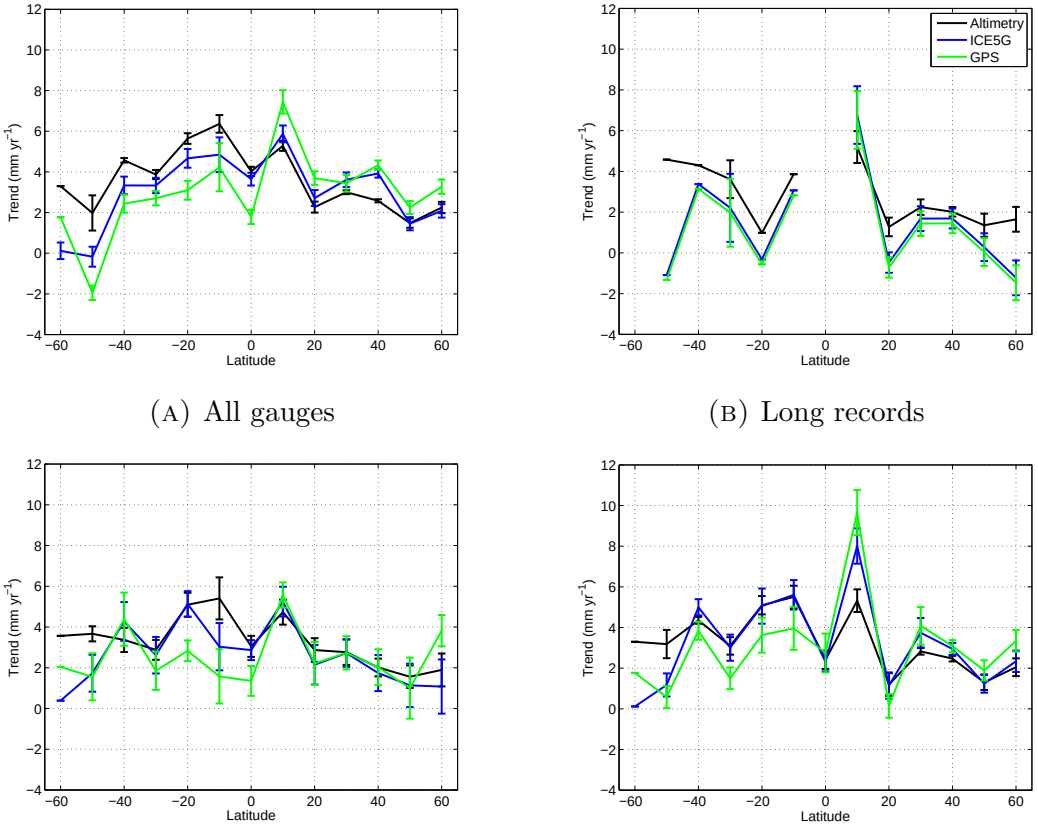

(A) All gauges

(B) Long records

(C) Spatially uniform gauges

(D) 500 gauges

FIGURE 3.21: Zonal averages of 1993 to 2010 trends in sea level for 4 tide gauge selections showing 3 separate corrections for VLD, altimetry at tide gauges (black), mass redistribution model (ICE-5G (Peltier, 2004) corrected (blue) and GPS corrected (green). All have the $G' + \overline{VLD}$ correction applied and show σ. (mm yr^{-1})

The structures we see from each subset are similar, and now it is shown that the tropics and Southern Hemisphere are responsible for bigger trends. The best agreement is between altimetry at tide gauges and tide gauges (ICE-5G corrected), using the 500 gauge subset. These are two independent measurements which are in strong agreement at nearly all latitudes. The GPS corrections compare better to the other 2 VLD corrections in the Northern Hemisphere but again they appear to have a negative offset in the Southern Hemisphere.

The figures (3.21 and 3.22) therefore appear to suggest that there is a latitudinal dependence of the trends in sea level between the years 1993 and 2010, where the trends are higher at the equator and at low latitudes, and trends are lower at high latitudes. Corrections for VLD trends are an important factor as different corrections can produce variability of up to 5 mm yr^{-1} at certain latitude bands.

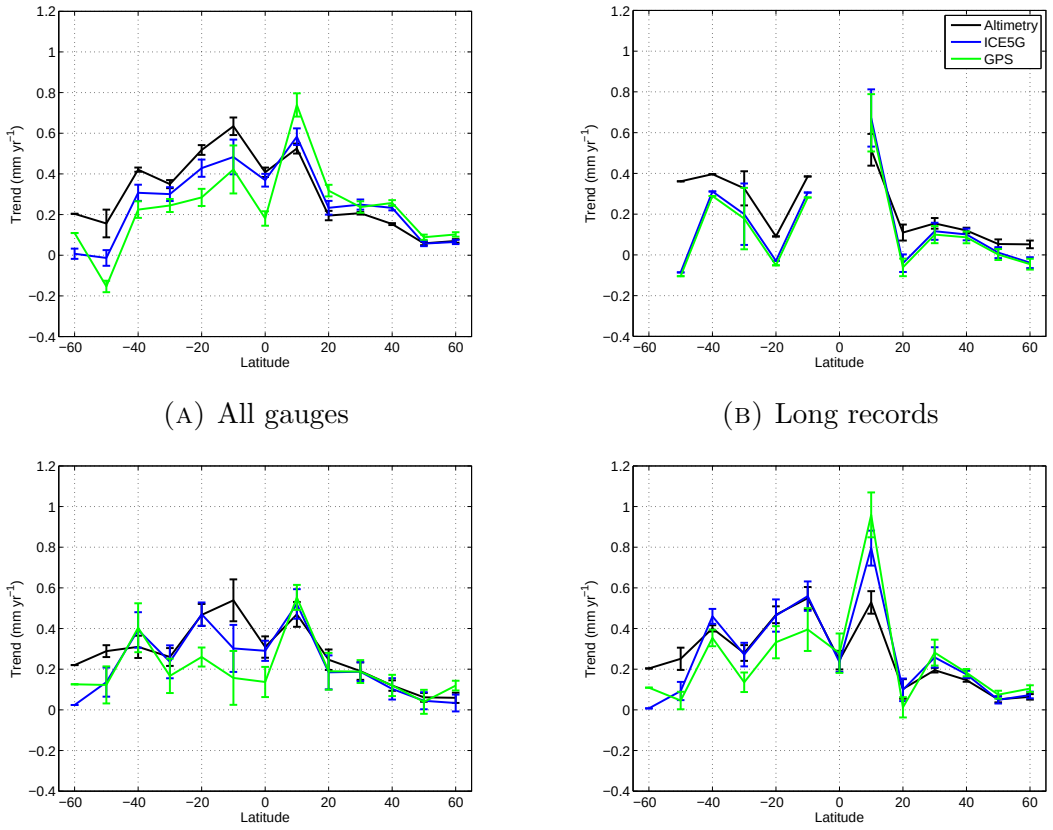

(A) All gauges

(B) Long records

(C) Spatially uniform gauges

(D) 500 gauges

FIGURE 3.22: Area weighted zonal averages of 1993 to 2010 trends in sea level. Values are as in figure (3.21) and then area weighted Each sub-figure shows altimetry at tide gauges (black), and gauges corrected for VLD from both ICE-5G (Peltier, 2004) (blue) and GPS (green). The zonal weights are formed from the area of ocean within the 10^{o} latitude band. The sum of the latitude bands will be the global trend for 1993 to 2010. The area of ocean at each latitude can be seen in figure (3.20) (mm yr^{-1})

Generally the difference is lower than this, and while exact values may differ, the general shape of the zonal average trend shows this pattern (higher at low latitudes and lower at high latitude). One exception to this pattern is the altimetry at tide gauge locations where the trend is also higher in the southern hemisphere. Another exception is the GPS correction where trends are generally lower in the southern hemisphere than the northern hemisphere once corrected, although the sparseness of GPS data at tide gauges is noted.

3.8 Discussion

This chapter details an in depth tide gauge analysis of global and zonally averaged trends. Due to the limitations of the time series, the result is sensitive to choice of tide gauge and correction for VLD.

We have shown global and zonal averages for 4 choices of tide gauge and 3 choices of VLD correction with one standard error. It is clear from figure (3.3a) that there are many more gauges over the Northern Hemisphere than the Southern Hemisphere. This spatial clustering is a valid reason to choose a subset of gauges which would more uniformly represent the world's oceans as suggested by Merrifield et al. (2009). Figure (3.5), showing the time series of sea surface heights annually as a function of latitude, highlights that there is also a bias to the Northern Hemisphere in the temporal completeness of data with large data gaps again in the Southern Hemisphere, especially for tide gauges with long time series where some latitudes are only represented by one long gauge. Figure (3.5) though, does show correlations of sea surface heights between gauges within the same time period but at different latitudes, and the ability to see these patterns provides one means to assess the quality of a chosen group of tide gauges. This is seen as 'stripes' of colours at certain years. This reveals that sea surface height is influenced by larger scale processes such as wind fields. The 'stripes' are seen best over the subsets of all and 500 gauges. After that the effect is hidden within the noise of the data. We investigate this further in Chapter 7 as we limit the gauges to east or west coastlines where we would expect to see propagation of physical process signals.

Trends for sea level rise averaged over latitude bands display higher trends in the tropics and Southern Hemisphere. The 3 corrections for VLD result in a range of values for the zonal average. Errors shown in figure (3.21) are one standard error (σ). The three methods generally agree within 2σ error. The area weighted trends as expected show that the main contribution to the global average is over the Southern Hemisphere as here there is more ocean area. Trends in the Southern Hemisphere are also larger than in the North.

While individual corrections for VLD are different, the general shape of the trend over latitude is similar. For each subset of gauges in figures (3.21 and 3.22) there appears to be a Southern Hemisphere difference with regard to the GPS corrections to VLD which could be suggestive of a reference frame issue. Trends over the

Northern Hemisphere are broadly consistent, but over the Southern Hemisphere where there is least data we see the largest spread in trend values.

From this detailed study we have found that the long time series subset has too few gauges especially in the Southern latitudes to accurately represent the zonal average between 60°N and 60°S. The uniform subset has an increase in the scatter of signals in the Southern Hemisphere (figures (3.21c) and (3.22c) although there is a coherence of signals in the North (figure (3.5c)).

For this study we mainly use τ calculated from the 500 gauge subset in our estimates of the mass component of sea level trends in Chapter 6, while also showing some results from all tide gauge records. The 500 gauge subset has the benefit of using the longer records, but has a more even spread of gauges over all latitudes and so provides a clearer estimate in the Southern Hemisphere than the long gauge records. Limiting some records compared to using all gauges reduces the impact of spatial clustering.

A further study could include averaging the various trends around a median solution, which would then include information from all solutions. This may have the effect of minimising some of the errors within a specific solution while enhancing the observations at latitudes where all solutions agree. Averaging solutions has not been used further here.

3.9 Summary

- The high quality and long time series of tide gauges make them a valuable record of sea level. Tide gauges were originally installed to provide data over shorter time scales for local purposes, i.e. for tidal prediction and harbour navigation. The global array of tide gauges then, is incomplete both spatially and temporally. We have compared the whole global array of research quality Revised Local Reference data from the Permanent Service for Mean Sea Level against 3 subsets of this array. The subsets were chosen for all records, long time series, uniform coverage or by using a simulated annealing algorithm to choose 500 optimum gauges.

- The global mean and zonal average results of sea level trends show that the selection of tide gauges is important to the results as the influence of a single tide gauge can add significant weighting when a region is represented by only a few tide gauges due to large regional trends in areas of high variability. We feel confident that using the 500 tide gauge subset is the best selection for this analysis due to the coherence of the data at most latitudes as seen in figure (3.5d) meaning that the 500 gauge set provides a balance between the benefits of a longer time series with the best spatial coverage. The 500 gauge subset agrees well when compared with all tide gauges as seen in figure (3.18d). The constraint that each gauge time series must be 70% complete over the time span of the trend is applied.

- Long time series gauges are mostly based in the Northern Hemisphere. The global trend from long gauges does not show an increase in recent trends, although the global trend from other selections of tide gauges does show the long term variability. This could suggest that the recent trend increase is located over the tropics and Southern Hemisphere. We find that the global trend increase is mainly due to tropical and Southern Hemisphere increases, which are poorly represented in the long tide gauge record selection.

- From this analysis it appears that trends in sea level from gauges in the higher latitudes between 1993 to 2010 are not as high as those in the tropics. While the 3 VLD corrections within each subset alter the magnitude of the trend, the general shape of higher trends over the tropics remains

- The zonal average of sea level trends for all subsets of tide gauges and all VLD corrections are in closest agreement over the latitudes 20^oN to

60^oN. Larger uncertainties lie in the Southern Hemisphere as there are fewer gauges. This uncertainty however, is not adequately portrayed by the statistical error, where over some latitude bands there is only one tide gauge. We address this limitation of statistical errors by re-evaluating the errors associated with our results in Chapter 6.

- We find that, with the 500 tide gauge subset, there is good agreement between trends in sea level corrected for VLD using the GIA model ICE-5G, and those measured by altimetry. The structure of the trends as a function of latitude is also close to that seen when correcting for VLD using GPS with the exception of a possible offset in the Southern Hemisphere (which could highlight a reference frame issue).

- We do not pursue using GPS corrections beyond this chapter because by using GPS measurements to correct for VLD, we are removing the VLD part of the fingerprint pattern associated with recent changes.

- There appears to be a latitudinal dependence on sea level trends between 1993 and 2010. While the various land corrections differ slightly on the exact magnitude of the trends, the general shape of this dependence as a function of latitude remains.

Chapter 4

Steric Height Trends in Sea Level

Our analysis of steric trend in sea level examines 5 global temperature and salinity gridded data sets. There is some variability between these data sets, even though they mostly use the same initial observational data, due to their analysis techniques. We find the zonal average of steric sea level trends from these 5 data sets and use their variability to assign an error term to the steric trends. We consider the impact of the new equation of state for seawater, the reference depth and trends over longer time scales. We use our results from this Chapter to remove the steric signal from the augmented dynamic topography calculated from both tide gauges in Chapter 3 and altimetry in Chapter 5.

4.1 The steric height component of sea level

Steric changes to sea water can be a useful indicator of changes to the global climate system of the atmosphere and oceans. Heat from the atmosphere is transferred to the ocean where it can be stored above and below the thermocline for centuries to thousands of years. When heat is transferred to the ocean it causes thermal expansion which is evident on the sea level. Thermal expansion is evaluated via the equation of state for sea water. In 2010 a new thermodynamically consistent equation of state for sea water was introduced by Trevor McDougall (McDougall and Barker, 2011). We use these equations to examine the density dependant component of sea level, the steric height. This, when added to the BSL (mass component), gives ocean volume which is equivalent to RSL, shown in equation

(4.1).

$$\underbrace{RSL}_{OceanVolume} = \underbrace{SSL}_{Steric} + \underbrace{BSL}_{OceanMass} \tag{4.1}$$

Steric sea level (m) is dynamic height ($m^2 s^{-2}$) divided by a constant gravitational acceleration, g_o (m s^{-2}) (McDougall and Barker, 2011). We use the dynamic height anomaly, obtained by integrating the specific volume anomaly from the ocean floor to the surface. Specific volume has the units (m^3 kg^{-1}) and is the inverse of density, being the volume divided by mass. The dynamic height is based upon the difference in geostrophic velocity between the surface pressure and a that at a reference level (Pa). As we wish to evaluate the whole water column, the reference level should be the ocean floor. Where data for the full water column is not available (Ishii and Kimoto, 2009, Levitus et al., 2009), we integrate to the deepest level. At the deepest level used we assume there to be no motion.

$$SSL = \frac{1}{g} \int_{p_b}^{p_s} \hat{\delta} \, dp \tag{4.2}$$

where
$\hat{\delta}$ = the specific volume anomaly (m^3 kg^{-1})
p_b = the pressure at the lowest level (Pa)
p_s = the pressure at the surface (Pa)
g_o = constant gravitational acceleration (9.7963 m s^{-2})
The integral of the specific volume anomaly is dependant on temperature and salinity. Variations in salinity will have regional effects due to the change in density and volume of fresher to saline water, especially in polar seas. Rye et al. (2014) have found that melting of ice around the Antarctic has increased local steric sea level due to freshening at a greater rate than the global mean. While local steric effects are important, halosteric contributions to the global trend in sea level are around an order of magnitude smaller than the thermosteric contributions (Antonov et al., 2002). We do not explore the halosteric and thermosteric components individually within this study.

The steric height was calculated using the deepest available layer of each data set within each grid square. The 5 data sets are available to varying depth layers, so the steric height was not calculated from the same depth for each data set. The effect of this was examined in subsection 4.7.2 and figure (4.12). Using a variable bathymetry enabled the steric height to be defined up to each coastline. The integral of the specific volume (steric height) at the coast will be zero as the

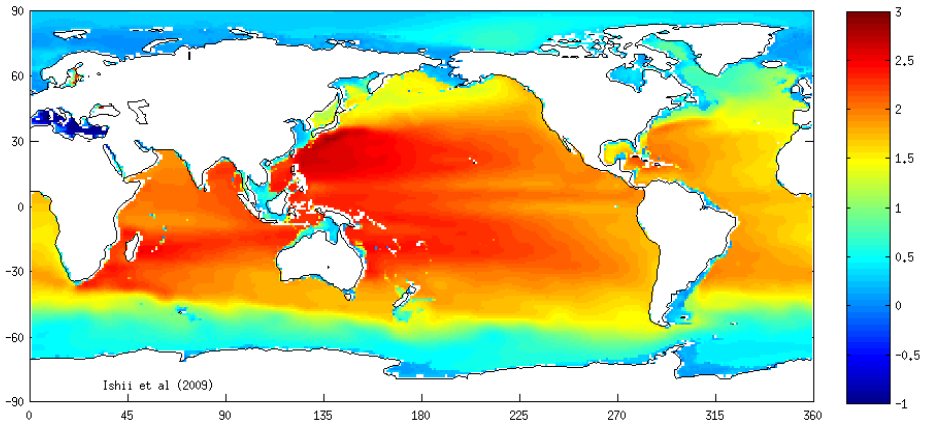

FIGURE 4.1: Annual mean steric height (m), with the global annual mean removed (Ishii and Kimoto, 2009) for the year 2009.

height of the water column there is zero. The coast may still be subject to the influence of a change in steric height but this signal will be from the open ocean and received as a change in sea level at the coast as a result of a horizontal pressure signal (Bingham and Hughes, 2012). This is significant as the basin wide steric height is compared with sea level from tide gauges. The annual mean steric height anomaly from the global mean, calculated from the Ishii and Kimoto (2009) data set is shown in figure (4.1). The distribution of the annual steric height anomaly has a latitudinal structure where the steric height is lower towards the poles and higher at lower latitudes. Evidence of the ocean circulation is evident in the steric height anomaly as the Pacific and Atlantic gyres and equatorial currents can be seen in the steric structure as high annual steric height values. Structure is also seen in the north and south Indian Ocean, and the boundary between the ocean basins and the Southern Ocean is well defined. The definition of the latitudinal structure in figure (4.1) provides more motivation for using latitudinal averages within this analysis.

4.2 Background

Sampling bias

Historic data must be treated with caution as the number of observational data within the gridded data set is limited, both spatially and temporally at certain times and in certain regions. The open ocean in the Southern Hemisphere is historically less observed than areas closer to land and sampling was seasonally biased,

being more confined to summer time at high latitudes due to weather restrictions. When assessing decadal trends in steric height, the irregular sampling of the subsurface ocean impacts estimates of the trends, as shown by Lyman and Johnson (2008), who state that the sampling locations between 1955 and 1966 were insufficient to reproduce the global trend during this time. Prior to the mid 1960s temperature profiles to around 300 m were taken using mechanical bathythermographs (MBTs). After the introduction of the expendable bathythermograph (XBT), MBTs were gradually phased out. XBTs sample temperature and pressure to depths of typically 460, 760 or 1800 m, with the two shallower depth ranges being most common, hence the depth range of certain gridded temperature and salinity products being 700m. Several studies have highlighted problems with the fall rate of the XBT (Gouretski and Koltermann, 2007, Hanawa et al., 1995, Heinmiller et al., 1983) and corrections have since been applied (Ingleby and Huddleston, 2007, Wijffels et al., 2008). Temperature errors with XBTs have been 0.1 to 0.2^{o} C. High precision data is available from research vessel based observations from CTDs (conductivity, temperature, depth) where both temperature and salinity are available to an accuracy of 0.002^{o} C and 0.005 psu respectively (Ingleby and Huddleston, 2007).

A large proportion of earlier sampling is confined to near coastal sites with large areas of the open ocean unobserved. ARGO floats have changed this completely to provide a more homogeneous coverage. ARGO floats are Lagrangian autonomous vertical profilers which compliment satellite altimetry by returning temperature, salinity and velocity data every 10 days from a depth of up to 2000 m, to the surface. From 1989 to the present day over 3500 floats have been placed in circulation in the global ocean by the Inernational ARGO Program (`http://www.argo.ucsd.edu,http://argo.jcommops.org`). Figure (4.2) highlights spatial differences between historical and present day sampling by comparing observational reports from January in both 1958 and 2010. There are, however, still areas at very high latitudes which are less sampled by ARGO. The floats' reliance on ocean currents means that those deployed at mid and low latitudes take time to travel to high latitudes. Deploying them at high latitudes is costly, and the seasonal growth of sea ice is a hindrance. These issues, however, are being addressed by the ARGO community (Roemmich et al., 2009). Recent deployment of some deep ocean ARGO floats will one day provide long time series of data to 4000 m and pilot experiments are under way for some floats to reach 6000 m (`http://www.argo.ucsd.edu/`).

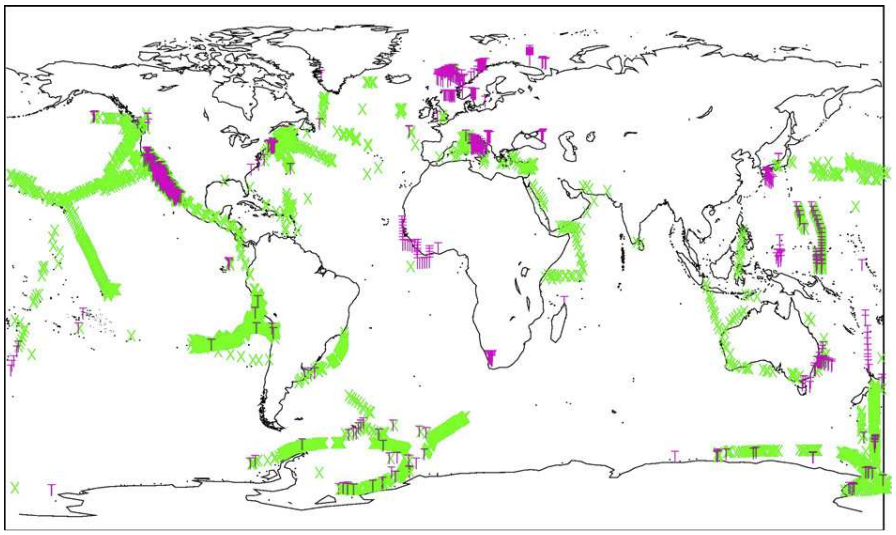

(A) January 1958

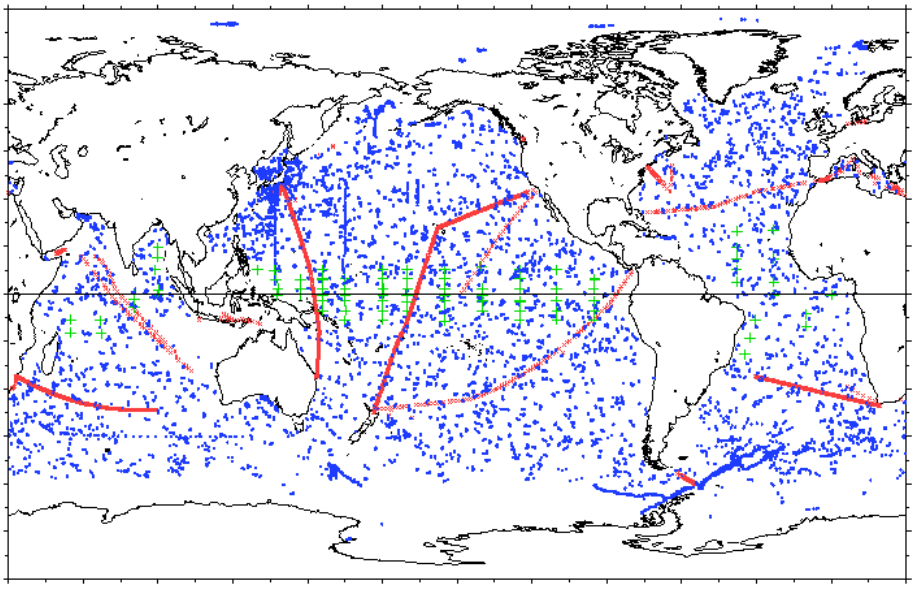

(B) January 2010

FIGURE 4.2: Observational subsurface temperature profile sampling for (A) January 1958 (Ingleby and Huddleston, 2007) (Green X - MBT data (3508 reports), purple T - ocean station data (855 reports)) and (B) January 2010, Climate Prediction Centre, NOAA. (red x - XBT probes (1654 reports), green + - moorings (3487 reports), blue O - ARGO floats - (14,530 reports))

Presently, data is available to 2000 m and therefore the abyssal ocean changes are still only monitored by ship board CTD casts.

Instrumental error

When considering changes to sea level resulting from steric contributions over

decadal time scales there will be an inevitable change in the instruments used to collect the data. Comparison of one instrument's record to another could lead to false assumptions unless they have been accurately calibrated. Since 1999 there was a dramatic increase in sampling, both at the surface and subsurface, within all ocean basins due to the introduction of ARGO floats. Around the same time the data also shows an increase in the heat content of some areas such as the Atlantic gyres and the Southern Ocean. Due to the short time scale of data recorded from ARGO floats their calibration is still ongoing and we have been careful not to make inferences about coinciding events in the data. The heat content estimates of Smith and Murphy (2007), discussed below, were tested with and without the ARGO data to confirm that the steric signals over the same time period were consistent (Williams et al., 2014) as regional thermosteric values can be sensitive to pressure bias from ARGO instruments (Barker et al., 2011). XBTs were the dominant source of ocean temperature profile data before ARGO floats. These have also been discovered to have instrumental error and all of the data sets that we use have been corrected for this (Gouretski and Koltermann, 2007, Ishii and Kimoto, 2009, Levitus et al., 2009, Wijffels et al., 2008)

Representational error

Unresolved observational points in the gridded data set are termed the representational error. The length scale of a grid square using a 1^o data set is around 100 km. Many oceanographic features, such as areas of high velocity currents, are of much finer scale (of order metres), and so are not represented by such a large grid. Many ocean models are now of a much finer scale to incorporate these features, however they are computationally expensive and are often on a regional scale for this reason. Representational error is often much larger than instrumental error (between 0.002^o and 0.2^o for temperature Ingleby and Huddleston (2007)) and the observed error from the gridded data set will be a combination of the two in the form shown in equation 4.3

$$\text{observation error} = \text{instrumental error} + \text{representational error} \tag{4.3}$$

Deep ocean warming

Song and Colberg (2011) examined the significance of deep ocean warming to sea level trends by using a modelled result for the steric contribution below 700m combined with Ishii and Kimoto (2009) data for the surface layer, GRACE estimates for the mass contribution and altimetry for the sea surface height. Their results

indicate that the deep ocean (below 700 m) could have contributed up to 1.1 mm yr^{-1} to the global mean between 1993-2008. They show that ocean circulation and dynamics distribute heat into the deep ocean, further explaining the unique regional patterns of absolute sea level trends from altimetry. If this steric value for the deep ocean is valid it would mean that observing and understanding changes in the deep ocean are vital for our interpretation and prediction of sea level trends. Purkey and Johnson (2010) also highlight the importance of the abyssal ocean for sea level. They report that their findings indicate a 0.1 mm yr^{-1} rise in global sea levels from the deep ocean (1000 - 4000 m) between the 1990s and the 2000s, and warming in the Southern Ocean contributed 1 mm yr^{-1} locally. Their study of abyssal ocean basin warming shows that ocean basins in the Southern Hemisphere have generally warmed more than those of the Northern Hemisphere. Advection from the source in the upper ocean through ocean circulation is one mechanism for the transportation of heat to deeper layers. Transportation time from Antarctic Bottom Water (AABW) to reach the North Pacific Ocean through advection is up to 1000 years, but this time is decreased to less than 50 years when propagated by Rossby or Kelvin waves (Nakano and Suginohara, 2002).

Steric estimates in the IPCC AR5 The IPCC AR5 report states that the correction for the XBT fall rate has been applied to the steric component of sea level since the IPCC AR4 report, and this correction has had the effect of doubling the estimated value of thermosteric sea level rise i the upper 700 m of ocean. This upper ocean warming is thought to have contributed 0.6 $\pm$0.2 mm yr^{-1} between 1970 and 2009. ARGO floats during more recent years can provide a more global coverage to a depth of 1000 m. Trends using ARGO between 2005-2010 range from 0.2 to 0.8 mm yr^{-1} (Leuliette and Willis, 2011, Stocker et al., 2013, Vaughan et al., 2013). The short time-scales of these estimates make them more uncertain and subject to natural variability. The IPCC AR5 estimates that the thermosteric component of sea level trends was 0.7 $\pm$0.3 mm yr^{-1} for the years 1993-2010 using XBT reconstructions updated from Domingues et al. (2008), (Stocker et al., 2013).

4.3 Data

We use 5 global gridded arrays to examine the steric contribution to global and zonal average sea level. The data compilations vary in their grid size, depth and duration as well as the data processing techniques which have been used to convert

the raw data into gridded formats. Table (4.1) briefly describes the data sets. The historical observational data which has been used to create the 5 temperature and salinity data sets is basically the same and what differs between these 5 products is the technique that has been used to create a gridded product, as well as the depth that the end product is available to. Many areas of the ocean are unsampled even today, and interpolation techniques are used to account for areas of missing data.

Data	Years	Reconstruction	Depth	Resolution (degrees)
Smith and Murphy (2007)	1950-2010	Covariance technique	full depth	1.25
Ingleby and Huddleston (2007)	1966-2010	Objective analysis	full depth	1
Ishii and Kimoto (2009)	1945-2010	Objective analysis	1500 m	1
Levitus et al. (2009)	1955-2010	Objective analysis	700 m	1
Carton et al. (2000)	1871-2008	Model reanalysis	full depth	0.5

TABLE 4.1: Overview of the 5 data sets used for the steric reanalysis

4.3.1 The Smith and Murphy (2007) dataset

Dr. Doug Smith (Hadley Centre for Climate Prediction and Research, Met Office, Exeter, UK) provided a 1.25° x 1.25° gridded full depth data set (Smith and Murphy, 2007) of both temperature and salinity, which uses a covariance technique to populate data sparse regions. The covariances are obtained from the coupled global climate model HadCM3 (Gordon et al., 2000), enabling them to be computed at the model resolution. This new technique aims to refine observational covariance techniques which have a much coarser resolution due to the lack of subsurface observational data. The lack of data potentially leads to large signals in remote areas being underestimated due to the correlation scale being too short, while also smoothing sharp gradients in regions where the estimated correlation scale is too long. Both the temperature and salinity data is available for the years 1950 to 2010, for full depth profiles. Smith and Murphy (2007) suggest that whilst this technique is currently in its infancy, as models become more realistic and sampling becomes more widespread (with the growth of ARGO coverage), analyses using model covariances will become increasingly important.

Raw data for this data set is used from ocean temperature and salinity observations from bottles, MBTs, XBTs and CTD probes as well as moored buoys and ARGO floats. For 1950-1955 data was taken from the World Ocean Database 2001 (Conkright et al., 2002) and the Enhanced Ocean Data Assimilation and

Climate prediction (ENACT) data set from 1956 onwards. Observations of sea surface temperature (SST) were taken from the Hadley Centre sea ice and SST data set (HadISST) (Smith and Murphy, 2007). Prior to HadCM3 analysis, data is averaged into a 1.25 degree grid. Smith and Murphy (2007) note the sparsity of data at depth, especially for salinity measurements and pre-ARGO years. Quality control flags were provided by Conkright et al. (2002) and data greater than 3 standard deviations from the climatology was also removed. Smith and Murphy (2007) noted that the smoothness of the Conkright et al. (2002) data led to anomalies in regions of high gradient such as the Gulf Stream when combined with the resolution of HadCM3 (1.25 x 1.25 degrees), therefore the Conkright et al. (2002) climatology was replaced with a mean of all observations binned in the HadCM3 grid for the period 1941-1996 provided that there were at least 5 observation. The standard deviation of instrumental error was taken as 0.1 K for temperature and 0.05 PSU for salinity. Representational and climatology errors were parametrized as a fraction of the monthly variability. Data results were assessed against the Ishii and Kimoto (2009) data set as well as tide gauges and altimetry.

4.3.2 The Ingleby and Huddleston (2007) dataset

Also used are temperature and salinity from the EN3 version 2a, Objective Analysis 1^{o} gridded data set (Ingleby and Huddleston, 2007) for the years 1966 to 2010, received directly from Dr. Simon Good (Hadley Centre for Climate Prediction and Research, Met Office, Exeter, UK). Data source for this dataset the World Ocean Database 2005 (Boyer et al., 2006), and supplemented with data from the Global Temperature and Salinity Profile Project `http://www.nodc.noaa.gov/GTSPP/` from 1990. ARGO data is also used from 1999 from the global data assembly centres (Coriolis `http://www.coriolis.eu.org/` and the Global Ocean Data Assimilation Experiment `http://www.usgodae.org/argo/argo.html`). Additional Arctic data was also included. The data were collated as part of the Arctic Synoptic Basin-wide Observations (ASBO) project by Takamasa Tsubouchi at the National Oceanography Centre Southampton `http://www.teacosi.org/asbo-project`.

Observation data in the vertical resolution is thinned to 42 depths. Data has been corrected for fall rate errors in XBTs as described in Gouretski and Koltermann (2007), Wijffels et al. (2008) and Hanawa et al. (1995). The correction discussed

by Hanawa et al. (1995) was complicated by the fact that most XBT tests performed by were from results collected in low latitudes. As colder water has a higher viscosity, the correction at high latitudes needs to be less than at low latitudes. Ingleby and Huddleston (2007) apply the fall rate correction factor to this dataset of 1.0336 for temperatures over 15° C. A correction of 1.00 was applied if the mean temperature of the region was below 5° C and a linear transition was applied in between. Superobbing, (the difference between observations and co-located backgrounds), of moored buoy reports gave daily averaging of the data allowing for consistency in the data over differing buoy types. Stability and duplicate checks, background and buddy checks were performed. A track check was performed following the reported position of the XBT or ARGO float. A maximum speed was applied of 15 m s^{-1} for ship data and 2 m s^{-1} for moored and profiling buoys. Constant values (suggesting that correct information had not been transmitted if 90% or more of the temperature levels over 100 m had the same value), spikes (denoting unusually large jumps in values, and so unrealistic data) and step checks (where unrealistic jumps are recorded) were analysed. The dataset also uses quality control results from altimetry using techniques documented in Guinehut et al. (2009).

The length scale of a 1 degree grid square is around 100 km. Ingleby and Huddleston (2007) suggest that improvements to the database could be met by tighter stability and other checks in certain geographical regions. For instance, locations of high variability, such as the Gulf Stream or Kuroshio Current and the steep thermocline at low latitudes have a large vertical and/or horizontal gradient which results in warm and cold clusters when observed from ship tracks crossing the current. As a result of the quality control checks, some of these observations can be rejected, and the mean within a grid square is much smoother than individual depth profiles. RMS error values are published in Ingleby and Huddleston (2007) and vary at each depth level. RMS error values range from 1.7° C - 0.07° C for temperature at the surface (5 m) and the sea floor (4983 m) respectively. RMS error values for salinity vary from 0.57 - 0.016 at the surface (5 m) and the sea floor (4983 m) respectively. In the absence of data, the Ingleby and Huddleston (2007) data set uses a background 1 day ocean forecast of the Forecasting Ocean Assimilation Model (FOAM), a climatological field for Global Seasonal (GloSea) or a persistence forecast for ENACT/ENSEMBLES. The background values are interpolated using bi-linear interpolation where possible to the nearest observation.

4.3.3 The Ishii and Kimoto (2009) dataset

The Ishii et al. (2005) (Ishii and Kimoto, 2009) data set was downloaded from `http://atm-phys.nies.go.jp/~ism/pub/ProjD/v6.9/`. The data is provided on a 1 degree grid with 24 depth levels from the surface to 1500 m. The XBT depth rate bias causing positive temperature values has been corrected for using the techniques described in Ishii and Kimoto (2009). The observed temperature and salinity data is provided by the World Ocean Database (WOD05) and the climatology is provided by the World Ocean Atlas (WOA05) both sourced from the National Oceanography Data Center (NODC), USA (Boyer et al., 2006). The GTSPP data is maintained by NODC under an international cooperation coordinated by the World Meteorological Organization and the Intergovernmental Oceanographic Commission (Ishii and Kimoto, 2009). In order to compensate for the sparseness of the World Ocean Database since 1990, data from the near real-time archive of the Global Temperature-Salinity Profile Program (GTSPP) was used. A set of XBT observations compiled by the Japan Oceanography Data Center were also included, provided by the Japan Maritime Self-Defense Force (JMSDF) from 1970 to 2003.

All observational data was inspected using quality control procedures described in Ishii et al. (2003, 2006). Observational data of each instrument type (XBT, CTD, CTD+BOTTLE) was averaged into monthly regional 1 degree boxes. The box averages were used to sample instruments at depth in order to compare instruments and obtain coefficients to estimate the fall rate bias. XBT and CTD+BOTTLE observations were found to be a maximum of 1.4 degrees latitude and one month time lag apart, therefore when calculating the box averages Ishii and Kimoto (2009) used observed deviations from the WOA05 climatology interpolated to the position and the date of the observation, rather than the full temperature values (Ishii and Kimoto, 2009) in an attempt to minimise the observational error through the representational error (equation (4.3)). Meso-scale eddies, human error and instrumental errors are reduced by the number of observations within the box. Ishii and Kimoto (2009) state that the XBT temperature measurement error is 0.2° C and the depth accuracy is a minimum of 5 m. CTD and bottle instrument error for temperature is stated to be much lower at 0.003° C and 0.02° C respectively. Although depth accuracy for CTD is stated to be 2 m, for bottle measurements it is a maximum of 15 m (at depths of 6,000 m) with smaller errors above 1,000 m. Monthly observations are shared between four neighbouring boxes and weighted

according to the distance to the centre of the box, with the sum of the weights for each observation being one.

4.3.4 The Levitus et al. (2009) dataset

Annual Levitus et al. (2009) data was downloaded from `http://www.nodc.noaa.gov/cgi-bin/OC5/WOA09/woa09.pl`. Gridded 1° fields of temperature are available from 1955 to 2010 over 15 levels to a maximum depth of 700 m. Annual salinity gridded fields were not available and therefore the steric height reconstructions in this study are calculated using their climatology for the salinity field. Temperature values within this data set relax to the climatology in the absence of data. All bathythermograph data within this set is corrected for instrumental bias using a technique similar to that shown by Gouretski and Koltermann (2007). Levitus et al. (2009) note that even after the time-varying fall rate correction has been applied, there are still substantial temperature differences from nearby XBT and CTD profiles in the upper 100 m of the ocean and therefore state that there is still work to be done on correcting historical data for bias errors. Their analysis, comparing data before and after the corrections are applied, results in a similar global ocean heat content trend from 1955-2003, but showing reduced inter-decadal variability, especially during 1970 to 1980. ARGO float data, corrected for systematic errors is also included. Levitus et al. (2009) climatological monthly means are computed by first averaging decadal monthly means to insure that the better sampled ARGO period in the last decade does not disproportionately weight the average. In forming the gridded product, the median value of observation within grid squares is used rather than the mean to reduce the influence of outliers.

4.3.5 The Carton et al. (2000) dataset

The Simple Ocean Data Assimilation (SODA) version 2.2.4 (Carton et al., 2000) modelled data was used to compare the other four gridded reanalysis. SODA data is available from 1871 to 2009 as full depth gridded temperature and salinity fields on a 0.5° grid on 40 levels. SODA is an assimilation of an ocean general model forecast based on the Geophysical Fluid Dynamics Laboratory Parallel Ocean Program. The data used to constrain the model analysis includes all available hydrographic profiles, insitu sea surface temperature and salinity data from ocean

station data, moored time series, and satellite altimetry from Geosat, ERS-1 and TOPEX/Poseidon including night time infra-red SST. SODA is used to construct a retrospective analysis of temperature, salinity, and current in the upper layers of the ocean globally. Data to constrain levels below this depth is limited. The study in this thesis uses the data from 1950 onwards.

4.3.6 Error analysis

The error analysis in this section is the same throughout Chapters 3 to 5 where the standard error of the mean is shown. This is calculated statistically as a function of latitude as the standard deviation of the mean (S, equation (4.4)) divided by the square root of the number of valid points (n). This is shown in equation (4.5) In figure (4.10), where the error is calculated as the difference between the zonally averaged data sets, the error is calculated as the standard deviation of the mean of the 5 data sets in each band (S) divided by the square root of the number of data sets (n).

$$S = \sqrt{\frac{1}{n}\sum_{i=1}^{n}(x_i - \overline{x})^2} \tag{4.4}$$

$$Error(\sigma) = \frac{S}{\sqrt{n}} \tag{4.5}$$

4.4 The thermodynamic equation for sea water TEOS-10

We use the recently updated official IAPSO, (the International Association for the Physical Sciences of the Oceans), equation of state for seawater, TEOS-10 which are based on Gibbs function formulation and derive all thermodynamic properties of seawater in a consistent manner (McDougall and Barker, 2011). The equations replace EOS-80 as the official description of sea water (McDougall et al., 2003). TEOS-10 has been formulated to eliminate errors currently within the description of the heat content of sea water. In the new description, the enthalpy of the system is used as the conservative variable rather than potential temperature. Enthalpy is a measure of the total energy of a thermodynamic system, measured in Joules [J]. When turbulent fluid parcels mix potential temperature is not conserved, partly

because of the variation of specific heat with salinity, yet enthalpy is. *Potential* enthalpy is used because of enthalpy's dependence on pressure. For example, an increase of 1000 dbar can cause an increase of enthalpy equivalent to 2.5°C. Potential enthalpy is the evaluation of a fluid parcel that is brought adiabatically and without salt exchange to the sea surface.

TEOS-10 uses a new variable, conservative temperature (CT), and requires absolute salinity (S_A) as the salinity variable to replace practical salinity (S_P). (The conversion of salinity is computed and practical salinity is still the observational variable recorded for consistency). Conservative temperature is a function of absolute salinity and therefore practical salinity must be changed to absolute salinity before it can be calculated. Conservative temperature is directly related to potential enthalpy through a constant, C_p^o.

$$C_p^o = 3991.867\ 957\ 119\ 63\ \text{J kg}^{-1}\ \text{K}^{-1}$$

The background and theory to the set up of the Gibbs functions in TEOS-10 is described in Appendix A (A30) of the TEOS-10 manual (McDougall and Barker, 2011). The new equation of state for seawater uses a 48 coefficient expression to calculate the density of sea water. This 48 coefficient expression is described in detail in Appendix K of the TEOS-10 manual (McDougall and Barker, 2011).

4.4.1 Absolute Salinity and Practical Salinity

Practical salinity is calculated from the conductivity of seawater. The thermodynamic properties of seawater, however, are more dependant on the mass composition of seawater than the conductivity, and the density of seawater is a function of absolute salinity as opposed to practical salinity. The Reference Composition of Seawater (Millero et al., 2008) has been defined by the Scientific Committee on Oceanographic Research (SCOR) and IAPSO (Wright, D. G. et al., 2011). Its use is necessary in the conversion of practical salinity to absolute salinity, representing a best estimate of the dissolved mass fraction in Standard Sea Water. The difference between practical and absolute salinity for all salinity values is around 0.165 g kg^{-1} which is approximately 80 times (0.43%) as large as the accuracy with which observational salinity can be measured at sea (McDougall, 2003). the

reference salinity is related to practical salinity with the equation 4.6

$$S_R = \left(\frac{35.165}{35}\right) gkg^{-1} \text{ x } S_P \tag{4.6}$$

The Gibbs function expression for Absolute Salinity is then expressed through this Reference Salinity using the equation 4.7

$$S_A = \left(\frac{35.165}{35}\right) gkg^{-1} \text{ x } S_P + \delta S_A(x, y, p) \tag{4.7}$$

where δS_A is the Absolute Salinity anomaly. The Absolute Salinity anomaly is determined by accurately measuring a sample in a laboratory using a vibrating beam densimeter. This density is compared to the sample's Practical Salinity. 811 seawater samples have been compared from around the globe. McDougall (2003) exploit a correlation between δS_A and the silicate concentration to produce a computer algorithm, which can be used as a look -up reference table to estimate $\delta S_A = S_A(x, y, p)$

The global map (figure (4.3e)) shows that areas of high salinity are most affected when comparing absolute and practical salinity, such as the Mediterranean and ocean gyres. The depth profiles (figures (4.3a-4.3d)) reveal that large differences occur in the deep ocean of the North Pacific which are not obvious from the surface map.

4.4.2 Conservative and Potential Temperature

The mean temperature structure of the Pacific (figure (4.4a)) and the Atlantic (figure (4.4b)) Oceans for 2008 shows that much of the heat is in the top 500 m, but because of the depth of the Ocean basins, increases in deeper layers when integrated over depth will also contribute to the steric height value. The plots shown in figure (4.5) show how the temperature is affected by the new equation of state for seawater. Figures (4.5a to 4.5d) show latitude transects as a function of depth of the Indian (100° E), the Pacific (200° E), the Atlantic (325° E) and a longitude transect in the Southern Ocean (55° S). Figure (4.5e) shows surface values for the difference between Conservative and Potential temperature. Temperatures are affected between -0.2 to 0.2° C. Coastal regions are sensitive and the marginal seas such as the Baltic and Mediterranean are highly sensitive. The upper 1000 m is the most affected depth layer.

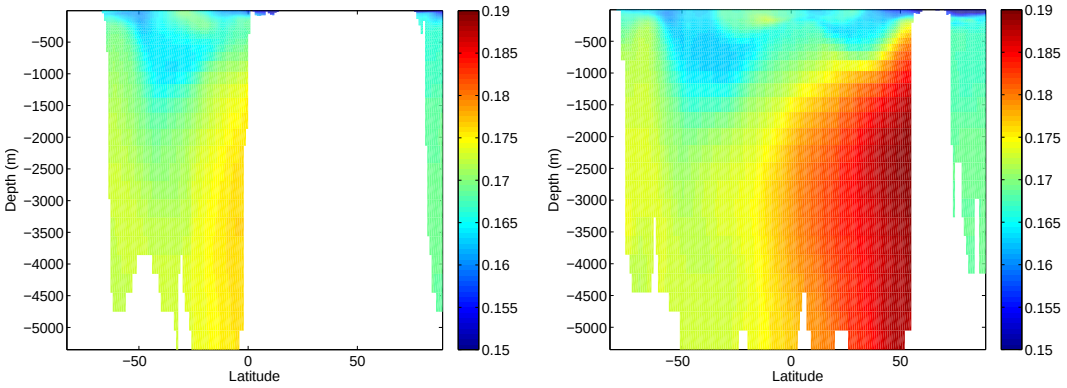

(A) Indian Ocean 100° E

(B) Pacific Ocean 200° E

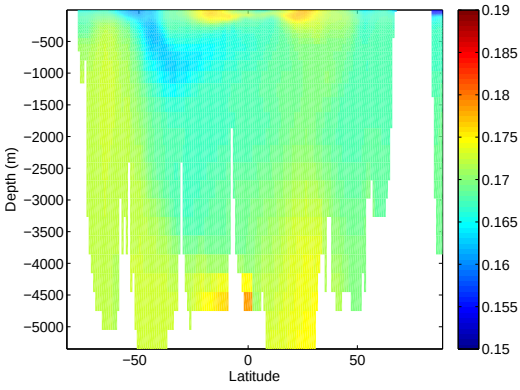

(C) Atlantic Ocean 325° E

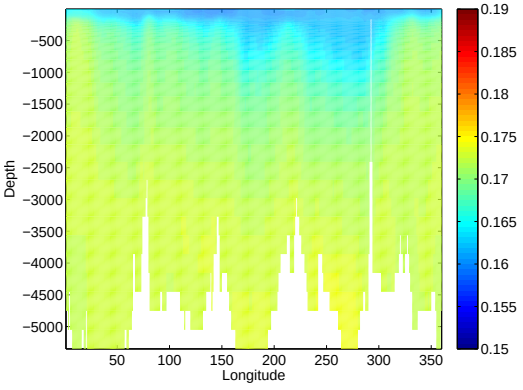

(D) Southern Ocean 55° S

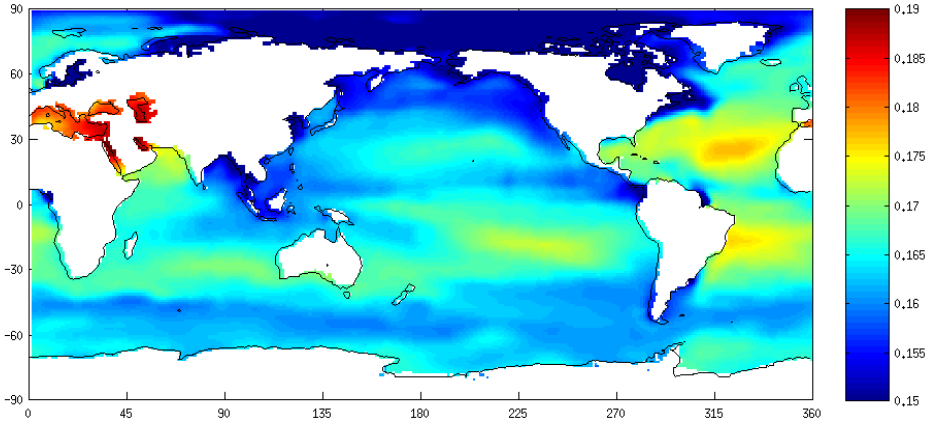

(E) S_A minus S_P surface map 2008

FIGURE 4.3: (4.3a-4.3d) Absolute Salinity minus Practical Salinity at 100°E, 200°E and 325°E and 55°S, cross sections of the Indian, Pacific and Atlantic and Southern Oceans (g kg^{-1}) during 2008. (4.3e) Absolute Salinity minus Practical Salinity surface annual mean 2008 (Ingleby and Huddleston, 2007)

.

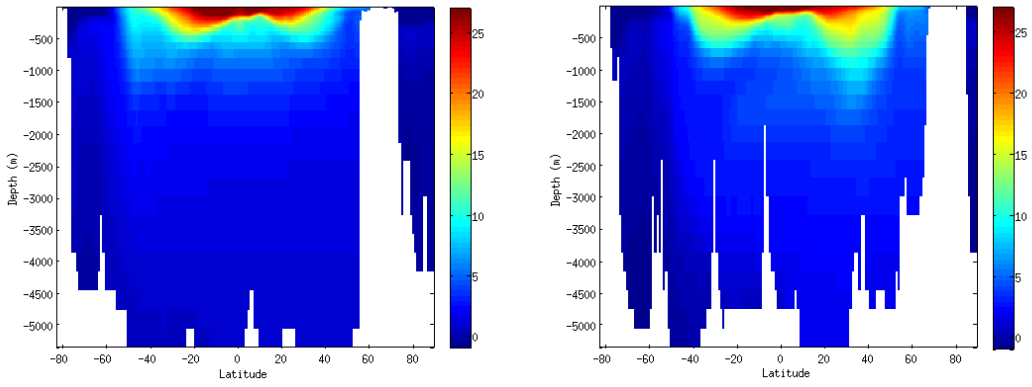

(A) 200E (B) 325E

FIGURE 4.4: Conservative Temperature mean depth profiles for 2008 (°C) (Ingleby and Huddleston, 2007)

4.5 Comparing the 5 data sets

The data sets were compared in various ways. By comparing annual variability of the 14° C isotherm we could analyse variability in the thermal structure at depth. The 14° C isotherm was used as it provided reasonable historical subsurface sampling, at a depth of around 200 m. This method is also used by Palmer and Haines (2009) for assessing the heat content of the ocean where they show that changes to the depth of the 14° C isotherm in the Atlantic was related to depression of the thermocline through wind driven factors and could be linked to variability seen in the North Atlantic Oscillation. The relative heat content refers to the heat content relative to an isotherm. By observing heat content relative to an isotherm as well as a fixed depth, some inferences to physical processes can be made i.e. surface warming or circulation-induced advection of local heat content change (Palmer and Haines, 2009).

Our 5 data sets agree within 2-4 m of the global-mean isotherm depth over more recent years, since the 1990's (Figure (4.6a)). Before this there is more spread between the 5 data sets of up to 10 m, although the general variability is consistent. Figures (4.6b, 4.6c and 4.6d) show the time series for the isotherm anomaly for the available length of each data set as 5 year running means centred on the middle year. The Atlantic Ocean has the largest variability of the 3 ocean basins with around 30 m increase in the depth of the 14° C isotherm since the early 1990's. All 5 data sets are in agreement with this trend although Carton et al. (2000) show that the magnitude of the depth increase is around 12 m. All 3 ocean basins show a deepening of the 14° C isotherm since 1993 which means that there is more

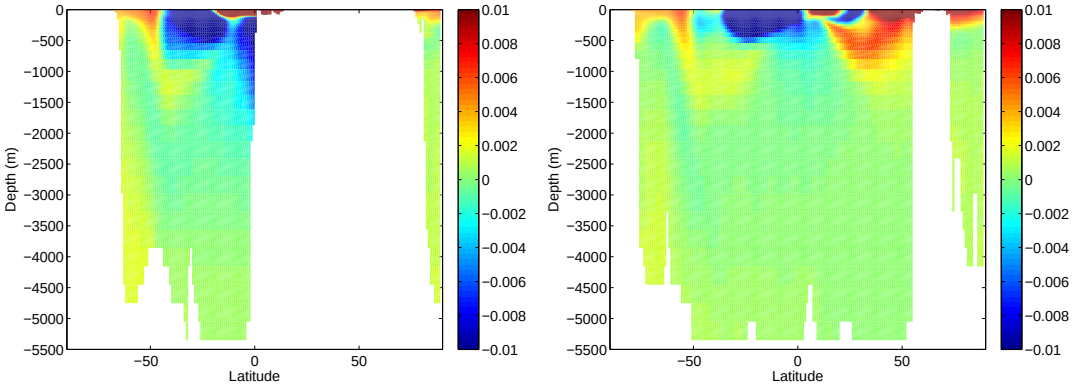

(A) Indian Ocean 100° E

(B) Pacific Ocean 200° E

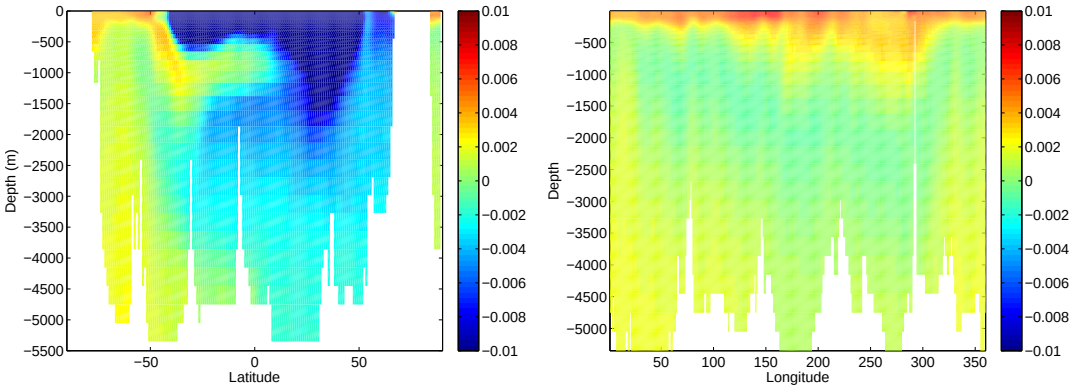

(C) Atlantic Ocean 325° E

(D) Southern Ocean 55° S

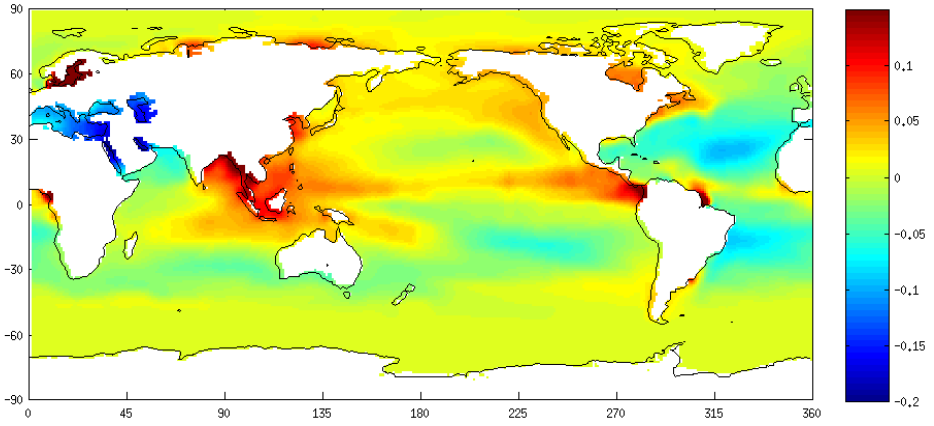

(E) CT minus PT surface map 2008

FIGURE 4.5: (4.5a-4.5d) Conservative Temperature minus Potential Temperature at 100° E, 200° E and 325° E and 55° S, cross sections of the Pacific and Atlantic Oceans (°C) during 2008. (4.5e) Conservative minus Potential Temperature surface annual mean 2008 (Ingleby and Huddleston, 2007)

water at 14° C or warmer in the water column in the Atlantic, Pacific and Indian oceans.

Figure (4.7) shows the annual time series of steric height as an anomaly of the average at each latitude for each of the 5 data sets. Carton et al. (2000) shows the most variability over the time span. The Ingleby and Huddleston (2007), Ishii and Kimoto (2009), Smith and Murphy (2007) and Levitus et al. (2009) data sets each show an increase in the steric height anomaly at most latitudes towards the most recent years. Some opposing patterns in the anomaly values are seen both at the equator and in the high latitudes of the Northern Hemisphere suggesting some long trend natural variability. The highest values in the steric anomaly are over the tropics and subtropics, although the Carton et al. (2000) data set does show some negative subtropical anomalies during 2007 to 2010 in the Southern Hemisphere. The very high northern latitudes (Arctic Ocean) also exhibits extreme anomaly values which also have opposing signs over the length of the time series. The patterns of variability in the Levitus et al. (2009) data set are smoother and more broad scale. The Carton et al. (2000) data set indicates to higher steric trends at the beginning of the time series during 1950-1960 especially in the Southern Hemisphere. This was not investigated in depth as the focus of the study was from 1993-2010, however this difference would need further consideration if the longer time series was to be used.

4.6 The global-average trend in steric height

The global trend in steric height (mm yr^{-1}) is plotted as the running mean of 18 year trends centred on the middle year, using the 5 data sets for comparison. These global trends are shown in Figure (4.8). The 5 data sets are in general agreement on the overall magnitude of the trend for the whole length of the time series, but they differ on the variability over its own record length. The Carton et al. (2000) data set is the most in disagreement with the other 4 data sets at the start of the time series, around 1962, but at this time historical sampling was much more sparse, where both the Ishii and Kimoto (2009) and Levitus et al. (2009) data sets rely on the climatology in the absence of data. The Ingleby and Huddleston (2007) data set has the most long time scale variability. The steric trends for 1993-2010 (or 1993-2008 for the Carton et al. (2000) data set) range from 0.39 mm yr^{-1} (Carton et al., 2000), to 0.67 mm yr^{-1} (Ingleby and Huddleston, 2007).

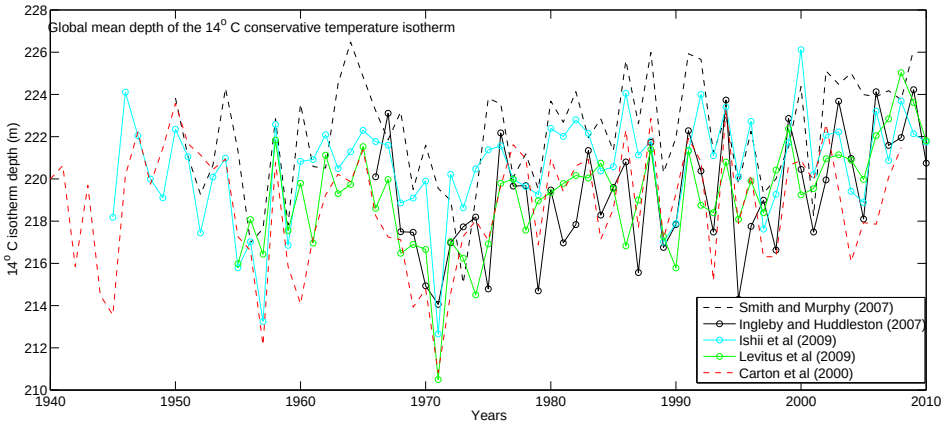

(A) Global-average time series comparing the 14° C isotherm for Smith and Murphy (2007) (black dash), Ingleby and Huddleston (2007)(black), (Ishii and Kimoto, 2009) (cyan), (Levitus et al., 2009) (green) and Carton et al. (2000) (red)

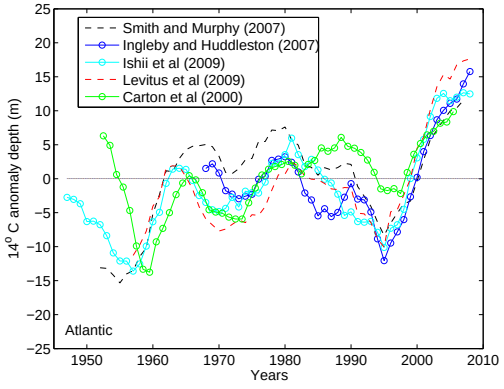

(B) Atlantic Ocean 14° C isotherm

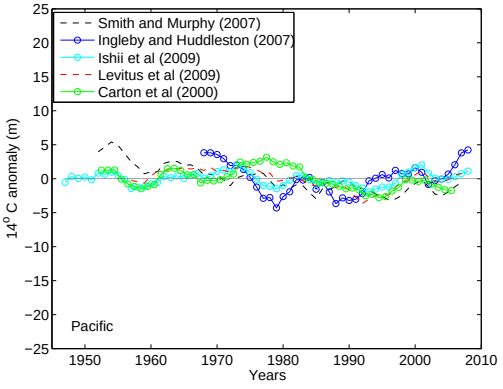

(C) Pacific Ocean 14° C isotherm

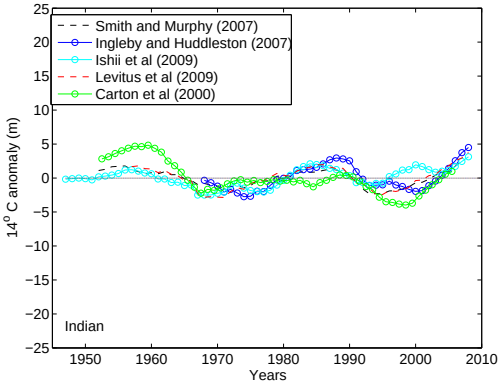

(D) Indian Ocean 14° C isotherm

FIGURE 4.6: Atlantic, Pacific and Indian Ocean comparison of 5 temperature data sets using the 14° C isotherm anomaly, relative to the long term average depth. Showing Smith and Murphy (2007) (black dash), Ingleby and Huddleston (2007) (blue), (Ishii and Kimoto, 2009) (cyan), (Levitus et al., 2009) (red) and Carton et al. (2000) (green) as 5 year running means centred on the middle year.

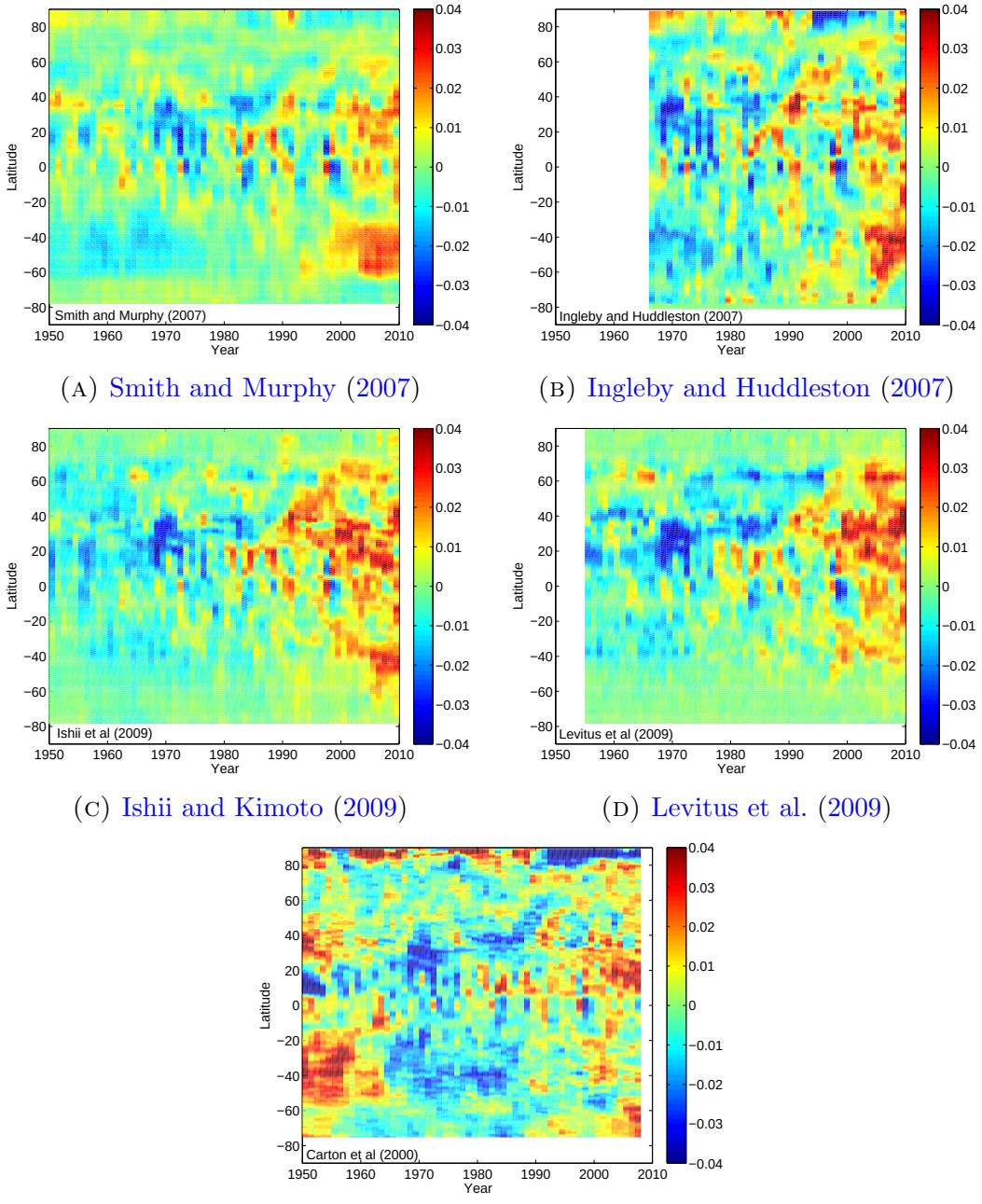

(A) Smith and Murphy (2007)

(B) Ingleby and Huddleston (2007)

(C) Ishii and Kimoto (2009)

(D) Levitus et al. (2009)

(E) Carton et al. (2000)

FIGURE 4.7: Latitudinal average of steric height anomaly (m) (anomaly calculated at each latitude over the time span) plotted as annual averages for each of the 5 data sets.

The trends for the whole length of the time series range from 0.14 mm yr^{-1} (1955-2010 for the Levitus et al. (2009) data set) to 0.32 mm yr^{-1} (1966-2010 for the Ingleby and Huddleston (2007) data set). Trends are both positive and negative at times meaning that the global ocean saw both periods of overall warming and overall cooling. The variance between these 5 data sets is used to calculate an error term for the steric component and is shown in Chapter 6 (figures (6.6a to 6.6d)).

The regional variability of trends in steric sea level (mm yr^{-1}) is shown between 1993 and 2010 for all 5 data sets in figure (4.9). The regional variability of the trends for 1993 to 2010 is in good agreement between the 5 different reconstructions. The positive trends in the West and South Pacific are common in all 5 reconstructions, as are the negative trends on the East Pacific. All 5 reconstructions show gyre scale opposing trends in the subtropical and subpolar gyres of the North Atlantic. The Indian Ocean shows mostly positive trends in all data sets apart from Carton et al. (2000), (the highest resolution model reconstruction, table 4.1), which shows much more local variability.

4.7 Zonal average of steric trends

The steric zonal average of 4 data sets (Ingleby and Huddleston, 2007, Ishii and Kimoto, 2009, Levitus et al., 2009, Smith and Murphy, 2007) is calculated for the time period 1993 to 2010 as shown in figure (4.10a). For the data set of Carton et al. (2000) we use the time period 1993 to 2008 to calculate the trend (due to data availability, table (4.1)). The zonal average is the mean steric value for each 10° latitude band between 85° S and 85° N, although when we use this zonal average analysis in other Chapters we only use values from -65° S and 65° N. The zonal average trend from each data set is shown with one standard error, where the error shown is the standard error between the 5 data sets. There is an approximate 1 mm yr^{-1} spread (but over 2 mm yr^{-1} at -40° S) between each of the 5 individual zonally averaged trends. Due to this variance between the 5 data sets we plot the mean of all 5 data sets which is shown in bold in blue. This mean of the 5 data sets is the steric zonal average trend that we use in further Chapters when we use the steric analysis. It is this mean of the 5 steric data sets that is subtracted from the tide gauge analysis in Chapter 3 and the altimetric analysis in Chapter 5.

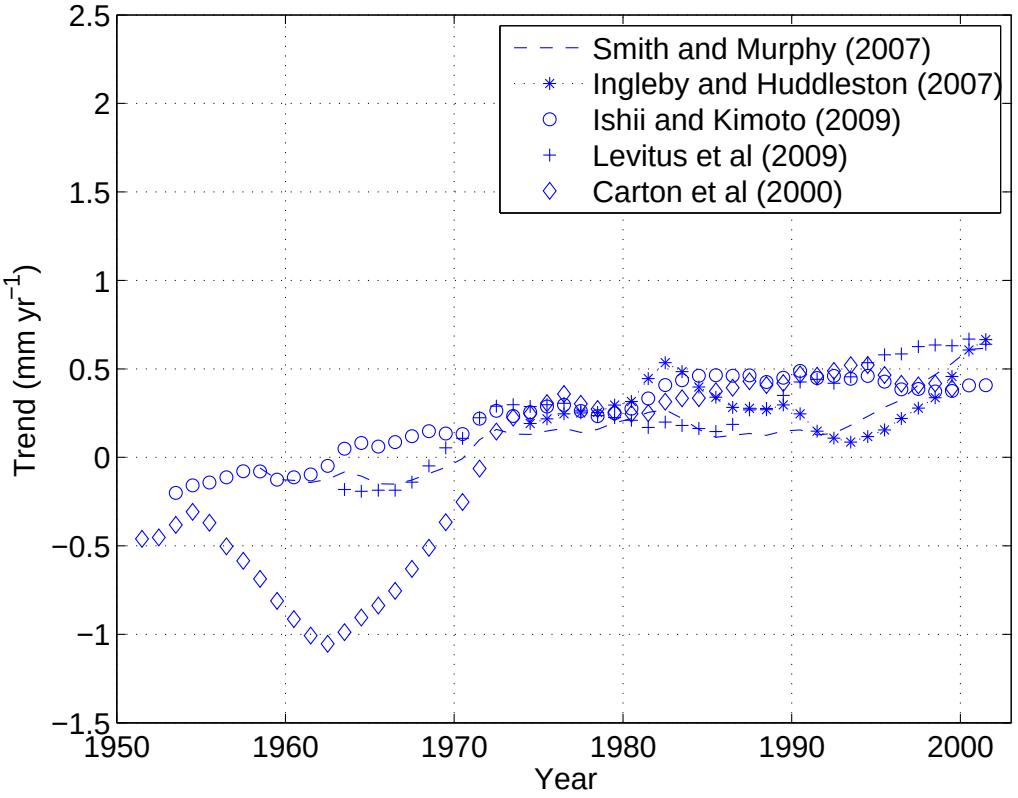

FIGURE 4.8: The area weighted global average steric mean trend calculated as 18 year running linear trends centred on the middle year for 5 data sets Smith and Murphy (2007) (- -), Ingleby and Huddleston (2007) (*), (Ishii and Kimoto, 2009) (∘) and (Levitus et al., 2009) (+) and Carton et al. (2000) (⋄).

The steric mean trend shows some latitudinal variability, being higher in the Southern Hemisphere than the Northern Hemisphere. Generally, the steric mean trend between 1993 and 2010 is around 1 mm yr^{-1} in the Southern Hemisphere and around 0.5 mm yr^{-1} in the Northern Hemisphere. The average steric mean trend is 0.83 ± 0.52 mm yr^{-1} for the years 1993 to 2010. This relatively large error shows that the uncertainty is fairly large in the steric estimate. It also shows that the difference between data sets is also significant, considering that all 5 data sets contain largely the same observations. By using the steric mean trend rather than a single data set we have tried to better account for the errors on the steric estimate for sea level trends.

Figures (4.10b and 4.10c) are shown for comparison with the trends computed over longer time scales. Figure (4.10b) is the steric zonal average between 1966 and 2010, and 4.10c is the steric zonal average for 1955 to 2010. The spread of the zonal trends is reduced in these longer term zonal averages. For reference, each data set is individually plotted with trends over the 3 time periods where

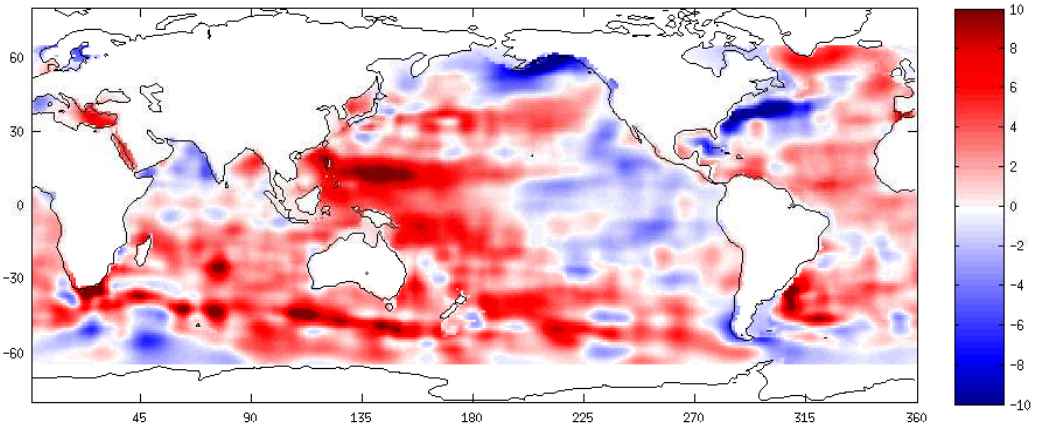

(A) Smith and Murphy (2007)

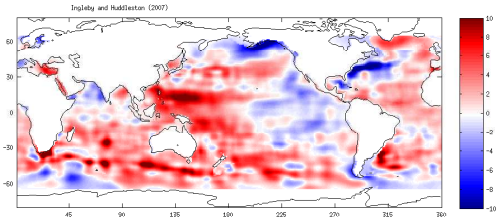

(B) Ingleby and Huddleston (2007)

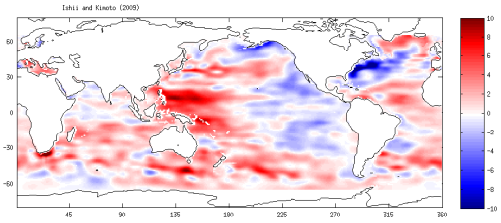

(C) (Ishii and Kimoto, 2009)

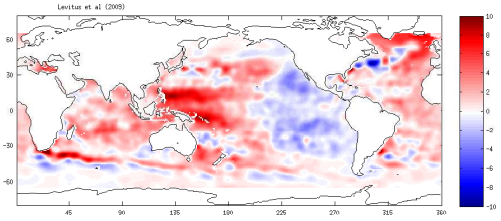

(D) (Levitus et al., 2009)

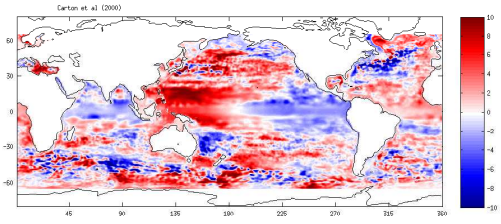

(E) Carton et al. (2000)

FIGURE 4.9: Steric trends between 1993 and 2010 (mm yr^{-1}) for 5 data sets.

available. Over the longer time period, trends are smaller for each data set. The mean trend between 1966 and 2010 is 0.43 ±0.07 mm yr^{-1} and the mean trend between 1955 and 2010 is 0.28 ±0.08 mm yr^{-1}.

4.7.1 Zonal averages for different time periods for each data set

Shown in figure (4.11) are the zonally averaged trends for each of the 5 steric data sets during the different time periods of 1955-2010 (black), 1966-2010 (green)

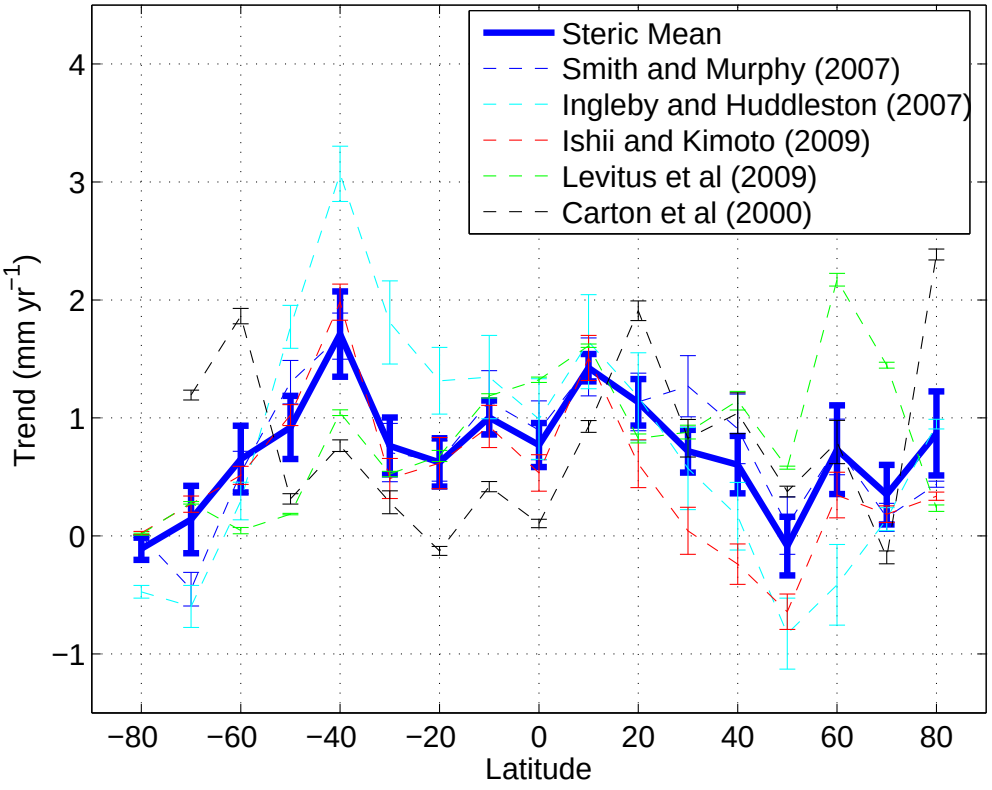

(A) Steric mean of 5 data sets for 1993 to 2010

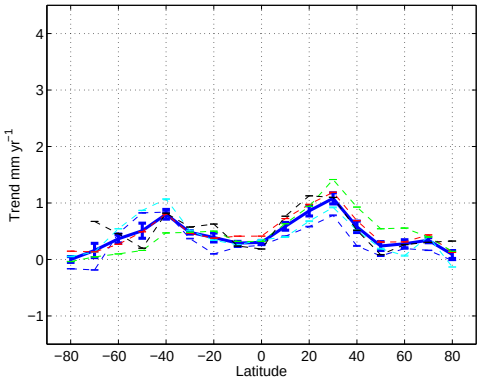

(B) Steric mean of 5 data sets for 1966 to 2010

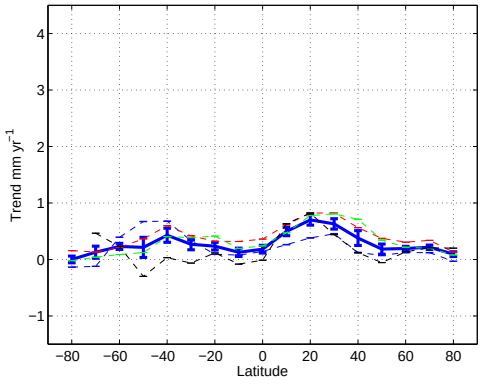

(C) Steric mean of 4 data sets for 1955 to 2010

FIGURE 4.10: Steric mean trends (mm yr^{-1}) (bold blue) as a function of latitude of the 5 data sets Smith and Murphy (2007) (blue dash), Ingleby and Huddleston (2007) (cyan), (Ishii and Kimoto, 2009) (red) and (Levitus et al., 2009) (green) and Carton et al. (2000) (black) for 3 different time periods (1993-2010, 1955-2010 and 1966-2010). Each data set is referenced to the deepest level available as stated in section 4.3.

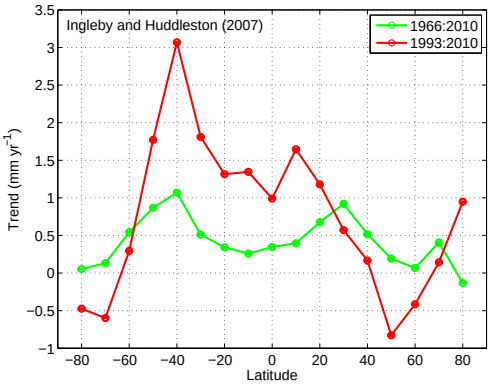

(A) Ingleby and Huddleston (2007)

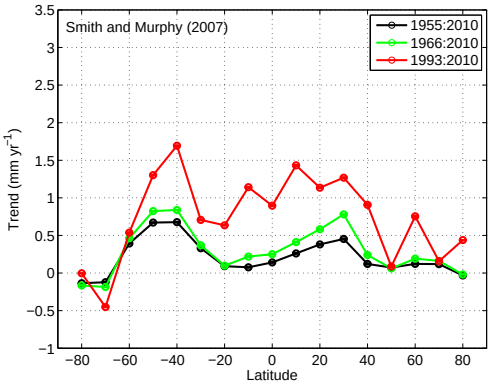

(B) Smith and Murphy (2007)

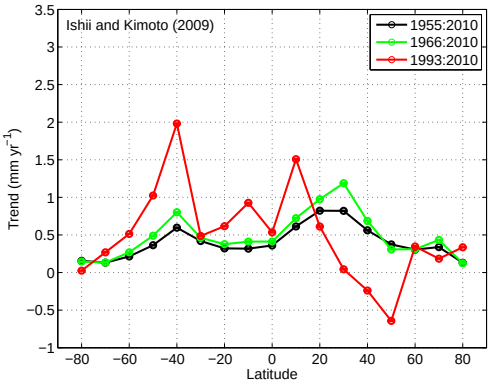

(C) Ishii and Kimoto (2009)

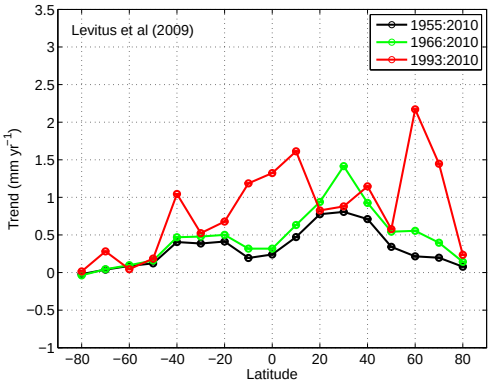

(D) Levitus et al. (2009)

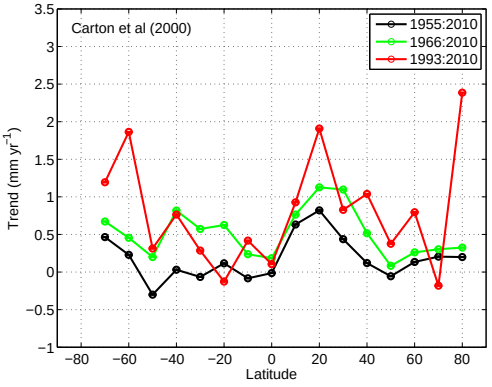

(E) Carton et al. (2000)

FIGURE 4.11: Zonal averages for trends during 3 time periods, (1955-2010 (black), 1966-2010 (green) and 1993-2010 (red)) where data was available for the 5 steric reconstructions (mm yr^{-1}).

and 1993-2010 (red), where the time span of each trend is based on the length of the time series (1955-2010 and 1966-2010), and the length of the altimetry period (1993-2010), measured in the units mm yr^{-1} and plotted as a function of latitude. As expected there is more variability during the shorter trend periods than the longer trend periods, due to smoothing of short time scale variability over longer trend periods. This feature is seen within the zonal averages of all of the 5 data sets, with the longest time period (1955-2010) showing least variability. The zonally averaged steric trends for 1955-2010 and 1966-2010 (where available) show highest trends at mid latitudes in both the northern and the southern hemispheres. This feature links to the latitudes where large ocean gyres are situated, and can be observed as high trends in the annual steric mean as shown in figure (4.1). These 2 peaks in the zonally averaged steric trends reach between 0.5 and 1 mm yr^{-1} in magnitude. The Ingleby and Huddleston (2007) and Smith and Murphy (2007) data sets show this peak to be roughly equal in the northern and southern hemispheres, while the Ishii and Kimoto (2009), Levitus et al. (2009) and Carton et al. (2000) data sets observe the steric trend peak to be larger in the northern hemisphere compared to the southern hemisphere. Comparison of the 1993-2010 zonally averaged steric trends shows much more variability than seen between the longer trends. The Ishii and Kimoto (2009) (figure (4.11c)) and the Ingleby and Huddleston (2007) (figure (4.11a)) data sets both observe a peak in trend in the southern hemisphere centred around 40^o S of around 2 and 3 mm yr^{-1} respectively. Both of these data sets also observe a minimum negative steric trend centred around 50^o N of less than -0.5 mm yr^{-1}.

4.7.2 The relevance of the reference depth

Our 5 reconstructions use gridded data from data sets of which 3 contain full depth data (Carton et al., 2000, Ingleby and Huddleston, 2007, Smith and Murphy, 2007), one is to 1500 m (Ishii and Kimoto, 2009) and one to 700m (Levitus et al., 2009). The steric height is evaluated from an assumed level of no motion. This is the deepest level available and is termed the reference depth. By recalculating the steric height using reference depths of 700 m, 1500 m and full depth only, we can evaluate the impact of the reference depth on the steric calculation. Figures (4.12a, 4.12b, 4.12c and 4.12d) show the results of the steric zonal average calculation when referenced to levels 700 m, 1500 m and full depth. The model environment of the Carton et al. (2000) data set in figure (4.12d) shows the least variability

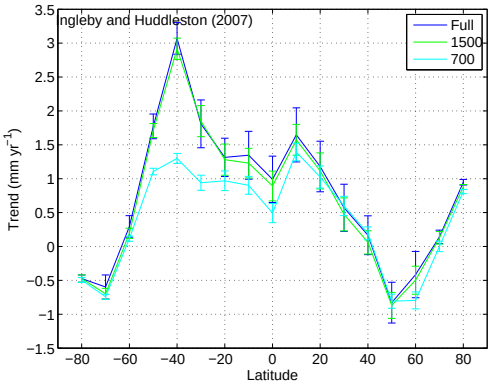

(A) Ingleby and Huddleston (2007)

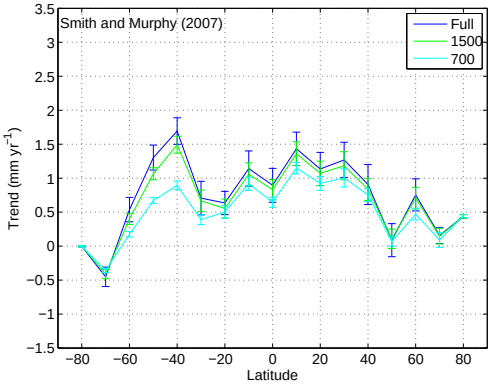

(B) Smith and Murphy (2007)

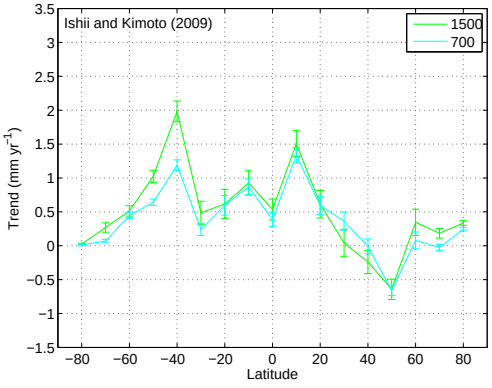

(C) Ishii and Kimoto (2009)

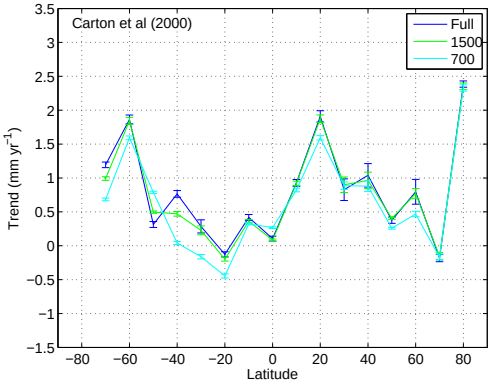

(D) Carton et al. (2000)

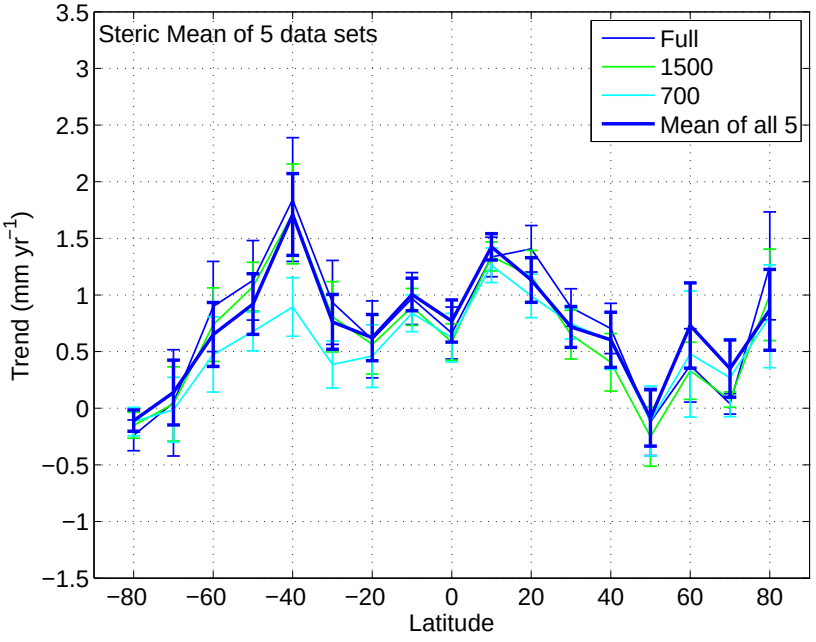

(E) Steric Mean of 5 data sets

FIGURE 4.12: The relevance of the reference depth was evaluated using the steric height calculated from an assumed level of no motion at 700 m (cyan), 1500 m (green) and full depth (blue). The error shown is one standard error for each 10 degree latitude band. Figure (4.12e) shows the zonal mean between all data sets for each of the 3 reference depths where data is available for trends during 1993 to 2010. The bold blue line compares the steric zonal average when the maximum reference depth available for each data set is used. (This is the same as the steric mean in figure (4.10a))

between this change in reference depth. Ingleby and Huddleston (2007), Ishii and Kimoto (2009), Smith and Murphy (2007) data sets (figures (4.12a - 4.12c)) all show slightly more variability, mostly within one standard error. The steric trend using a 700 m reference depth (cyan) shows regional trends that are generally lower than trends where the reference depth is 1500 m or full depth. This makes sense as we would expect some of the trend signal to come from deeper within the water column. The differences in trend outside of one standard error are generally located in the Southern Hemisphere.

Figure (4.12e)shows the steric mean of the 5 data sets for each reference depth. The bold blue line is the mean of the 5 data sets to their individual maximum depth. The 3 deepest steric zonal mean trends are within error and therefore we have confidence that the mean of 5 data sets referenced to their deepest level is well representative of the zonal average, but caution should be used when using steric trends which are not referenced to full depth. It should also be noted that the observations which go into the gridded products is very limited below 2000 m (and even at this depth only since ARGO floats). Therefore, even a gridded product which is to full depth will have large errors when giving values for the deep ocean. In order to quantify the true steric component to sea level trends more full depth observations are needed.

4.8 Summary

- The steric component of sea level is calculated from the specific volume anomaly using temperature and salinity data and the equation of state. Examined in this chapter are 5 temperature and salinity gridded data sets, which are used to evaluate and compare the steric height.

- The new equation of state, TEOS-10 is used. TEOS-10 introduces the variable Conservative Temperature and uses Absolute Salinity to produce a thermodynamically consistent set of equations to describe sea water and reduce errors in heat content and steric height calculations.

- The IPCC AR5 states that the steric contribution to sea level trends account for 0.7 ±0.3 mm yr^{-1} to sea level rise between 1993 to 2010 (Stocker et al., 2013). The IPCC AR4 had previously suggested that the steric contribution was closer to 50% of the contribution to total sea level rise (Bindoff et al., 2007, Lombard et al., 2005), showing that there is still some uncertainty regarding sea level trends and the sea level budget. This uncertainty is further complicated by the lack of historical data making it hard to calculate long term trends and the lack of deep ocean observations.

- Five data sets have been examined to compare the steric trends calculated from temperature and salinity data. There are considerable differences, as well as some similarities, between the data sets. This is true when the data sets are examined as isothermal layer depths, global average time series, regional average trends for 1993 to 2010 and zonal averages of trends for 1993 to 2010. The data sets tend to agree on the more prominent steric signals such as deepening of the 14^{o} C isotherm in the Atlantic (figure (4.6b)) and the East and West opposing steric trends in the Pacific Ocean between 1993 and 2010 (figures (4.9a, 4.9b, 4.9c, 4.9d and 4.9e)). The data sets differ in terms of the time scale of the variability, as seen in the global average steric trends time series (figure (4.8)).

- While the regional trends look similar in their spatial pattern, the magnitude of the zonal averages can vary between 1 and 2 mm yr^{-1}. For this reason the mean of the zonal average of the 5 data sets is used in Chapter 6 to estimate the mass component of sea level trends. The variance between the zonal average of the steric trends from the 5 data sets is used to estimate

the error. The steric mean of the zonally averaged trends calculated using 5 temperature and salinity data sets is 0.83 ± 0.52 mm yr^{-1} for the years 1993 to 2010 in this study. The significance of unobserved trends from the deep ocean should not be under-estimated. If the model analysis from Song and Colberg (2011), suggesting that an unobserved 1.1 mm yr^{-1} could have contributed to the steric trend between 1993 and 2008, is accurate then this would have a significant on both the steric zonal average and the calculated errors. This large steric trend from the deep ocean has not yet been observed with instruments and would need the deep ARGO floats (up to 6,000 m deep) to have global coverage before it could be detected on a regional scale.

Chapter 5

Sea Level Trends from Altimeter Measurements

The aim of this Chapter is to provide a view of sea surface height which is not constrained to be at the coast. The results will then subsequently be used to diagnose mass contributions from this sea surface height, after correction for the GIA response has been applied. The aim in this Chapter is also to assess the skill of our tide gauge analysis, which is known to have spatial bias. The constraint of the altimetry data is the comparatively short time scale for which there is data.

In this Chapter the spatial and zonal averages of trends from altimetry data are calculated for the time period 1993 to 2010. Changes in the gravity and global average VLD as a result of GIA are removed, so that the results can be used to compare with trends calculated from tide gauges in Chapter 3. We also compare regional and zonally averaged trends to the regional trends from our steric analysis over the same time period in Chapter 4 and we present the residual as an estimate for the mass component from the difference between these altimetry and steric trends.

5.1 Absolute sea level

T = Dynamic Topography
G_o = Geoid
G = Gravitational equipotential surface
τ = Augmented Dynamic Topography
VLD = Vertical Land Displacement
ASL = Absolute Sea Level
RSL = Relative Sea Level

Absolute sea level (ASL) is defined as the height of the sea surface above a reference ellipsoid measured from the centre of mass of the Earth. ASL is the definition of the sea surface that we measure with altimetry (figure (5.1)). Altimeters calculate the ASL by measuring the distance from the satellites to the ellipsoid (H) minus the distance to the sea surface (R).

The definition of G is also measured from the ellipsoid as the distance to the equipotential surface. This equipotential surface describes where the ocean would settle in equilibrium in the absence of wind, currents or change through time in the density structure of the water column.

Altimetry measurements differ from tide gauge measurements (in Chapter 3) in that measurements are from a high orbit (over 1,300 km) and therefore the altimetric measurements are not affected by vertical land displacement VLD. Tide gauges and altimetry are related through VLD such that

$$ASL = RSL + VLD \tag{5.1}$$

While the altimeter instrument is not moving up and down with any vertical land displacement, the sea surface can still be influenced by the movement of the ocean floor. There is a direct influence (if the ocean floor gets deeper on average then the global mean absolute sea level will fall) and an indirect influence as the land movement changes the mass distribution of the whole Earth. This can be taken into account by the fact that there will be a subsequent change in the equipotential surface G, as dynamic topography T is defined as the distance of the sea surface from G. There is only modelled output available for changes to G. Gravity satellite GRACE does observe changes in G but currently only has data available for half of the altimetry period. We use a combined modelled solution for the change in G

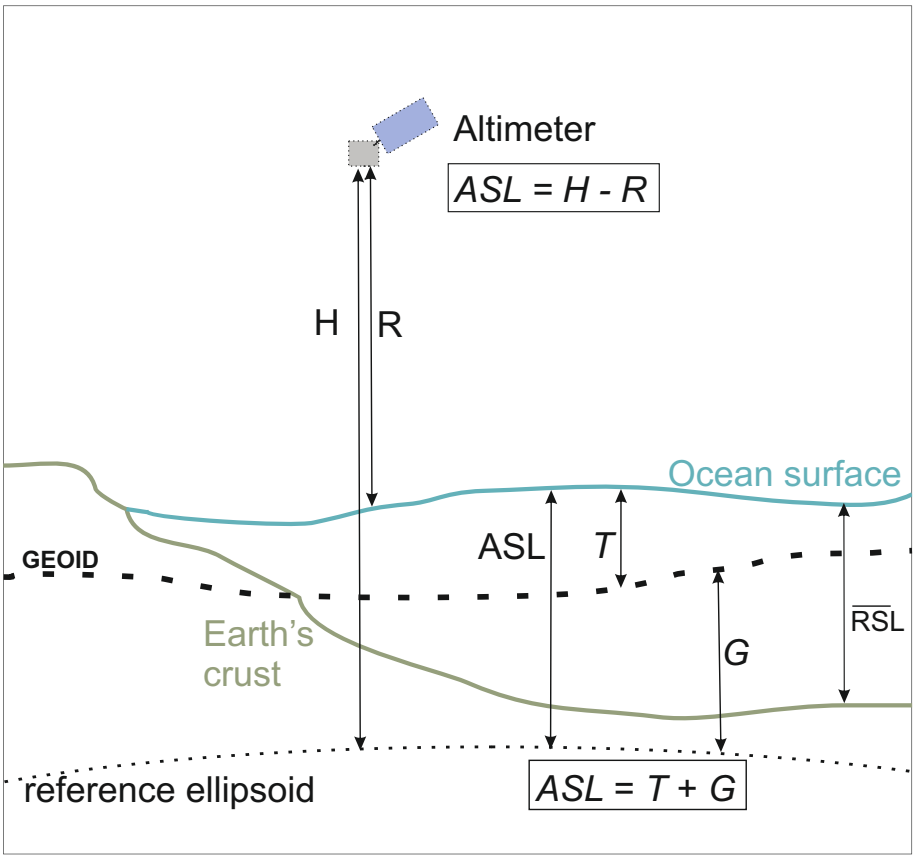

FIGURE 5.1: Schematic to show definitions and measurements from satellite altimetry. The reference ellipsoid (black dotted line) is the reference for ASL measurements. The geoid G_o (black dashed line) is the exact equipotential surface from which the dynamic topography T is measured to the ocean surface (blue line). G_o and G are referenced to the reference ellipsoid. The Earth's crust (brown line) is from where RSL is measured to the ocean surface.

and mean VLD due to the effects of GIA provided by Mark Tamisiea (National Oceanography Centre, Liverpool) (Tamisiea et al., 2001). Data for any changes in G unrelated to GIA, which includes recent melting, have not been corrected for. We use this remaining G and VLD response to compare our estimates with the fingerprints in Chapter 6.

In addition, we define dynamic topography (T) as the distance of the sea surface from the potential surface G and the dynamic topography is used to infer geostrophic currents (Hughes and Bingham, 2008). The three variables ASL, T

and G relate to one another as in equation (5.2) and (2.5).

$$ASL = T + G \tag{5.2}$$

When we consider the augmented dynamic topography, τ, we are using the dynamic topography T plus the mean global relative sea level $\overline{RSL}$. As set out in Chapter 2 equation 2.9, this allows for change in the dynamic topography plus change in the the water column from G to the crust.

$$\tau = T + \overline{RSL}. \tag{5.3}$$

Substituting T from equation 5.2 and using a substitution for RSL from a time average of equation 5.1 we can rewrite equation 5.3 as

$$\tau = ASL - G + \overline{ASL} - \overline{VLD}$$

where

$$\overline{ASL} \approx \overline{G} \qquad \text{and} \qquad G' = G - \overline{G}$$

where G' is the equipotential surface undulation, we then find that

$$\tau = ASL - (G' + \overline{VLD}) \tag{5.4}$$

This Chapter takes absolute sea level as measured by altimetry and, using model output for the change in G plus the mean crustal displacement (of the sea floor) (Tamisiea et al., 2001), corrects for changes due to GIA. The resulting approximate augmented dynamic topography will then be compared with approximate augmented dynamic topography as calculated from tide gauges in Chapter 3, steric reconstructions from Chapter 4 and used to evaluate the mass component to sea level in Chapter 6. The augmented dynamic topography (τ) is approximate because we have only corrected for GIA and not other sources of VLD or G displacement. These effects will be accounted for in the fingerprint calculation in Chapter 6.

5.2 Some background

Sea level observed by both tide gauges and altimetry includes both steric and mass contributions. The effects of large natural events such as volcanic eruptions are seen to be significant in the modelled global mean sea level record (Church et al., 2005), as a sudden increase in aerosols decreases ocean temperatures, affecting the steric component. It is also reported that water storage in dams, which has increased since the 1950s, has decreased global sea levels by up to 30 mm (Chao et al., 2008).

Several recent global mean sea level studies using both tide gauges and altimetry have trends that generally agree (Church and White, 2011, Holgate and Woodworth, 2004, Jevrejeva et al., 2006), especially over the more recent, better sampled period. Global mean sea level trends from altimetry for the period 1993 to 2009 were 3.2 ± 0.4 mm yr^{-1} (Church et al., 2013). At the time of the IPCC fourth assessment report it was thought that the global mean sea level trends over this period were made up of around 50% contributions from the steric and mass components. Willis et al. (2004) concluded that over the 1990s, 1.6 ± 0.3 mm yr^{-1} was the steric contribution compared with about 3 mm yr^{-1} from altimetry, while Lombard et al. (2005) found that the 1993 to 2008 steric trend was 1.7 ± 0.4 mm r^{-1} compared to 3.2 ± 0.2 mm yr^{-1} from altimetry. ARGO data used in these studies to determine the steric trend was in its infancy, and the altimetry dataset was only 10 years old. We now know that decadal and longer timescales still retain natural variability and using short trends will not distinguish between this decadal variability and a long term climate change.

More recently, in the IPCC AR5, the contributions to global mean sea level rise have been revised and it is now estimated that steric sea level accounts for 30% of the global sea level budget for 1993 to 2010 (Stocker et al., 2013).

5.3 Data

Satellite altimetry data is used from the Archiving, Validation and Interpretation of Satellite Oceanographic Data (AVISO) from 1993, which is in the format of a 1/3 degree spatially and 7 day temporal resolution. The altimeter products were

produced by Ssalto/Duacs and distributed by AVISO, with support from CNES `http://www.aviso.oceanobs.com/duacs/`.

Data is obtained from the satellites TOPEX/Poseidon with follow on missions Jason-1 and Jason-2 (joint United States (NASA) and French (CNES) orbital missions launched in 1992, 2001 and 2008 respectively to track changes in sea level with radar altimeters), and European Remote Sensing satellites (ERS 1 then 2) with the follow on mission Environmental Satellite (Envisat), launched by the European Space Agency (ESA) in 1991, 1995 and 2002 respectively.

The uniform gridded product that we use is derived from (TOPEX/Poseidon or Jason) and (ERS or Envisat) data at all times except for 29 Dec 1993 to 15 Mar 1995 when only Topex/Poseidon data were available.

For the AVISO product that we use, data has been corrected for instrumental errors and errors due to atmospheric and ionospheric signal propagation delays and sea state bias, representing a tendency for there to be stronger reflections from wave troughs than from crests. Geophysical corrections are also applied including the ocean and pole tides, and the precise orbit is determined (Ablain et al., 2009). These corrections are processed by the Centre Multimissions Altimétrique, which is part of the Segment Sol Multimissions d'Altimétrie, d'Orbitographie et de localisation précise (Ssalto), (http://www.aviso.oceanobs.com/en/data/product-information/ssalto.html). The Centre Multimissions Altimétrique applies precise quality controls to the geophysical data and monitors for instrumental drift. The data used within this thesis is at level 4, where cross-calibration between multi-satellite missions has been combined to produce gridded data. Data has also been inverse barometer corrected for atmospheric pressure.

The time average of the dynamic topography T (cm) is shown in figure (5.2) as an 18 year mean between the years 1993 to 2010. Satellite altimetry measures the absolute sea level ASL as the height above the ellipsoid. To correct this to dynamic topography, an independent measure of G is required. The AVISO product assumes G to be unchanging, so G changes due to GIA and other processes remain in the altimeter product.

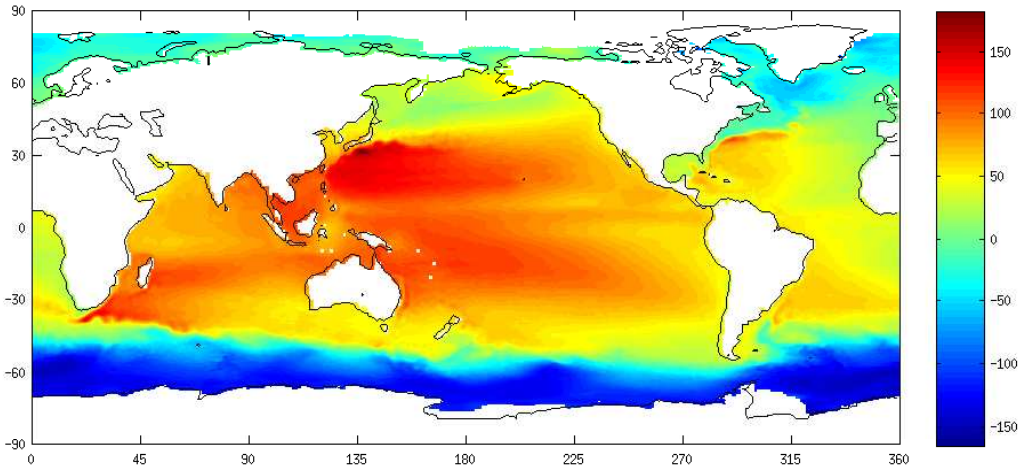

FIGURE 5.2: Global 18 year mean dynamic topography from AVISO altimetry for the years 1993 to 2010 (cm).

5.3.1 The global mean dynamic topography

The ocean's regional dynamic topography is not level, but influenced by a complex combination of processes. The largest contributor to deviation from the mean sea surface is G, where height differences can be ±100 m. Changes in density due to salinity and temperature differences over long and short times scales set up small and large scale circulation patterns which we term the dynamic topography. The addition of mass to the ocean via freshwater addition also affects the dynamic topography. Since satellite altimetry brought near global coverage to measurements of this dynamic topography, our understanding of the structure of the global ocean has increased rapidly.

Figure (5.2) shows the mean dynamic topography between 1993 and 2010, the same 18 year time period that we later use to calculate the regional structure of trends in sea level. Mean dynamic topography is high in tropical and subtropical regions, lower in high latitudes and higher in the Indian and Pacific Oceans when compared to the Atlantic. The highest mean dynamic topography is south east of Japan and the lowest is in the Weddell Sea. Large-scale gyre systems in the subtropics can be distinguished by higher dynamic topography. There is a sharp gradient of dynamic height between the high southern latitudes where the cool fresh circumpolar water of the Antarctic and the warmer tropical water in the southern basins of the Indian, Pacific and Atlantic which are associated with the Antarctic Circumpolar Current.

There are intense boundary currents linked to gradients in dynamic topography, such as the Gulf Stream and the Aghulas Current.

Ocean circulation is determined by the winds and the density structure as well as constrained by the Earth's rotation. We have analysed the trends in the density structure based on compilations of historical data contributing to steric height in Chapter 4. To minimise trends from wind stress variability, we use 18 year trends in our study to reduce the inter annual variability. Wind stress may indirectly produce longer term variability by changing the density structure of the ocean, but this effect is part of the steric variability.

5.4 The global trend

The AVISO data covers latitudes between 82°S to 82°N, which are the inclinations of ERS-1/2 and Envisat. At every available data point we calculate the 18 year linear trend between 1993 and 2010. At very high latitudes in both the Northern and Southern hemispheres there are some exceptional trends. These trends range from 1500 to -2000 mm yr^{-1} which is up to 3 orders of magnitude higher than current global mean sea level trends. We determine these extreme trends to be a consequence of sparse data sampling and poor temporal coverage resulting from the presence of sea ice. For this reason we limit our study to 65°S to 65°N inclusive.

5.4.1 Inland Seas

The Caspian Sea is an inland sea and not directly connected to the Global Ocean. Figure (5.3) shows that the Caspian Sea contributes a large negative trend which affects global average trend between 35°N and 55°N. Other semi-enclosed seas such as the Black Sea, the Baltic Sea, the Labrador Sea and to some extent the Mediterranean Sea also impact zonal averages, but have been included due to their link with the Global Ocean. The Caspian Sea data, however, is removed due to its isolation from the global ocean. The resultant map following these corrections is shown in figure (5.5). No colour saturation has been applied. The resultant trend is absolute sea level as measured by altimetry. The trends range from -15.0 to 22.6 mm yr^{-1}. These extreme trends are found in regions with strong dynamical signals, such as the Southern Ocean and western boundary currents. Henceforth,

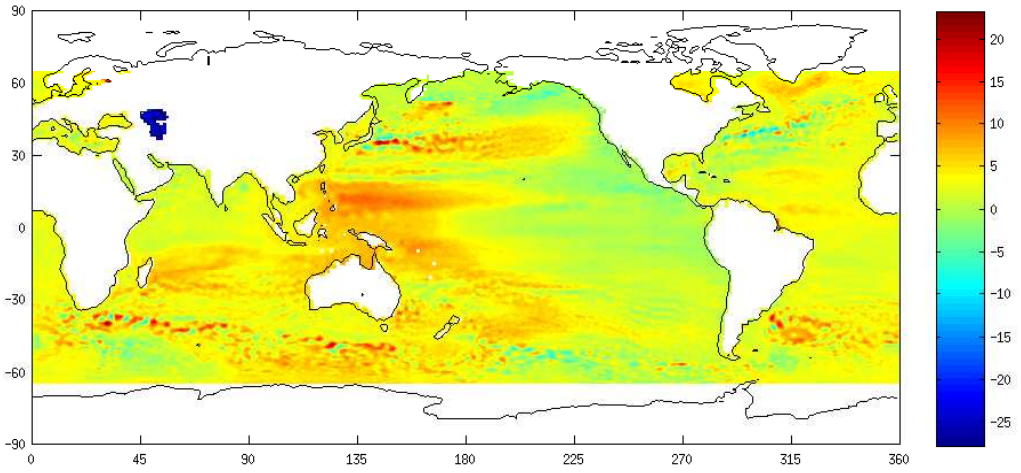

FIGURE 5.3: AVISO altimetry linear trend for the years 1993 to 2010 including the Caspian Sea's low negative trend, (mm yr^{-1}).

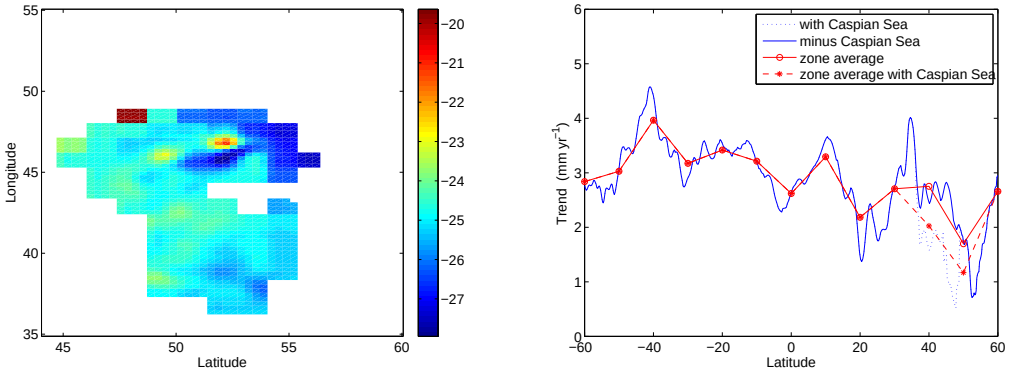

(A) The Caspian Sea. (B) Latitude averages of AVISO.

FIGURE 5.4: Local variability of the Caspian Sea (5.4a) and it's influence on the zonal average (5.4b) (mm yr^{-1}).

colours are often shown saturated at ±10 mm yr^{-1} to reveal the variability within ocean basins as shown in figure (5.6).

5.5 *GIA* corrections to the altimetry data

To compare the sea level trends with our steric reconstructions, we have to remove any influence from changes in the G and global average of crustal displacement.

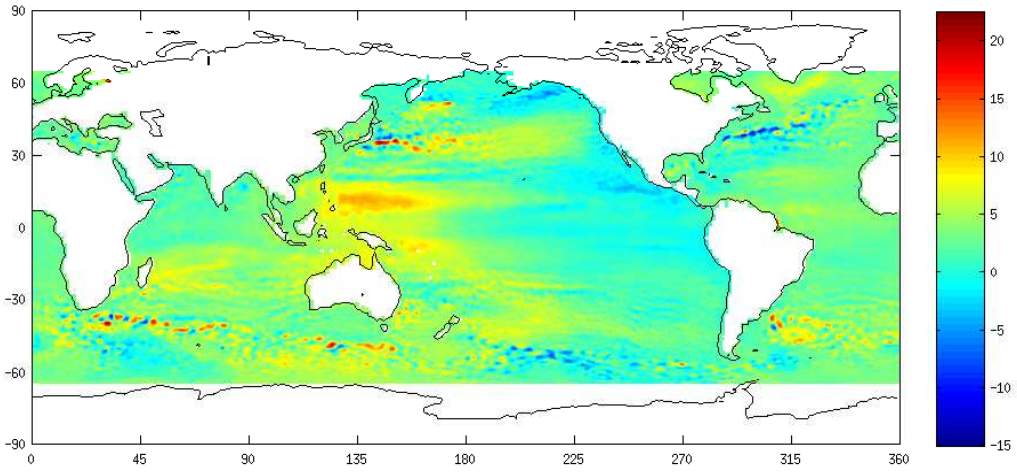

FIGURE 5.5: AVISO altimetry measure of absolute sea level linear trend for the years 1993 to 2010 with the Caspian Sea removed, (mm yr^{-1}). No colour saturation has been applied.

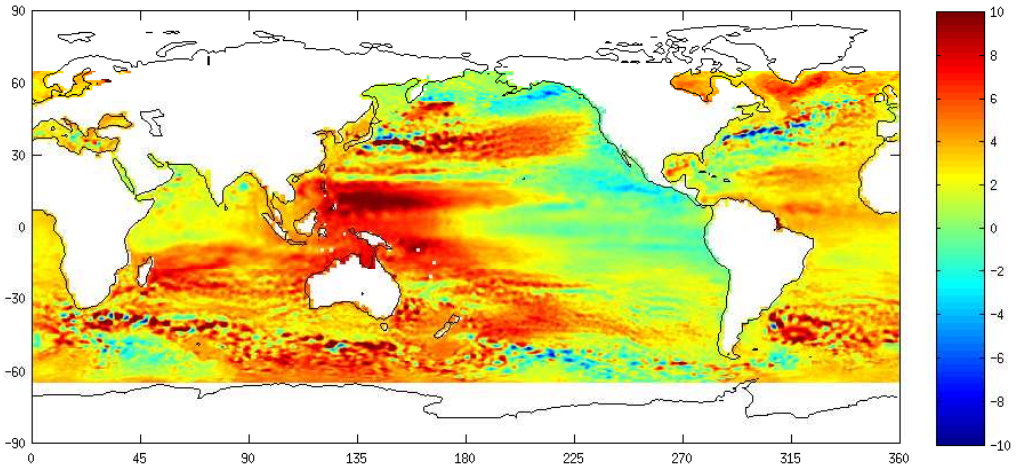

FIGURE 5.6: AVISO altimetry measure of absolute sea level linear trend for the years 1993 to 2010 with the Caspian Sea removed, (mm yr^{-1}). Colour saturation has been limited to ± 10.

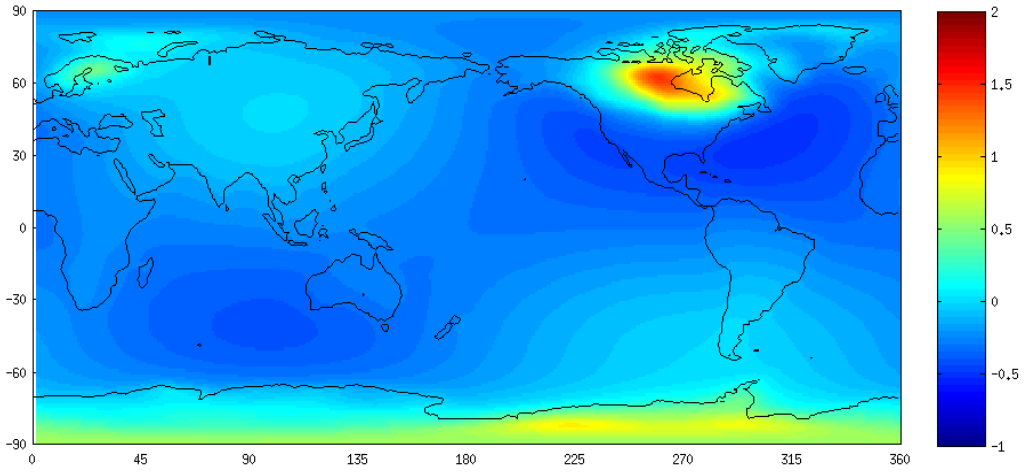

FIGURE 5.7: Spatial redistribution of G plus global ocean average vertical crustal displacement as a result from Glacial Isostatic Adjustment, (mm yr^{-1}). This is the sum of the terms $(\Delta G'_{GIA} + \overline{VLD}_{GIA})$ in equation (5.5).

The complete correction from ASL to τ is given by equation (5.5)

$$\begin{aligned} \tau = ASL &- (G'_{GIA} + \overline{VLD}_{GIA}) \qquad \xleftarrow{\text{GIA correction}} \\ &- (G'_{other} + \overline{VLD}_{other}) \end{aligned} \tag{5.5}$$

In order to calculate the augmented dynamic topography we must subtract the change in G and global average of vertical crustal displacement. We can subtract the part of this change which is due to GIA from modelled results (Tamisiea et al., 2001), and shown in figure (5.7).

Areas with largest values for the $(\Delta G'_{GIA} + \overline{VLD}_{GIA})$ term are mostly found over land, over areas which had large volumes of ice during the last glacial period. Many areas over ocean basins have a negative value, which then adds a positive trend once subtracted from the absolute sea level trend. This correction is the 0.3 mm yr^{-1} which is often added as a 'correction' to the global average trend, but has a variable spatial distribution (figure (5.7)). We subtract the $(\Delta G'_{GIA} + \overline{VLD}_{GIA})$ correction from absolute sea level at each latitude and longitude grid point. There is no measurement over this time span of 1993 to 2010 for the $(\Delta G'_{other} + \overline{VLD}_{other})$ and so this remains in the signal. The GRACE gravimetry satellite does measure this but there is only currently a short time series. As with the tide gauge calculation in Chapter 3, we use the fact that this remaining signal

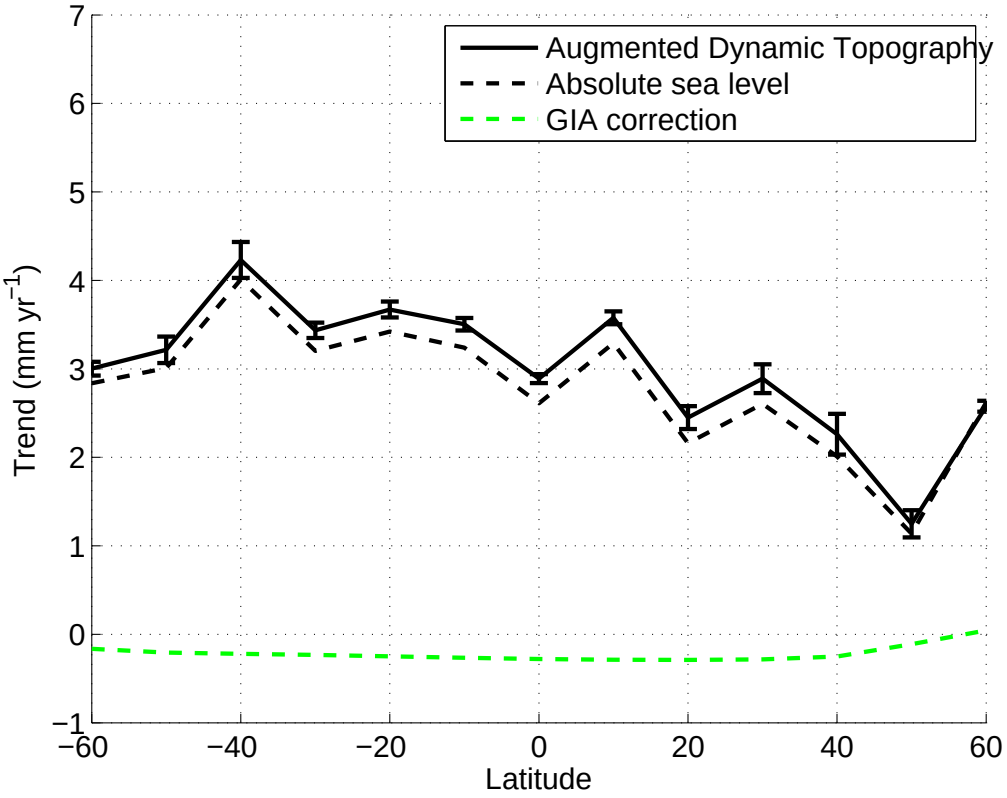

FIGURE 5.8: The zonal average of augmented dynamic topography with one standard error as calculated from $ASL - (G' + \overline{VLD})$, (mm yr^{-1}).

contains the $(\Delta G'_{other} + \overline{VLD}_{other})$ to compare our results with the fingerprints in Chapter 6.

5.6 Altimetry at tide gauges

The two separate zonal averages of augmented dynamic topography trends from tide gauges and altimetry are different. Augmented dynamic topography calculated using altimetry shows higher trends in the Southern Hemisphere and lower trends in the Northern Hemisphere (figure (5.8)), whereas augmented dynamic topography calculated using tide gauges shows higher trends in the tropics with lower trends in the higher latitudes of the Northern and Southern Hemisphere (figure (3.21)). In order to view the influence of sparse spatial sampling of tide gauges against the zonal average at each grid point of altimetry, the altimetry data is sampled at the tide gauge locations and used to construct zonal averages, in the same way as with the tide gauges. The nearest latitude and longitude point to

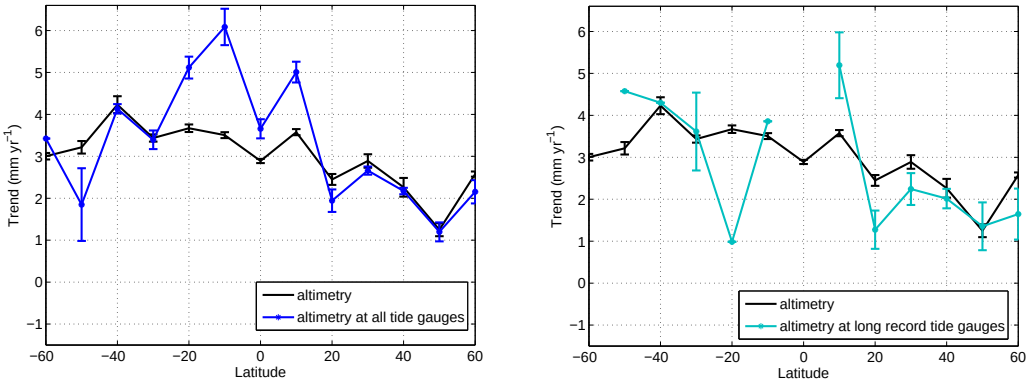

(A) Altimetry (black) and altimetry at all tide gauge records (blue)

(B) Altimetry (black) and altimetry at the long tide gauge records (blue).

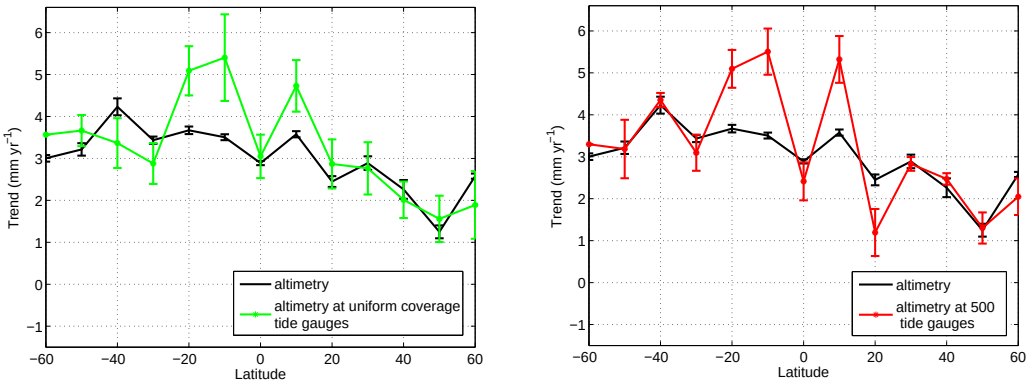

(C) Altimetry (black) and altimetry at the uniform coverage tide gauge records (green).

(D) Altimetry (black) and altimetry at the 500 tide gauge records set (red).

FIGURE 5.9: Zonal average of the trend in AVISO altimetry for 1993-2010 (mm yr^{-1}), calculated at every grid point (black) with the zonal average of altimetry calculated at tide gauge locations, using all tide gauges (figure (5.9a)), long record gauges (figure (5.9b)), the uniform coverage gauges (figure (5.9c)), and the 500 record set (figure (5.9d)) as set out in Chapter 3.

the tide gauge location was used where possible. Retrieval of altimeter data close to the coast is spatially variable, which means that the nearest point compared to a tide gauge could be between 25 and 50 km away. Tide gauges sited within estuarine environments are also difficult to compare with retrievals from altimetry data. Whenever possible we use the mean of a weighted grid result from the four surrounding altimetry points to the tide gauge location. The weight applied is calculated using the inverse of a haversine formula (which finds distances between latitude and longitude points) from the distance of the altimetry point to the tide gauge using their latitude and longitude co-ordinates. If no altimetry data is found in the four surrounding grid points then the process is repeated up to 2 grid squares away.

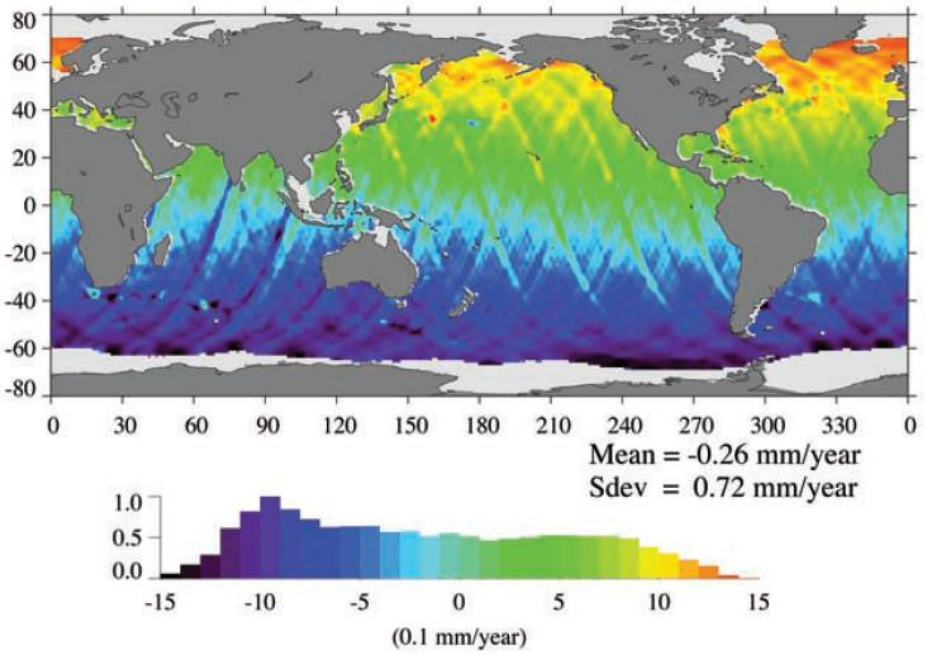

FIGURE 5.10: Image from (Beckley et al., 2007) showing regional TOPEX (1993-2002) SSH trend differences from the ITRF2005 minus CSR95 orbit differences, (0.1 mm yr^{-1}).

Figure (5.9) shows plots of both the zonal average of altimetry data and the zonal average of altimetry at tide gauges (colours) for the four subsets tide gauges as set out in Chapter 3. Larger values for the altimetry at tide gauges can be seen in the tropics for all of the four subsets. Therefore, we confirm that the difference in trend at the tropics is largely caused by sparse sampling of tide gauges within the tropics. This sparse sampling spans regions of high variation in sea level trends and variability (e.g. the zonal equitorial bands), which is often the reason for the tide gauge locations, so that the high variability in these regions can be monitored. This coarse sampling, though, causes an over estimation in the zonal average due to lack of gauges at other locations at these tropical latitudes. The zonal average of altimetry at tide gauges using the long time series gauge subset shows the most difference from the zonal average of altimetry at every grid point (seen in figure (5.9b)). As these gauges are chosen for their temporal coverage rather than their spatial coverage, the larger deviation from the zonal trend implies that the spatial bias in enhanced within this subset.

5.7 Reference frames

Although altimetry now has a time series of over 20 years, this is still relatively short in terms of some climatic variability. Issues with reference frame and orbital accuracy are important to be aware of as they could be intrinsically biasing the data. Figure (5.10) from the study by Beckley et al. (2007) shows an example of the result of recent orbital differences between the International Terrestrial Reference Frame 2005 (ITRF2005) for Jason-1 altimetry and those using the Centre for Space Research 1995 (CSR95) terrestrial reference frame for TOPEX/Poseidon between 1993 and 2002. Differences in the orbital lengths result in differences in the sea surface height (SSH) and its trend is shown in figure (5.10). There are differences of ± 1.5 mm yr^{-1} at high latitudes, leading to apparent higher trends in the Southern Hemisphere (purple and blue) and apparent lower trends in the Northern Hemisphere (orange and yellow). Our data uses more recent orbits and reference frames, so we would expect smaller errors, however, reference frame issues with new technologies and relatively short time series should always be treated with caution.

Altimetry data has been validated and compared with in situ time series as a reference to observe any drifts and Valladeau et al. (2012)

5.8 Discussion

Jevrejeva et al. (2008) found that correlations of monthly mean regional sea level and monthly mean regional upper 700 m of heat content varied between 0.3 and 0.8 between the years 1955 and 2003, with the largest correlations seen in the Atlantic Ocean and the lowest correlations seen in the Pacific and Indian oceans. Jevrejeva et al. (2008) also found that the increase in global sea level trend could not be full explained by the increase and decreases in the trend in global ocean heat content trends, proposing that the mismatch could in part be explained by the increase in mass into the global ocean. When the regional trend maps for 1993 and 2010 for augmented dynamic topography from AVISO altimetry, shown in figure (5.11a), are compared with steric sea level using the Ingleby and Huddleston (2007) data set as shown in figure (5.11b), we see regional similarities which suggest that patterns in regional trends for this time period are dominated by steric effects .

When we compare the residual trends by subtracting the steric topography (figure (5.11b)) from the augmented dynamic topography (5.11a) we find that many of those regional similarities disappear. This is shown in figure (5.11c) using the Ingleby and Huddleston (2007) data set. The residuals from the same augmented dynamic topography (5.11a) with the other four steric data sets subtracted are shown in figure (fig:regionalMass).

This study uses the AVISO altimetry gridded data set within this Chapter. Data sets from other sources are available and strength would be added to the conclusions if comparisons with other data sets were analysed. Other data sets include a revised data set (Ablain et al., 2015) produced from satellite altimeter time series (TOPEX/Poseidon, Jason-1, Jason-2 and ERS-1/ERS-2/Envisat) by the European Space Agency (ESA) as part of their Climate Change Initiative (CCI) program (`www.esa-sealevel-cci.org`). The CCI has recently developed new algorithms where more that 50 years of altimetry data were processed for the production of an 18 year long time series (1993-2010) of sea level. Several validation processes have assessed the internal consistency of specific mission-related systems from instrumental parameters to geophysical corrections. Global multi-mission comparisons have allowed for better coherence between different altimetry systems through comparison of the sea surface height data. Sea level differences have also been computed between in-situ sea level measurements from tide gauges and ARGO floats allowing for the detection of drifts and jumps in time series (Ablain et al., 2015).

The augmented dynamic topography shows mostly positive or no significantly negative trends over all latitudes while also displaying regional structure. The most striking regional pattern is the sharp east and west contrast over the Pacific Ocean. This east - west contrast is also seen in steric trends, where the eastern Pacific basin shows mostly negative trends for this time period and the western Pacific basin shows contrasting positive trends. This contrasting response has been shown to be caused by multidecadal shifts in the trade winds, also leading to changes in the shallow meridional overturning circulation in the Pacific (Feng et al., 2011). There is also a strong correlation to the Pacific Decadal Oscillation as shown by Zhang and Church (2012). It is likely that these contrasting basin scale trends will switch signs in the future (Merrifield et al., 2012). The highest trends in augmented dynamic topography are found in the West Pacific and extend to

parts of the Indian Ocean and Southern Ocean. High steric trends also appear in these regions.

The residual trend map (figure (5.11c)), has less regional structure and has mostly positive or minimally negative trends except for regions where the dynamics are seen to dominate such as the Antarctic Circumpolar Current and along western boundary currents. This is not surprising as we know that the augmented dynamic topography is not corrected for dynamical signals. Consequently we do not focus on the detail within the residual map but rather focus on the broad scale distribution of trends as zonal averages in Chapter 6.

The augmented dynamic topography trends in figure (5.13) are the same as the Figure (5.8), and show the zonal average values that we then use in Chapter 6 to estimate the mass component of sea level trends. Trends are shown with one standard error. There is a clear zonal dependence within the trend values. Higher trends are in the Southern Hemisphere compared to those in the Northern Hemisphere, especially between 20^o N and 60^o N where zonal averages of trends are lowest. The maximum zonal average trend is 4.23 mm yr^{-1} at 40^o S and the minimum zonal average trend is 1.24 mm yr^{-1} at 50^o N. All zonal average trends in the Southern Hemisphere are above 3 mm yr^{-1} whereas all zonal average trends in the Northern Hemisphere at higher latitudes than 10^o N are below 3 mm yr^{-1}.

The τ trends in figure (5.13) are shown with the tide gauge trends of τ for the same time period (1993 - 2010) as introduced in Chapter 3 in figure (3.21). The tide gauge trends show the 3 VLD corrections for the 4 subsets of tide gauges. The altimetry derived τ trends (black) are the same for each of the figures (5.14a-5.14d). The altimetry at tide gauges (grey), as previously discussed and shown separately in figures (5.9a - 5.9d), enables us to understand the spatial bias of the tide gauge locations, while the tide gauges corrected for land movement with the GIA model (blue) and GPS (green) provide an independent zonal average that calculated using altimetry. As discussed in Chapter 3, the GPS corrected tide gauges introduce a second spatial bias due to current availability of GPS data at tide gauges as well as including the land displacement signal from any recent melting, which we hope to use to compare with the fingerprints in Chapter 6. Therefore the GPS corrected tide gauges are not followed through to further Chapters. Future studies using tide gauges would greatly benefit, however, from GPS data at each tide gauge location.

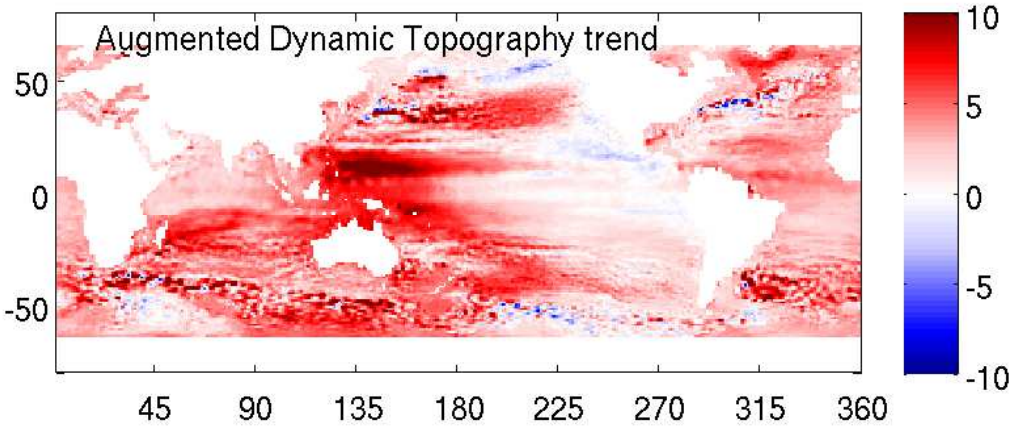

(A) Augmented dynamic topography trend calculated from AVISO altimetry and reduced to a 1° grid for the years 1993 to 2010, (mm yr^{-1}).

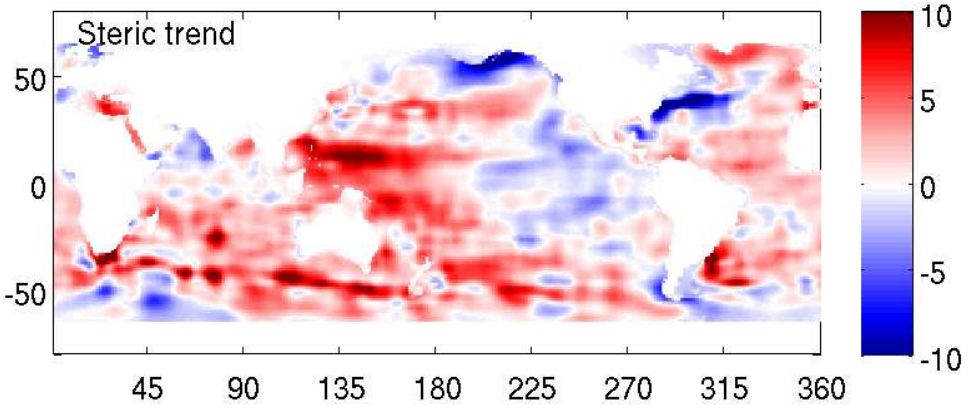

(B) Steric trend calculated from the Ingleby and Huddleston (2007) data set (as shown in figure (4.9b)) for the years 1993 to 2010, (mm yr^{-1}).

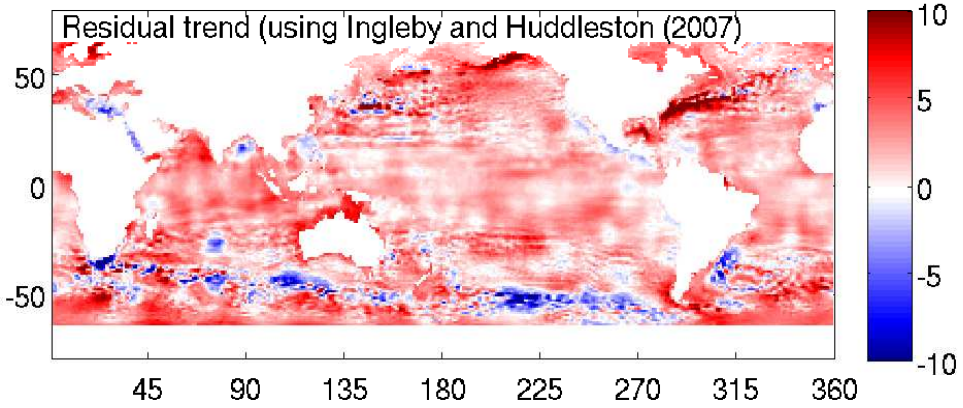

(C) Residual trend calculated from AVISO altimetry trend (1° grid) minus steric trend (using the Ingleby and Huddleston (2007) data set) for the years 1993 to 2010, (mm yr^{-1}).

FIGURE 5.11: The residual trend (figure (5.11c)) of augmented dynamic topography from AVISO altimetry (figure (5.11a)) with the steric trend subtracted (figure (5.11b)) for the years 1993 to 2010, (mm yr^{-1}).

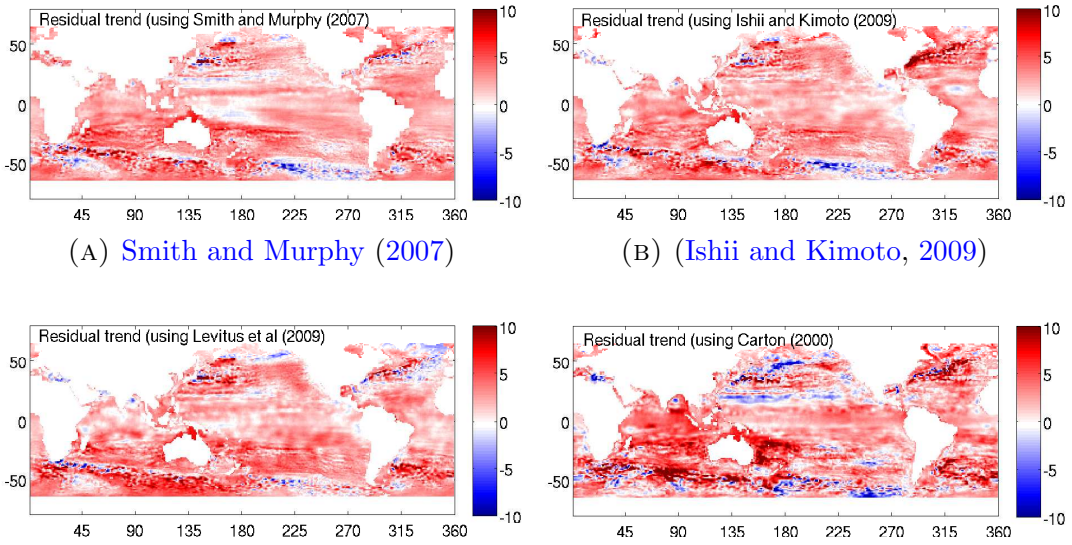

(A) Smith and Murphy (2007) (B) (Ishii and Kimoto, 2009)

(C) (Levitus et al., 2009) (D) Carton et al. (2000)

FIGURE 5.12: Residual trends between 1993 and 2010, (mm yr^{-1}) from augmented dynamic topography (1° grid from AVISO) with steric trend subtracted. Figures (5.12a-5.12d) show the regional residual trend from each steric data set.

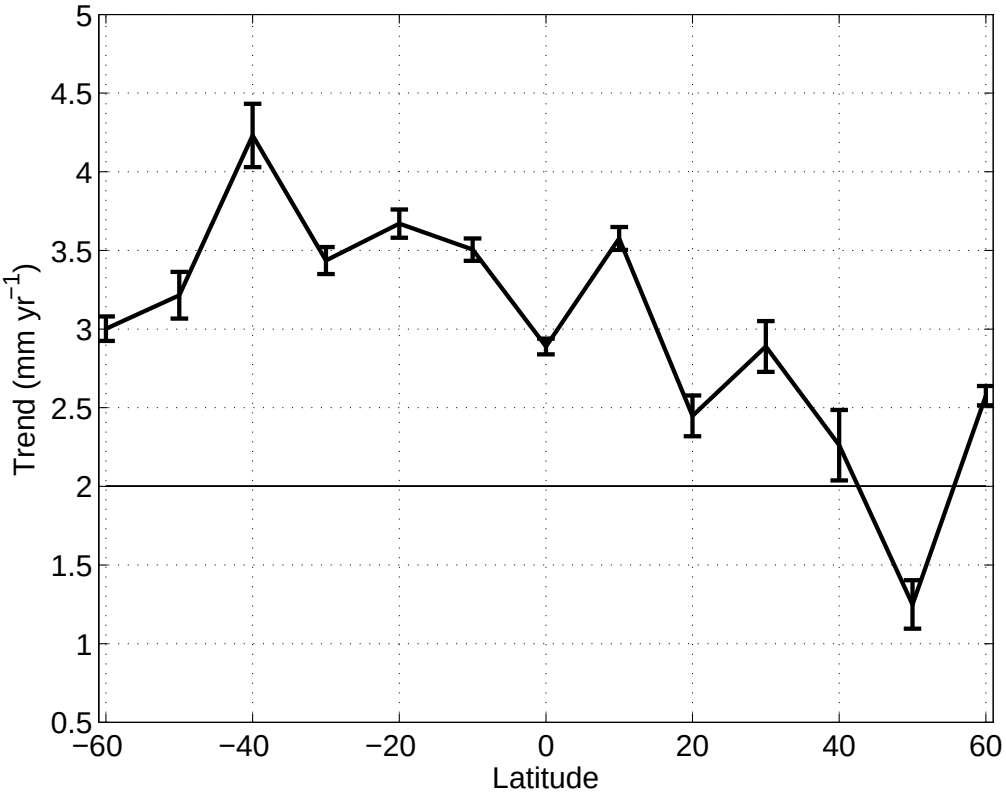

FIGURE 5.13: Zonal average of the trend in AVISO altimetry trends between 1993 to 2010 with one standard error (mm yr^{-1}). The 2 mm yr^{-1} line is shown for reference.

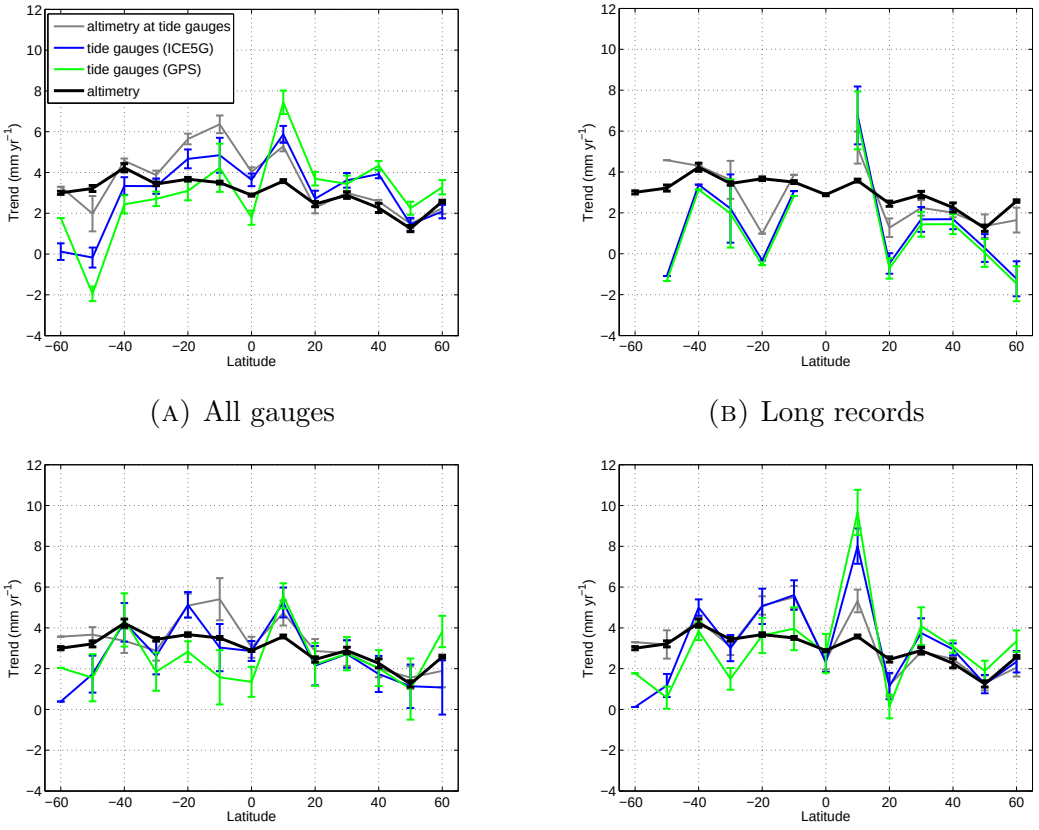

(A) All gauges

(B) Long records

(C) Spatially uniform gauges

(D) 500 gauges

FIGURE 5.14: Zonally averaged trends of augmented dynamic topography from 1993 to 2010 for 4 tide gauge selections showing 3 separate corrections for VLD, altimetry at tide gauges (grey), mass redistribution model (ICE-5G (Peltier, 2004) corrected (blue) and GPS corrected (green) and compared with the zonal average of altimetry derived augmented dynamic topography for the same time period (black). All trends show one standard error σ. (mm yr^{-1}). Tide gauge derived values in this figure are the same as in figure (3.21) and altimetry derived values are the same as in figure (5.8)

Figures (5.14a-5.14d) highlight the smoother curve of the altimetry derived τ compared to the tide gauge derived τ. This is true for all of the four subsets and both land corrections applied.

5.9 Summary

- AVISO altimetry is used to calculate absolute sea level trends between the years 1993 to 2010.
- Influences to global trends from inland seas such as the Caspian Sea are removed as they are not linked to the global ocean directly, and so that their large negative trend does affect the zonal average 5.4b.
- Trends in ASL show defined spatial patterns especially over the Pacific Ocean, where the West Pacific shows relatively high positive trends which extend into the Indian and Southern Oceans. The East Pacific, in contrast, shows negative trends. These patterns have been shown to correlate well with long term natural variability such as the Pacific Decadal Oscillation (Merrifield et al., 2012)
- The AVISO altimetry absolute sea level trends are changed into augmented dynamic topography τ by removing the changes to G plus a globally average crustal displacement term using modelled estimates (Tamisiea et al., 2001). The augmented dynamic topography is approximate because only the change in G and globally averaged crustal displacement from GIA are removed from the ASL. Any changes which remain from other sources are not removed. This includes the effect from recent melting of Greenland, West Antarctica and glaciers. The fact that these recent effects remain in the approximate τ results we use later in Chapter 6 to compare with the fingerprints.
- The regional spatial structure of the augmented dynamic topography is shown to be similar to the steric regional trends, so that the patterns in the regional trends are set by the steric component to sea level. When the steric component is subtracted from τ, the residual (implied mass contribution plus movement errors) accounts for these spatial patterns, except over regions of high dynamics such as the Antarctic Circumpolar Current and western boundary currents. These dynamical signals are to be expected as we do not remove any dynamical signals from our trends.
- The results of the approximate augmented dynamic topography trends calculated from altimetry are then able to be compared with the approximate augmented dynamic topography calculated in Chapter 3 using tide gauges, and the steric trends calculated in Chapter 4.

- When we limit our sampling of altimetry trends to tide gauge locations, we find higher trends over tropical and subtropical latitudes. We also see high trends at these latitudes in our tide gauge analysis in Chapter 3. This result shows that these increased trends are due to sparse spatial sampling of tide gauges at these latitudes. There is very good agreement, however, in the Northern Hemisphere, at latitudes north of 20^{o} N. This shows that the tide gauge network is able to recreate the zonal average of trends between 1993 and 2010 in these regions.

- These results show that there is a Hemispheric bias in the zonal average of augmented dynamic topography trends between 1993 and 2010. We show that there are increased trends in the Southern Hemisphere and tropics as compared to the Northern Hemisphere.

Chapter 6

Calculation of the Implied Mass Component of Sea Level Trends

In this Chapter we estimate the spatial distribution of the mass component of sea level trends using three estimates of GIA corrected sea level (RSL when measured by tide gauges, ASL when measured by altimetry) from our 500 gauge subset (Chapter 3), altimetry (Chapter 5) and the steric estimates (Chapter 4). It will be seen that globally, the spatial pattern of the mass trend has less spatial variability than the steric trend pattern. We would expect this response as mass signals are quickly communicated across the globe. What spatial variability there is in the mass trend is largely due to gravity and VLD changes. The dynamical signal remains in the mass trend pattern in our analysis. For the 18 year time period assessed here this dynamical signal is potentially adding to the trend in the signal and will be caused by some of the larger scale variability discussed in Chapters 1 and 2. In order to pick out this large scale variability, we assess the latitudinal average of mass trends in 10 degree bands. Our altimetry based results show an increase in the mass trend over the Southern Hemisphere, while our tide gauge based results show an increase in trend over the tropics, which we have shown to be caused by the spatial bias of tide gauges (Chapter 5).

Modelled gravity and VLD changes of mass redistribution from ice melt, or 'fingerprints' (Tamisiea et al., 2001), give the spatial fields of mass redistribution based on 1 mm yr^{-1} melting of the Earth's two ice sheets and glaciers. We compare our mass trends to findings in the IPCC Fifth Assessment Report of modelled and

observed cryosphere changes by using these combined gravity and VLD fingerprints for West Antarctica, Greenland and glaciers to determine mass estimates for each source as a least squares solution. From this solution we obtain melting rates which show a large scatter when compared to the IPCC AR5 report. This mismatch is an indication that the actual picture involves a complex combination of all components of the Earth's hydrological and cryological system. We weight our mass estimates to reflect our levels of confidence over each latitude band from reasons such as the number of gauges per band, and thus we are also able to obtain more realistic error estimates on our mass loss rates. The fitted values are generally within 2 standard errors of the IPCC AR5 values.

6.1 Introduction

The natural variability of the mass component of sea level results from exchanges in water mass between the cryosphere, atmosphere and land with the open ocean. Church et al. (2011) noted that during 1961 to 2008 the cryospheric contribution to sea level rise increased, especially during the 1990s, while the thermosteric contribution over the same period increased less rapidly.

6.1.1 Land exchange

The interaction with the land is dictated by water storage through dam building, groundwater depletion and natural storage. In their evaluation of the sea level budget Church et al. (2011) estimate that there is a net negative impact on sea level during the period 1993 to 2008 due to land exchange which breaks down as -0.3 ± 0.15 mm yr^{-1} due to dam retention, 0.35 ± 0.07 mm yr^{-1} due to groundwater depletion and -0.14 ± 0.10 mm yr^{-1} due to natural terrestrial storage. Church et al. (2011) note that during the period 1972 to 2008 the natural storage had a positive influence on sea level trends, being 0.07 ± 0.10 mm yr^{-1}. Interestingly, natural terrestrial storage does play a small but significant contribution to the variability. Fasullo et al. (2013) examine an anomalous drop of 7 mm in global mean sea level during 2010 to 2011. During this period there was an exceptionally strong La Niña. GRACE satellite anomalies show continental-scale precipitation over Australia, which combined with Australia's unique endorheic basins (retaining basins with no outflow to the ocean) led to natural water retention on a larger

scale than usually seen. Church et al. (2011) calculate the total terrestrial influence on sea level to be negative for the period 1993 to 2008 (-0.08 ± 0.19 mm yr^{-1}) and therefore we assume that for the period 1993 to 2010 the main contribution to the mass component of sea level is from the cryosphere. However, the fact that the net land storage term is small does not necessarily imply small regional variations and therefore there may be a significant effect on the fingerprints.

6.1.2 Exchange with the cryosphere

Studies of the cryosphere have developed since the deployment of remote sensing equipment such as GPS (since 1992), ICESat (2004-2010) and GRACE (since 2002) satellites and LiDAR (light detection and ranging) technologies, altimetry, ERS (European remote sensing) since 1991 and SAR (synthetic aperture radar). Historically, glacier terminus position and aerial photography measurements have been used to estimate changes in size of ice sheets and glaciers. Out of 200,000 glaciers globally, only 120 have long time series (since the 1980s). Of these 120, most are low elevation, easily accessible glaciers which are measured and extrapolated. Only 37 glaciers have uninterrupted time series of over 40 years (Vaughan et al., 2013). Glacier growth and retreat has been observed to be complex by repeat airborne altimetry. Guyot Glacier in Icy Bay, Alaska thinned by over 100 m at its terminus between 2007 to 2009 and yet Yahtse Glacier terminus nearby thickened by 80 m during the same time period (Arendt, 2011), revealing that repeat measurements of all glaciers is essential to adequately assess glacier-ocean exchange.

More recently, CryoSat-2 has been purpose developed by the European Space Agency (ESA) for measuring ice thickness and monitoring changes to the ice sheets in Greenland and Antarctica. The satellite was launched in 2010. It's orbit reaches latitudes of 88° north and south, extending the current range of radar satellite orbits to give better polar coverage. Improvements to the on-board instrumentation include a Synthetic Aperture Interferometric Radar Altimeter (SIRAL), (`http://www.esa.int`), designed to be effective at the ocean-ice sheet margins and providing fine spatial resolution at areas of steep terrain.

Cryospheric estimates are reported in both gigatonnes (Gt) and the equivalent in sea level (mm). One Gt is approximately equal to one cubic kilometre of freshwater

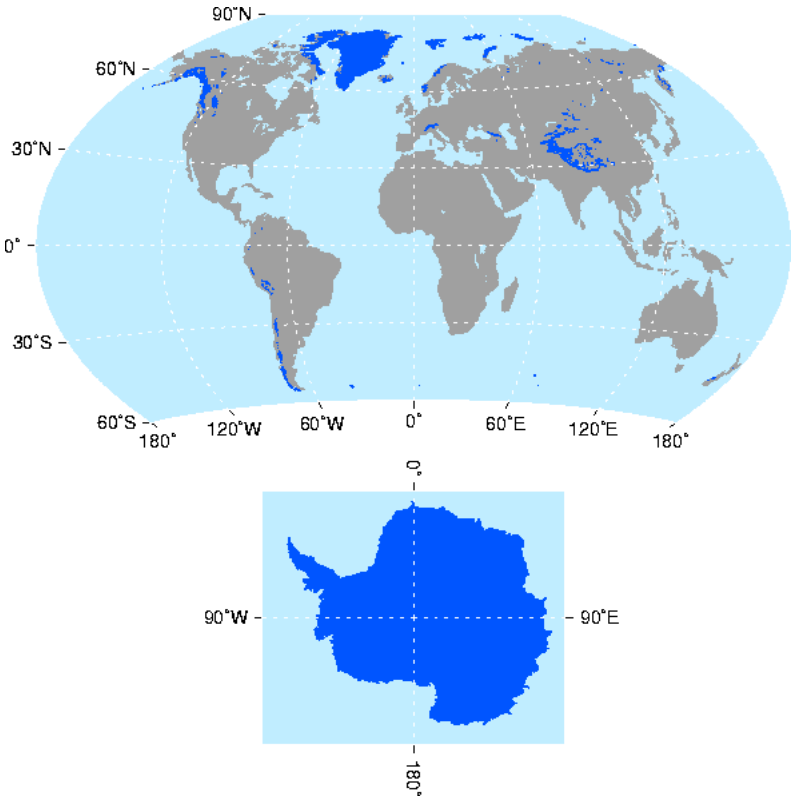

FIGURE 6.1: Map showing areas of the cryosphere (dark blue) taken from the National Snow and Ice Data Center at the University of Colorado. `http://nsidc.org/glims/`

(1.1 km^3 of ice), and 362.5 Gt of ice removed from the land and immersed in the oceans will cause roughly 1 mm of global sea level rise (Cogley, 2012).

6.1.3 Ice sheets

The Greenland Ice Sheet is 3367 m at its thickest point. Most of the ice is above sea level and therefore would contribute 7.3 m to globally averaged sea level if melted (Alley et al., 2010). Record melting was achieved during 2005, 2007, 2010 and 2012 leading to debate on the effect on sea levels (Harper et al., 2012). The IPCC fifth assessment states that there is *very high confidence* that the Greenland Ice Sheet has lost mass over the last two decades and therefore contributed to global sea level rise (Vaughan et al., 2013). Melting is thought to have accelerated in recent years and an extreme melting of most areas over the Ice Sheet was observed in July 2012, when multiple records were set in terms of surface temperature, surface mass balance change and surface run off. Relative to 1979 and some of the earliest satellite reports, melting of the Greenland Ice Sheet now begins around one month

earlier at low elevations (Tedesco et al., 2013). Estimates suggest that Greenland is currently losing 121 ± 28 Gt yr^{-1}, equating to 0.33 ± 0.08 mm yr^{-1} in sea level rise (Jacob et al., 2012, Vaughan et al., 2013).

The Antarctic Ice Sheet has 58.3 equivalent sea level metres, covering 8.3% of the Earth's land surface (Stocker et al., 2013). Evidence of recent Antarctic mass change has been helped by satellite gravity missions such as GRACE in recent years and the Antarctic Ice Sheet is reported with high levels of confidence to be losing mass (Ivins et al., 2013). Estimates suggest that Antarctica is currently losing 88 ± 35 Gt yr^{-1}, equating to 0.24 ± 0.10 mm yr^{-1} in sea level rise (Vaughan et al., 2013).

Changes in ice sheet mass are diagnosed through mass balance estimates (from input and output fluxes), satellite altimetry or through gravity observations from the GRACE satellites. Using this data Shepherd et al. (2012) estimate that the polar ice sheets have contributed on average 0.59 ± 0.20 mm yr^{-1} to global sea level between 1992 and 2011. For comparison, geological records suggest that these two ice sheets contributed sustained rates of sea level rise of 10 mm yr^{-1} when coming out of the last glacial maximum (Church et al., 2008). Mass budgets, however are still uncertain by up to 15% due to incomplete ice thickness mapping (Vaughan et al., 2013). While West Antarctica and the Antarctic peninsula are contributing to sea level rise the role of East Antarctica it is still uncertain, as snowfall driven mass gains observed during 2009, combined with short records make it difficult to determine longer trends (Shepherd et al., 2012).

6.1.4 Glaciers

Glaciers are thought to be a significant contributor to recent sea level rise although large uncertainties were reported in the IPCC Fifth Assessment Report (Stocker et al., 2013) due to both a lack of data and a global database. Mass loss from glaciers is thought to have increased since the 1960s and over 600 glaciers have reportedly disappeared (Vaughan et al., 2013), especially Alaska's marine terminating glaciers which have been losing mass more rapidly since the mid 1990s (Arendt, 2011). Thinning and ice loss associated with dynamic instability is causing rapid retreat and glaciers such as Alaska's Columbia Glacier, which once maintained a steady state are now in retreat (Meier et al., 2007). 75% of Himalayan Glaciers are also thought to be in retreat (Bolch et al., 2012).

The mass estimates of fresh water stored in glaciers range (shown in sea level equivalent, SLE) from 0.35 ±0.07 m SLE (Grinsted, 2013), to 0.43 ±0.06 m SLE (Huss and Farinotti, 2012) and 0.6 ±0.07 m SLE (Radic and Hock, 2011). Melting of glaciers contributed 0.76 ± 0.37 mm yr^{-1} to global sea level between 1993 to 2009 (Cogley, 2012).

6.1.5 Measuring the mass component

While measured observations of ice sheets and glaciers are sparse, techniques and coverage for global and regional ocean mass trends are even more so. Techniques currently in use include GRACE satellite gravimetry (Cazenave et al., 2009, Chambers and Schröter, 2011, Chambers and Willis, 2010) and (for the annual cycle only), Ocean Bottom Pressure Recorders (Hughes et al., 2012). Marcos et al. (2011) found that regional distributions of ocean mass were highly variable compared to global averages especially on short time scales and that inter annual comparisons between the northern and southern hemispheres of the Pacific and Atlantic Ocean basins revealed mass exchanges. Regional variability is strongly correlated with atmospheric indices and wind forcing (Tsimplis et al., 2013) and this basin scale effect is recorded in tide gauges (Calafat et al., 2012).

Model estimates of the redistribution of mass due to ice melt from the polar regions of Greenland, West Antarctica and glaciers is shown in the fingerprints of mass redistribution as shown by Tamisiea et al. (2001). These estimates provide 3 individual global responses to gravitational changes caused by the shift of mass from the cryosphere to the ocean. We use these 3 estimates within this chapter by weighting them with the most recent estimates of ice melt at each region as reported in IPCC's Fifth Assessment Report (Stocker et al., 2013). The fingerprint patterns show that within around 2000 km of the ice melt source there is a decrease in sea level. Beyond this distance an increase in sea level is observed (Mitrovica et al., 2011). The physics connecting the redistribution of sea level and ice melt has been published for over a century (Clark et al., 1978, Woodward, 1888), and recent rapid ice melting over the globe leading to the possibility that they might be able to be measured has led to recent revisions (Tamisiea and Mitrovica, 2011).

6.2 The implied mass

The mass contribution to global sea level trends has recently been termed the **barystatic** component (Gregory et al., 2012). The mass component to sea level in this thesis is termed *barystatic sea level*, BSL. Barystatic sea level trend defines the increase or decrease of mass in the ocean and is independent of vertical land displacement and any resultant change in the Earth's geopotential. It is given by the trend in augmented dynamic topography, after correction for steric sea level change. This definition is extended to a local form of BSL which represents the sum of any total mass loss change, plus dynamic bottom pressure change (the latter is assumed to be small).

SSL = steric sea level
BSL = barystatic sea level
RSL = relative sea level
ASL = absolute sea level
VLD = vertical land displacement
G = gravitational potential surface
τ = augmented dynamic topography

Our definition of augmented dynamic topography is provided in Chapter 2 in equations (2.17) and (6.3), shown again in equations (6.1) and (6.3). and applied in Chapters 3 and 5. Tide gauge data is applied using equation (6.1), which refers to relative sea level and includes the VLD signal.

$$\tau = RSL + VLD - (G' + \overline{VLD}) \tag{6.1}$$

$$= RSL - (G' - VLD') \tag{6.2}$$

While using altimetry data equation (6.3) is used, which refers to absolute sea level. The difference between equations (6.1) and (6.3) being the VLD term.

$$\tau = ASL - (G' + \overline{VLD}). \tag{6.3}$$

The steric signal is removed from τ using the estimate shown Chapter 4, as set out in the definition in equation (6.4). This gives the estimate for BSL.

$$\tau = BSL + SSL \tag{6.4}$$

Combining equations (6.1) and (6.4) the BSL definition can be written in full. The SSL is common to both definitions of BSL as it is independent of VLD.

$$BSL = \tau - SSL \tag{6.5}$$
$$= RSL - SSL + VLD - (G' + \overline{VLD}) \tag{6.6}$$
$$= ASL - SSL - (G' + \overline{VLD}) \tag{6.7}$$

In this Chapter we compare the zonal distribution of the fingerprint trends to the diagnosed zonal distribution of our barystatic sea level trends, after GIA corrections have been applied. This comparison assumes that any remaining change to the gravitational potential surface is caused by recent melting from ice sheets and glaciers. We show barystatic sea level separated into the GIA and nonGIA (other) components in equation (6.8) using relative sea level (for tide gauge data).

$$\overbrace{RSL - SSL + \overline{VLD}_{GIA} - (G'_{GIA} + \overline{VLD}_{GIA})}^{GIA \text{ correction}}$$
$$= \underbrace{BSL - VLD_{other} + (G'_{other} + \overline{VLD}_{other})}_{\text{fingerprint + mass (+ errors and dynamics)}} \tag{6.8}$$

Equation (6.9) using absolute sea level (for altimetry data).

$$\overbrace{ASL - SSL - (G'_{GIA} + \overline{VLD}_{GIA})}^{GIA \text{ correction}}$$
$$= \underbrace{BSL + (G'_{other} + \overline{VLD}_{other})}_{\text{fingerprint + mass (+ errors and dynamics)}} \tag{6.9}$$

The parts of the equation in red show the variables that have been identified throughout previous Chapters. The zonal average of the barystatic sea level trend then becomes, in principle, equal to the fingerprint (i.e. the change in the G from melting other than GIA (as well as other reasons, which we are assigning as our error) minus the mean vertical land displacement). We show the mass trends later in figures (6.7 - 6.9). It should be noted that removing the land displacement from tide gauge trends using GPS removes not only the GIA correction, but also any recent melting effects and therefore using GPS as a solution does not allow us to compare our results with the fingerprints. We do not, therefore, carry the GPS-based estimate of sea level change from Chapter 4 forward into this Chapter.

6.3 Fingerprints

The modelled gravity and vertical land displacement fingerprints (Tamisiea et al., 2001) in figure (6.2) are provided by Dr Mark Tamisiea (NOC Liverpool). They show that the redistribution of ocean mass after ice melt from three sources, either the ice sheets at Greenland, West Antarctica, or glaciers is not uniform, but has a unique pattern. The increase of sea level appears in the far field, away from the source of melting. This is shown in figures (6.2a - 6.2f) as the theoretical redistribution of mass when assumed uniform melting at a source of the equivalent to 1 mm yr^{-1} of melting occurs. The fingerprints are observed differently by tide gauges and altimetry due to the added VLD that tide gauges also observe making the tide gauge response appear larger. This effect potentially makes the exaggerated fingerprint signal from tide gauges easier to observe in the data.

In figure (6.2a) the source of ice melt is Greenland. Around Greenland a decrease in sea level trend is observed and it is at best several 1000 km away before we see a trend increase in sea level. In figure (6.2c) the reverse signal is seen as the ice loss source is around West Antarctica which causes a decrease in sea level trend locally and an increase in sea level trend mostly in the tropics and Northern Hemisphere. In figure (6.2e) the decrease in trend is focused around glacial sites, with an increase in trend elsewhere.

In the altimetry view, this pattern of redistribution is a result of the loss of gravitational attraction between the ice and the ocean as the ice melts. When ice is held within the cryosphere on ice sheets and glaciers, it has mass and therefore a gravitational attraction towards other bodies' mass such as the ocean. As the ocean is liquid it is pulled towards the ice mass as a direct result of this attraction. As the ice mass reduces, its gravitational pull weakens and the ocean is not as attracted to it. This then appears as a fall in sea level locally where the ice has melted.

The pattern of redistribution from the tide gauge view of the fingerprints occurs from the same physical process as for the altimetry view. Here though, RSL measured by tide gauges is also affected by the land displacement. The geopotential (Earth's gravitational field) is also affected by this land displacement that is induced and the resultant redistribution of mantle after the ice has melted. It is this feature, of redistribution from the effects of gravity and solid earth displacement,

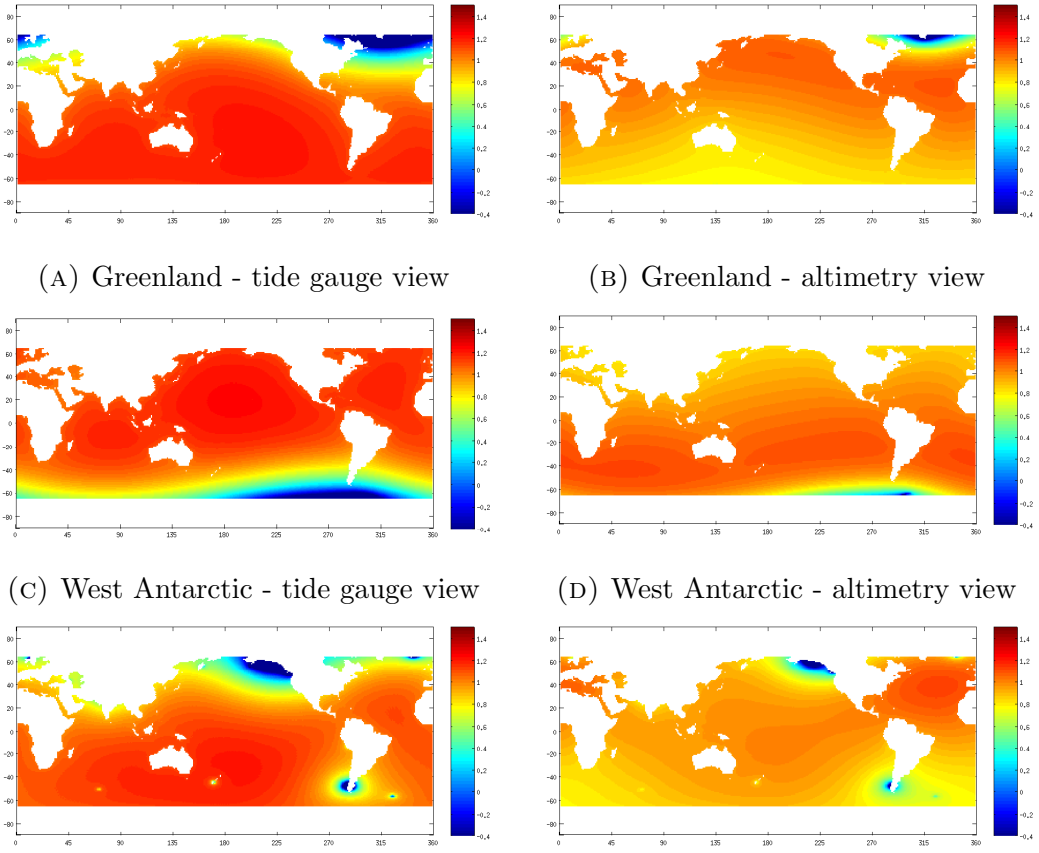

(A) Greenland - tide gauge view

(B) Greenland - altimetry view

(C) West Antarctic - tide gauge view

(D) West Antarctic - altimetry view

(E) Glacial - tide gauge view

(F) Glacial - altimetry view

FIGURE 6.2: Fingerprints showing the tide gauge and altimetry views for melting at Greenland (6.2a,6.2b), West Antarctic (6.2c,6.2d) and Glaciers (6.2e,6.2f) equivalent to a sea level rise of 1mm yr^{-1}. (Tamisiea et al., 2001)

that we will use to interpret the distribution of our zonally averaged ocean mass results.

The zonal averages of each of the 3 fingerprints can be seen in figure (6.3a) for Greenland, figure (6.3b) for West Antarctica and figure (6.3c) for glaciers. These 3 figures each show the tide gauge view (dashed) and altimetry view (solid). The more extreme tide gauge view is clear, especially at the latitudes local to the ice melt. The Greenland fingerprint has the largest range of rates between the latitude bands of the 3 fingerprints. The rate is negative at the source of melting, meaning that sea level here will drop. The response tends to level off further from the source. The West Antarctic zonally averaged fingerprint (figure (6.3b)) shows a reduced, but not negative, trend at the same latitude as the source, unlike the higher resolution map (figures (6.2c and 6.2d)). The range of the West Antarctic zonally averaged fingerprint is smaller than the Greenland zonally averaged fingerprint

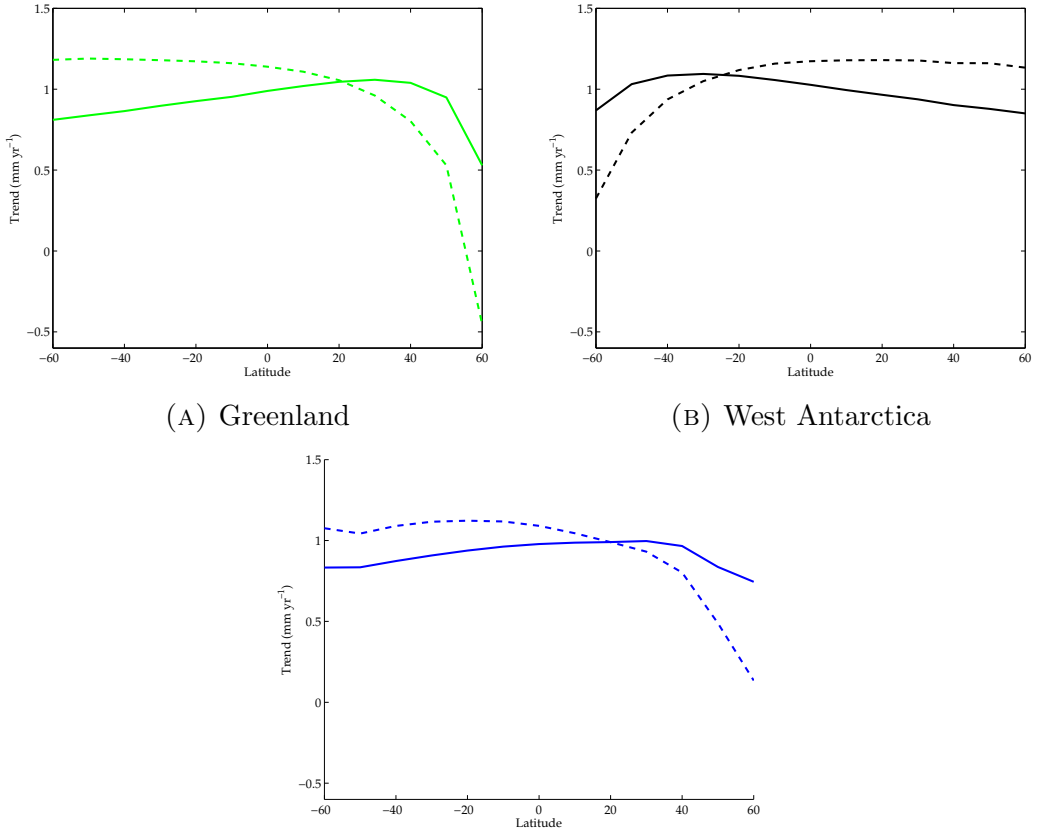

(A) Greenland

(B) West Antarctica

(C) Glaciers

FIGURE 6.3: The zonal average of each of the three fingerprint maps shown in figure (6.2). Both tide gauge (dash) and altimetry (solid) values are shown. Trends are in mm yr^{-1} assuming in each case an ice mass loss equivalent to 1mm yr^{-1} in global-average sea level.

although similar to the range of the zonally averaged glacial fingerprint.

Our analysis also includes an alternative to the glacial fingerprint, a simplified redistribution from all other sources which is equal at every latitude. While in theory there is a fingerprint for each different glacial region, the data is not available to constrain them all. To assess sensitivity of our results to the use of this glacial fingerprint, we use the 'other' fingerprint, which is simply a constant over latitude.

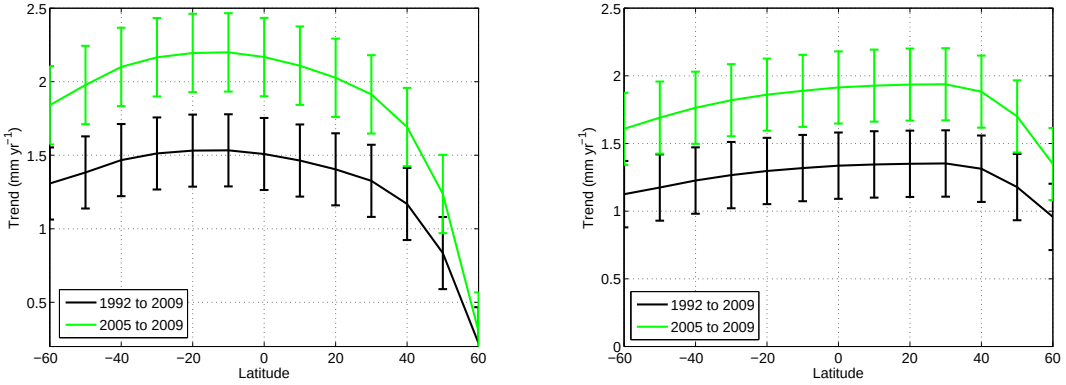

(A) Tide gauge. (B) Altimetry

FIGURE 6.4: Sum of Greenland, West Antarctica and glacial fingerprints when weighted with respective values of equivalent sea level trends for the time periods 1993 to 2009 (black), and 2005 to 2009 (green) as reported in IPCC Fifth Assessment Report. Showing both tide gauge (6.4a) and altimetry (6.4b) perspectives.

6.4 Expectation of fingerprint response using IPCC AR5 values

Figure (6.4) takes the IPCC AR5-quoted values for the contribution to sea level trends due to ice melt during 1993 to 2009 from Greenland, West Antarctic and glacial fingerprints. These values for 1993 to 2009 are 0.34 ±0.06 mm yr^{-1} for Greenland, 0.24 ±0.09 mm yr^{-1} for West Antarctica and 0.77 ±0.22 mm yr^{-1} for glaciers, giving a total contribution of 1.35 mm yr^{-1}. The spatially weighted fingerprints are then summed to find a combined distribution and shown with overall estimated errors (black) (Vaughan et al., 2013).

The green line shows the sum of the 3 fingerprints weighted by 2005 to 2009 values for comparison. These more recent values are 0.61 ±0.18 mm yr^{-1} for Greenland, 0.4 ±0.19 mm yr^{-1} for West Antarctica and 0.92 ±0.05 mm yr^{-1} for glaciers, and so for 2005 to 2010 compared to 1992 to 2009 the values are almost twice as large for all 3 melt sources combined (Vaughan et al., 2013). The total contribution during 2005 to 2010 from these estimates is 1.93 mm yr^{-1}. The errors from the two estimates are 2-3 times as large for the later period for West Antarctica and Greenland. The errors are over half the size during the later period for glaciers, possibly reflecting the increase in data available in glacier measurements, but also reflecting the increased uncertainty in melt rates of the two Ice Sheets.

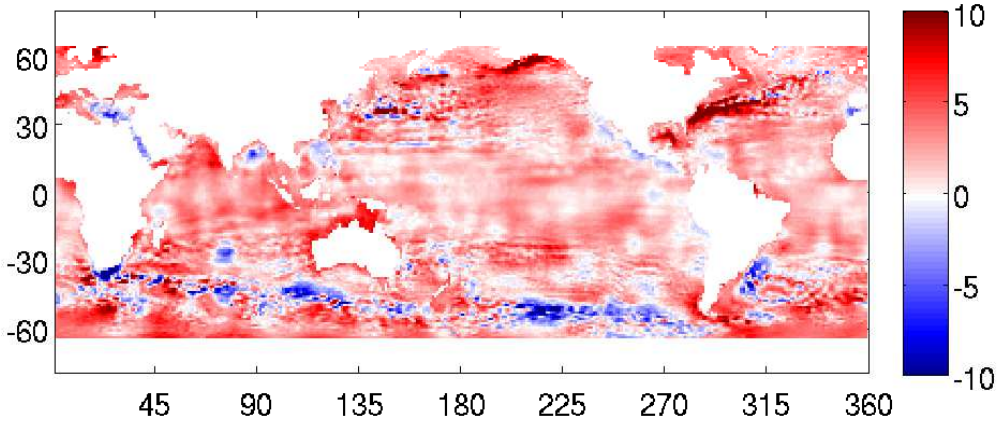

FIGURE 6.5: Mass trends calculated from AVISO altimetry reduced to a 1° grid and corrected for *GIA*, minus steric (using the Ingleby and Huddleston (2007) data set) trends for the years 1993 to 2010 (mm yr^{-1}). This is the same as figure (5.11c) apart from the *GIA* correction

6.5 Comparing total and steric sea level

We have two independent estimates for total sea level from either tide gauges or satellite altimetry. In order to compare the distribution of the implied mass component we resize the altimetry data from a 1/3° to fit a 1° grid by using the value of the nearest latitude and longitude data point. This is shown in figure (6.5). Compared to the sea surface height trends as seen in altimetry maps and steric trends, the map of implied mass trends has much less regional complexity. Most areas of ocean are showing positive trends with the exception of the Antarctic Circumpolar Current and some enclosed seas. Western boundary currents also show high variability, suggesting that the dynamical signals are either not resolved within the steric correction, or produce dynamic bottom pressure signals and therefore contribute to the error in our fitting of fingerprints. In other words, our definition of the mass component to sea level trends includes local dynamics in bottom pressure as well as the fingerprints.

Taking the implied mass trend as a function of latitude allows us to examine this broad scale mass trend without attempting to interpret the finer scale resolution of the map in figure (6.5) which is at 1 degree resolution. The latitudinal approach also allows us to compare the altimetry results with tide gauges.

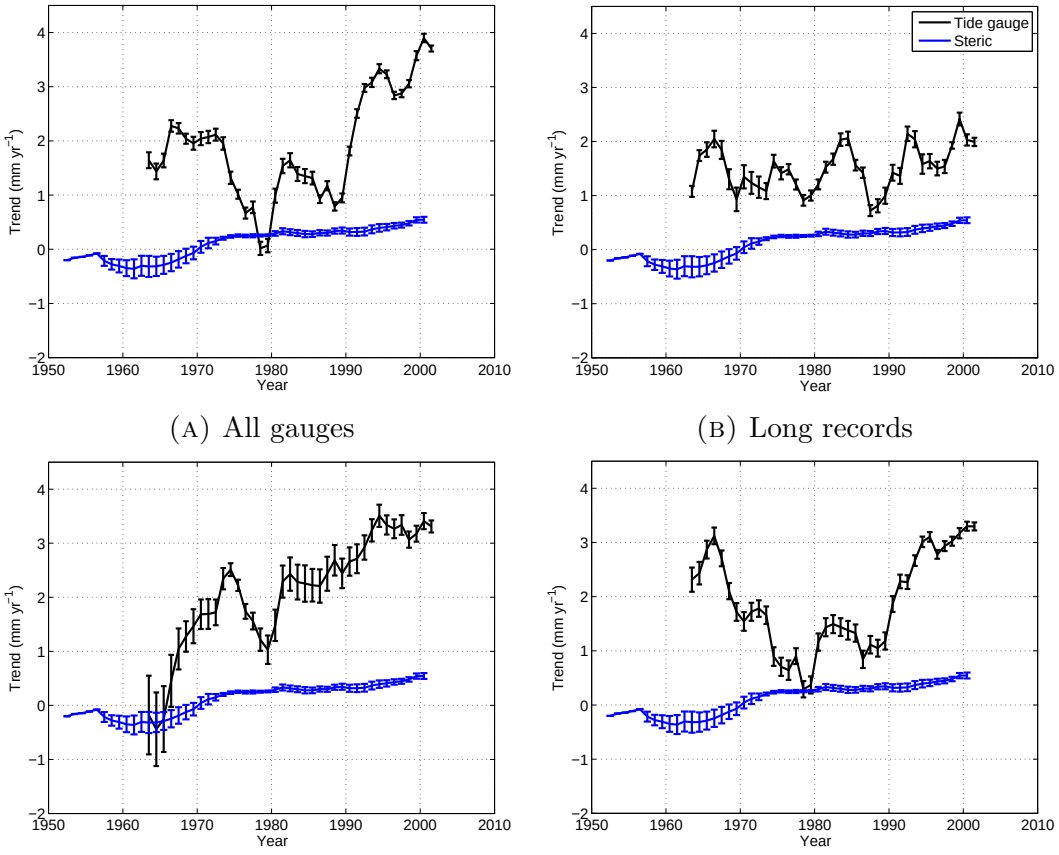

(A) All gauges

(B) Long records

(C) Uniform spatial coverage

(D) 500 gauges

FIGURE 6.6: Global average trends in both sea level using tide gauges, *GIA* corrected (Peltier, 2004)(black), and 18 year steric trends using the mean of 5 data sets ((Carton et al., 2000, Ingleby and Huddleston, 2007, Ishii and Kimoto, 2009, Levitus et al., 2009, Smith et al., 2007)(blue) (mm yr^{-1}), both with one standard error. Running trends are calculated every year as 18 year linear trends centred on the middle year

6.5.1 Mass trends from tide gauges

We show estimates of the mass component to sea level trends as a function of latitude from our 500 tide gauge subset in figure (6.8). An alternative figure showing mass estimates using all tide gauges is shown in Appendix A. Using corrections as in equation (6.8) to our tide gauge estimate (using the model ICE-5G (black dash) . A black solid line highlights the 2 mm yr^{-1} trend. Our estimates of mass trends at high latitudes are lower than our estimate over the tropics, especially in the Northern Hemisphere. Some of these higher trends we know to be due to spatial sampling, as shown in Chapter 5, where the spatial sampling of altimetry against altimetry at tide gauges leads to increased trends over the tropics.

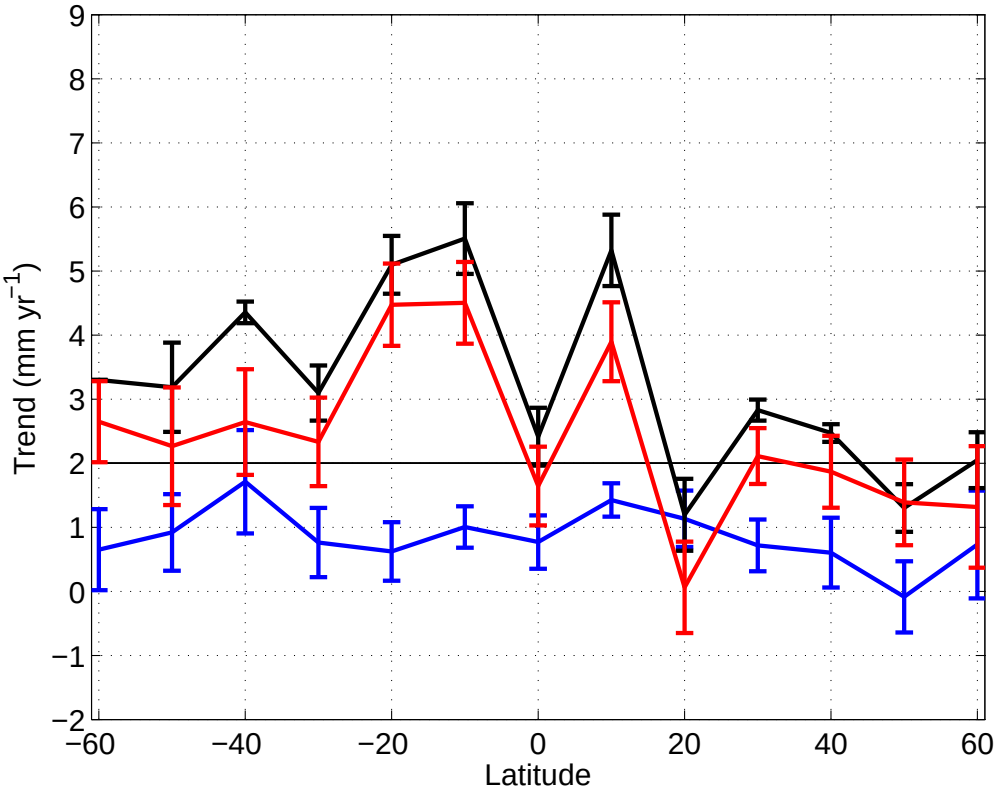

FIGURE 6.7: The zonal averages of implied mass trend (red solid) shown as the zonal average from augmented dynamic topography trend calculated from altimetry at 500 gauges (black solid) minus the zonal mean trend of 5 steric reconstructions (blue) for the years 1993 to 2010, with one standard error (mm yr^{-1}).

For comparison we include mass estimated using altimetry at tide gauges (black solid) (figure (6.7)). We subtract the steric trend (blue) from the $(G' + \overline{VLD})$ corrected zonally averaged trends to acquire zonally averaged mass trends (red solid).

6.5.2 Mass trends from altimetry

In figure (6.9) can be seen the mass component to sea level trends for 1993 to 2010 calculated using altimetry (red) as described in equation (6.9). The zonally averaged augmented dynamic topography calculated in Chapter 5 is the black line. From this one can see the latitudinal structure of higher trends (between 3 and 4 mm yr^{-1}) is in the southern hemisphere, decreasing within the northern hemisphere to around 2 mm yr^{-1}. The steric trends for this period (blue) show some slight variability with latitude, generally around 1 mm yr^{-1} in the southern

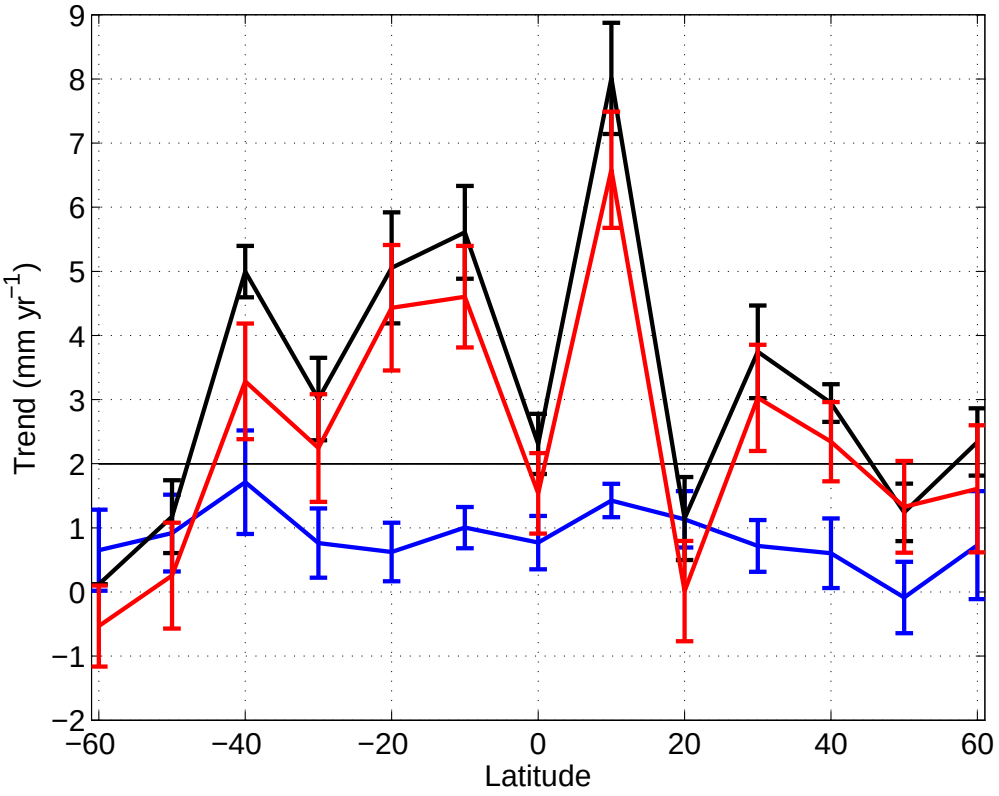

FIGURE 6.8: The zonal averages of implied mass trend (red dash) are shown as the zonal average from augmented dynamic topography trend calculated from 500 gauges (black dash) minus the zonal mean trend of 5 steric reconstructions (blue) for the years 1993 to 2010, with one standard error (mm yr^{-1}).

hemisphere and decreasing to a minimum trend at 50° N. The 2 mm yr^{-1} grid line is highlighted in bold to emphasize the latitudes where the mass trend is higher and lower than this. All latitudes in the southern hemisphere are above 2 mm yr^{-1} whereas all latitudes are around or below this line in the northern hemisphere.

6.5.3 Mass derived from full depth steric only

We repeated the implied mass calculation using only the 3 steric data sets which reached full depth, Ingleby and Huddleston (2007), Smith and Murphy (2007) and Carton and Giese (2008). It can be seen in figure (4.12e) that the zonal average is affected by the depth to which the steric height is calculated. We show this figure again in figure (6.10), now limiting the zonal averages to 60° S to 60° N and only comparing the full depth steric zonal mean (cyan) to the steric zonal mean of all 5 data sets (blue).

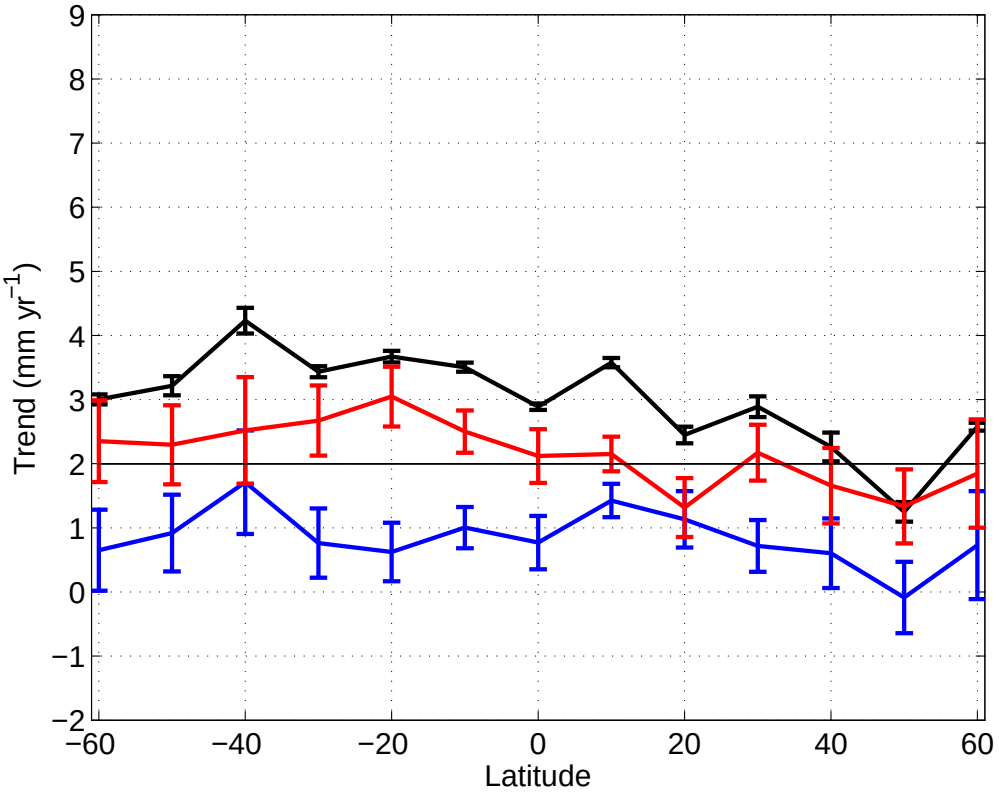

FIGURE 6.9: The zonal average of implied mass trend (red) is shown as the zonal average from augmented dynamic topography trend calculated from altimetry (black) minus the zonal average of steric height trend (blue) for the years 1993 to 2010, with one standard error (mm yr^{-1}).

The resultant trends for the implied mass are similar when using the 3 full depth steric trends to those using all 5 steric reconstructions. There is still a lack of observational data in the deep ocean, however, and it is still uncertain whether this result would remain the same in the event of good spatial sampling.

6.6 Solving for the melt rate coefficients

The results of our estimated distributions of the mass component to sea level trends. Both tide gauges and altimetry are used to solve for the melt rate coefficients using a least squares analysis. These coefficients signify the rate of ice melt (in mm yr^{-1}) from Greenland, West Antarctica and glaciers, as proposed by the distribution of the fingerprints. Our analysis so far has removed all variables written in red from equations (6.9 and 6.8), leaving the resulting signal described

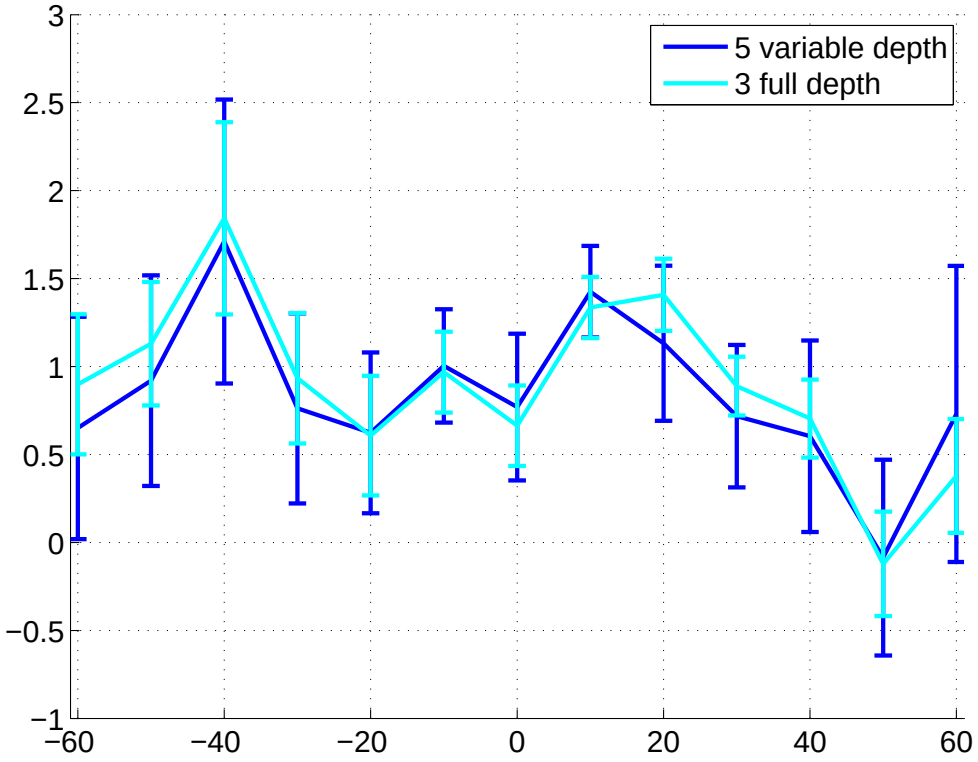

FIGURE 6.10: Steric zonal average of 5 reconstructions compared with the 3 full depth reconstructions, Ingleby and Huddleston (2007), Smith and Murphy (2007) and Carton and Giese (2008) for the years 1993 to 2010, with one standard error (mm yr^{-1}).

by the fingerprint alone (plus the dynamic bottom pressure which we are neglecting). Therefore fitting fingerprints to these curves should provide the amplitude of melting required to make the fit.

The return of the ordinary least squares solution to the linear system of equations solves for $\boldsymbol{x}$ in equation (6.10)

$$\boldsymbol{Ax} = \boldsymbol{b} \tag{6.10}$$

where $\boldsymbol{A}$ is the theoretical spatial pattern of the 3 fingerprints. The zonal average used is shown in figure (6.3). Each fingerprint is a 13-point vector representing each latitude band, and A is a matrix comprising of the three vectors. Different fingerprints are used for altimetry and tide gauge curves.

The 3 point vector $\boldsymbol{x}$ represents the unknown amplitudes of the three contributions. Solving for $\boldsymbol{x}$ will give 3 single values, each representing melt rates from either West Antarctica, Greenland or glaciers.

The right hand side, $\boldsymbol{b}$ is the measured barystatic signal from our analysis and the

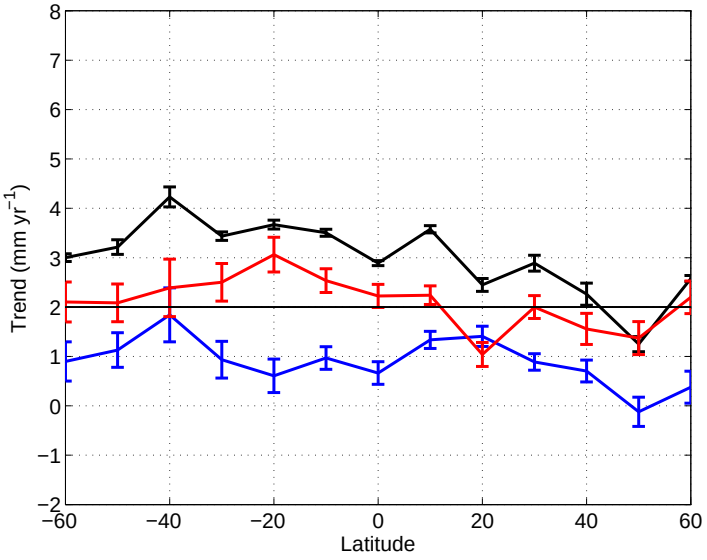

(A) Altimetry

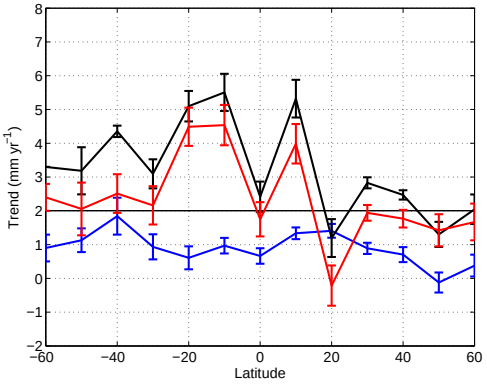

(B) Altimetry at 500 tide gauges

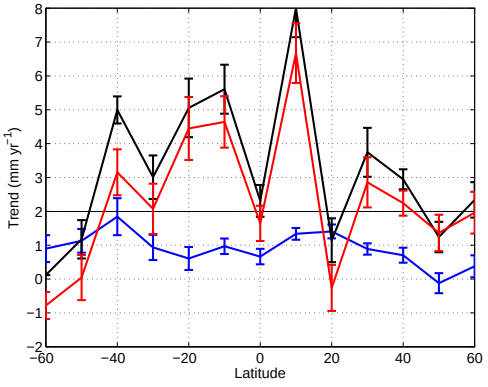

(C) 500 tide gauges

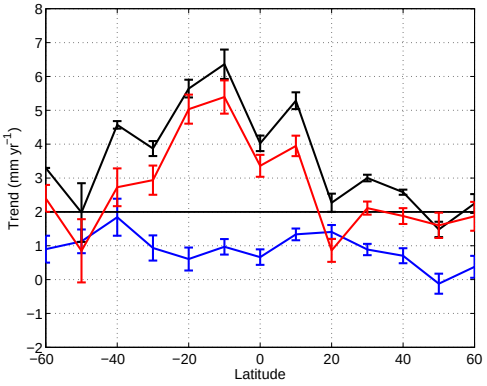

(D) Altimetry at all tide gauges

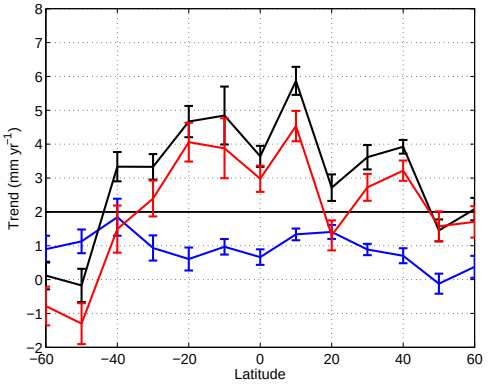

(E) All tide gauges

FIGURE 6.11: The zonal averages of implied mass trends (red) are shown as the zonal average from augmented dynamic topography trend (black) calculated from altimetry (6.11a), altimetry at 500 tide gauges (6.11b), 500 tide gauges (6.11c), altimetry at all tide gauges (6.11d), and all tide gauges (6.11e), minus the zonal average of full depth steric height trend (blue). The full depth zonally averaged steric trend is calculated using only the mean of the 3 full depth steric reanalysis (Ingleby and Huddleston (2007), Smith and Murphy (2007) and Carton and Giese (2008)), for the years 1993 to 2010, (mm yr^{-1}). All show one standard error.

zonal average is used as a 13-point vector representing each latitude band.

It is noted that this method allows for both positive and negative coefficients and the algorithm can combine high positive with low negative coefficients in order to produce the smallest misfit. For these instances the negative coefficients either represent the retention of mass, or how additional fingerprints are needed for more plausible results, or that the fingerprints are too similar to be distinguished by the data.

6.7 Coefficient results

When solving for the melt rate coefficients, we use all, as well as combinations, of the available 3 fingerprints. Limiting the number of fingerprints to produce the fit reveals the quality of the fit and shows the behaviour of the least squares algorithm in producing the best fit with the fingerprints to our mass estimates. We separately analyse the coefficients derived when using

- altimetry
- altimetry at 500 tide gauges
- 500 tide gauges, GIA corrected for land displacement.

We solve for the coefficients using each of these three estimates using the following combinations of fingerprints

- West Antarctica
- Greenland
- A third function
- West Antarctica, Greenland and a third function
- West Antarctica and Greenland
- West Antarctica and a third function
- Greenland and a third function

Fingerprint used		West Antarctica	std error on coeff	rms misfit	Greenland	std error on coeff	rms misfit	other	std error on coeff	rms misfit
data source	coefficient									
Altimetry	West Antarctica	2.204	*0.112*	*0.159*	-	-	*0.410*	-	-	*0.258*
	Greenland	-	-		2.287	*0.192*		-	-	
	Other	-	-		-	-		2.153	*0.141*	
	total	2.204			2.287			2.153		

TABLE 6.1: Simple table of fits from the mass trend as calculated from altimetry to one fingerprint, therefore we assume all melting is from one source. The other contribution represents a spatially constant fingerprint. Units are mm yr^{-1}

The third function is either the glacial fingerprint (figures (6.12e and 6.12f)), which is labelled *Glaciers* or a uniform spatial constant, which is labelled *other*. The uniform constant is there to address all other additional mass trends other than West Antarctica and Greenland.

Weighted fits are also calculated (discussed in section 6.8) and both the weighted and unweighted coefficients are shown.

Simple fits

In order to simplify the calculation we fit each fingerprint individually to the mass estimate. If this was realistic it would imply that all of the mass trend was produced from one source of melting, either West Antarctica, Greenland or a third function. To simplify the calculation further, we assume first that the polar ice sheets *only* are responsible for the shape of the latitudinal distribution and the third function represents a trend which is equal at all latitudes. This third function represents a 'eustatic' contribution from an unknown general source. The standard error on the fitted coefficients and the root mean square misfit are shown alongside. Errors are based on the assumption that all 13 points have equal observational errors (and therefore equal weighting) with an overall scaling determined by the misfit.

Table 6.1 gives the results for the altimetry derived curve to the 3 individual fits, with the standard error and rms misfit for each. When we fit our mass estimate from altimetry to the West Antarctic fingerprint altimetry view (table 6.1), we find a coefficient of 2.20 ± 0.11 mm yr^{-1} (bold blue outline). We are only fitting one fingerprint and therefore only find one coefficient. The standard error is 0.11

mm yr^{-1} and the rms error is 0.16 mm yr^{-1}. The coefficient therefore is of the same order of magnitude that we are expecting from the mass contribution, but we know that this is a simplification of the physics as not all of the melting is sourced from West Antarctica. When we repeat this simple solution and fit the Greenland fingerprint only (bold green outline), the coefficient is now 2.29 ± 0.19 mm yr^{-1}. Fitting the simple function only, other (bold cyan outline), gives a coefficient of 2.15 ± 0.14 mm yr^{-1}. Finding a similar fit for the fingerprints and the flat simple fit is not really surprising as the fingerprints, as well as the mass trend, do not have a large gradient over latitude. The important result here is that when we fit the fingerprints individually to our mass estimated trend calculated from altimetry we find that the magnitude of total mass trend is of the expected magnitude. We give the **total** combined contribution at the bottom of the column, taken as the sum of each coefficient and representing the total mass trend.

Similar magnitudes of coefficients are seen when we use our tide gauge estimates as shown in table (6.2). Tide gauges (grey band) are compared here with altimetry at tide gauges (green band). Mass derived from tide gauges is the fit to the *tide gauge view fingerprint*. Mass derived from altimetry at tide gauges is the fit to the *altimetry view fingerprint*.

Using the relevant fingerprints, the coefficients are calculated as before. The simplest result are shown in table 6.2 as one coefficient for separate fits to individual fingerprints. The fit with the West Antarctic fingerprint shown with bold blue outline is 2.26 ± 0.34 mm yr^{-1} from tide gauges and 2.84 ± 0.35 mm yr^{-1} from altimetry at tide gauges. The fit with the Greenland fingerprint, shown with the green outline and the fit with the simple function (other) is shown with the cyan outline. The results show that the coefficients from the tide gauge fit are all lower than the coefficients from the fit with altimetry at tide gauges, but that the errors when the fit is with tide gauges are all slightly larger. All of the fits are around the right order of magnitude that we would expect from the mass trend, however, IPCC AR5 melting rates suggest a combined rate of 1.35 mm yr^{-1} whereas our results are about 2 mm yr^{-1} or more.

We then introduce our least squares solution as the fit from all 3 fingerprints to our mass estimates. We now have 3 coefficient results which represent melting from West Antarctica, Greenland and 'other' (red outline). There are 3 separate results shown in table 6.3. Altimetry (blue band), altimetry at tide gauges (green band) and tide gauge results (grey band) results each have their 3 contributions. Also

Fingerprint used		West Antarctica	std error on coeff	rms misfit	Greenland	std error on coeff	rms misfit	other	std error on coeff	rms misfit
data source	coefficient									
500 Tide Gauge (altimetry at TGs)	West Antarctica	2.836	*0.352*	*1.567*	-	-	*1.842*	-	-	*1.897*
	Greenland	-	-		2.968	*0.406*		-	-	
	Other	-	-		-	-		2.742	*0.382*	
	total	2.836			2.968			2.742		
500 Tide Gauge GIA corrected	West Antarctica	2.258	*0.343*	*1.732*	-	-	*3.419*	-	-	*2.802*
	Greenland	-	-		1.979	*0.494*		-	-	
	Other	-	-		-	-		2.189	*0.464*	
	total	2.258			1.9786			2.189		

TABLE 6.2: Simple table of coefficients from a least square evaluation between the mass curve as calculated from tide gauges (grey band) to *one* fingerprint, where we assume all melting is from one source. The other contribution represents a globally-uniform sea level rise

shown is the standard error on each coefficient and the root mean square misfit of the overall profile. Taking the altimetry coefficients we see that our fit states that the melt rate from West Antarctica is 4.51 ± 0.13 mm yr^{-1}which is larger than we expect. This fit, however, also states that the rates from Greenland and glaciers are negative, at -1.20 ± 0.13 mm yr^{-1} and -1.18 ± 0.13 mm yr^{-1} respectively. Within one standard error these fits are still negative and we know this not to be representing the current situation as all three of these locations are seen to be losing ice mass, rather than gaining. Therefore, we assume that the algorithm is using the negative shape of the fingerprint to make the best fit while also attempting to fit the relatively smooth curve of the fingerprint to the dynamically noisy data of our mass estimate as well as the lack of latitudinal structure making the fingerprint difficult to fit to. The coefficients are plotted in figure (6.12). The amplitudes of West Antarctic (blue), Greenland (green) and glacial (cyan) coefficients from the fit of 3 fingerprints with altimetry (6.12a), tide gauges at altimetry (6.12c) and tide gauges (6.12e) are plotted with one standard error with the IPCC 1993 to 2009 respective value. These coefficients then weight the respective fingerprint and when all 3 are summed, reconstruct BSL (red dash). This can be compared

Fingerprint used		West Antarctic, Greenland, other	std error on coeff	rms misfit
data source	coefficient			
Altimetry	West Antarctica	4.507	*1.213*	*0.128*
	Greenland	-1.200	*0.754*	
	Other	-1.176	*1.220*	
	total	2.131		
500 Tide Gauge (altimetry at TGs)	West Antarctica	8.748	*4.188*	*1.521*
	Greenland	0.559	*2.602*	
	Other	-6.367	*4.211*	
	total	2.940		
500 Tide Gauge GIA corrected	West Antarctica	5.558	*1.283*	*1.155*
	Greenland	1.171	*0.696*	
	Other	-4.675	*1.65*	
	total	2.054		

TABLE 6.3: Simple table of coefficients from a least square evaluation between the mass trend as calculated from altimetry (blue band), altimetry at tide gauges (green band) or tide gauges (grey band) to all 3 fingerprints (from West Antarctica, Greenland and glaciers), therefore assuming melting from all 3 sources. The 'other' fingerprint is assumed to be a constant rate over the entire ocean.

to our estimate of BSL (red) from altimetry (6.12b), altimetry at tide gauges (6.12d) and tide gauges (6.12f).

For all 3 of our estimates, the resultant fit from reconstructing the coefficients fits our mass estimates well. The size of the coefficients, however are either too large or too negative. The result from tide gauges (figures (6.12e and 6.12f)) is within two standard errors of the IPCC estimate. Ultimately, when a negative coefficient is produced, the shape of the implied fingerprint is not one that we would expect and is physically implausible.

Our final combination is to fit least squares from using 2 fingerprints. We combine West Antarctica and Greenland, West Antarctica and glaciers, and Greenland and glaciers, to produce 2 coefficients representing the corresponding contribution. When using just 2 fingerprints, we find some of our most realistic results within error and present these results in table (6.4). The standard error for each fingerprint fit (std) and rms of the overall fit are also shown.

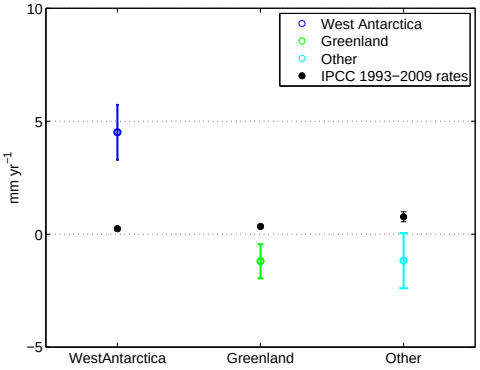

(A) Altimetry derived mass (mm yr^{-1})

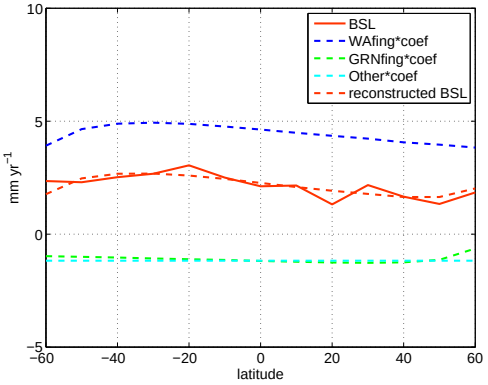

(B) Altimetry derived mass (mm yr^{-1})

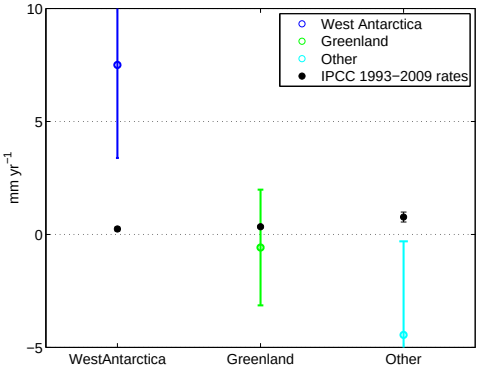

(C) Altimetry at tide gauge derived mass (mm yr^{-1})

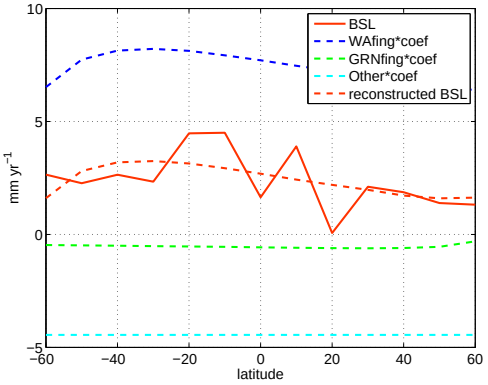

(D) Altimetry at tide gauge derived mass (mm yr^{-1})

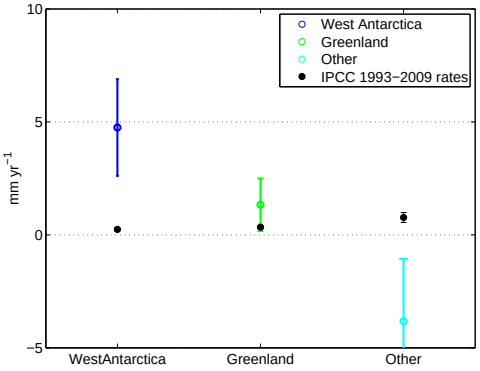

(E) Tide gauge derived mass (mm yr^{-1})

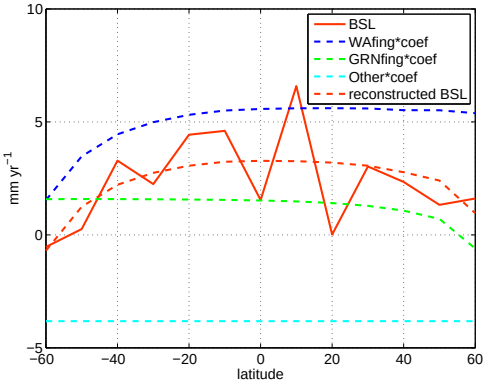

(F) Tide gauge derived mass (mm yr^{-1})

FIGURE 6.12: Amplitudes of West Antarctic (blue), Greenland (green) and other (cyan) coefficients from the simple fit (where the other term is constant at every latitude), between 3 fingerprints and altimetry (6.12a), tide gauges at altimetry (6.12c) and tide gauges (6.12e). The altimetry and altimetry at tide gauges are fit to the altimetry view fingerprint and the tide gauges are fit to the tide gauge view fingerprint. The coefficients for each case then weight the relevant fingerprints and when summed, reconstruct the mass component (red dash) compared to our 3 estimates of mass (red) from altimetry (figure (6.12b)), altimetry at tide gauges (figure (6.12d)) and tide gauges (figure (6.12f)) mm yr^{-1}.

Fingerprint used		West Antarctic, Greenland	std error on coeff	rms misfit	West Antarctica and glaciers	std error on coeff	rms misfit	Greenland and glaciers	std error on coeff	rms misfit
data source	coefficient									
Altimetry	West Antarctica	3.533	*0.670*	*0.127*	4.014	*1.252*	*1.146*	-	-	*0.276*
	Greenland	-1.430	*0.713*		-	-		-0.484	*1.072*	
	Other	-	-		-1.791	*1.235*		2.600	*0.994*	
	total	2.103			2.222			2.116		
500 Tide Gauge (altimetry at TGs)	West Antarctica	3.475	*2.451*	*1.699*	7.266	*3.808*	*1.346*	-	-	*1.782*
	Greenland	-0.688	*2.608*		-	-		0.613	*2.724*	
	Other	-	-		-4.744	*3.756*		1.834	*2.524*	
	total	2.787			2.522			2.447		
500 Tide Gauge GIA corrected	West Antarctica	2.271	*0.693*	*1.889*	4.119	*2.098*	*3.305*	-	-	*3.020*
	Greenland	-0.015	*0.711*		-	-		0.395	*1.088*	
	Other	-	-		-1.909	*2.233*		1.818	*1.130*	
	total	2.256			2.211			2.213		

TABLE 6.4: Simple table of coefficients from a least square evaluation between the mass trend as calculated from altimetry (blue band), altimetry at tide gauges (green band) or tide gauges (grey band) to all 3 fingerprints (from West Antarctica, Greenland and glaciers), therefore assuming melting from all 3 sources. The glacial fingerprint is simplified by the assumption that the distribution is uniform at each latitude

6.7.1 Assessing the robustness of the analysis

We assess the robustness of our least squares evaluation with the fingerprints by re-analysing the 7 fingerprint combinations in 2 ways

- Including the glacial fingerprint
- Weighting the least squares fit

The full set of results from the least squares analysis are shown over 4 tables at the end of this Chapter:

1. The simplified fit using the constant 'other' fingerprint (table 6.5),
2. The weighted simplified fit using the constant 'other' fingerprint (table 6.6)
3. The coefficients from using all 3 fingerprints (table 6.7) and
4. A weighted fit using all 3 fingerprints (table 6.8).

6.8 Weighting the results

We next chose to weight our mass curves, giving more weight to latitude bands over which we had more confidence with our results. For instance, we know that at 60° S in our tide gauge analysis that we only have one tide gauge (Chapter 3) therefore we down-weight this latitude band to restrict the influence in the least squares fit. Weights are applied differently to altimetry, tide gauge and steric data. The weights are proportional to inverse variances.

Calculating the weights

Steric

We used the variance of the 5 steric reconstructions ($mm^2\ yr^{-2}$) as a steric weight as in equation (6.11).

$$V(S) = variance(5 \text{ global steric arrays}) \tag{6.11}$$

Spatial sampling error of tide gauges

We assume the tide gauge error is dominated by sampling error. In order to quantify this we assume that the error variance is inversely proportional to the number of tide gauges in a latitude band and use altimetry to make an estimate of the constant of proportionality. We do this by comparing true zonal band averages from altimetry with averages from altimetry sampled from tide gauge sites only.

The absolute difference between the zonal average of augmented dynamic topography (τ) calculated using altimetry at each grid point, compared to the zonal average of τ calculated using altimetry at tide gauge locations is shown in equation (6.12).

$$\tau_{diff} = |\tau_{ALTza} - \tau_{ALTtg}| \tag{6.12}$$

We plotted the square of this absolute difference against latitude, together with the scaled inverse of the number of tide gauges within each latitude band (figure (6.13)). The weight was a value which allowed for the inverse of the number of tide gauges per latitude band to account for 70% of our difference values, as expected if the error is to represent approximately one standard error. By using this technique we gain a way of estimating sampling error variance in each latitude band due to the number of tide gauges in each band, while putting this into the correct units of variance through the scaling factor of the difference squared. The scaling factor

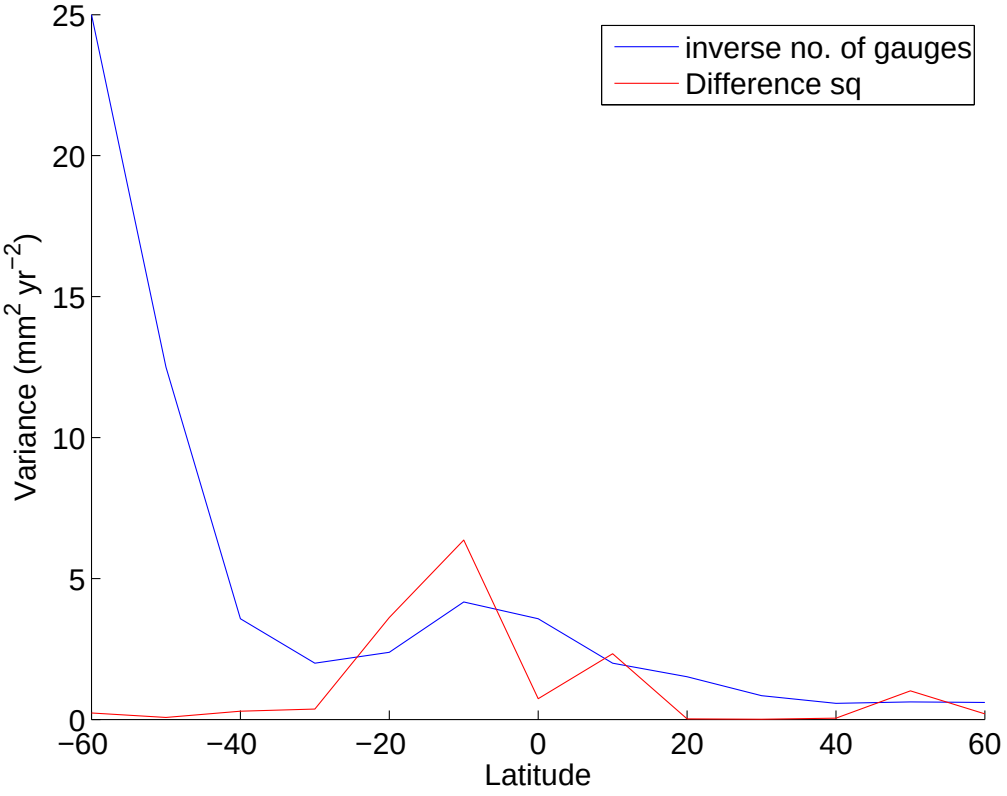

FIGURE 6.13: The square of the difference (mm^2 yr^{-2}) in trend between the zonal average of altimetry compared to the zonal average of altimetry at tide gauges (red), with the weighted inverse of the number of tide gauges per latitude (blue)

that enabled this was 50 mm^2 yr^{-2}. This was used to obtain $V(TG)$ in equation (6.13).

$$V(TG) = \frac{50mm^2yr^{-2}}{\text{n}^o \text{ of gauges within latitude band}} \tag{6.13}$$

Altimetry weight We assume the presence of ice at certain latitudes will affect our results and therefore contribute to the uncertainty. We assume a 1.5 mm yr^{-1} error at the highest latitudes and a 0.5 mm yr−1 at all other latitudes. The altimetry variance $V(A)$ is the square of these values.

Applying the weights The total variance is calculated as the root sum of the square of each relevant individual variance. The weights are then calculated as

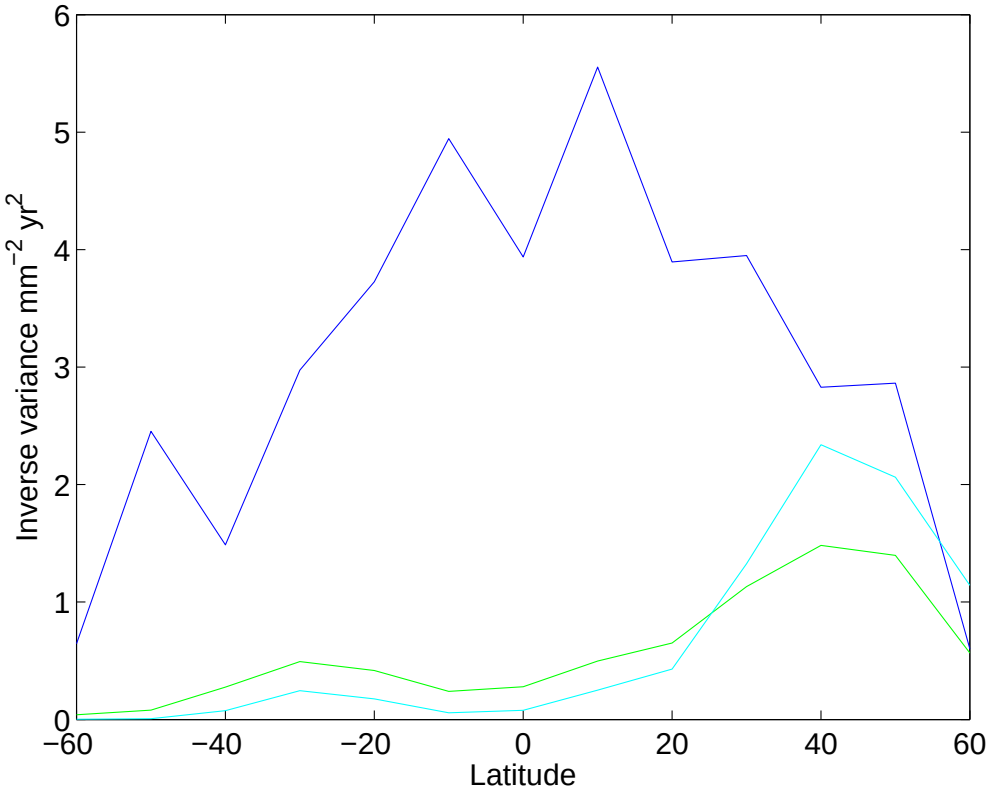

FIGURE 6.14: Each weighting term (mm^{-2} yr^2) as a function of latitude shows proportionally how the data is weighted. Altimetry weight (blue), Altimetry at tide gauges (green), tide gauges (cyan).

the inverse variance (mm^2 yr^{-2})$^{-1}$.

$$\text{Steric only} = \frac{1}{V(S)} \tag{6.14a}$$

$$\text{Altimetry} = \frac{1}{V(S) + V(A)} \tag{6.14b}$$

$$\text{Tide gauge} = \frac{1}{V(S) + V(TG)} \tag{6.14c}$$

$$\text{Altimetry at tide gauges} = \frac{1}{V(S) + V(A) + V(TG)} \tag{6.14d}$$

Figure (6.14) shows the inverse variance weights which are used proportionally as the weighting term as a function of latitude.

6.9 Weighted coefficient results

The aim of weighting the least squares fit is to try to reduce the tendency to over fit parts of the curve which are poorly determined. Table 6.8 shows the values of the coefficients with the weighting applied. The glacial fingerprint rather than the simplified uniform version is used. We see both decreases and increases in trends as well as the errors. The resultant fit when plotted, though, has a shape as a function of latitude which is more similar to the IPCC AR5 weighted result (figure (6.4)). The values of the coefficients range from lower or higher than the expected melt rate (from IPCC AR5 values), yet the sum of these coefficients for each fingerprint combination is reasonably similar. This sum is approximately 2.2 mm yr^{-1} in both the altimetry and altimetry at tide gauge analysis, but higher, approximately 2.7 mm yr^{-1} when using tide gauges.

Coefficients calculated from altimetry

The coefficients from the altimetry evaluation do not improve by applying a weight for combination a of 2 and 3 fingerprints. An improvement is seen for the cases where a single fingerprint is used and in each of these 3 cases there is an increase in the error associated with the fit.

Coefficients calculated from altimetry at tide gauges

The coefficients from the altimetry at tide gauge locations behave in a similar way to those derived using altimetry. We do not see an improvement when using 2 or 3 fingerprints. When using a single fingerprint in the least squares fit we do see an improvement and in the case of using the glacial fingerprint only, we also see a reduction in error.

Coefficients calculated from tide gauges

The coefficients evaluated using 3 fingerprints do not see an improvement for the tide gauge calculation. There is however, a good improvement when using the 2 fingerprints from West Antarctica and Greenland, where both of the results now lie within one standard error of IPCC AR5 values. The other weighted combinations of 2 fingerprints, West Antarctica/glacial and Greenland/glacial produce a reduced error and slight improvement with reduced error respectively. For the single fingerprint calculation, when weighted, the fit is improved for the West Antarctic fingerprint fit, no improvement for the glacial fingerprint fit, and reduced errors for the Greenland fingerprint fit.

6.9.1 Tables of results

The results are shown in table 6.5 (500 gauges fit to fingerprints from West Antarctica and Greenland, with simplified 'other' fit), table 6.6 (as for table 6.5 but weighted as outlined in section 6.8), and tables 6.7 and 6.8 (coefficients of a least square fit with all 3 fingerprints, unweighted and weighted respectively). In each table, a set of results from combinations of fingerprints is shown, for example, fits are made with individual fingerprints alone, all 3 fingerprints or combinations of 2 of the fingerprints.

We plot some of the results which come within one standard error to the IPCC AR5 values and are shown on each plot in black as the quoted sea level contributions from West Antarctica (0.24 ± 0.09 mm yr^{-1}), Greenland (0.34 ± 0.06 mm yr^{-1} and glaciers (0.77 ± 0.22 mm yr^{-1}). The plotted results can be seen in the table as outlined in yellow. Figure (6.15) shows the coefficients when using the Greenland plus other contributions. As the West Antarctic fingerprint is not used in this figure, any contribution from there will show in the 'other' coefficient, and this contribution would be higher accordingly.

Figure (6.16) shows results from weighted fits. Figure (6.16a) shows the coefficients from a fit with the mass curve calculated using altimetry at tide gauges with the Greenland fingerprint and simple 'other' contribution. The result is within error of the IPCC AR5 values, although the error is quite large. This combination assumes no melting from West Antarctica. Figures (6.16b and 6.16c) are the coefficients from weighted fits with 500 tide gauges with the West Antarctic and Greenland fingerprints, and with the Greenland and simple 'other' fingerprints respectively. Both results show higher contributions than IPCC AR5 values, although both results are also within 2 standard errors of IPCC values. The errors in these two cases are small, (around 0.4 - 0.6 mm yr^{-1}) although still larger than IPCC AR5 error values.

The weighted figure (6.16b) can be compared with the unweighted figure (6.17), both showing a fit using West Antarctica and Greenland. The errors are larger in the unweighted fit, however the value for Greenland melt is reduced to 0.37 ±0.97 mm yr^{-1}, comparing very well with the IPCC AR5 value 0.34 ±0.06 mm yr^{-1}. The coefficient representing West Antarctic melt in the unweighted case however is larger than observations suggest at 2.07 ±0.94 mm yr^{-1}. In this case, the

mathematical fitting is constrained at latitudes where there is larger uncertainty (60° S), and may not reflect a valid result.

Figure (6.18) shows weighted fits from the fourth table, table 6.8), with West Antarctica and Greenland coefficients in figure (6.18a) and West Antarctic and glacier coefficients in figure (6.18b). The results in these figures compare within 2σ of the IPCC AR5 values.

6.10 Redefining the errors on rates from tide gauges and altimetry using weights

Throughout this thesis the standard error is used on the fitted trend as the reported error. While this is a statistically correct representation of the error it does not account for sampling error in the estimates of zonal average trends. Therefore, weights calculated in section 6.8 are used to redefine these errors. They are shown in figure (6.19). The errors on the mass trend derived from altimetry become larger at the higher latitudes and are also influenced by the latitudinal steric variability. The mass trend derived from both altimetry at tide gauges and tide gauges corrected for GIA with ICE5G shows very large errors at latitudes 60° S and 50° S and also within the tropics. The northern latitudes from 30° N to 60° N have smaller errors which are more similar to those from altimetry.

Figure (6.19) also shows estimates of the mass trend as a function of latitude (red) with the IPCC AR5 weighted fingerprints (black). Figure (6.19a) shows the altimetry and altimetry at tide gauge mass estimates (red) with the 3 summed altimetry fingerprints weighted with IPCC AR5 melt rates. Figure (6.19b) shows the mass estimate from tide gauges (red) with the 3 tide gauge view fingerprints weighted with IPCC AR5 values (black). While our results are higher than the published estimates and the curves are more defined, our estimate does fit with more recent melt rates for the altimetry estimate. The fact that the estimates are close suggests that with a longer time series the fingerprints from recent ice melt would be able to be detected using altimetry.

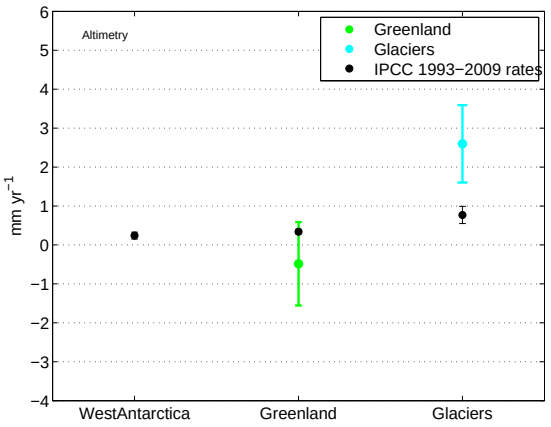

(A) Amplitudes of coefficients from mass calculated using GIA corrected altimetry fit with Greenland and other (as shown in table 6.5). mm yr^{-1}

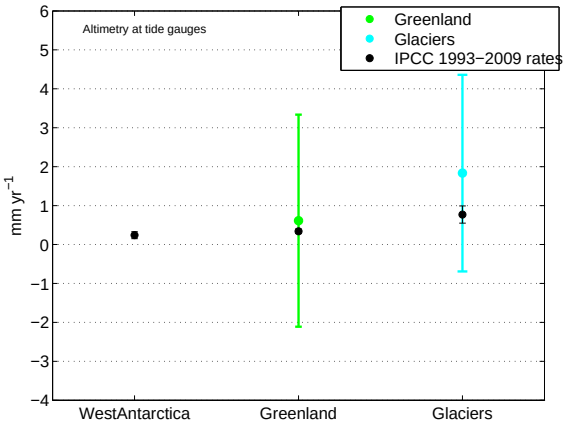

(B) Amplitudes of coefficients from mass calculated using GIA corrected altimetry at 500 tide gauges fit with Greenland and other (as shown in table 6.5). mm yr^{-1}

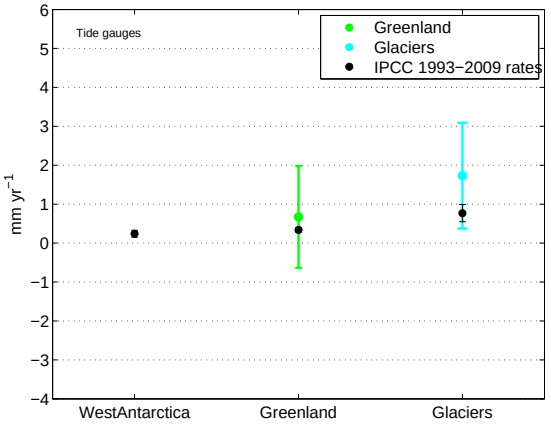

(C) Amplitudes of coefficients from mass calculated from 500 GIA corrected tide gauges fit with Greenland and other (as shown in table 6.5). mm yr^{-1}

FIGURE 6.15: Greenland fingerprints plus 'other' function spatial fingerprint which is the same with latitude from table 6.5 (highlighted yellow).

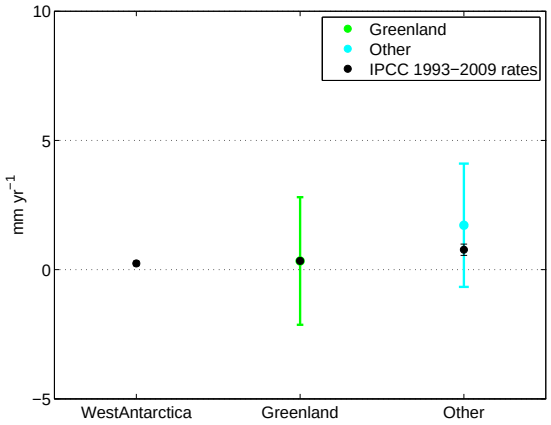

(A) Amplitudes of coefficients from an altimetry at tide gauges based weighted fit of mass with Greenland and 'other' fingerprints (mm yr^{-1})

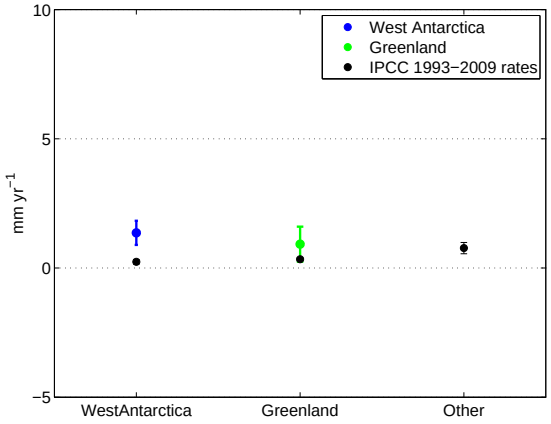

(B) Amplitudes from tide gauges. West Antarctica and Greenland, weighted fit (mm yr^{-1}).

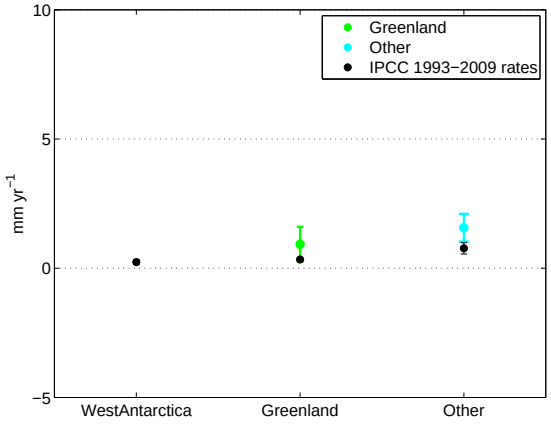

(C) Amplitudes from tide gauges. Greenland and other, weighted fit (mm yr^{-1}).

FIGURE 6.16: Coefficients of weighted fit with combinations of West Antarctic and Greenland fingerprints and 'other' spatial fingerprint (equal at all latitudes), with mass calculated using altimetry at tide gauges. Documented in table 6.6 (highlighted yellow).

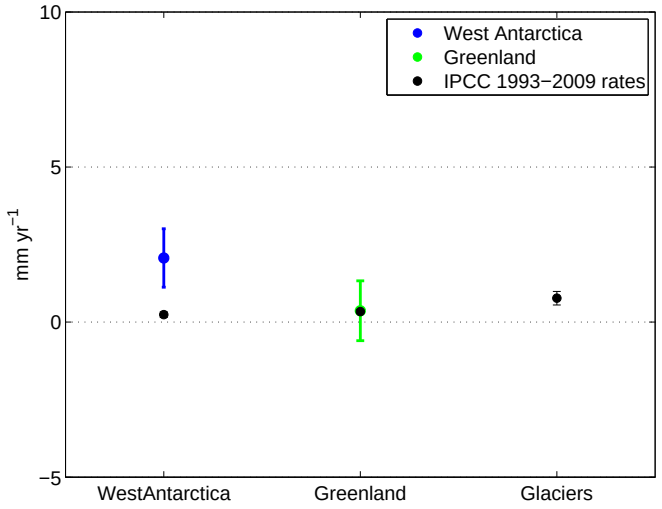

FIGURE 6.17: Coefficients from a least square fit of mass trends from tide gauges with combined fingerprints from West Antarctica and Greenland (mm yr^{-1}). Documented in table 6.7 (highlighted yellow).

6.11 Discussion

Analysing the mass component to sea level requires a detailed set of equations which we have set out at the beginning of this Chapter. Consideration of observational reference frame, VLD and changes to the Earth's geopotential are crucial. Our set of equations allow comparison of mass derived from both altimetry and tide gauges. Both altimetry and tide gauge trends appear to display a latitudinal dependence in mass trend distribution, with higher trends in the southern hemisphere from altimetry, and higher trends over the tropics and southern hemisphere from tide gauges. We can identify that some of the higher trends over the tropics in the tide gauge evaluation are due to spatial bias in tide gauges.

Fingerprints are used to compare the magnitude of our trends to those from the IPCC AR5 by weighting each of the 3 fingerprints with a published value of both global sea level (from the sum of combined melt rates shown in tables 6.5 -6.8). When weighted by these values and summed together the fingerprints display a similar latitudinal dependence, being lower at higher latitudes than mid latitudes and the tropics. Our 3 mass estimates are generally higher than the IPCC AR5 weighted fingerprints predict. Altimetry at tide gauge fits produce higher total sum of contributions than the altimetry fits and the tide gauges fits for almost every solution. We know that the spatial bias of tide gauges for this time period results in higher than expected mass trends at low latitudes. This, combined with

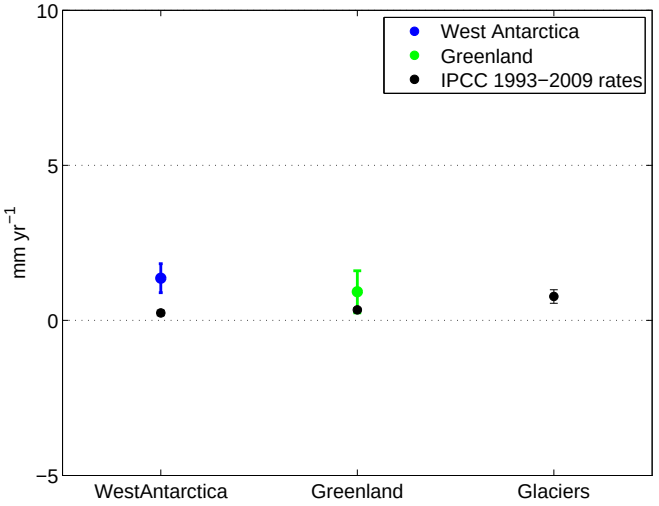

(A) Amplitudes from tide gauges. West Antarctica and Greenland, weighted fit. mm yr^{-1}

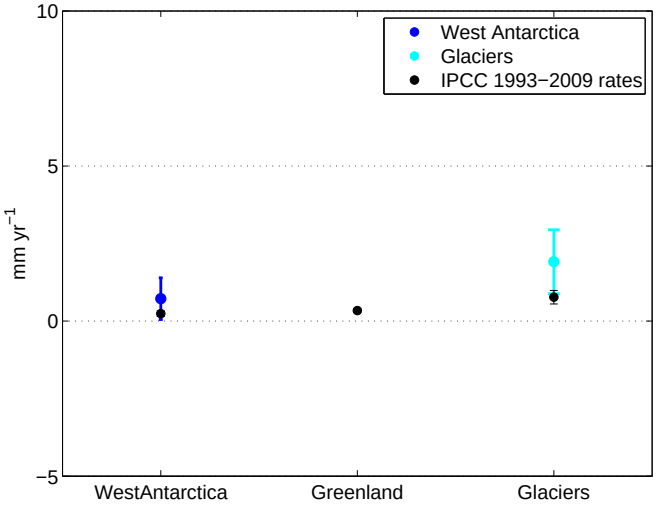

(B) Amplitudes from tide gauges. West Antarctic and glacial, weighted fit. mm yr^{-1}

FIGURE 6.18: West Antarctic and Greenland (6.18a) and West Antarctic and glacial coefficients (6.18b) calculated using tide gauges with a weighted fit. Documented in table 6.8 (highlighted yellow).

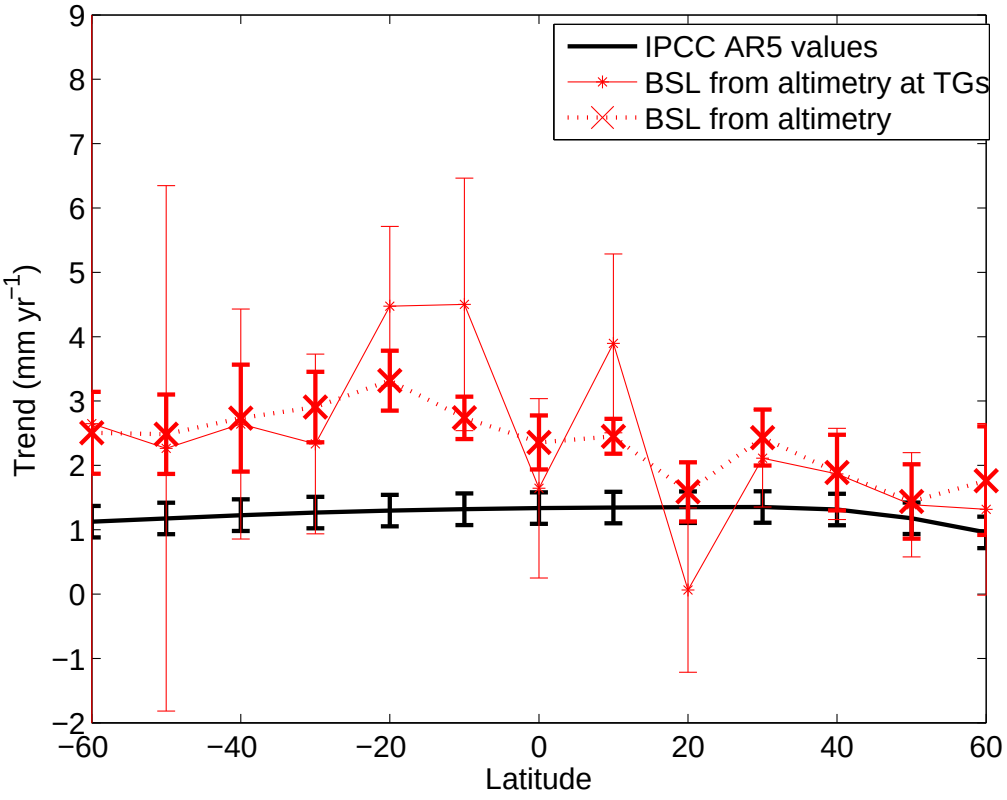

(A) Altimetry

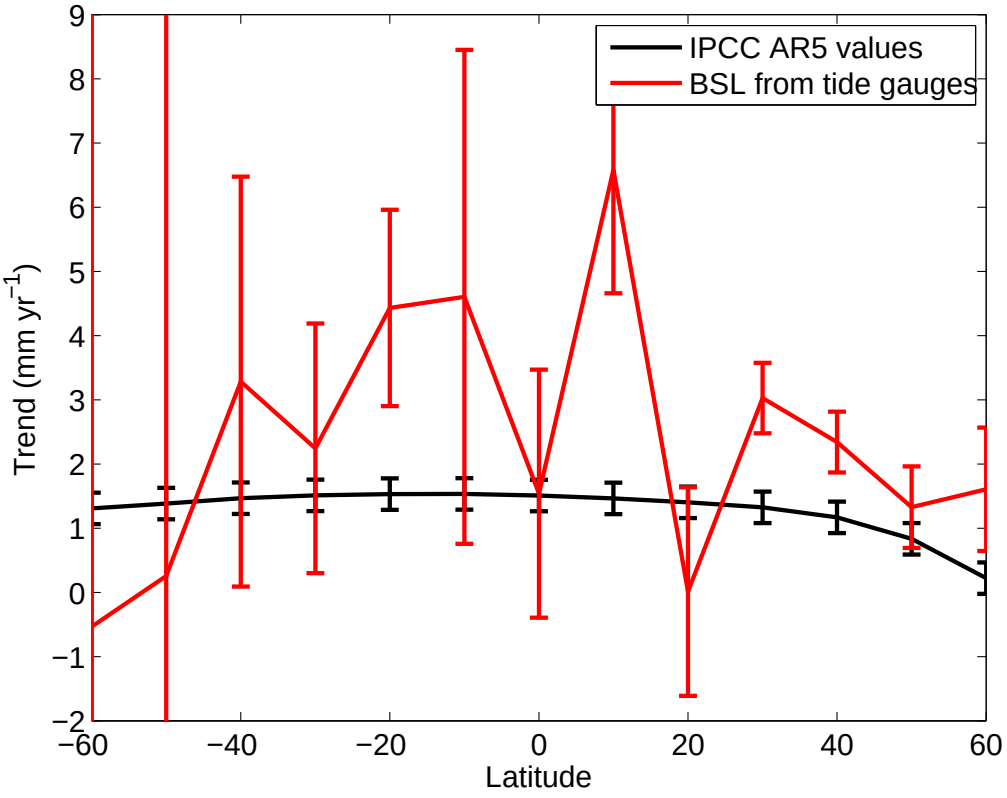

(B) Tide gauge

FIGURE 6.19: Comparing mass trends (red), (with standard error and revised error weighting documented in section 6.10) calculated using altimetry (bold x and dots) and altimetry at tide gauges (solid) (figure (6.19a)) and tide gauges (figure (6.19b)) for 1993 to 2010 to the West Antarctic, Greenland and glacial fingerprints. Fingerprints have been weighted with IPCC AR5 1993 to 2009 trends and summed, with quoted error (black).

the 'flatter' altimetry fingerprints, produces a fit which we know to have inherent errors.

We show 3 versions of our results. One has a glacial contribution which is independent of latitude, the second includes the glacial fingerprint and the third includes the 'uniform melting' glacial fingerprint and applies a weighting term to reflect latitudinal variation in observational errors. The resultant coefficients are displayed in tables 6.5, 6.7 and 6.8.

Our first simple analysis with the West Antarctic and Greenland fingerprint and a flat response independent of latitude representing every other contribution to the mass component including glaciers produces a set of plausible melting rates (as coefficients) within error (when compared to IPCC AR5) for each single fingerprint fit, and for the 2 fingerprint combination Greenland/glacier. We find a good fit from tide gauges for the 2 fingerprint combination West Antarctica/Greenland but altimetry and altimetry at tide gauges do not produce as good a result.

When the glacial fingerprint is included, as opposed to the simplified contribution, the fit improves in most cases. The only case where the coefficients become significantly larger (i.e. worse) is the Greenland/glacier combined fit.

Results from applying the weighting mostly improve the fit of the single fingerprint and/or the error, but the weighting does not improve most of the combined fingerprint results. The exception to this is the coefficients from the tide gauge result when using the West Antarctic/Greenland combined fingerprints, where this combination gives the best result. This combination of fingerprint produces plausible coefficients for all of our analysis.

The fingerprint analysis produces the most plausible coefficient values when we use 1 or 2 combinations. In the physical world there will not merely be 3 fingerprints to explain the complexity of changes in the geopotential of Earth. For example, hydrological changes and the decrease in terrestrial storage (Church et al., 2011) are significant and will also have their own fingerprint, as will the redistribution of ocean mass due to circulation patterns and changes to the solid Earth below the ocean basin. The data also remains dynamically 'noisy' over this relatively short period of time where long trend variability still influences spatial trends over this time scale. Using GRACE data would provide a check for these results, however the relatively short time scale of the GRACE time series is unlikely enough this far to distinguish the fingerprint signal from background noise.

The errors on the IPCC AR5 values are very small (± 0.09 mm yr^{-1}, ± 0.06 mm yr^{-1} and ± 0.22 mm yr^{-1} errors for melt rates at West Antarctica, Greenland and glaciers respectively for 1993 to 2009). Our errors are often much larger, based on the least squares algorithm allowing negative trends and so a wide spread between the values of the coefficients. While the errors on the IPCC AR5 results appear small, the statistical error does not always represent the actual error.

6.12 Summary

- Estimates of the mass contribution to sea level trends can be derived from tide gauges and altimetry using VLD (for tide gauges) and steric sea level.
- Global trends show that total global sea level is increasing at a faster rate than steric sea level.
- Steric trends are responsible for the regional variability. When the steric trend is removed, the mass trend has a much less structured regional pattern, although in our analysis the dynamics remain. This can be seen in areas of high dynamical signals such as the Antarctic Circumpolar Current and western boundary currents (Figure (6.5)).
- The mass component has less regional structure than the steric component, therefore an intermediate view between the global and the regional trends can be used to show mass trends as zonal averages. Trends here are averaged into 10^{o} latitude bands. Zonal averaging also helps to account for the sparse data coverage in some areas.
- Three estimates in Chapter 6 show the mass distribution using altimetry, altimetry at tide gauges and tide gauges. Tide gauge estimates appear larger than altimetry estimates. We showed in Chapter 5 (using altimetry and altimetry at tide gauges) that the sparse spatial distribution of tide gauges leads to higher trends than expected at the equator and low latitudes. Altimetry estimates of the mass component show higher trends in the Southern Hemisphere than those in the Northern Hemisphere. Altimetry at tide gauges shows a similar pattern to altimetry over the whole latitude band, although the trends are larger. Tide gauge estimates of the mass component show higher trends in the tropics and lower trends at high latitudes.
- Mass estimates are fitted to the fingerprints to obtain coefficients which represent melt rates from each ice melt source (assuming our mass estimates are accurate and the parametrization was complete and correct). We use 4 different combinations of the fingerprint to test the results. These are a simple 'other' fingerprint which has no structure as a function of latitude but accounts for all melting apart from the ice caps, combined with . We also use the 3 fingerprints from West Antarctica, Greenland and a simple glacier

fingerprint. The other two combinations are weighted versions of these two combinations.

- The results are shown in 4 tables at the end of this Chapter.
- We revise our errors to represent our confidence in the observations
- The least square fit contributions generally sum up to just over 2 mm yr^{-1}. This is higher that reported in the IPCC AR5 (1.35 mm yr^{-1}), although there is still much uncertainty as to the size of the contributions to the mass component of sea level trends. Estimates from CryoSat-2 and GRACE will help to constrain this uncertainty for future estimates. Long term and historical trend analysis, though will continue to rely on tide gauge and altimetry data.

Fingerprint used		West Antarctica	std error on coeff	rms misfit	Greenland	std error on coeff	rms misfit	other	std error on coeff	rms misfit	West Antarctic, Greenland, other	std error on coeff	rms misfit	West Antarctic, Greenland	std error on coeff	rms misfit	West Antarctica and other	std error on coeff	rms misfit	Greenland and other	std error on coeff	rms misfit
data source	coefficient																					
Altimetry	West Antarctica	2.20	0.11		-	-		-	-		4.51	1.21		3.53	0.67		4.01	1.25		-	-	
	Greenland	-	-	0.16	2.29	0.19	0.41	-	-	0.26	-1.20	0.75	0.13	-1.43	0.71	0.13	-	-	1.15	-0.48	1.07	0.28
	Other	-	-		-	-		2.15	0.14		-1.18	1.22		-	-		-1.79	1.23		2.60	0.99	
	total	2.20			2.29			2.15			2.13			2.10			2.22			2.12		
500 Tide Gauge (altimetry at TGs)	West Antarctica	2.84	0.35		-	-		-	-		8.75	4.19		3.48	2.45		7.27	3.81		-	-	
	Greenland	-	-	1.57	2.97	0.41	1.84	-	-	1.90	0.56	2.60	1.52	-0.69	2.61	1.70	-	-	1.35	0.61	2.72	1.78
	Other	-	-		-	-		2.74	0.38		-6.37	4.21		-	-		-4.74	3.76		1.83	2.52	
	total	2.84			2.97			2.74			2.94			2.79			2.52			2.45		
500 Tide Gauge GIA corrected	West Antarctica	2.26	0.34		-	-		-	-		5.56	1.28		2.27	0.69		4.12	2.10		-	-	
	Greenland	-	-	1.73	1.98	0.49	3.42	-	-	2.80	1.17	0.70	1.15	-0.01	0.71	1.89	-	-	3.30	0.40	1.09	3.02
	Other	-	-		-	-		2.19	0.46		-4.68	1.65		-	-		-1.91	2.23		1.82	1.13	
	total	2.26			1.98			2.19			2.05			2.26			2.21			2.21		

TABLE 6.5: Coefficients from West Antarctica, Greenland and other sources. The table shows the resultant coefficients from a least squares evaluation as outlined in section 6.6. The solutions are seperately found using 3 data sources: altimetry (blue row), altimetry at tide gauges (green row) and tide gauges corrected for *GIA* using Peltier (2004) (grey row). Each of the 3 data sources shows the coefficients of 7 solutions. These 7 solutions are derived from using either all, or a combination, of the fingerprints. The other function (inclusive of glaciers, land based water storage and other hydrological processes) is spatially constant. The results are shown with one standard error of each coefficient as well as the root mean squared error of the misfit between the original data and the sum of the fits. The sum of the coefficients for each solution is found below each solution. Solutions outlined in yellow are plotted in figures (6.15a, 6.15b and 6.15c). All values in mm yr^{-1}

Fingerprint used		West Antarctica	std error on coeff	rms misfit	Greenland	std error on coeff	rms misfit	other	std error on coeff	rms misfit	West Antarctic, Greenland, other	std error on coeff	rms misfit	West Antarctic, Greenland	std error on coeff	rms misfit	West Antarctica and other	std error on coeff	rms misfit	Greenland and other	std error on coeff	rms misfit
Weighted data source	coefficient																					
Altimetry	West Antarctica	2.18	0.11	0.51	-	-	1.19	-	-	0.84	5.33	1.35	0.34	4.10	0.75	0.35	5.63	1.32	1.40	-	-	0.80
	Greenland	-	-		2.21	0.18		-	-		-1.14	1.10		-1.99	0.77		-	-		-2.07	1.63	
	Other	-	-		-	-		2.16	0.15		-2.06	1.89		-	-		-3.46	1.32		4.16	1.58	
	total	2.18			2.21			2.16			2.13			2.10			2.17			2.09		
500 Tide Gauge (altimetry at TGs)	West Antarctica	2.18	0.31	0.66	-	-	0.81	-	-	0.78	8.25	3.76	0.63	3.72	2.08	0.69	8.18	3.56	0.57	-	-	0.85
	Greenland	-	-		2.10	0.34		-	-		-0.31	2.15		-1.54	2.05		-	-		0.33	2.47	
	Other	-	-		-	-		2.04	0.32		-5.54	3.89		-	-		-5.74	3.40		1.72	2.39	
	total	2.18			2.10			2.04			2.41			2.19			2.44			2.05		
500 Tide Gauge GIA corrected	West Antarctica	1.87	0.29	0.93	-	-	1.40	-	-	0.93	-0.69	9.52	0.95	1.36	0.47	0.87	0.84	9.76	1.01	-	-	0.86
	Greenland	-	-		2.50	0.52		-	-		0.94	0.71		0.92	0.68		-	-		0.93	0.67	
	Other	-	-		-	-		2.16	0.34		2.36	10.95		-	-		1.19	11.31		1.57	0.54	
	total	1.87			2.50			2.16			2.61			2.28			2.03			2.50		

TABLE 6.6: Weighted coefficients from West Antarctica, Greenland and other sources. The table shows the resultant coefficients from a least squares evaluation as outlined in section 6.6. The solutions are seperately found using 3 data sources: altimetry (blue row), altimetry at tide gauges (green row) and tide gauges corrected for *GIA* using Peltier (2004) (grey row). Each of the 3 data sources shows the coefficients for 7 solutions. These 7 solutions are derived from using either all, or a combination, of the fingerprints. The other function (inclusive of glaciers, land based water storage and other hydrological processes) is spatially constant. Solutions are comparable to those in table (6.5) in that the same fingerprints and data are used to calculate the result, the difference is that the solution is now weighted (as set out in subsection (6.8) to reflect our confidence in the spatial resolution of the data. The results are shown with one standard error of each coefficient as well as the root mean squared error of the misfit between the original data and the sum of the fits. All values in mm yr^{-1}

Fingerprint used		West Antarctica	std error on coeff	rms misfit	Greenland	std error on coeff	rms misfit	glaciers	std error on coeff	rms misfit	West Antarctic, Greenland, Glaciers	std error on coeff	rms misfit	West Antarctic, Greenland	std error on coeff	rms misfit	West Antarctica and glaciers	std error on coeff	rms misfit	Greenland and glaciers	std error on coeff	rms misfit
Data source	coefficient																					
Altimetry	West Antarctica	2.20	0.11	0.16	-	-	0.41	-	-	0.29	3.74	1.24	0.14	3.53	0.69	0.13	4.16	1.08	0.13	-	-	0.24
	Greenland	-	-		2.29	0.19		-	-		-1.16	1.56		-1.43	0.73		-	-		-3.31	1.83	
	Glaciers	-	-		-	-		2.35	0.16		-0.50	2.49		-	-		-2.11	1.16		5.69	1.85	
	total	2.20			2.29			2.35			2.08			2.10			2.04			2.38		
500 Tide Gauge (altimetry at TGs)	West Antarctica	2.47	0.33	1.41	-	-	1.71	-	-	1.59	5.05	4.23	1.62	3.82	2.30	1.49	4.98	3.59	1.47	-	-	1.68
	Greenland	-	-		2.57	0.39		-	-		0.20	5.33		-1.45	2.45		-	-		-2.71	4.84	
	Glaciers	-	-		-	-		2.63	0.38		-3.00	8.50		-	-		-2.71	3.87		5.36	4.90	
	total	2.47			2.57			2.63			2.26			2.37			2.27			2.66		
500 Tide Gauge GIA corrected	West Antarctica	2.37	0.47	3.23	-	-	4.59	-	-	3.99	2.27	1.81	3.82	2.07	0.94	3.48	2.00	1.21	3.49	-	-	4.02
	Greenland	-	-		2.18	0.57		-	-		0.97	4.62		0.37	0.96		-	-		-3.17	3.30	
	Glaciers	-	-		-	-		2.46	0.57		-0.85	6.34		-	-		0.45	1.33		5.81	3.53	
	total	2.37			2.18			2.46			2.39			2.43			2.45			2.64		

TABLE 6.7: Coefficients from West Antarctica, Greenland and glaciers. The table shows the resultant coefficients from a least squares evaluation as outlined in section 6.6. The solutions are seperately found using 3 data sources: altimetry (blue row), altimetry at tide gauges (green row) and tide gauges corrected for GIA using Peltier (2004) (grey row). Each of the 3 data sources shows the coefficients for 7 solutions. These 7 solutions are derived from using either all, or a combination, of the fingerprints. The results are shown with one standard error of each coefficient as well as the root mean squared error of the misfit between the original data and the sum of the fits. All values in mm yr^{-1}

Fingerprint used		West Antarctica	std error on coeff	rms misfit	Greenland	std error on coeff	rms misfit	glaciers	std error on coeff	rms misfit	West Antarctic, Greenland, Glaciers	std error on coeff	rms misfit	West Antarctic, Greenland	std error on coeff	rms misfit	West Antarctica and glaciers	std error on coeff	rms misfit	Greenland and glaciers	std error on coeff	rms misfit
Weighted data source	coefficient																					
Altimetry	West Antarctica	2.18	*0.11*		-	-		-	-		3.47	*1.33*		4.10	*0.75*		4.52	*1.11*		-	-	
	Greenland	-	-	*0.51*	2.21	*0.18*	*1.19*	-	-	*0.91*	-3.37	*2.51*	*0.37*	-1.99	*0.77*	*0.35*	-	-	*0.40*	-7.22	*2.51*	*0.57*
	Glaciers	-	-		-	-		2.29	*0.16*		2.07	*3.59*		-	-		-2.49	*1.18*		9.70	*2.58*	
	total	2.18			2.21			2.29			2.17			2.10			2.03			2.47		
500 Tide Gauge (altimetry at TGs)	West Antarctica	2.18	*0.31*		-	-		-	-		4.95	*4.09*		3.72	*2.08*		5.01	*3.38*		-	-	
	Greenland	-	-	*0.66*	2.10	*0.34*	*0.81*	-	-	*0.75*	-0.13	*4.52*	*0.75*	-1.54	*2.05*	*0.69*	-	-	*0.68*	-2.85	*4.00*	*0.78*
	Glaciers	-	-		-	-		2.21	*0.34*		-2.72	*7.71*		-	-		-2.92	*3.48*		5.18	*4.17*	
	total	2.18			2.10			2.21			2.09			2.19			2.09			2.33		
500 Tide Gauge GIA corrected	West Antarctica	1.87	*0.29*		-	-		-	-		-0.13	*1.03*		1.36	*0.47*		0.72	*0.67*		-	-	
	Greenland	-	-	*0.93*	2.50	*0.52*	*1.40*	-	-	*0.78*	-2.31	*2.11*	*0.76*	0.92	*0.68*	*0.87*	-	-	*0.77*	-2.10	*1.31*	*0.69*
	Glaciers	-	-		-	-		2.93	*0.41*		5.47	*3.40*		-	-		1.91	*1.03*		5.07	*1.38*	
	total	1.87			2.50			2.93			3.02			2.28			2.64			2.96		

TABLE 6.8: Weighted coefficients from West Antarctica, Greenland and glaciers. The table shows the resultant coefficients from a weighted least squares evaluation as outlined in section 6.6. The solutions are comparable to those set out as in table (6.7) in that they use the same fingerprints and data to calculate the coefficients, except now the least squares fit is weighted as set out in subsection (6.8) to reflect our confidence in the spatial resolution of the data. The results are shown with one standard error of each coefficient as well as the root mean squared error of the misfit between the original data and the sum of the fits. All values in mm yr^{-1}

Chapter 7

Discussion and analysis

This thesis has described how there is currently a need to calculate the distribution of the trend in the mass component of sea level rise from polar ice sheet and glacial melting. Direct measurements of global ocean mass have only been possible since the launch of the GRACE satellites in 2002 therefore, prior to then we must infer mass estimates using available observations such as tide gauges, altimetry and measurements of temperature and salinity. From our results, it appears that the redistribution of mass trends may have a latitudinal dependence, which is of local importance for predicting sea level trends if those trends persist, because of the relationship between mean sea level and storm surges and the risk of coastal flooding.

Chapter 1 has described current knowledge of sea level trends within the scientific community. Sea level is a major indicator of the effects of climate change due to its coupling with the Earth's atmosphere as well as the ocean's ability to store heat. The deep and abyssal ocean is able to store this heat for hundreds of years and warmer oceans imply changes for marine life, ocean currents and tropical storm intensity, as well as sea level changes through thermal expansion. Sea level trends are currently observed through the 100+ year records of the tide gauge network and the altimeter record since 1993. There are currently many studies which observe and model sea level, heat content and ocean mass flux, however this problem has been readdressed here due to the current broad range of scientific expertise in tide gauge observations, altimetry observations, geodesy and ocean heat content at the National Oceanography Centre in Liverpool and the University of Liverpool.

Chapter 2 has set out a concise set of equations relating relative (RSL) and absolute sea level (ASL) to steric sea level (SSL) through the introduced term augmented dynamic topography (τ). This requires knowledge of the spatial redistribution of the gravity field as mass is moved from the poles to the ocean through melting. The term used in Chapter 2 to allow for gravity changes is ($G' + \overline{VLD}$) and this term corrects sea level trends for gravity changes since the last glacial maximum due to GIA. In order to identify recent melting we look at barystatic sea level (BSL). This term refers to the distribution of the mass component of sea level trends once the changes in the spatial gravity field have been removed. This enables us to compare our results with the fingerprint analysis as described by Tamisiea et al. (2001). This analysis involves using techniques from various disciplines in oceanography and Earth science together. Often terms have slightly different definitions between disciplines, such as the definition for the geoid G_o. The set of equations formulated in Chapter 2 sets out the physical relationship between these disciplines mathematically enabling RSL (tide gauge), ASL (altimetric) and geodetic relationships to be used correctly.

In Chapter 3 the observations from tide gauges (RSL) show how the choice of subset of tide gauges is important when looking at large scale regional and global trends in sea level. This issue has been addressed by sea level scientists already, and some of those choices have been compared in Chapter 3 (spatially uniform gauge records by Merrifield et al. (2009) and long record tide gauges by Holgate and Woodworth (2004)). While using long tide gauge records is the most desirable (as record completeness is important for calculating long time-scale trends), we find that using this subset creates a bias towards the northern hemisphere which does not reveal the recent increase in the global sea level trend shown in the spatially uniform set. This mismatch suggests that the signal for the increase in trend originates from the tropics and/or southern hemisphere. Trends calculated from tide gauges are also complicated by the fact that the observed signal is relative to the land. Current corrections for vertical land displacement (VLD) are incomplete, although due to the increased availability of GPS receivers at tide gauge locations this difficulty could become resolved within the next decade for future observations, although use of GPS data to correct historical data is limited by the need to assume a steady rate of motion in order to extrapolate the past. While using tide gauges requires knowledge of the spatial bias of the global network to enable interpretation of large scale observations, the RSL signal becomes more sensitive due to recent melting (after the removal of Global Isostatic adjustment

(GIA) effects) when compared with gravity fingerprints, where the land effects enhance the magnitude of the observed response near to the area of ice melt. The zonally averaged view in Chapter 3 is more sparsely popluated with tide gauges at latitudes in the tropics and southern hemisphere and the magnitudes of trends within these latitude bands will undoubtedly have larger errors than those calculated using a statistical error. This issue has been addressed in Chapter 6 where the errors have been re-analysed.

Chapter 4 has evaluated the steric contribution to sea level trends. Comparison of the zonal averages of 5 gridded temperature and salinity data sets reveals differences, produced both from the interpolation technique used to infill for missing data and the depth to which the data set is available. The mapped steric trends for 1993 - 2010 reveal that the local structure of sea level trends are generally set by steric trends. This steric component, though, only accounts for around a third of the total global sea level trend in magnitude. The global steric trends in this analysis for the 1993 - 2010 period range from 0.59 ±0.19 to 1.03 ±0.12 mm yr^{-1} (Ishii and Kimoto (2009) and Smith and Murphy (2007) respectively) and the mean steric trend from all 5 data sets is 0.92 ±0.12 mm yr^{-1}. The larger mass component is expected then to display a different structure spatially to the steric trend. Hovmöller plots in figure (4.7) reveal an increase in steric height for all 5 data sets since around the year 2000. This rise occurs over most latitudes, and is especially apparent at tropical latitudes. The steric analysis also looked at the importance of the reference depth that is used to calculate the steric trends by limiting the depth to which the data was integrated to (see figure (4.12e)). The zonal average in this study found that the calculation of steric height was influenced by the choice of reference depth at latitudes between 30° S and 50° S in the southern hemisphere, where using a reference depth of 700 m underestimated the local steric height trend by up to 1 ±0.5 mm yr^{-1}. The reference depth was also important in the northern hemisphere, especially between 60° N, where the steric height was overestimated by using a reference depth of 700 m, and 80° N, where steric height was underestimated when a 700 m reference depth was used (although further results only extend to 60° N in this study). The differences between the 5 data sets prompted the use of the mean of all 5 data sets to provide the steric zonal average trend that is then used in the remaining Chapters, and the standard error of the 5 data sets at each latitude band to be used as the steric error value.

Sea level trends from altimetry are calculated in Chapter 5. This analysis enables us to compare total sea level trends (figure (5.11a)) with steric trends (figure (5.11b)), and then calculate the difference between total and steric, called the residual trend (figures (5.11c and 5.12)). We are able to show that the regional trends are less apparent in the residual trend, although areas where there are strong dynamical signals remain, which we would expect from the theoretical background in Chapter 2. Chapter 5 also plots the zonal average of altimetry with the zonal average of altimetry values at tide gauge locations (figure (5.9)) which enables us to evaluate the effect of the sparse spatial sampling of the tide gauge network. This study has shown that the spatial bias of tide gauges over-estimates trends in tropical latitudes, although, apart from this, zonal trends from altimetry at tide gauge locations are able to reproduce the zonal average of altimetry trends at each grid point reasonably well. The tide gauge network sampling is able to reproduce the zonal average trend best in the northern hemisphere but appears to over-estimate trends by over 2 mm yr^{-1} between latitudes 20 ^{o} S to 10 ^{o} N when all tide gauges and the 500 gauge subset are used.

Chapter 6 has shown our estimates of mass redistribution trends calculated using data from Chapters 3, 4 and 5. A global estimate of mass distribution trends calculated using altimetry minus steric trends for the years 1993-2010 is shown in figure (6.5). This map of mass trends does not show the same spatial patterns as total sea level trends, τ (figure (5.11a)), and steric trends, SSL (figure (5.11b) and figures (4.9a - 4.9e)). Instead, the mass trends appear more evenly distributed with the exception of areas that are known to have large dynamical signals. It is known that the mass component of sea level trends has increased rapidly during recent years as large scale melting has been observed of the polar ice sheets and glaciers. It is also known that theory suggests that trends in the redistribution of ice melt will not be uniform, but will be higher further away from the source than near to it. This theory is shown using fingerprints (Tamisiea et al., 2001) in figure (6.2). We zonally average estimated mass trends to better observe the large scale pattern of mass redistribution, as well as to compare them with the fingerprints. The results show that our mass estimates are higher in the southern hemisphere when we use altimetry observations (figures (6.7 and 6.9)), and higher in the tropics when we use tide gauge observations (figure (6.8)). These results show that the distribution pattern of the zonal mass trends persists when only full depth steric data sets are used (figures (6.11a - 6.11e)).

In order to assess the zonal distribution of the mass trends, zonal averages of the 3 fingerprints are used to calculate a simple least squares fit. The three mass trend estimates are individually fitted to various combinations of the fingerprints, and the coefficients are recorded in the tables (6.5 - 6.8). One problem with fitting the tide gauge zonal trends to the fingerprints is that there is only one tide gauge at 60° S and therefore we have to assume a large error. This problem was addressed by a re-evaluation of the errors based on the number of tide gauges within a latitude band and the square of the difference between zonal altimetry trends and zonal altimetry trends at tide gauge locations. These new error values also served as a weighting term which was used to calculate a weighted least squares fit between the mass estimates and the fingerprints. Some of the coefficients that were produced from the fits were plotted (with 1 standard error) as the contributions from West Antarctica, Greenland and glaciers in figures (6.15, 6.16 and 6.17) together with the published contributions from the IPCC AR5 (Stocker et al., 2013) shown in black. Due to the noise in the observation data and large errors in the southern hemisphere the data only provides weak constraints on the coefficients of the 3 fingerprints, although the results are improved when the glacial fingerprint is included, suggesting that glacial melt is significant to the zonal mass trend redistribution pattern.

The 3 IPCC AR5 melt rate contributions for West Antarctica, Greenland and glaciers were used to weight the corresponding fingerprint and summed to produce the expected redistribution pattern under these melt rate constraints. The results are plotted (black), with our mass trend estimates (red) showing altimetry in figure (6.19a) and tide gauges in figure (6.19b). The zonally averaged mass trends derived from observations are higher than the IPCC AR5 weighted fingerprints at all latitudes meaning that either some of the choices for the observational estimates have led to an over estimation in mass rates (for instance choice of steric rate), the observational errors are creating a bias, or the zonally averaged average view includes large long time-scale dynamical signals in ocean mass that remain included in the data. The difference in zonal rates could also be a result of underestimation of the melt rates from the 3 defined sources or an increase in mass from other sources such as from land storage.

7.1 Basin scale distributions

Holgate and Woodworth (2004) found that coastal sea level trends were significantly higher than the global mean when comparing tide gauge trends with altimetry suggesting spatial bias from tide gauges. They also showed that, when using simulated tide gauges by taking each coastal grid point from altimetry and comparing with the global altimetric mean, that coastal trends remained higher, at 3.7 mm yr^{-1} compared to 2.8 mm yr^{-1} from altimetry during 1993 to 2002. This suggests that, even without spatial bias, coastal trends are telling a slightly different story to altimetry. Altimetry does not yet have the resolution globally to reach the coastline, and therefore tide gauges still provide an independent reference to coastal sea level trends. We have shown that, when there are enough tide gauges, the data can represent that seen in the zonal average from altimetry. Global and regional tide gauge analysis will also benefit from development of GPS as land displacement is still a major issue when evaluating large scale trends. Analysis of the mass component of sea level trends will benefit greatly from a longer time series of GRACE in order to verify results.

Thompson and Merrifield (2014) make the observation that the asymmetric distribution of zonally averaged trends in sea level during the altimetry period is exceptional compared to other periods and brought about by wind-driven ocean volume redistribution. Their analysis identifies this redistribution using tide gauge trends but rather than sorting trends as a function of latitude, as in Merrifield et al. (2009), they observe regionally averaged trends as well as northern and southern regions (which are not centred on the equator). Thompson and Merrifield (2014) also find that southern trends are larger than northern trends during a recent 20 year period which they attribute to a departure from a historical mode of volume redistribution between southern regions attributed to the Southern Annular Mode (SAM) and coinciding with a maximum in the rate of sea level rise during recent decades. These findings would help to explain why the rates from mass estimates in Chapter 6 are higher in the southern hemisphere. Thompson and Merrifield (2014) explain their results as a redistribution of mass trends from northern regions to southern regions, where the trends in the south are further enhanced due to a unique change unseen in the rest of the historical record. This change, they show, is in part due to a departure in the historical redistribution between the Indian and South Pacific Ocean regions. While zonal averages are able to estimate the broadscale distribution of mass, the basin scale, wind-driven, decadal

and multi-decadal redistribution of mass could potentially be misinterpreted. In order to better interpret the zonal averages, a basin wide study would be valuable.

7.1.1 East and West contrasts

Bingham and Hughes (2012) show that there is a decoupling between the open ocean and the coast, especially on the western ocean boundaries. This could partly explain the differences that we see between tide gauges and altimetry here. In order to view the Eastern and Western boundaries separately we select tide gauges from the East and West coasts respectively and plot their time series as a function of latitude in figures (7.1b, 7.1a, 7.1d and 7.1c). We de-trend the time series to highlight the variability. There are large gaps where we do not have observations, however there are modes of variability which can be seen to be coherent over broad stretches of coastline. There is correlated variability as a function of latitude for both Eastern and Western boundaries, although the variability along the Western boundaries is more intense.

There is little apparent relationship between the Eastern and Western boundaries, although some possible opposing variability of the Eastern and Western boundaries at mid latitudes in the North Pacific. There is possibly a connection between extreme events in the Western Atlantic and the Eastern Pacific at high latitudes, although further investigation would be necessary to confirm a correlation.

An interesting follow on from our analysis of the mass component of sea level trends would be to analyse trends as a function of latitude using only the Eastern boundary tide gauges separately, although the even more sparse data in the East Atlantic would be an issue. One aspect of this study concluded that the dynamical signal remained in the residual component. By using only Eastern boundary gauges, the western boundary currents would be excluded removing some of that dynamical signal from the observations.

7.2 Changes in rates

In Chapter 4 the zonal average for trends over longer time scales was shown in figures (4.10b) (1966 - 2010) and (4.10c) (1955 - 2010). Zonal average steric trends

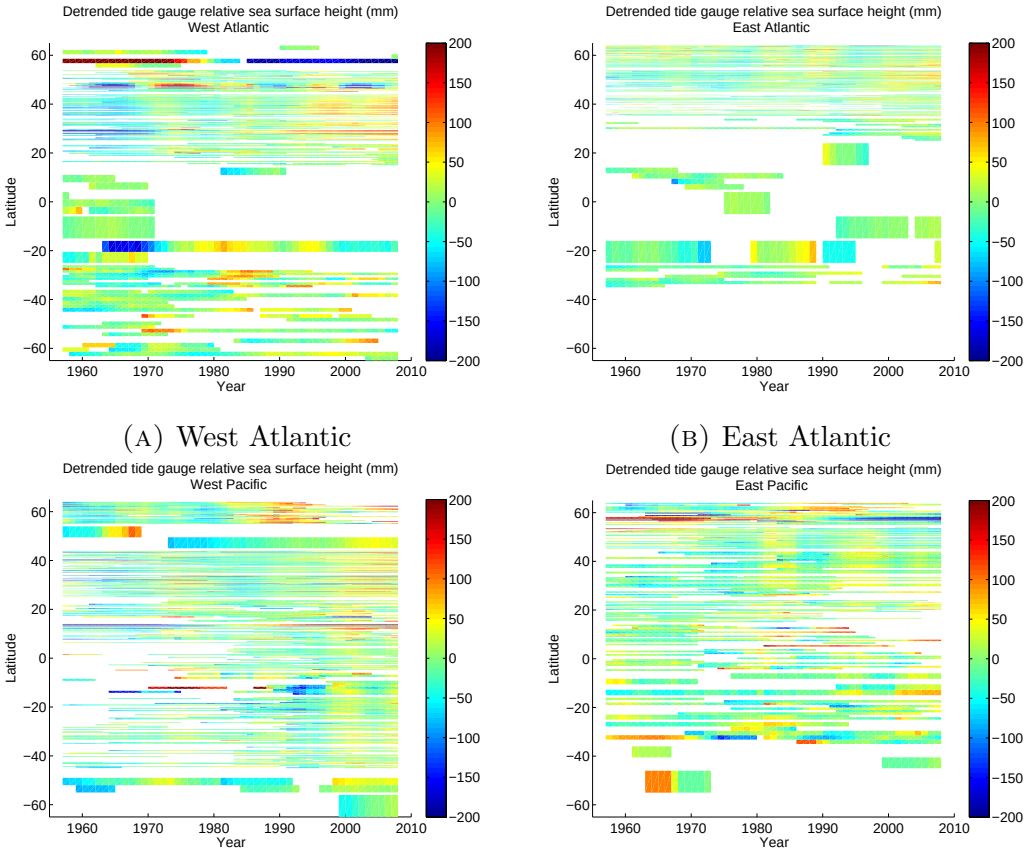

(A) West Atlantic

(B) East Atlantic

(C) West Pacific

(D) East Pacific

FIGURE 7.1: Tide gauge relative sea surface heights de-trended for the period 1955 to 2010 and plotted as a function of latitude (mm)

for these two time periods have been positive at all latitudes and both figures show that highest trends between both 1966-2010 and 1955-2010 occurred centred around low latitudes in the northern hemisphere (30^o N and 20^o N respectively).

Global altimetry annual data begins in 1993 and therefore τ derived from altimetry cannot be used for direct comparison with steric sea level over longer time periods. It has been shown in various ways in Chapter 3 how the spatial bias of the tide gauges alters the global and zonal average trends and therefore it is with this in mind that we observe with caution trends over longer time-scales, using tide gauges that have long time series data available. From the analysis in Chapter 3 where tide gauges with long records are observed, we might expect zonal averages of tide gauge trends to be over-estimated at tropical latitudes and with a large error in the southern hemisphere. Zonally averaged tide gauge trends are also not observed in the tropics for the 1993-2010 period using the criterion that the record must be 70% complete in order for the trend to be calculated.

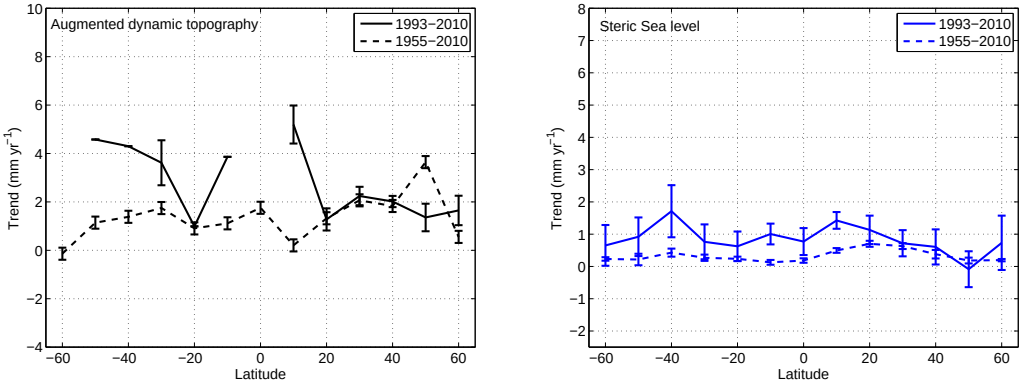

(A) Trends in augmented dynamic topography (1993-2010 as in figure (3.21b)

(B) Trends in steric sea level (as in figures (4.10a and 4.10c

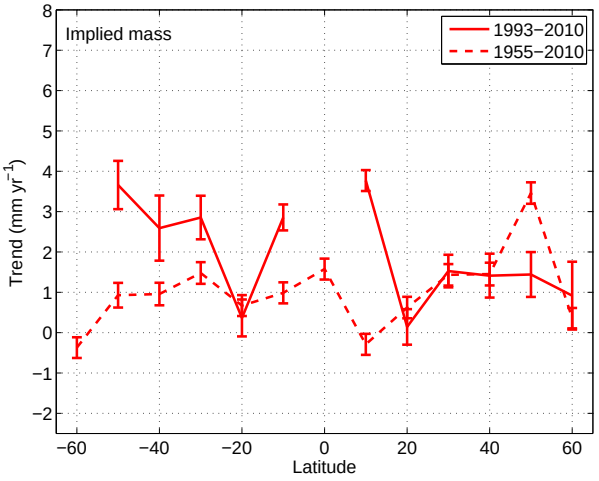

(C) Trends in implied mass from long record tide gauges

FIGURE 7.2: Zonal trends of τ (black), SSL (blue) and implied mass (red) calculated using long record tide gauges for τ and 5 steric gridded data sets for SSL, for the period 1955-2010 (dashed line), corrected for VLD using the difference of altimetry trends over the period 1993-2010 using the assumption that trend difference remained constant throughout. Also shown are zonal trends during 1993-2010 (solid line), using the same long records tide gauge subset (mm yr^{-1}).

The VLD correction applied to the tide gauges is the difference calculated between the tide gauge trend and the trend for altimetry at tide gauges during 1993-2010, with the assumption that the trend difference had remained constant. Figure 7.2a shows the zonal average of long time series trends during the period 1955-2010 (black dashed line) and the period 1993-2010 (black line). The global trend for the years 1955-2010, calculated as the sum of the ocean area weighted zonal trends, is 1.27 ±0.25 mm yr^{-1} compared to 2.82 ±0.42 mm yr^{-1} for the years 1993-2010.

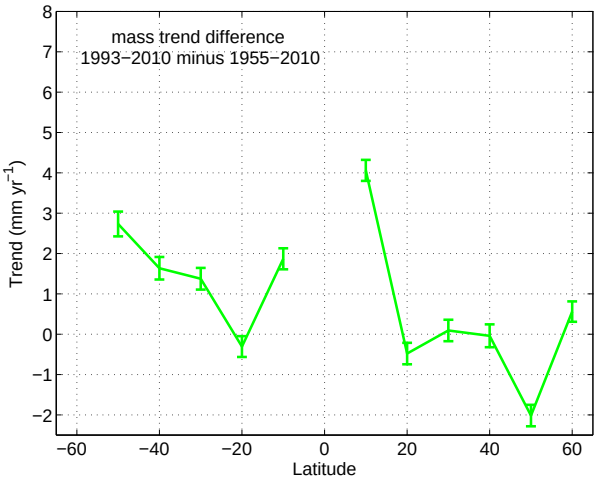

FIGURE 7.3: Implied mass trend difference between 1993-2010 minus 1955-2010 trends (mm yr^{-1}).

Steric trends (shown in figure (7.2b))are larger over the more recent period although during this period ocean sampling observations also increased rapidly due to ARGO floats. Global steric trends for 1955-2010 were calculated as 0.34 ±0.05 mm yr^{-1} compared to 0.92 ±0.12 mm yr^{-1} for 1993-2010. Zonal averages of steric trends have increased the most in the tropics and southern hemisphere. Details of basin scale steric trends will be lost during the zonal averaging. For example, high trends in the North Atlantic will be cancelled out by lower than the average trends in the North Pacific.

The implied mass trends (figure (7.2c)) show the recent increase in trends in the southern hemisphere when compared to the longer time period. A further investigation could plot a comparison of the first half of the time series against the second half to view the changes over the length of the time series by comparing trends of the same length. One aspect of comparing longer trends with shorter trends is that there is increased natural variability in the shorter trend record.

Figure (7.3) shows the difference in the mass trend between the whole length of the time series and the recent years (1993-2010 minus 1955-2010). Results in Chapter 5 have concluded that tide gauge trends are higher in the tropics due to spatial bias. If we assume this to be true and therefore discount the high trend at 10^{o} N then we observe an average trend difference in southern latitudes to be 1.46 ±0.42 mm yr^{-1} and an average trend difference in northern latitudes to be -0.38 ±0.40 mm yr^{-1}.

7.3 Mass trends from each steric reconstruction

In Chapter 6 the mass analysis used the mean of 5 steric data sets, as well as showing the mean of the 3 full depth steric data sets. Shown here in figures (7.4, 7.5 and 7.6) are mass estimates calculated from each individual steric data set when the steric is removed from the zonal average of altimetry, 500 tide gauges and all tide gauges respectively (all GIA corrected and tide gauges corrected for VLD using the ICE5G model data). The steric data set used in each instance is labelled on each figure. It is unclear whether one of these 5 steric reconstructions is better than another. All are widely used in current published work. The mean steric zonal rate from all 5 data sets is not substantially different to the mean rate using only the 3 full depth data sets, however this is probably mainly a reflection of an absence of observational data.

Altimetry derived mass

Differences in the altimetry derived mass trends of the 5 data sets are not confined to a single latitude band, but are seen both in the northern and southern hemispheres. Both the Ingleby and Huddleston (2007) and the Ishii and Kimoto (2009) data sets show mass trends above 2 mm yr^{-1} in the northern hemisphere, whereas the Smith and Murphy (2007), Levitus et al. (2009) and Carton et al. (2000) data sets all have mass trends calculated below 2 mm yr^{-1} in the north. All but the Ingleby and Huddleston (2007) data set have higher mass trends in the southern hemisphere. The Ingleby and Huddleston (2007) steric data set can explain more of the latitudinal variability in zonally averaged trends of τ than other data sets (figure (7.5b)).

Tide gauge derived mass

Figures (7.5 and 7.6) also show the zonally averaged trends from 5 individual steric data sets and the estimated mass component implied by τ (calculated from 500 gauges and all gauges respectively) minus SSL. All figures generally show higher mass trends in the tropics than at high latitudes. The main differences in mass trends from individual steric analysis are lower mass trends at 40^o S using only the Ingleby and Huddleston (2007) data set, and lower mass trends at 20^o N using only the Carton et al. (2000) data set due to higher SSL trends within these zonal bands compared to the other steric data sets.

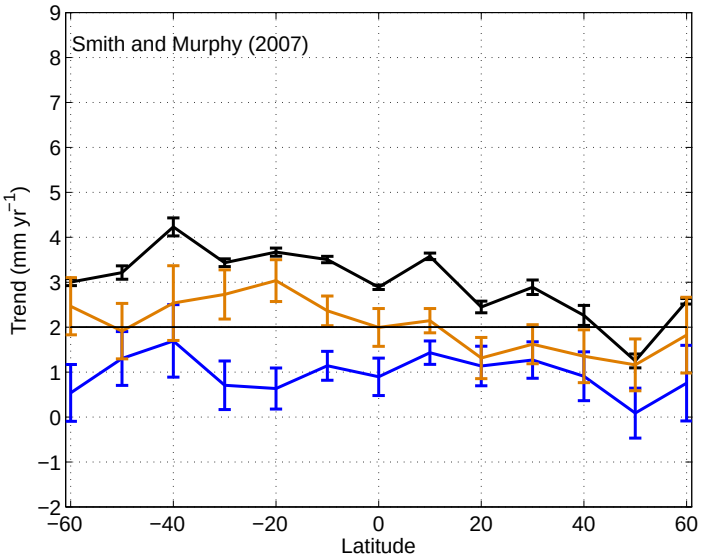

(A) Smith and Murphy (2007)

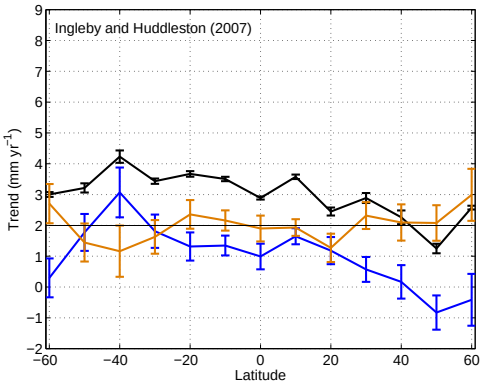

(B) Ingleby and Huddleston (2007)

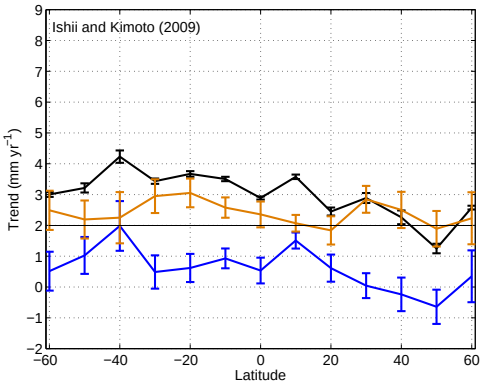

(C) Ishii and Kimoto (2009)

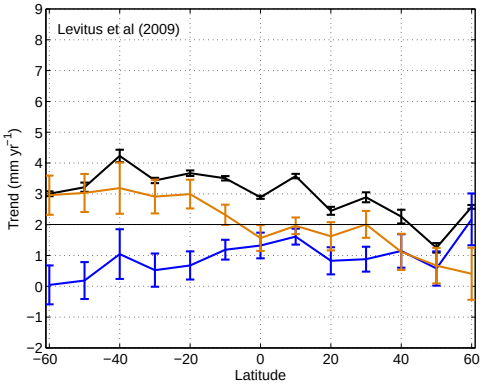

(D) Levitus et al. (2009)

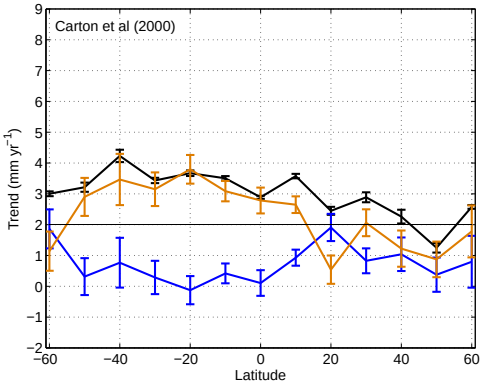

(E) Carton et al. (2000)

FIGURE 7.4: Implied mass trends (orange) between 1993-2010 when using altimetry (black) minus each of the 5 steric data sets individually as labelled on figures (7.4a-7.4e) (blue), mm yr^{-1}.

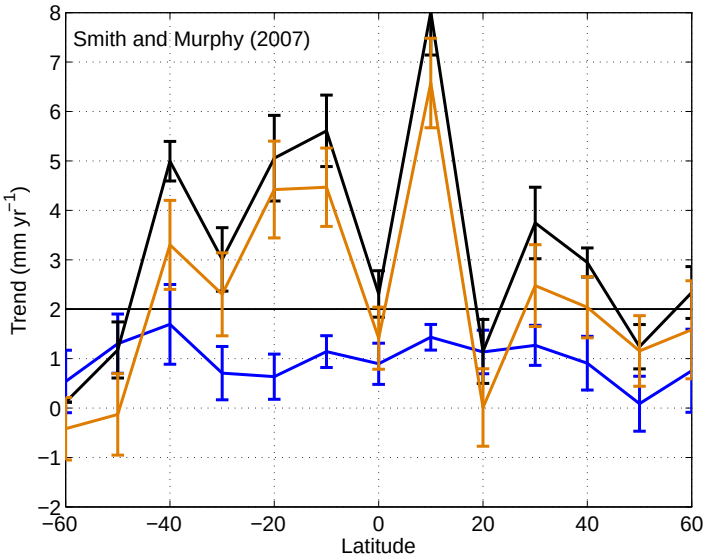

(A) Smith and Murphy (2007)

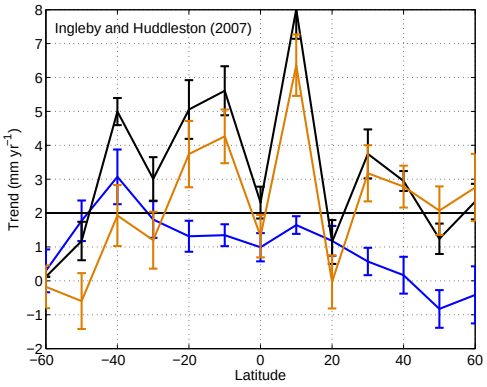

(B) Ingleby and Huddleston (2007)

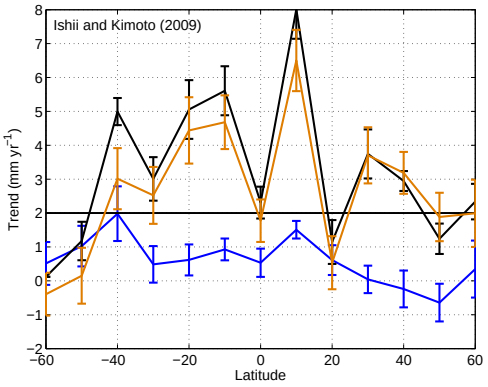

(C) Ishii and Kimoto (2009)

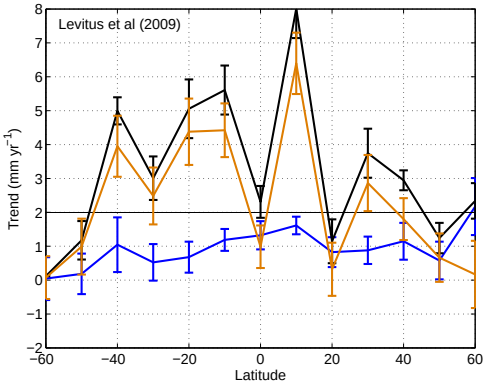

(D) Levitus et al. (2009)

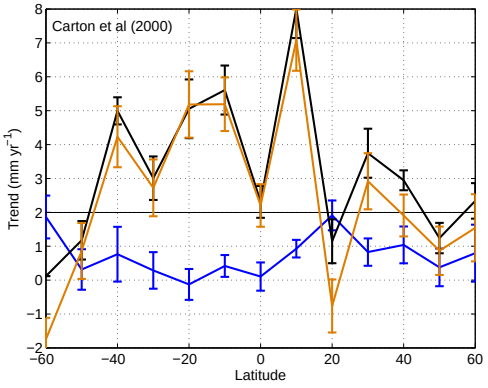

(E) Carton et al. (2000)

FIGURE 7.5: Implied mass trends (orange) between 1993-2010 when using 500 tide gauges corrected for *GIA* using Peltier (2004) (black) minus each of the 5 steric data sets individually as labelled on figures (7.5a-7.5e)(blue), mm yr^{-1}.

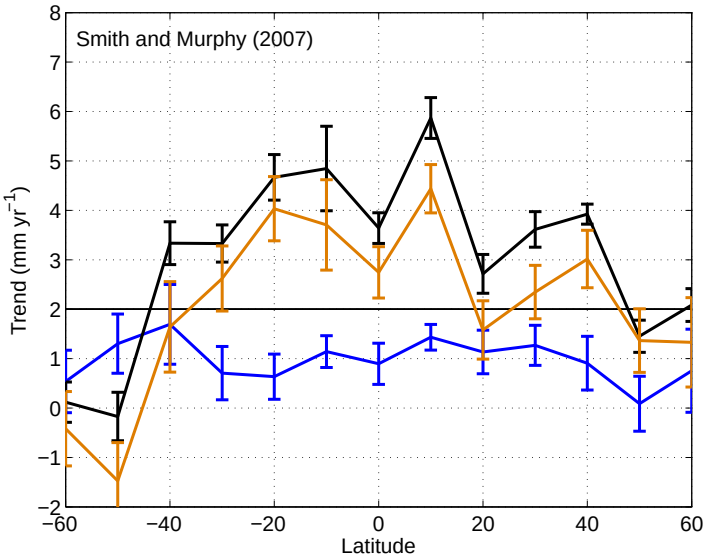

(A) Smith and Murphy (2007)

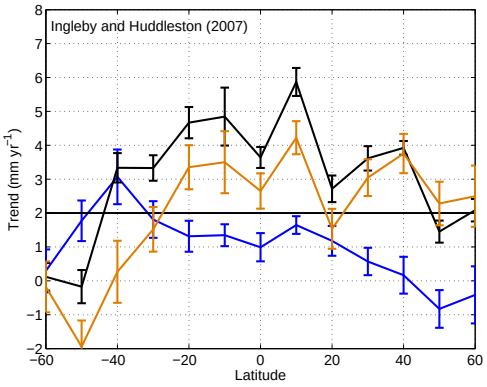

(B) Ingleby and Huddleston (2007)

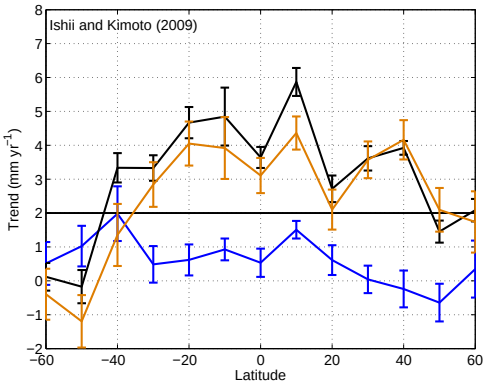

(C) Ishii and Kimoto (2009)

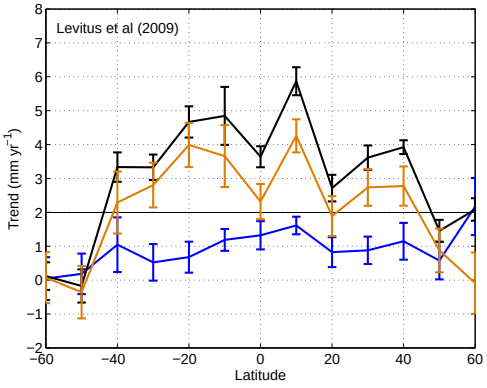

(D) Levitus et al. (2009)

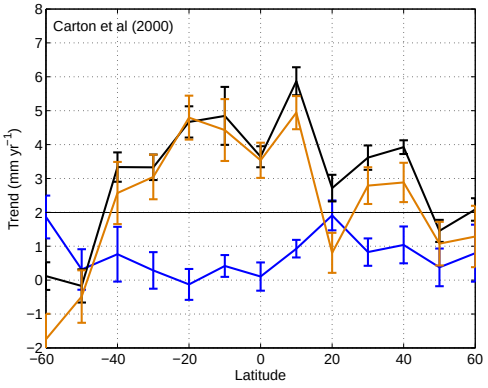

(E) Carton et al. (2000)

FIGURE 7.6: Implied mass trends (orange) between 1993-2010 when using all tide gauges corrected for *GIA* using Peltier (2004) (black), minus each of the 5 steric data sets individually as labelled on figures (7.6a-7.6e) (blue), mm yr^{-1}.

7.4 Mass redistribution compared to higher recent rates

GRACE estimates for the melt rates of West Antarctica, Greenland and glaciers are higher than estimates from other sources, although the estimates are over a shorter time scale (2005-2010 compared to 1993-2010). The IPCC AR5 states that 2005 - 2010 (1993 - 2010) rates of melting for glaciers was 0.92 ±0.08 mm yr^{-1} (0.94 ±0.07 mm yr^{-1}), for Greenland was 0.61 ±0.30 mm yr^{-1} (0.34 ±0.10 mm yr^{-1}) and for West Antarctica was 0.40 ±0.31 mm yr^{-1} (0.24 ±0.15 mm yr^{-1}). The total sum of these 3 sources is 1.93 ±0.44 mm yr^{-1} (1.52 ±0.19 mm yr^{-1}) (Stocker et al., 2013).

Melt rates over shorter time periods are often enhanced due to natural variability and therefore comparing rates calculated during different time periods should always be treated with extreme caution. Some validity could be argued for comparing the GRACE rates to other estimates despite the shortness of record, as GRACE observations are the most comprehensive measurements of the ice sheets and glaciers to date. Previous glaciological measurements have relied on measuring ice retreat and run off rates, where most of the ice is unreachable or unseen, whereas GRACE directly measures the whole ice mass through gravity measurements. It is plausible that previous measurements have underestimated the melt rates from ice sheets. Only a longer observational period from GRACE will be able to ascertain whether these higher rates are caused by an underestimation of melt rates using conventional measuring techniques, short term natural variability or even some errors not accounted for in the GRACE measurement.

Assuming that the GRACE melt rates reflect an underestimation by previous observations, the 3 fingerprints are weighted with GRACE rates and shown in figure (7.7) with the mass trends calculated in Chapter 6 from altimetry (figure (7.7a)) and 500 tide gauges (figure (7.7b)). The mass estimates for the two latter figures have not been changed to show rates from 1993 - 2010. This experiment compares two different time period and is done with caution. Comparison of two different time periods would generally be meaningless. The comparison here in figures (7.7a and 7.7b) is really an experiment to observe whether our mass estimates compare better with higher rates. Doubling the 1993-2010 melt rates from the 3 sources would have been a similar approach.

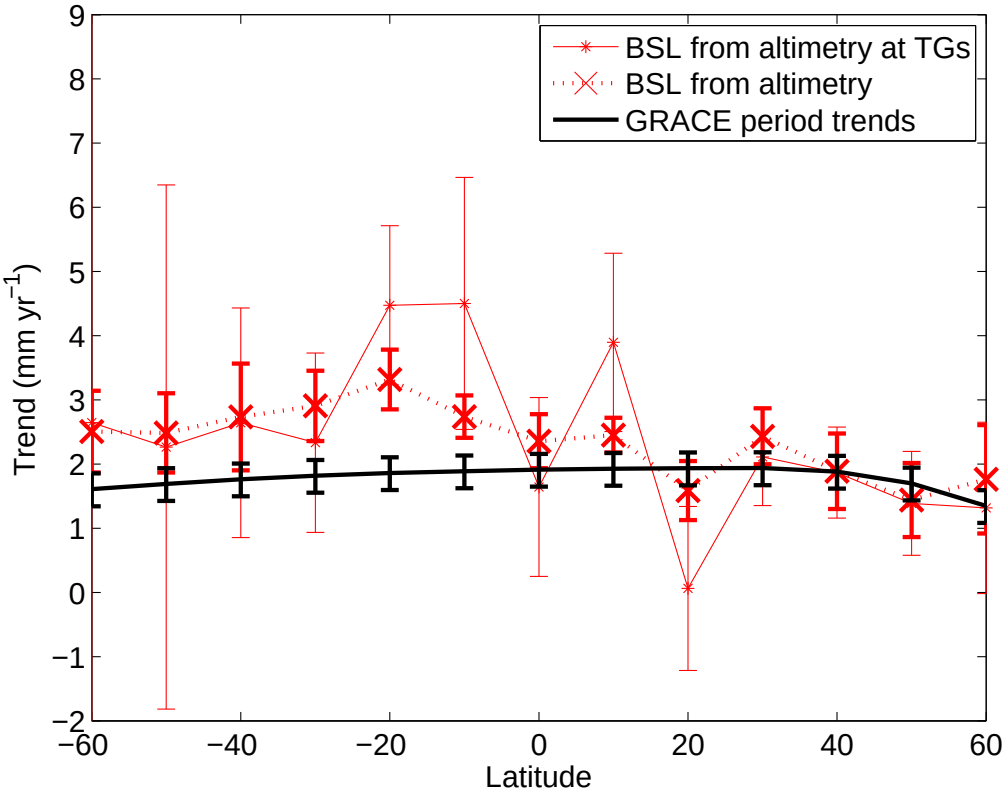

(A) Altimetry

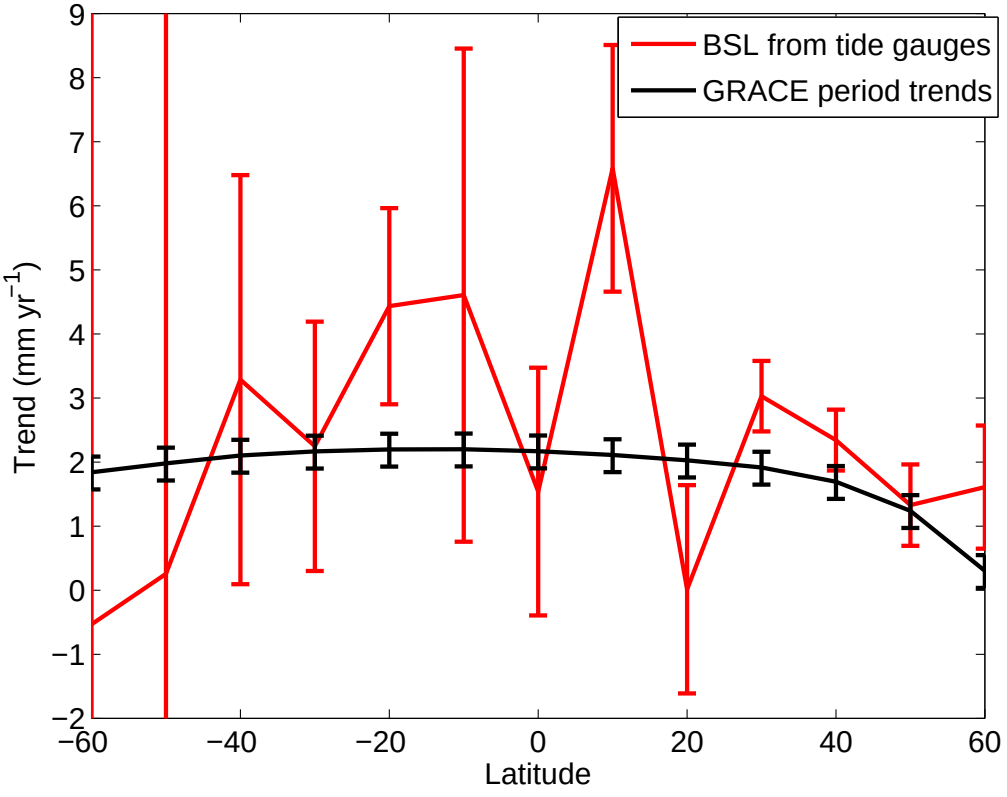

(B) Tide gauge

FIGURE 7.7: Comparing mass trends (red), (with standard error and revised error weighting documented in section 6.10) calculated using altimetry (bold x and dots) and altimetry at tide gauges (solid) (figure (7.7a)) and tide gauges (figure (7.7b)) for 1993 to 2010 to the West Antarctic, Greenland and glacial fingerprints. Fingerprints have been weighted with the magnitude of the IPCC AR5 2005 to 2010 trends and summed, with quoted error (black).

The magnitude of the mass estimates from both altimetry and tide gauges compare better with the zonally averaged fingerprint when weighted with higher melting rates from GRACE than with the lower melting rates of the pre-GRACE observational period as shown in Chapter 6, figure (6.19). The tide gauge estimates show variability between zonal bands of over 6 mm yr^{-1} but with large error values. The altimetry estimates (figure (7.7a)) compare well with the weighted fingerprint trends especially in the northern hemisphere from 20° N - 60° N where the two zonal averages compare closely within error. The higher mass trends compared to the weighted fingerprint trends at all zonally averaged latitudes in the southern hemisphere (up to 1.2 mm yr^{-1} difference) are still unexplained.

Trying to reproduce this shape of the mass curve by weighting the fingerprints systematically with plausible values does not replicate these higher southern hemisphere yet lower northern hemisphere trends. Dynamical factors are the most likely explanation as we know that the dynamical bottom pressure signal remains in the mass estimates.

7.5 Future development

The errors in this study were always going to be increased by the spatial bias of the tide gauge network and the relatively short length of altimetry data available. Insight has been gained into the spatial bias of various subsets of tide gauges by observing the zonally averaged trends of altimetry at tide gauge locations. More could be learned about historical spatial bias of tide gauge and steric observations by using GRACE observations, as the time series grows. Tide gauge and steric observations are invaluable for their length of time series and with more understanding of the effects of the spatial bias, interpretation of longer trends will become clearer.

The implications for sea level trends from our results are important. We already know from altimetry that ASL trends are highest in the Western Pacific for the years 1993 to 2010. We have shown how the regional trends are dominated by the steric signal, but that the scale of the global trend is set by the mass contribution, and that this mass contribution is distributed preferentially at latitudes in the Southern Hemisphere. This is an important result for low lying coastal atolls and vulnerable areas within these regions. Future observations will determine whether

this trend persists, making coastal regions in the southern hemisphere even more vulnerable, or whether large scale climatic variability combined with basin scale circulation patterns will combine to partially cancel the effect of these latitudinally dependant higher trends.

A more comprehensive GPS network co-located with tide gauges will alleviate tide gauge VLD issues. Trend differences between the 3 VLD corrections discussed in Chapter 3 can vary by up to 4 mm yr^{-1} of the zonal average and GPS receivers at exact tide gauge locations need to become available. Having accurate VLD data at every tide gauge would mean that data from gauges in vulnerable regions would be able to be used more confidently within global and regional tide gauge assessments. One looks forward to using these future data sets.

Appendix A

Coefficients from all tide gauges

In Chapter 6 we showed the barystatic sea level trends derived from altimetry and tide gauges and assessed the coefficients of melting from West Antarctica, Greenland and glaciers using a least squares method and the fingerprints. Chapter 6 shows the tide gauge results calculated from the sub set of 500 gauges. Here we show an alternative set of results of the coefficients produced from using all tide gauges.

Fingerprint used		West Antarctic, Greenland, Glaciers	std	mse	West Antarctic, Greenland	std	mse	West Antarctica	std	mse	Greenland	std	mse	West Antarctica and glaciers	std	mse	Greenland and glaciers	std	mse	glaciers	std	mse
Data source	coefficient																					
Altimetry	West Antarctica	3.74	1.24		3.53	0.69		2.20	0.11		-	-		4.16	1.08		-	-		-	-	
	Greenland	-1.16	1.56	0.14	-1.43	0.73	0.13	-	-	0.16	2.29	0.19	0.41	-	-	0.13	-3.31	1.83	0.24	-	-	0.29
	Glaciers	-0.50	2.49		-	-		-	-		-	-		-2.11	1.16		5.69	1.85		2.35	0.16	
	total	2.08			2.10			2.20			2.29			2.04			2.38			2.35		
All Tide Gauge (altimetry at TGs)	West Antarctica	3.40	4.54		3.48	2.45		2.84	0.35		-	-		3.68	3.86		-	-		-	-	
	Greenland	-0.79	5.73	1.87	-0.69	2.61	1.70	-	-	1.57	2.97	0.41	1.84	-	-	1.70	-2.75	4.99	1.79	-	-	1.69
	Glaciers	0.19	9.12		-	-		-	-		-	-		-0.92	4.16		5.81	5.06		3.04	0.39	
	total	2.80			2.79			2.84			2.97			2.77			3.06			3.04		
All Tide Gauge GIA corrected	West Antarctica	3.03	1.31		2.27	0.69		2.26	0.34		-	-		2.40	0.89		-	-		-	-	
	Greenland	2.22	3.33	1.98	-0.01	0.71	1.89	-	-	1.73	1.98	0.49	3.42	-	-	1.88	-3.30	2.74	2.77	-	-	2.87
	Glaciers	-3.15	4.57		-	-		-	-		-	-		-0.17	0.98		5.73	2.94		2.24	0.49	
	total	2.10			2.26			2.26			1.98			2.23			2.43			2.24		

TABLE A.1: The table shows the coefficients from a fit where all tide gauges were used in the analysis. As for Chapter 6 but using all tide gauges. Yellow coefficients are plotted in figure (A.2).

Fingerprint used		West Antarctic, Greenland,	std	mse	West Antarctic, Greenland	std	mse	West Antarctica	std	mse	Greenland	std	mse	West Antarctica and glaciers	std	mse	Greenland and glaciers	std	mse	glaciers	std	mse
Weighted data source	coefficient																					
Altimetry	West Antarctica	3.47	1.33		4.10	0.75		2.18	0.11		-	-		4.52	1.11		-	-		-	-	
	Greenland	-3.37	2.51	0.37	-1.99	0.77	0.35	-	-	0.51	2.21	0.18	1.19	-	-	0.40	-7.22	2.51	0.57	-	-	0.91
	Glaciers	2.07	3.59		-	-		-	-		-	-		-2.49	1.18		9.70	2.58		2.29	0.16	
	total	2.17			2.10			2.18			2.21			2.03			2.47			2.29		
All Tide Gauge (altimetry at TGs)	West Antarctica	6.42	3.73		5.07	1.95		2.63	0.29		-	-		6.72	3.06		-	-		-	-	
	Greenland	-0.71	4.44	0.74	-2.42	1.91	0.69	-	-	0.72	2.50	0.34	1.02	-	-	0.68	-4.62	4.14	0.87	-	-	0.89
	Glaciers	-3.16	7.34		-	-		-	-		-	-		-4.20	3.13		7.46	4.33		2.65	0.33	
	total	2.56			2.66			2.63			2.50			2.52			2.84			2.65		
All Tide Gauge GIA corrected	West Antarctica	0.35	0.65		1.44	0.35		2.31	0.21		-	-		0.75	0.45		-	-		-	-	
	Greenland	-1.24	1.43	0.39	1.37	0.48	0.48	-	-	0.77	3.13	0.35	1.14	-	-	0.38	-1.79	0.97	0.36	-	-	0.44
	Glaciers	4.20	2.20		-	-		-	-		-	-		2.39	0.66		5.24	1.02		3.41	0.23	
	total	3.31			2.81			2.31			3.13			3.14			3.45			3.41		

TABLE A.2: The table shows the weighted coefficients from a fit where all tide gauges were used in the analysis. As for Chapter 6 but using all tide gauges in a weighted fit

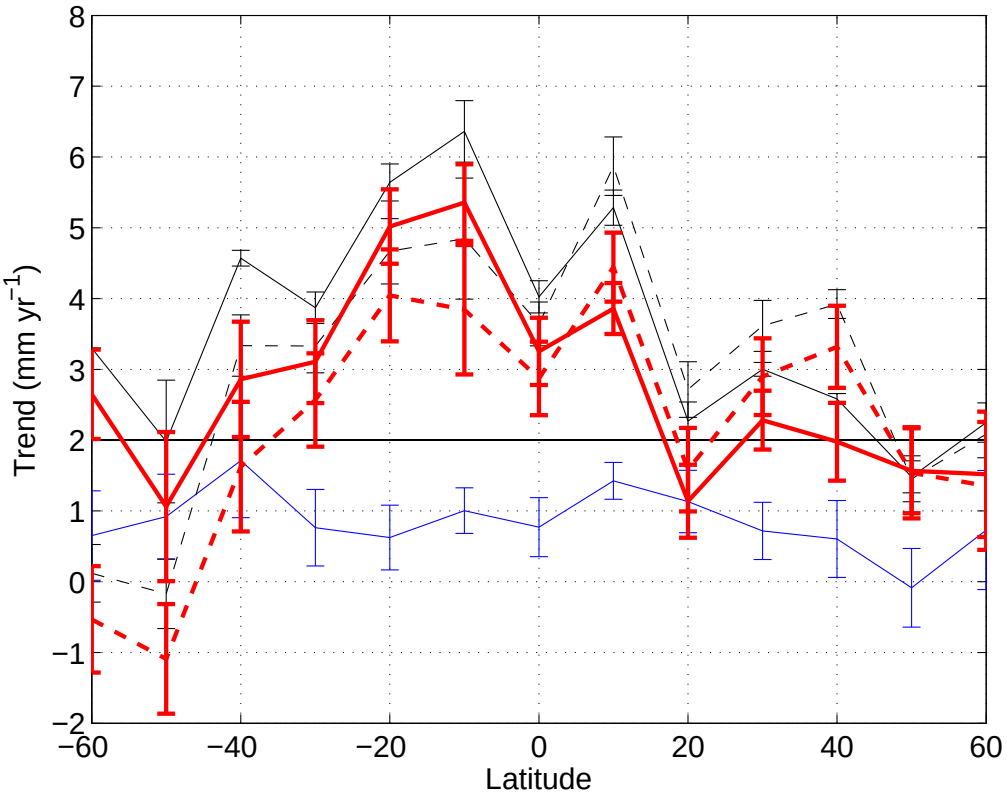

FIGURE A.1: All tide gauges were used to estimate the zonal mass distribution. Tide gauges corrected with ICE-5G (black dash), altimetry at tide gauges (black), steric (blue), mass from tide gauges (red dash), mass from altimetry at tide gauges (red)

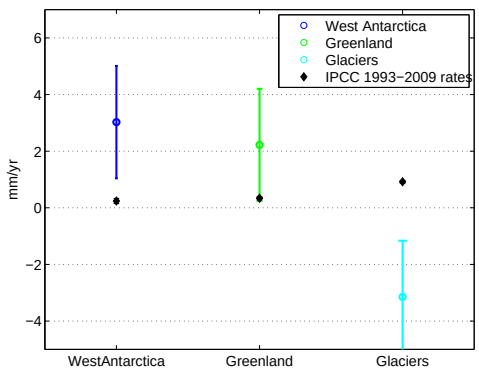

(A) Amplitudes from tide gauges using West Antarctic, Greenland and glacier fingerprints (mm yr^{-1})

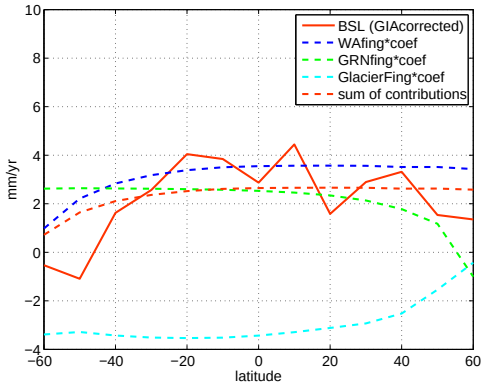

(B) Amplitudes from tide gauges using West Antarctic, Greenland and glacier fingerprints (mm yr^{-1})

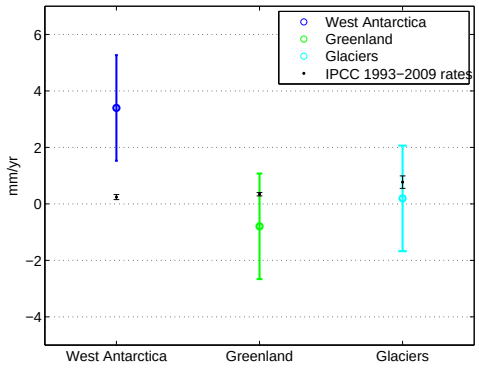

(C) Amplitudes from altimetry at tide gauges using West Antarctic, Greenland and glacier fingerprints (mm yr^{-1})

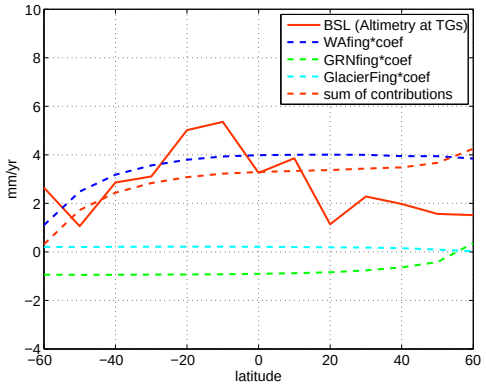

(D) Amplitudes from altimetry at tide gauges using West Antarctic, Greenland and glacier fingerprints (mm yr^{-1})

FIGURE A.2: Unweighted coefficient contributions taken from table (A.1) of tide gauge (figures (A.2a and A.2b) and altimetry at tide gauge (figures (A.2c and A.2d) coefficients using West Antarctic, Greenland and glacier fingerprints (mm yr^{-1})

Bibliography

Ablain, M., A. Cazenave, G. Larnicol, M. Balmaseda, P. Cipollini, Y. Faugère, M. J. Fernandes, O. Henry, J. A. Johannessen, P. Knudsen, O. Andersen, J. Legeais, B. Meyssignac, N. Picot, M. Roca, S. Rudenko, M. G. Scharffenberg, D. Stammer, G. Timms, and J. Benveniste (2015). Improved sea level record over the satellite altimetry era (1993–2010) from the Climate Change Initiative project. *Ocean Science 11*(1), 67–82.

Ablain, M., A. Cazenave, G. Valladeau, and S. Guinehut (2009). A new assessment of the error budget of global mean sea level rate estimated by satellite altimetry over 1993–2008. *Ocean Science 5*(2), 193–201.

Adam, D. (2002). Gravity measurement: Amazing grace. *Nature 416*(6876), 10–11.

Alley, R. B., J. Andrews, J. Brigham-Grette, G. Clarke, K. Cuffey, J. Fitzpatrick, S. Funder, S. Marshall, G. Miller, J. Mitrovica, D. Muhs, B. Otto-Bliesner, L. Polyak, and J. White (2010). History of the greenland ice sheet: paleoclimatic insights. *Special Theme: Arctic Palaeoclimate Synthesis (PP. 1674-1790) 29*(15–16), 1728–1756.

Antonov, J. I., S. Levitus, and T. P. Boyer (2002). Steric sea level variations during 1957–1994: Importance of salinity. *Journal of Geophysical Research: Oceans 107*(C12), 8013.

Arendt, A. A. (2011). Assessing the status of alaska's glaciers. *Science 332*(6033), 1044 –1045.

Barker, P. M., J. R. Dunn, C. M. Domingues, and S. E. Wijffels (2011). Pressure sensor drifts in argo and their impacts. *Journal of Atmospheric and Oceanic Technology 28*(8), 1036–1049.

Beckley, B. D., F. G. Lemoine, S. B. Luthcke, R. D. Ray, and N. P. Zelensky (2007). A reassessment of global and regional mean sea level trends from TOPEX and jason-1 altimetry based on revised reference frame and orbits. *Geophysical Research Letters 34*(14), L14608.

Bindoff, N., J. Willebrand, V. Artale, A. Cazenave, J. Gregory, S. Gulev, K. Hanawa, C. Quere, S. Levitus, Y. Nojiri, C. Shum, L. Talley, and A. Unnikrishnan (2007). Observations: Oceanic climate change and sea level. In *Climate Change 2007: The physical Science Basis. Contribution of Working Group 1 to the Fourth Assessment Report of the Intergovernmental Panel on Climate Change [Solomon, S., D. Qin, M. Manning, Z. Chen, M. Marquis, K.B. Averyt, M. Tignor and H.L. Miller (eds.)]*., AR4 WG1. Cambridge, United Kingdom and New York, NY, USA: Cambridge University Press.

Bingham, R. J. and C. W. Hughes (2012). Local diagnostics to estimate density-induced sea level variations over topography and along coastlines. *Journal of Geophysical Research 117*(C1), C01013.

Boening, C., J. K. Willis, F. W. Landerer, R. S. Nerem, and J. Fasullo (2012). The 2011 La Niña: So strong, the oceans fell. *Geophysical Research Letters 39*(19), L19602.

Bolch, T., A. Kulkarni, A. Kääb, C. Huggel, F. Paul, J. G. Cogley, H. Frey, J. S. Kargel, K. Fujita, M. Scheel, S. Bajracharya, and M. Stoffel (2012). The state and fate of himalayan glaciers. *Science 336*(6079), 310 –314.

Bouin, M. N. and G. Wöppelmann (2010). Land motion estimates from GPS at tide gauges: a geophysical evaluation. *Geophysical Journal International 180*(1), 193–209.

Boyer, T., J. Antonov, H. Garcia, D. Johnson, R. Locarnini, A. Mishonov, M. Pitcher, O. Baranova, and I. Smolyar (2006). *World Ocean Database 2005.* S. Levitus, Ed., NOAA Atlas NESDIS 60, U.S. Government Printing Office, Washington, D.C.,.

Calafat, F. M., D. P. Chambers, and M. N. Tsimplis (2012). Mechanisms of decadal sea level variability in the eastern north atlantic and the mediterranean sea. *Journal of Geophysical Research 117*(C9), C09022.

Carton, J. A., G. Chepurin, X. Cao, and B. Giese (2000). A simple ocean data assimilation analysis of the global upper ocean 1950–95. part i: Methodology. *Journal of Physical Oceanography 30*(2), 294–309.

Carton, J. A. and B. S. Giese (2008). A reanalysis of ocean climate using simple ocean data assimilation (SODA). *Monthly Weather Riview 136*, 2999–3017.

Cazenave, A., K. Dominh, S. Guinehut, E. Berthier, W. Llovel, G. Ramillien, M. Ablain, and G. Larnicol (2009). Sea level budget over 2003–2008: A reevaluation from GRACE space gravimetry, satellite altimetry and argo. *Global and Planetary Change 65*(1–2), 83–88.

Cazenave, A., K. Dominh, F. Ponchaut, L. Soudarin, J. F. Cretaux, and C. Le Provost (1999). Sea level changes from topex-poseidon altimetry and tide gauges, and vertical crustal motions from DORIS. *Geophysical Research Letters 26*(14), 2077–2080.

Cazenave, A. and W. Llovel (2010). Contemporary sea level rise. *Annual Review of Marine Science 2*, 145 – 173.

Chambers, D. P. and J. Schröter (2011). Measuring ocean mass variability from satellite gravimetry. *Journal of Geodynamics 52*(5), 333–343.

Chambers, D. P. and J. K. Willis (2010). A global evaluation of ocean bottom pressure from GRACE, OMCT, and steric-corrected altimetry. *Journal of Atmospheric & Oceanic Technology 27*(8), 1395–1402.

Chao, B. F., Y. H. Wu, and Y. S. Li (2008). Impact of artificial reservoir water impoundment on global sea level. *Science 320*(5873), 212–214.

Chelton, D. B., J. C. Ries, B. J. Haines, L.-L. Fu, and P. S. Callahan (2001). Chapter 1 Satellite Altimetry. In Lee-Lueng Fu and Anny Cazenave (Ed.), *International Geophysics*, Volume Volume 69, pp. 1–11. Academic Press.

Church, J., P. Clark, A. Cazenave, J. Gregory, S. Jevrejeva, A. Levermann, M. Merrifield, G. Milne, R. Nerem, P. Nunn, A. Payne, W. Pfeffer, D. Stammer, and A. Unnikrishnan (2013). *Sea Level Change*, Book section 13, pp. 1137–1216. Cambridge, United Kingdom and New York, NY, USA: Cambridge University Press.

Church, J. and N. White (2011). Sea-Level Rise from the Late 19th to the Early 21st Century. *Surveys in Geophysics 32*(4-5), 585–602.

Church, J., N. White, T. Aarup, W. Wilson, P. Woodworth, C. Domingues, J. Hunter, and K. Lambeck (2008). Understanding global sea levels: past, present and future. *Sustainability Science 3*(1), 9–22.

Church, J. A. and N. J. White (2006). A 20th century acceleration in global sea-level rise. *Geophysical Research Letters 33*(1), L01602.

Church, J. A., N. J. White, and J. M. Arblaster (2005). Significant decadal-scale impact of volcanic eruptions on sea level and ocean heat content. *Nature 438*(7064), 74–77.

Church, J. A., N. J. White, R. Coleman, K. Lambeck, and J. X. Mitrovica (2004). Estimates of the regional distribution of sea level rise over the 1950–2000 period. *Journal of Climate 17*(13), 2609–2625.

Church, J. A., N. J. White, L. F. Konikow, C. M. Domingues, J. G. Cogley, E. Rignot, J. M. Gregory, M. R. van den Broeke, A. J. Monaghan, and I. Velicogna (2011). Revisiting the earth's sea-level and energy budgets from 1961 to 2008. *Geophysical Research Letters 38*(18), L18601.

Clark, J. A., W. E. Farrell, and W. Peltier (1978). Global changes in postglacial sea level: A numerical calculation. *Quaternary Research 9*(3), 265–287.

Cogley, G. (2012). Chapter 8 - the future of the world's glaciers. In A. Henderson-Sellers and K. McGuffie (Eds.), *The Future of the World's Climate (Second Edition)*, pp. 197–222. Boston: Elsevier.

Conkright, M., R. Locarnini, H. Garcia, T. O'Brien, T. Boyer, C. Stephens, and J. Antonov (2002). World Ocean Atlas 2001: Objective Analyses, Data Statistics, and Figures, CD-ROM Documentation.

Domingues, C. M., J. A. Church, N. J. White, P. J. Gleckler, S. E. Wijffels, P. M. Barker, and J. R. Dunn (2008). Improved estimates of upper-ocean warming and multi-decadal sea-level rise. *Nature 453*(7198), 1090–1093.

Dutton, A. and K. Lambeck (2012). Ice Volume and Sea Level During the Last Interglacial. *Science 337*(6091), 216–219.

Fasullo, J. T., C. Boening, F. W. Landerer, and R. S. Nerem (2013). Australia's unique influence on global sea level in 2010–2011. *Geophysical Research Letters 40*(16), 4368–4373.

Feng, M., C. Boning, A. Biastoch, E. Behrens, E. Weller, and Y. Masumoto (2011). The reversal of the multi-decadal trends of the equatorial pacific easterly winds, and the indonesian throughflow and leeuwin current transports. *Geophysical Research Letters 38*(11), L11604.

Gehrels, W. R. and P. L. Woodworth (2013). When did modern rates of sea-level rise start? *Global and Planetary Change 100*(0), 263–277.

Gille, S. T. (2002). Warming of the Southern Ocean Since the 1950s. *Science 295*(5558), 1275–1277.

Gordon, C., C. Cooper, C. A. Senior, H. Banks, J. M. Gregory, T. C. Johns, J. F. B. Mitchell, and R. A. Wood (2000). The simulation of SST, sea ice extents and ocean heat transports in a version of the hadley centre coupled model without flux adjustments. *Climate Dynamics 16*(2-3), 147–168.

Gornitz, V. (2009). Sea Level Change, Post-Glacial. In V. Gornitz (Ed.), *Encyclopedia of Paleoclimatology and Ancient Environments*, Encyclopedia of Earth Sciences Series, pp. 887–893. Springer Netherlands.

Gouretski, V. and K.-P. Koltermann (2007). How much is the ocean really warming? *Geophysical Research Letters, 34, L01610*.

Gregory, J. M., N. J. White, J. A. Church, M. F. P. Bierkens, J. E. Box, M. R. van den Broeke, J. G. Cogley, X. Fettweis, E. Hanna, P. Huybrechts, L. F. Konikow, P. W. Leclercq, B. Marzeion, J. Oerlemans, M. E. Tamisiea, Y. Wada, L. M. Wake, and R. S. W. van de Wal (2012). Twentieth-century global-mean sea level rise: Is the whole greater than the sum of the parts? *Journal of Climate 26*(13), 4476–4499.

Grinsted, A. (2013). An estimate of global glacier volume. *The Cryosphere 7*(1), 141–151.

Grinsted, A., J. C. Moore, and S. Jevrejeva (2007). Observational evidence for volcanic impact on sea level and the global water cycle. *Proceedings of the National Academy of Sciences 104*(50), 19730–19734.

Guinehut, S., C. Coatanoan, A.-L. Dhomps, P.-Y. Le Traon, and G. Larnicol (2009). On the Use of Satellite Altimeter Data in Argo Quality Control. *Journal of Atmospheric and Oceanic Technology 26*(2), 395–402.

Haigh, I. D., M. Eliot, and C. Pattiaratchi (2011). Global influences of the 18.61 year nodal cycle and 8.85 year cycle of lunar perigee on high tidal levels. *Journal of Geophysical Research: Oceans 116*(C6), C06025.

Hanawa, K., P. Rual, R. Bailey, A. Sy, and M. Szabados (1995). A new depth-time equation for sippican or TSK t-7, t-6 and t-4 expendable bathythermographs (XBT). *Deep Sea Research Part I: Oceanographic Research Papers 42*(8), 1423–1451.

Harper, J., N. Humphrey, W. T. Pfeffer, J. Brown, and X. Fettweis (2012). Greenland ice-sheet contribution to sea-level rise buffered by meltwater storage in firn. *Nature 491*(7423), 240–243.

Hay, C. C., E. Morrow, R. E. Kopp, and J. X. Mitrovica (2015). Probabilistic reanalysis of twentieth-century sea-level rise. *Nature 517*(7535), 481–484.

Heinmiller, R. H., C. C. Ebbesmeyer, B. A. Taft, D. B. Olson, and O. P. Nikitin (1983). Systematic errors in expendable bathythermograph (XBT) profiles. *Deep Sea Research Part A. Oceanographic Research Papers 30*(11), 1185–1196.

Holgate, S. J. (2007). On the decadal rates of sea level change during the twentieth century. *Geophysical Research Letters 34*(1), L01602.

Holgate, S. J., A. Matthews, P. L. Woodworth, L. J. Rickards, M. E. Tamisiea, E. Bradshaw, P. R. Foden, K. M. Gordon, S. Jevrejeva, and J. Pugh (2012). New data systems and products at the permanent service for mean sea level. *Journal of Coastal Research*, 493–504.

Holgate, S. J. and P. L. Woodworth (2004). Evidence for enhanced coastal sea level rise during the 1990s. *Geophysical Research Letters 31*(7), L07305.

Hughes, C. W. and R. J. Bingham (2008). An oceanographer's guide to GOCE and the geoid. *Ocean Science 4*(1), 15–29.

Hughes, C. W., M. E. Tamisiea, R. J. Bingham, and J. Williams (2012). Weighing the ocean: Using a single mooring to measure changes in the mass of the ocean. *Geophysical Research Letters 39*(17), L17602.

Huss, M. and D. Farinotti (2012). Distributed ice thickness and volume of all glaciers around the globe. *Journal of Geophysical Research: Earth Surface 117*(F4), F04010.

IERS (2010). IERS Conventions. International Earth Rotation and Reference Systems Service (IERS) Technical Note No. 36 (eds. G. Petit and B. Luzam).

Ingleby, B. and M. Huddleston (2007). Quality control of ocean temperature and salinity profiles – historical and real-time data. *Journal of Marine Systems 65*(1-4), 158–175.

Ishii, M. and M. Kimoto (2009). Reevaluation of historical ocean heat content variations with time-varying XBT and MBT depth bias corrections. *Journal of Oceanography 65*(3), 287–299.

Ishii, M., M. Kimoto, and M. Kachi (2003). Historical Ocean Subsurface Temperature Analysis with Error Estimates. *Monthly Weather Review 131*(1), 51–73.

Ishii, M., M. Kimoto, and M. Kachi (2005). Subsurface Temperature And Salinity Analyses. Frontier Research System for Global Change. Japan Marine Science and Technology Center.

Ishii, M., M. Kimoto, K. Sakamoto, and S.-I. Iwasaki (2006). Steric sea level changes estimated from historical ocean subsurface temperature and salinity analyses. *Journal of Oceanography 62*(2), 155–170.

Ivins, E. R., T. S. James, J. Wahr, E. J. O. Schrama, F. W. Landerer, and K. M. Simon (2013). Antarctic contribution to sea level rise observed by GRACE with improved GIA correction. *Journal of Geophysical Research: Solid Earth 118*(6), 3126–3141.

Jacob, T., J. Wahr, W. T. Pfeffer, and S. Swenson (2012). Recent contributions of glaciers and ice caps to sea level rise. *Nature 482*(7386), 514–518.

Jevrejeva, S., A. Grinsted, and J. C. Moore (2009). Anthropogenic forcing dominates sea level rise since 1850. *Geophysical Research Letters. 36*(20), L20706.

Jevrejeva, S., A. Grinsted, J. C. Moore, and S. Holgate (2006). Nonlinear trends and multiyear cycles in sea level records. *Journal of Geophysical Research: Oceans 111*(C9), C09012.

Jevrejeva, S., J. Moore, A. Grinsted, A. Matthews, and G. Spada (2014). Trends and acceleration in global and regional sea levels since 1807. *Global and Planetary Change 113*(0), 11–22.

Jevrejeva, S., J. C. Moore, and A. Grinsted (2008). Relative importance of mass and volume changes to global sea level rise. *Journal of Geophysical Research 113*(D8), D08105.

Jevrejeva, S., J. C. Moore, A. Grinsted, and P. L. Woodworth (2008). Recent global sea level acceleration started over 200 years ago? *Geophysical Research Letters 35*(8), L08715.

Johnson, G. C. (2008). Quantifying antarctic bottom water and north atlantic deep water volumes. *Journal of Geophysical Research 113*(C5), C05027.

King, M. A., M. Keshin, P. L. Whitehouse, I. D. Thomas, G. Milne, and R. E. M. Riva (2012). Regional biases in absolute sea-level estimates from tide gauge data due to residual unmodeled vertical land movement. *Geophysical Research Letters 39*(14), L14604.

Kopp, R. E., F. J. Simons, J. X. Mitrovica, A. C. Maloof, and M. Oppenheimer (2009). Probabilistic assessment of sea level during the last interglacial stage. *Nature 462*(7275), 863–867.

Kouketsu, S., T. Doi, T. Kawano, S. Masuda, N. Sugiura, Y. Sasaki, T. Toyoda, H. Igarashi, Y. Kawai, K. Katsumata, H. Uchida, M. Fukasawa, and T. Awaji (2011). Deep ocean heat content changes estimated from observation and reanalysis product and their influence on sea level change. *Journal of Geophysical Research 116*(C3), C03012.

Leuliette, E. W., R. S. Nerem, and G. T. Mitchum (2004). Calibration of TOPEX/-Poseidon and Jason Altimeter Data to Construct a Continuous Record of Mean Sea Level Change. *Marine Geodesy 27*(1/2), 79–94.

Leuliette, E. W. and R. Scharroo (2010). Integrating Jason-2 into a Multiple-Altimeter Climate Data Record. *Marine Geodesy 33*(sup1), 504–517.

Leuliette, E. W. and J. K. Willis (2011). Balancing the sea level budget. *Oceanography 24*(2), 122–129.

Levitus, S., J. I. Antonov, T. P. Boyer, R. A. Locarnini, H. E. Garcia, and A. V. Mishonov (2009). Global ocean heat content 1955–2008 in light of recently revealed instrumentation problems. *Geophysical Research Letters 36*(7), L07608.

Listing, J. (1873). Über unsere jetzige Kenntniss der Gestalt und Grösse der Erde. In *Nachrichten von der Koenig!. Gesellschaft der Wissenschaften und der G.A. Universitaet zu Goettingen*, Volume No 3, pp. 33–98. Goettingen VLG der Dietrichschen Buchhandlung.

Llovel, W., B. Meyssignac, and A. Cazenave (2011). Steric sea level variations over 2004–2010 as a function of region and depth: Inference on the mass component variability in the north atlantic ocean. *Geophysical Research Letters 38*(15), L15608.

Lombard, A., A. Cazenave, K. DoMinh, C. Cabanes, and R. S. Nerem (2005). Thermosteric sea level rise for the past 50 years; comparison with tide gauges and inference on water mass contribution. *Global and Planetary Change 48*(4), 303–312.

Lorbacher, K., S. J. Marsland, J. A. Church, S. M. Griffies, and D. Stammer (2012). Rapid barotropic sea level rise from ice sheet melting. *Journal of Geophysical Research 117*(C6), C06003.

Lozier, M. S., S. Leadbetter, R. G. Williams, V. Roussenov, M. S. C. Reed, and N. J. Moore (2008). The spatial pattern and mechanisms of heat-content change in the north atlantic. *Science 319*(5864), 800 –803.

Lyman, J. M., S. A. Good, V. V. Gouretski, M. Ishii, G. C. Johnson, M. D. Palmer, D. M. Smith, and J. K. Willis (2010). Robust warming of the global upper ocean. *Nature 465*(7296), 334–337.

Lyman, J. M. and G. C. Johnson (2008). Estimating annual global upper-ocean heat content anomalies despite irregular in situ ocean sampling*. *Journal of Climate 21*(21), 5629–5641.

Marcos, M., F. M. Calafat, W. Llovel, D. Gomis, and B. Meyssignac (2011). Regional distribution of steric and mass contributions to sea level changes. *Global and Planetary Change 76*(3–4), 206–218.

McDougall, T. J. (2003). Potential enthalpy: A conservative oceanic variable for evaluating heat content and heat fluxes. *Journal of Physical Oceanography 33*(5), 945–963.

McDougall, T. J. and P. M. Barker (2011). *Getting started with TEOS-10 and the Gibbs Seawater (GSW) Oceanographic Toolbox*. SCOR/IAPSO WG127.

McDougall, T. J., D. R. Jackett, D. G. Wright, and R. Feistel (2003). Accurate and computationally efficient algorithms for potential temperature and density of seawater. *Journal of Atmospheric and Oceanic Technology 20*(5), 730–741.

McKay, N. P., J. T. Overpeck, and B. L. Otto-Bliesner (2011). The role of ocean thermal expansion in Last Interglacial sea level rise. *Geophysical Research Letters 38*(14), L14605.

Meier, M. F., M. B. Dyurgerov, U. K. Rick, S. O'Neel, W. T. Pfeffer, R. S. Anderson, S. P. Anderson, and A. F. Glazovsky (2007). Glaciers dominate eustatic sea-level rise in the 21st century. *Science 317*(5841), 1064–1067.

Merrifield, M. A., S. T. Merrifield, and G. T. Mitchum (2009). An anomalous recent acceleration of global sea level rise. *Journal of Climate 22*(21), 5772–5781.

Merrifield, M. A., P. R. Thompson, and M. Lander (2012). Multidecadal sea level anomalies and trends in the western tropical pacific. *Geophysical Research Letters 39*(13), L13602.

Miller, K. G., J. D. Wright, J. V. Browning, A. Kulpecz, M. Kominz, T. R. Naish, B. S. Cramer, Y. Rosenthal, W. R. Peltier, and S. Sosdian (2012). High tide of the warm Pliocene: Implications of global sea level for Antarctic deglaciation. *Geology*.

Millero, F. J., R. Feistel, D. G. Wright, and T. J. McDougall (2008). The composition of standard seawater and the definition of the reference-composition salinity scale. *Deep Sea Research Part I: Oceanographic Research Papers 55*(1), 50–72.

Mitchum, G. T., R. S. Nerem, M. A. Merrifield, and W. R. Gehrels (2010). Modern sea-level-change estimates. In *Understanding Sea-Level Rise and Variability*, pp. 122–142. Wiley-Blackwell.

Mitrovica, J. X., N. Gomez, E. Morrow, C. Hay, K. Latychev, and M. E. Tamisiea (2011). On the robustness of predictions of sea level fingerprints. *Geophysical Journal International 187*(2), 729–742.

Nakano, H. and N. Suginohara (2002). Importance of the eastern indian ocean for the abyssal pacific. *Journal of Geophysical Research: Oceans 107*(C12), 3219.

Nerem, R. S., D. P. Chambers, C. Choe, and G. T. Mitchum (2010). Estimating Mean Sea Level Change from the TOPEX and Jason Altimeter Missions. *Marine Geodesy 33*(sup1), 435–446.

Nerem, R. S., r. Leuliette, and A. Cazenave (2006). Present-day sea-level change: A review. *La Terre observée depuis l'espace Observing the Earth from space 338*(14–15), 1077–1083.

Nerem, R. S. and G. T. Mitchum (2002). Estimates of vertical crustal motion derived from differences of TOPEX/POSEIDON and tide gauge sea level measurements. *Geophysical Research Letters 29*(19), 1934.

Palmer, M. D. and K. Haines (2009). Estimating oceanic heat content change using isotherms. *Journal of Climate 22*(19), 4953–4969.

Peltier (2004). Global glacial isostacy and the surface of the ice age earth: The ICE-5G (VM2) model and grace. *Annual Review of Earth and Planetary Sciences 32*, 111–149.

Peltier, W. (2001). Chapter 4 global glacial isostatic adjustment and modern instrumental records of relative sea level history. In M. S. K. a. S. P. L. Bruce C. Douglas (Ed.), *International Geophysics*, Volume Volume 75, pp. 65–95. Academic Press.

Pugh, D. and P. Woodworth (2014). *Sea-Level Science. Understanding Tides, Surges, Tsunamis and Mean Sea-Level Changes*. Cambridge University Press.

Purkey, S. G. and G. C. Johnson (2010). Warming of global abyssal and deep southern ocean waters between the 1990s and 2000s: Contributions to global heat and sea level rise budgets. *Journal of Climate 23*(23), 6336–6351.

Purkey, S. G. and G. C. Johnson (2012). Global contraction of antarctic bottom water between the 1980s and 2000s. *Journal of Climate 25*(17), 5830–5844.

Quinn, K. J. and R. M. Ponte (2010). Uncertainty in ocean mass trends from grace. *Geophysical Journal International 181*(2), 762–768.

Radic, V. and R. Hock (2011). Regionally differentiated contribution of mountain glaciers and ice caps to future sea-level rise. *Nature Geoscience 4*(2), 91–94.

Rhein, M., S. Rintoul, S. Aoki, E. Campos, D. Chambers, R. Feely, S. Gulev, G. Johnson, S. Josey, A. Kostianoy, C. Mauritzen, D. Roemmich, L. Talley, and

F. Wang (2013). *Observations: Ocean*, Book section 3, pp. 255–316. Cambridge, United Kingdom and New York, NY, USA: Cambridge University Press.

Roemmich, D., W. John Gould, and J. Gilson (2012). 135 years of global ocean warming between the challenger expedition and the argo programme. *Nature Climate Change advance online publication*.

Roemmich, D., G. Johnson, S. Riser, R. Davis, J. Gilson, W. Owens, S. Garzoli, C. Schmid, and M. Ignaszewski (2009). The Argo Program: Observing the global ocean with profiling floats. *Oceanography 22*(2), 34–43.

Rye, C. D., A. C. Naveira Garabato, P. R. Holland, M. P. Meredith, A. J. George Nurser, C. W. Hughes, A. C. Coward, and D. J. Webb (2014). Rapid sea-level rise along the antarctic margins in response to increased glacial discharge. *Nature Geoscience advance online publication*.

Sallenger, A. H., K. S. Doran, and P. A. Howd (2012). Hotspot of accelerated sea-level rise on the atlantic coast of north america. *Nature Climate Change 2*(12), 884–888.

Santamaría-Gómez, A., M. Gravelle, X. Collilieux, M. Guichard, B. M. Míguez, P. Tiphaneau, and G. Wöppelmann (2012). Mitigating the effects of vertical land motion in tide gauge records using a state-of-the-art GPS velocity field. *Global and Planetary Change 98–99*(0), 6–17.

Santamaría-Gómez, A., M. Gravelle, and G. Wöppelmann (2014). Long-term vertical land motion from double-differenced tide gauge and satellite altimetry data. *Journal of Geodesy 88*(3), 207–222.

Shepherd, A., E. R. Ivins, G. A, V. R. Barletta, M. J. Bentley, S. Bettadpur, K. H. Briggs, D. H. Bromwich, R. Forsberg, N. Galin, M. Horwath, S. Jacobs, I. Joughin, M. A. King, J. T. M. Lenaerts, J. Li, S. R. M. Ligtenberg, A. Luckman, S. B. Luthcke, M. McMillan, R. Meister, G. Milne, J. Mouginot, A. Muir, J. P. Nicolas, J. Paden, A. J. Payne, H. Pritchard, E. Rignot, H. Rott, L. S. Sørensen, T. A. Scambos, B. Scheuchl, E. J. O. Schrama, B. Smith, A. V. Sundal, J. H. van Angelen, W. J. van de Berg, M. R. van den Broeke, D. G. Vaughan, I. Velicogna, J. Wahr, P. L. Whitehouse, D. J. Wingham, D. Yi, D. Young, and H. J. Zwally (2012). A reconciled estimate of ice-sheet mass balance. *Science 338*(6111), 1183–1189.

Smith, D. M., S. Cusack, A. W. Colman, C. K. Folland, G. R. Harris, and J. M. Murphy (2007). Improved surface temperature prediction for the coming decade from a global climate model. *Science 317*(5839), 796 –799.

Smith, D. M. and J. M. Murphy (2007). An objective ocean temperature and salinity analysis using covariances from a global climate model. *Journal of Geophysical Research 112*(C2), C02022.

Solomon, S., D. Qin, M. Manning, Z. Chen, M. Marquis, K. Averyt, M. Tigor, and H. e. Miller (2007). Contribution of Working Group I to the Fourth Assessment Report of the Intergovernmental Panel on Climate Change, 2007.

Song, Y. T. and F. Colberg (2011). Deep ocean warming assessed from altimeters, gravity recovery and climate experiment, in situ measurements, and a non-boussinesq ocean general circulation model. *Journal of Geophysical Research 116*(C2), C02020.

Stocker, T., D. Qin, G. Plattner, L. Alexander, S. Allen, N. Bindoff, F. Breon, J. Church, U. Cubasch, S. Emori, P. Forster, P. Friedlingstein, N. Gillett, J. Gregory, D. Hartmann, E. Jansen, B. Kirtman, R. Knutti, K. Krishna Kumar, P. Lemke, J. Marotzke, V. Masson-Delmotte, G. Meehl, I. Mokhov, S. Piao, V. Ramaswamy, D. Randall, M. Rhein, M. Rojas, C. Sabine, D. Shindell, L. Talley, D. Vaughan, and S.-P. Xie (2013). *Climate Change 2013: The Physical Science Basis. Contribution of Working Group I to the Fifth Assessment Report of the Intergovernmental Panel on Climate Change*. Cambridge, United Kingdom and New York, NY, USA: Cambridge University Press.

Tai, C.-K. (2011). Inferring the global mean sea level from a global tide gauge network. *Acta Oceanologica Sinica 30*(4), 102–106.

Tamisiea, M. E. (2011). Ongoing glacial isostatic contributions to observations of sea level change. *Geophysical Journal International 186*(3), 1036–1044.

Tamisiea, M. E. and J. X. Mitrovica (2011). The moving boundaries of sea level change: Understanding the origins of geographic variability. *Oceanography 24*(2), 24–39.

Tamisiea, M. E., J. X. Mitrovica, G. A. Milne, and J. L. Davis (2001). Global geoid and sea level changes due to present-day ice mass fluctuations. *Journal of Geophysical Research: Solid Earth 106*(B12), 30849–30863.

Tedesco, M., X. Fettweis, T. Mote, J. Wahr, P. Alexander, J. E. Box, and B. Wouters (2013). Evidence and analysis of 2012 greenland records from spaceborne observations, a regional climate model and reanalysis data. *The Cryosphere 7*(2), 615–630.

Thompson, P. R. and M. A. Merrifield (2014). A unique asymmetry in the pattern of recent sea level change. *Geophysical Research Letters 41*(21), 7675–7683.

Tsimplis, M. N., F. M. Calafat, M. Marcos, G. Jordà, D. Gomis, L. Fenoglio-Marc, M. V. Struglia, S. A. Josey, and D. Chambers (2013). The effect of the NAO on sea level and on mass changes in the mediterranean sea. *Journal of Geophysical Research: Oceans 118*(2), 944–952.

Valladeau, G., J. F. Legeais, M. Ablain, S. Guinehut, and N. Picot (2012). Comparing altimetry with tide gauges and argo profiling floats for data quality assessment and mean sea level studies. *Marine Geodesy 35*(sup1), 42–60.

Vaughan, D., J. Comiso, I. Allison, J. Carrasco, G. Kaser, R. Kwok, P. Mote, T. Murray, F. Paul, J. Ren, E. Rignot, O. Solomina, K. Steffen, and T. Zhang (2013). *Observations: Cryosphere In: Climate Change 2013: The Physical Science Basis. Contribution of Working Group I to the Fifth Assessment Report of the Intergovernmental Panel on Climate Change*, Book section 4, pp. 317–382. Cambridge, United Kingdom and New York, NY, USA: Cambridge University Press.

Wake, L., G. Milne, and E. Leuliette (2006). 20th century sea-level change along the eastern US: Unravelling the contributions from steric changes, greenland ice sheet mass balance and late pleistocene glacial loading. *Earth and Planetary Science Letters 250*(3–4), 572–580.

Wijffels, S. E., J. Willis, C. M. Domingues, P. Barker, N. J. White, A. Gronell, K. Ridgway, and J. A. Church (2008). Changing expendable bathythermograph fall rates and their impact on estimates of thermosteric sea level rise. *Journal of Climate 21*(21), 5657–5672.

Williams, J. and C. W. Hughes (2012). The coherence of small island sea-level with the wider ocean: a model study. *Ocean Science 9*(5).

Williams, J., C. W. Hughes, M. E. Tamisiea, and S. D. P. Williams (2014). Weighing the ocean with bottom-pressure sensors: robustness of the ocean mass annual cycle estimate. *Ocean Science 10*(4), 701–718.

Williams, R. G., V. Roussenov, D. Smith, and M. S. Lozier (2014). Decadal evolution of ocean thermal anomalies in the north atlantic: The effects of ekman, overturning, and horizontal transport. *Journal of Climate 27*(2), 698–719.

Willis, J. K., D. Roemmich, and B. Cornuelle (2004). Interannual variability in upper ocean heat content, temperature, and thermosteric expansion on global scales. *Journal of Geophysical Research 109*(C12), C12036.

Woodward, R. S. (1888). On the form and position of the sea level with special references to its dependence on superficial masses symmetrically disposed about a normal to the earth's surface. *Bulletin of the United States Geological Survey* (48).

Woodworth, P., P. Foden, J. Pugh, A. Mathews, T. Aarup, A. Aman, E. Nkebi, J. Odametey, R. Facey, M. Y. A. Esmail, and M. Ashraf (2009). Insight into long term sea level change based on new tide gauge installations at Takoradi, Aden and Karachi. *International Hydrographic Review 1*, 18–23.

Woodworth, P., M. Menéndez, and W. Roland Gehrels (2011). Evidence for Century-Timescale Acceleration in Mean Sea Levels and for Recent Changes in Extreme Sea Levels. *Surveys in Geophysics 32*(4-5), 603–618.

Woodworth, P. L. (1990). A search for accelerations in records of european mean sea level. *International Journal of Climatology 10*(2), 129–143.

Woodworth, P. L. (2011). A note on the nodal tide in sea level records. *Journal of Coastal Research*, 316–323.

Woodworth, P. L. and D. L. Blackman (2004). Evidence for systematic changes in extreme high waters since the mid-1970s. *Journal of Climate 17*(6), 1190–1197.

Woodworth, P. L., N. J. White, S. Jevrejeva, S. J. Holgate, J. A. Church, and W. R. Gehrels (2009). Evidence for the accelerations of sea level on multi-decade and century timescales. *International Journal of Climatology 29*(6), 777–789.

Wright, D. G., Pawlowicz, R., McDougall, T. J., Feistel, R., and Marion, G. M. (2011). Absolute salinity, "density salinity" and the reference-composition salinity scale: present and future use in the seawater standard TEOS-10. *Ocean Science Copernicus Publications 7*(1).

Wunsch, C., R. M. Ponte, and P. Heimbach (2007). Decadal trends in sea level patterns: 1993–2004. *Journal of Climate 20*(24), 5889–5911.

Zhang, X. and J. A. Church (2012). Sea level trends, interannual and decadal variability in the pacific ocean. *Geophysical Research Letters 39*(21), L21701.